Angular approach based multiphysics modeling of electric motors for analyzing dynamic behaviors under the influence of different architectures

Xiaowen Li

N°d'ordre NNT : 2021LYSE048

THESE de DOCTORAT DE L'UNIVERSITE DE LYON
opérée au sein de
L'INSA LYON

Ecole Doctorale N° 162 MEGA
Mécanique, Énergétique, Génie Civil, Acoustique

Spécialité/ discipline de doctorat :
GÉNIE MÉCANIQUE

Soutenue publiquement le 01/09/2021, par :
Xiaowen LI

Angular approach based multiphysics modeling of electric motors for analyzing dynamic behaviors under the influence of different architectures

---

Devant le jury composé de :

HETZLER, Hartmut	Professeur	Université Kassel	Examinateur
LEMAIRE SEMAIL, Betty	Professeur	Université Lille 1	Rapporteure
CHEVALLIER, Gael	Professeur	L'institut FEMTO-ST	Rapporteur
MCCLELLAND, Mike	Directeur R&D	NIDEC LEROY-SOMER	Examinateur
CLERC, Guy	Professeur	Université Lyon 1	Examinateur
BOURDON, Adeline	Maître de Conférences	INSA-LYON	Encadrant de thèse
REMOND, Didier	Professeur	INSA-LYON	Directeur de thèse
KOECHLIN, Samuel	Responsable mécanique	NIDEC LEROY-SOMER	Invité

Département FEDORA – INSA Lyon - Ecoles Doctorales

SIGLE	ECOLE DOCTORALE	NOM ET COORDONNEES DU RESPONSABLE
CHIMIE	**CHIMIE DE LYON** **https://www.edchimie-lyon.fr** Sec. : Renée EL MELHEM Bât. Blaise PASCAL, 3e étage secretariat@edchimie-lyon.fr	**M. Stéphane DANIELE** C2P2-CPE LYON-UMR 5265 Bâtiment F308, BP 2077 43 Boulevard du 11 novembre 1918 69616 Villeurbanne **directeur@edchimie-lyon.fr**
E.E.A.	**ÉLECTRONIQUE, ÉLECTROTECHNIQUE, AUTOMATIQUE** **https://edeea.universite-lyon.fr** Sec. : Stéphanie CAUVIN Bâtiment Direction INSA Lyon Tél : 04.72.43.71.70 secretariat.edeea@insa-lyon.fr	**M. Philippe DELACHARTRE** INSA LYON Laboratoire CREATIS Bâtiment Blaise Pascal, 7 avenue Jean Capelle 69621 Villeurbanne CEDEX Tél : 04.72.43.88.63 **philippe.delachartre@insa-lyon.fr**
E2M2	**ÉVOLUTION, ÉCOSYSTÈME, MICROBIOLOGIE, MODÉLISATION** **http://e2m2.universite-lyon.fr** Sec. : Sylvie ROBERJOT Bât. Atrium, UCB Lyon 1 Tél : 04.72.44.83.62 secretariat.e2m2@univ-lyon1.fr	**M. Philippe NORMAND** Université Claude Bernard Lyon 1 UMR 5557 Lab. d'Ecologie Microbienne Bâtiment Mendel 43, boulevard du 11 Novembre 1918 69 622 Villeurbanne CEDEX **philippe.normand@univ-lyon1.fr**
EDISS	**INTERDISCIPLINAIRE SCIENCES-SANTÉ** **http://ediss.universite-lyon.fr** Sec. : Sylvie ROBERJOT Bât. Atrium, UCB Lyon 1 Tél : 04.72.44.83.62 secretariat.ediss@univ-lyon1.fr	**Mme Sylvie RICARD-BLUM** Institut de Chimie et Biochimie Moléculaires et Supramoléculaires (ICBMS) - UMR 5246 CNRS - Université Lyon 1 Bâtiment Raulin - 2ème étage Nord 43 Boulevard du 11 novembre 1918 69622 Villeurbanne Cedex Tél : +33(0)4 72 44 82 32 **sylvie.ricard-blum@univ-lyon1.fr**
INFOMATHS	**INFORMATIQUE ET MATHÉMATIQUES** **http://edinfomaths.universite-lyon.fr** Sec. : Renée EL MELHEM Bât. Blaise PASCAL, 3e étage Tél : 04.72.43.80.46 infomaths@univ-lyon1.fr	**M. Hamamache KHEDDOUCI** Université Claude Bernard Lyon 1 Bât. Nautibus 43, Boulevard du 11 novembre 1918 69 622 Villeurbanne Cedex France Tél : 04.72.44.83.69 **hamamache.kheddouci@univ-lyon1.fr**
Matériaux	**MATÉRIAUX DE LYON** **http://ed34.universite-lyon.fr** Sec. : Yann DE ORDENANA Tél : 04.72.18.62.44 yann.de-ordenana@ec-lyon.fr	**M. Stéphane BENAYOUN** Ecole Centrale de Lyon Laboratoire LTDS 36 avenue Guy de Collongue 69134 Ecully CEDEX Tél : 04.72.18.64.37 **stephane.benayoun@ec-lyon.fr**
MEGA	**MÉCANIQUE, ÉNERGÉTIQUE, GÉNIE CIVIL, ACOUSTIQUE** **http://edmega.universite-lyon.fr** Sec. : Stéphanie CAUVIN Tél : 04.72.43.71.70 Bâtiment Direction INSA Lyon mega@insa-lyon.fr	**M. Jocelyn BONJOUR** INSA Lyon Laboratoire CETHIL Bâtiment Sadi-Carnot 9, rue de la Physique 69621 Villeurbanne CEDEX **jocelyn.bonjour@insa-lyon.fr**
ScSo	**ScSo*** **https://edsciencessociales.universite-lyon.fr** Sec. : Mélina FAVETON INSA : J.Y. TOUSSAINT Tél : 04.78.69.77.79 melina.faveton@univ-lyon2.fr	**M. Christian MONTES** Université Lumière Lyon 2 86 Rue Pasteur 69365 Lyon CEDEX 07 **christian.montes@univ-lyon2.fr**

*ScSo : Histoire, Géographie, Aménagement, Urbanisme, Archéologie, Science politique, Sociologie, Anthropologie

Acknowledgments

This thesis was financed by the French National Agency of Research and Technology (ANRT) and the Company Nidec Leroy Somer. All the research works were carried out mainly in the laboratory LaMCoS of INSA Lyon and at the company of Nidec. Foremostly, I would like to express my gratitude to these organizations and all the people behind for having offered me this opportunity to work on this project.

I owe my deepest gratitude for my research supervisors: Mr. Didier REMOND and Mrs. Adeline BOURDON for their continuous support and encouragement during my Ph.D. career. I will never forget their words: "Don't hesitate to ask us anytime if you have any question." It's their patience that made me pass through all the difficulties over the past three years. The same gratitude is also dedicated to my technical supervisors: Mr. Samuel KOECHLIN and Mr. Dany PRIETO for their professional assistance and valuable guidance in the industrial field.

I would like to sincerely thank the members of my Ph.D. examining committee, Mr. Hartmut HETZLER, Mrs. Betty LEMAIRE SEMAIL, Mr. Gael CHEVALLIER, Mr. Mike MCCLELLAND and Mr. Guy CLERC for reviewing my work and attending my defense during this difficult time. Their insight comments really help me to improve this research work.

My life in the team "Dynamique et Contrôle des Structures (DCS) " of LaMCoS has been enlightened by the presence of many kind and caring friends: Afaf, Guillaume, Florian, Yvon, Jonathan, Roberto, Etienne, Aroua, Clement, Sébastien, Carlos, Quang Thinh,... Their help and companionship will never be forgotten. Special thank to our best secretary Zahia for helping us solve many problems in administrative procedures. Same appreciation also goes for my colleagues in the company: Darelle, David, Stephani, ... for helping me realize this project.

Finally, I am forever indebted to my family especially my parents for their endless love and unconditional support during my whole life. They gave me life, raised me up and work hard to let me realize my dream. I am also grateful to my boyfriend, Yang, for sharing every joy and frustrating moment during my Ph. D. life. It's his love and company to encourage me to finish this work.

Abstract

The requirement for a more compact solution in electrical machines leads to a design trend of increasing rotational speeds and lightening mechanical structures. These changes can lead to non-linear vibrations and even to the rotor-stator contact in the worst case. These vibrational phenomena are mainly generated by the unbalanced magnetic pull (UMP) inside the machine due to the air gap eccentricity. In order to study the influence of different architectures on these complex vibrational phenomena, a multiphysics electrical machine model with strong electro-magnetic-mechanical couplings is developed in this thesis. The different interaction paths between the UMP force and the radial displacements of the rotor have been introduced to fully strengthen this coupling considered on both radial and rotational movements. The proposed model is established on the basis of the angular approach so that an originality of this work lies in the fine understanding of the instantaneous angular velocity (or angle-time relationship) of the motor shaft. This originality also provides the formalism and the framework to solve the problems in the non-stationary operating conditions. The mixed mesh/nodal permeance network is also adopted to model the deformed magnetic field under the effect of the rotor eccentricity and the mass eccentricity. This multiphysics model is validated by comparing with a more classical finite element model in the quasi-static regime. Two traditional electric motor architectures (the squirrel cage induction motor and the permanent magnet synchronous motor) are chosen as examples of the application of the proposed model. The physical characteristics of the UMP force and its frequency components associated with the input static eccentricity are studied in the case of the induction motor. Then, the self-excited vibration of the rotor is analyzed through the UMP waveform and the radial displacements of the rotor center in the case of a permanent magnet synchronous motor architecture. The resonance peak generated at the modified natural frequency by the mass unbalance excitation is also identified from the two results. The two models are finally used respectively to study the influence of different mechanical structures and the effect of different winding configurations.

KEYWORDS: Multiphysics model, Electric motors, Angular approach, Rotor eccentricity, Mass eccentricity, Unbalanced magnetic pull, Non-stationary operating conditions

Contents

List of Figures

List of Tables

Chapter 1

Introduction

Contents

1.1 Motivation for this work

Electric motors are important devices to convert electrical energy into mechanical work. They have been widely used in many industrial fields since the first electric motor was created in the 1740s. With the development of technology, people are not just satisfied with its stable operation in a steady state but also try to ensure its optimized dynamic behavior over the entire speed range. On the other hand, in order to avoid the extra energy loss and to reduce the working space, some non-traditional motor integration architectures are invented to get a more compact mechanical assembled structure as shown in FIG.1.1.

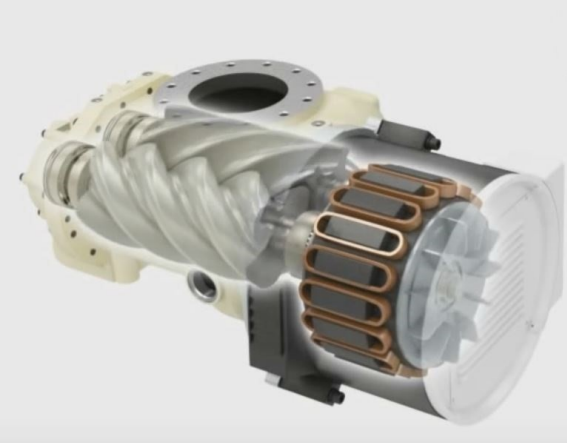

Figure 1.1: Example of a screw compressor with an integrated permanent magnet motor (@ Nidec Leroy Somer)

The original flange motor with a coupling is replaced by a simple permanent magnet synchronous motor (PMSM). This PMSM is integrated directly on the same shaft of the screw compressor without the alignment by another bearing unit. This kind of structure introduces easily the problems of vibration, noise and the instability on its dynamic behavior. In the worst case, the rotor-stator contact has been encountered during its operation in the reality.

This abnormal vibration phenomena could be explained as the appearance of unbalanced magnetic pull (UMP) induced inside of the electrical machine due to the air gap eccentricity. In such kinds of architectures, when the electrical machine is set up on the cantilevered shaft or it is installed on a relatively flexible long shaft between two bearings, the rotor center axis will be inevitably misaligned with the stator center axis under the gravity of the rotor. This misalignment introduces the difference in the air gap length around the periphery of the rotor. As mentioned in [2], the energy convert mainly takes place in the area of the air gap. In the mode of the electric motor, most of the electromagnetic energy is converted into mechanical work in the form of the radial and tangential force components. All the tangential force components are integrated along the periphery of the air gap to constitute the electromagnetic torque while those radial force components usually offset each other in the case with the uniform air gap. Since the air gap eccentric-

ity is induced, those magnetic radial force components reveal as a resultant radial force inside of the electrical machine which is called as UMP. Once it is produced, the UMP will pull the rotor roughly in the direction of the minimum air gap and continue to increase the air gap eccentricity. As the result, some noise vibration and harshness (NVH) problems appear inside of the machine.

Therefore, this thesis is dedicated to analyze the air gap eccentricity effects on the dynamic behavior of electric motors in different architectures in order to better understand and simulate the nonlinear phenomena inside of the machine that lead to unstable dynamic behaviors. Considering that the electric motor is a multiphysics highly coupled system between the mechanical field and the electromagnetic field, it is meaningless to create a model about only one subsystem or analyze the model of each subsystem separately. In order to obtain a more realistic model of electric motors which can also be applied in non-stationary operations, a multiphysics model with the strong electro-magneto-mechanical coupling is established based on the angular approach in this research work.

1.2 Literature review

Different modeling tools and methods are emerged and developed in the recent decades in order to satisfy the increasing requirements for the reliability design of electrical machines. They can be generally separated in three categories [3]: analytical methods; numerical methods and hybrid methods (as the combination of the first two). The analytical method is often adopted in evaluating the global performance and identifying the characteristic parameters in the electrical machine while the numerical method is usually applied in the early design stage of the new product or in the verification about the local phenomena inside of the machine. Each of them has their advantages and shortcomings.

Although many different models are created to describe the mechanic and electromagnetic field in the electrical machine during the past years, the two subsystems are often discussed separately. On the one hand, the researchers who work on the diagnostic of the defeats through the electrical signals concentrate more on the modeling of the electromagnetic field. The mechanical structure is not necessary to them and the mechanical variables like the electromagnetic torque and the UMP due to the air gap eccentricity are treated as the output of the model. On the other hand, the researchers who want to study the reaction of the rotation shaft under the excitation of UMP focus more on describing the mechanical structure and in this case those mechanical variables are considered as the input values generated from the simplified electromagnetic model with a defined movement. Very few of them has taken the strong electro-magneto-mechanical coupling into consideration due to their different research goals. However in order to better describe and predict the transient dynamic behavior of the electric motor, this strong coupling should be considered in the multiphysics model since the electric motor is a highly coupled multiphysics system.

Therefore, different models in the literature to describe respectively the electromagnetic field and mechanical structure of electrical machines are firstly reviewed in this

section. Their characteristics are introduced and compared to provide the reason for the choice of the final adopted method. In accordance with the research object, this review is limited to the radial flux and rotating field motors which are described as the two-dimensional (2D) problem. An introduction about the angular approach is provided later to demonstrate its advantages in performing the simulations in non-stationary operations. Since this research work is based on a multiphysics model about an induction motor (IM) developed by a former PhD student [1, 4], the general introduction about this previous model as well as the corresponding corrections and improvements need to be realized in this research work are presented separately in the final part of this section.

1.2.1 Electromagnetic modeling

The most difficult part about simulating the electrical machine with the eccentric rotor is to describe the distorted magnetic field along the periphery of the air-gap with different rotor eccentricities. The analysis about the steady state of the electric motor is usually based on a static magnetic modeling with an instant input electric current value. It is then coupled with an electrical differential equation which is used to describe the time history of the input electric current variation in order to realize the dynamic simulation in the electromagnetic field. Thus, a review on the electromagnetic modeling based on two traditional methods is discussed in this subsection.

1.2.1.1 Analytical methods

The analytical method is based on the resolution of Maxwell's equations which is very fast and precise for the optimization of electric motors. Several models for different situations are designed in the framework of this method.

Air gap permeance approach also known as **Permeance harmonic method** is firstly proposed by R. Belmans et al. in [5] to describe the distribution of the magnetic flux density B over the contour of the air gap from the product of the air gap permeance Λ and the synthesis fundamental magnetomotive force (MMF) $\mathcal{F}$:

$$B = \Lambda \cdot \mathcal{F} \tag{1.1}$$

Based on the rotating field approach, the MMF is either induced directly from the theories of armature winding [4,27,29,31,33] or is calculated by integrating the current density around a closed path based on the Ampere's law [6] [7] [5]. The air gap permeance of the eccentric rotor is usually developed with Fourier series expansion method. As discussed in [8], if the eccentricity is assumed to be small, only the direct current (DC) component, the first-order component and the second-order component need to be considered. The radial and tangential component of the air-gap flux density are achieved separately by applying EQ.1.1. And the density of electromagnetic force acting on the rotor is expressed according to Maxwell Stress Tensor method. Since the tangential component of the flux density is proved to be much smaller than the radial one, the normal force density can be determined by neglecting the tangential component [27,29] to finally achieve the UMP by

integration of the Maxwell stress on the rotor surface. With the assumption of the small eccentricity, the simple analytical expressions about the UMP are obtained to extract the equivalent electromagnetic stiffness by dividing them about each relative displacement [9] [8] for explaining the negative spring effect of UMP. This model is adopted by Zhu et al.[10] and D.G.Dorrell et al. [7] to analyze the rotor eccentricity induced vibration in respectively the single-phase and three-phase IM. A. Borisavljevic et al. [9], Chen. et al. [8] and B.Lapotre et al.[11] also apply this method to investigate the UMP in the PMSM. Based on a critical re-formulation of the air-gap MMF, this model is employed by A.D.Gerlando [6] to discuss the homopolar term in isotropic electrical machines.

In order to achieve a more precise result about the distribution of the magnetic field in electrical machines, **Exact subdomain analysis** is appeared to divide the whole electrical machine section into several subdomains and the analytical solution of Poisson's equations (in the permanent magnet (PM)), of Laplace's equations (in the air gap and stator rotor semi-slot) and of Helmholtz's equations (in the rotor bar) to describe the scalar magnetic potential distributions in different subdomains are solved respectively. It is firstly put forward by Zhu et al. [12] [13] to predict the instantaneous magnetic field distribution from the open-circuit field and the armature reaction field in PM brushless direct current (BLDC) motors. And then it is adopted by U.Kim et al. to study the rotor eccentricity effects on the same electric motor without [14] and with [15] the slotting effect where the slotting effect is explained by a newly redefined boundary value problem in polar coordinates in the annular air gap/magnet region. Based on the same model, the magnetically induced vibration is analyzed in [16] by identifying the characteristic frequencies in the generated UMP and the cogging torque under both static and dynamic rotor eccentricity. They introduced the perturbation method to treat the nonlinear boundary conditions caused by the rotor eccentricity which is reused by D.Kim et al. in [17] to study the UMP in a Toroidally Wound BLDC Motor. The model of U.Kim is improved by Kumar et al. [18] to simulate the stator iron with the finite thickness and the finite permeability. This method can be also applied in the modeling of double cage rotor IM in healthy and broken bars conditions by Boughrara et al. [19]. The superposition method is extended in [20] to predict the UMP of PMSM with the rotor eccentricity.

When facing some complex geometrical domains, the **conformal transformation method** is applied to calculate their field distributions in a easier way. It is also known as **Conformal mapping method** which is used to convert the problem of an irregular form into a regular form through the transformation of the coordinate. By maintaining the same solution of Laplace's equation in both the original and transformed domain, the field distribution from a complex geometrical domain can be worked out if its transformation in the simple domain is known. For a better application, the magnet is often ignored and the stator slots are assumed to be infinitely deep rectilinear and in a small number. Combining with the impedance approach, D. G. Dorrell et al. [21] used it to compare the UMP in a double layer IM with series and parallel windings. Li et al.[22] applied it to establish a new analytical model for slotted PM motors with rotor eccentricity in order to analyze the relationship between the eccentricity effect and design parameters. It is also employed by S.T.Boroujeni et al. [23] for modeling the air gap flux density in the slotless eccen-

tric surface mounted PM machines by combining the perturbation analysis. The slotting effects on the air gap field can be explained either by a Carter factor correction [21] or by introducing a 2D relative permeance function derived by the conformal transformation [24]. The real air gap flux density is calculated by multiplying the flux density from the slotless stator motor by the relative permeance function. It is also adopted by Zhu et al. [25] [26] to extend the model based on the Exact subdomain analysis to account for the effects of stator slot openings on the magnetic field distribution.

The three analytical methods discussed before focus more on the modeling of the static electromagnetic model. The instantaneous magnetic field is calculated at a certain moment with a given instant current source value and a defined rotor position. In order to simulate the dynamic behavior of the electrical machine, the electric circuits should be coupled with the magnetic field based on the multi-loop theory [27] to construct a transient model. **Winding function approach** emerged to realize this coupling. It is based on the coupled magnetic circuit theory and build up by describing the machine as a set of multiple inductive circuits coupled together where the current in each circuit is considered as an independent variable [28]. Taken the IM as an example [29], the voltage equations are used to define the three phase stator windings and n_r short circuits in the rotor squirrel cage where the electric parts are represented by the real stator and rotor phases resistances and their terminal electrical voltages while the magnetic parts are composed of the stator and rotor linkage flux defined by the self- and mutual- inductance matrices. The inductances are usually calculated by means of winding functions which are able to consider all the harmonic components at once. The final set of differential equations is then solved for each rotor position by adding a simple mechanical motion equation [30] [31]. The electromagnetic torque can be achieved from the magnetic coenergy with respect to the rotor position by neglecting the magnetic saturation effect. Therefore, this method can be employed to simulate both transient and steady-state behavior of the electric motor without the assumption of the sinusoidal currents. By combining with the Frozen Permeability method, this model is also applied in an insert type surface-mounted PMSM [32] for analyzing separately the PM torque and reluctance torque in this motor. It is demonstrated that when the Frozen Permeability method is adopted, the average torque separation can only be performed correctly by virtual work principle.

However, the classic Winding function approach is not suitable for the modeling of eccentricities since it cannot consider air gap variations. **Modified winding function approach** for the inductance calculation considering the air-gap eccentricity is therefore proposed. S.Nandi et al. [33] [34] use it to analyze the performance of a three-phase IM with the mixed eccentricity. It is then developed by H.R.Akbari [35] to model the rotor misalignment in each axially-divided cross section for calculating the inductance under the axial non-uniformity conditions considering the rotor skewing and several rotor asymmetries. It is also adopted by Tian et al.[36] to identify the characteristics of stator current under composite faults of broken bar and static eccentricity in a squirrel cage IM. Tu et al. [36] apply it in a large synchronous generator with parallel connected windings for the real-time simulation of the internal faults. Magnetic saturation effect is often neglected in this method, but it can be taken into account by introducing the saturation

factor along a particular region of the air-gap circumference in a saturated IM [28] or in a salient-pole synchronous generator [37]. Modified winding function approach can be combined with Air gap permeance approach to create an accurate transient model about a cage IM. It could be used for calculating the UMP due to eccentric rotors [33,34] where some second order effects such as the skin effect in the rotor bars are considered by modifying the bar and end-ring resistance values. It can also be applied to explore the spectral signatures on stator currents under the dynamic eccentricity [31].

Overall, the analytical model is simple and compact, only a few parameters are needed to describe the whole system so that it takes very few calculating time to simulate the steady-state of the motor's operation point. However its high efficiency on the simulation is realized by sacrificing the detailed information about the local geometry inside of the machine thus it's difficult to take into account precisely some nonlinear phenomena like the magnetic saturation effect in the model and it's hard to perform the dynamic simulation in non-stationary operations since every characteristic parameters should be re-identified once the operation point of the motor is changed.

1.2.1.2 Numerical methods

Magnetic saturation effect of the iron core part is usually ignored in the analytical model since only the magnetic field of the air gap is taken into account for the calculation of electromagnetic forces due to its importance as the main area for the electromechanical energy transfer. Numerical methods are needed to establish more accurate models with the complex geometry affected by the local nonlinear phenomena.

Finite element models (FEMs) One of the most popular numerical methods is the finite element (FE) method. Its principle is to divide the continuous target field into finite units and then to express the solution of each unit by the interpolation function that can satisfy the boundary conditions. Therefore the solution of the entire field is obtained. Due to its adaptability in different kinds of problems, it has been wildly used by numerous researchers for calculating the magnetic field distribution in different types of electrical machines. It is often employed as the contrast for the verification of analytical models. As mentioned before, only 2D FEM is going to be discussed in this work and it is classified as the static FEM and the dynamic FEM.

The **static FEM** in the electrical machine is used to work out the distribution of the magnetic field at a certain moment with a given current value and at a determined operation point. A 2D FEM is adopted by Wang et al.[38] to compute the radial force in a bearingless PM DC motor. S.Jagasics et al. [39] used it in a private finite element analysis (FEA) software to compare the performances of the PMSM with different rotor configurations through their cogging torques and torque ripples. This 2D FEM about the iron core field can also combine with the analytical solution of the air gap field to establish an **hybrid model** of the magnetic field calculation for slotted/slotless PM machines [40]. Moreover, Zhu et al. [41] determine the frequency components and order of electromagnetic radial forces of asynchronous motors by the approximate analytical method which

are corrected later by FEM in ANSYS software. It is shown that the combination of the theory algorithm and FEM can make an accurate analysis about the UMP in asynchronous motors with the static eccentricity.

The **dynamic FEM** is also known as the **time-stepping FEM** for the solutions in the transient state. It is firstly proposed by Debortoli et al.[42] to investigate the effect of the rotor eccentricity and of parallel windings in the IM. The distribution of air gap flux density is expressed as the function of the space and the time which should be analyzed using a 2D Fast Fourier Transform (FFT) technique. Based on the time-stepping FEM, Rodriguez et al. [43] use an in-house 2D FEA program to determine the signatures of dynamic eccentricity in the vibration pattern of induction machines which are validated by the experiment part. This method is then adopted by Ebrahimi et al. [44] [45] [46] for diagnosing gradually different kinds of rotor eccentricities, magnetic and electrical faults in PMSMs. The spectrum analysis of stator current is considered as the useful tool for noninvasive vibration monitoring of the PMSM. The similar eccentricity fault diagnose is also realized in a line start PMSM to study its two operation modes [47] and the influence of the rotor eccentricity on the torque of the IM is discussed later in [48]. Different winding topologies between the distributed winding and the concentric winding are studied with the time-stepping FEM in respectively the interior PM motor (IPM) [49] and the brushless alternating current (AC) motor [50]. The model of Debortoli can be realized directly in a commercial software Maxwell 2D transient module by Zhou et al. to calculate the UMP under the static eccentricity but with different stator winding setups [51] and to analyze the UMP with dynamic eccentricities during starting period [52]. Recently, it is extended in the IPM by Aggarwal et al. [53] for the analysis of UMP considering the stator core vibration.

Based on an analytical model with the parameters estimated from FEM simulation results, a low-order model to calculate the electromagnetic force on a whirling cage rotor in the IM is firstly proposed by Arkkio et al.[54]. The rotor whirling motion could be generated by the mass unbalance in the reality which is reproduced by the active magnetic bearings in the experimental part. The motion of the rotor is obtained by changing the finite element (FE) mesh in the air gap. It is suggested to apply in the rotor dynamic analysis instead of the time-consuming FE simulation. This model is adopted by Tenhunen et al. to study respectively the effects of equalizing currents [55] and of the saturation [56] on the electromagnetic forces in the IM. An impulse method introduced in [57] is utilized in the FEA to calculate the force between the stator and the rotor. The eccentric motion of the rigid cage rotor is extended into the cylindrical circular whirling motion, symmetric conical whirling motion and the combination of the two to calculate the electromagnetic forces with various rotor eccentricities [58] in the form of multi-slice 2D models by applying the superposition method. The same model is then developed in the transient state to take into account an arbitrary eccentric motion of the cage rotor [59] and the UMP calculation from this model is verified in [60]. Furthermore, this **low-order parametric force model** is also employed by Burakov et al. to compare the UMP mitigation effects from the stator parallel paths and the rotor cage in separately IM [61] and in salient-pole synchronous machines [62]. Although this force model has several advantages as mentioned

in [62]:

- It allows simple, quick and accurate calculation of the electromagnetic force at a desired whirling frequency value or in a certain range of whirling frequencies.
- The same model parameters can be directly used at different values of whirling radius and whirling frequency.
- The model can be integrated into the mechanical analysis to study the electromechanical interactions in electrical machines in an efficient way.
- The model can be applied in both synchronous and induction machines and it is accommodated also to different winding configurations.

There are still some limitations need to be improved such as:

- The parameters need to be estimated from FEM simulation results and they have to be re-estimated when the operating point (supply voltage, load torque etc.) of a machine is changed.
- This model is based on the assumption of spatial linearity which means that the eccentricity force is a linear function of rotor eccentricity.

Magnetic Equivalent Circuit models Although the FEM are ready to provide the accurate results about the distribution of the magnetic field from different kinds of electrical machines, their computation time may be massive when simulating the dynamic behavior in the transient state or coupling with other electrical and structural models. As mentioned in [2], one of the numerical model often adopted in the machine transient analysis is the **Magnetic Equivalent Circuit (MEC)** approach. It is firstly proposed by Laithwaite [63] and by Carpenter [64]. In order to calculate the magnetic field distribution in the cross section of the electrical machine, MEC approach divided the whole field into a network of flux tubes which are composed of the passive elements (like the reluctance or the permeance of each flux tube) and the active elements (like the MMF sources). A node with a scalar magnetic potential is formed at the connection of several flux tubes. Due to the similarity between the electric circuits and the magnetic circuits [64], the Ohm's and Kirchhoff's laws are employed in the whole network of permeances (or reluctances) to describe the relation between the magnetic flux and the magnetic potentials. Therefore MEC models are also called as **Permeance network models (PNMs)** or **Reluctance network models (RNMs)** in literatures. The PNM is actually one kind of FEM with special and coarse meshes. There are mainly two differences between PNM and FEM: First, the number of meshes defined in PNM is less than that from a traditional FEM so that the PNM can take into account the spatial dependencies as in FEM but is computationally less intense. Second, the direction of the magnetic flux through each element should be defined with the determination of the mesh in PNM while this direction is one of the results from FEM. Overall, PNM is a good compromise between the analytical models and the traditional numerical model FEM.

An electrical model with the current source is coupled to the magnetic model based on PNM in [65] to construct a "$\lambda - i$ model" in order to analyze both transient and steady state performance of a salient pole synchronous motor and this model is validated in the case with the magnetic saturation in [66]. Another "$V - i$ model" from the combination among the electrical model with voltage supply, magnetic and dynamic models is established by P. Sewell et al.[67] to study the dynamic behavior of the IM. The PNM can also be applied in other different kinds of electrical machines such as switched reluctance motors [68] [69] and synchronous reluctance motors [70]. The permeance network in the iron core part is usually determined according to the geometry of the stator and of the rotor and the air gap permeance network should be defined based on the mesh from the previous two. If the rotor motion is taken into consideration, the air gap permeance network need to be modified at each iteration time step. All these bring the difficulty in calculating the air gap permeance values so that there are generally two techniques [71] to realize this calculation: the Ostovic model [72] and the FEM. The Ostovic model is developed from the PNM so that it has the best compatibility with the MEC approach and since it is employed in this research, its modeling information is going to be introduced after in the thesis. Although the other one is not adopted in this work, it still has its own advantages which can be referred to. J.Farooq et al.[71] describes the air gap permeance function from the FEM results which is then simplified by the interpolation method. The air gap permeance is accurately calculated but only for the symmetrical case. In addition by applying the analytical method, the magnetic field distribution around the air gap can be achieved directly. H.Ghoizada et al. [73] combine the analytical magnetic field solution of the air gap with the PNM about the rest of the machine to include the magnetic saturation effect. Similarly, all the permeances are calculated from PNM and the MMF of d and q axis are calculated from winding functions in order to obtain air gap flux density based on the air gap permeance approach in [74] [75]. In order to account for the slotting effects, the conformal mapping method is also applied to calculate the air gap magnetic vector potential [76] [77] [72]. These PNM with partial usage of the analytical models or numerical methods are known as **hybrid models** of the electrical field.

By choosing different unknowns and applying different Kirchhoff's laws in the PNM, the permeance network equations are established in three different forms: the nodal based PNM, the mesh based PNM and the mesh/nodal mixed PNM. They are essentially the same algebraical equations so that they perform equally in the case without magnetic saturation effect. However when this local nonlinear effect is taken into consideration, some evident differences appear between their performances. To achieve a clear understanding of them, they are going to be explained in the following based on the PNM about an IM.

As illustrated in FIG.1.2, if the magnetic potential of each node $\{u\}$ are chosen as the unknowns to calculate the magnetic flux traveling through each branch $\{\phi\}$ in the PNM and Kirchhoff current law (KCL) is applied at each node considering that the sum of the flux entering each node equals to those leaving this node $\sum \phi = 0$, a **nodal based PNM** is established with its final permeance network equations displayed as:

$$[P(\{u\})] \cdot \{u\} = \{\phi\} \tag{1.2}$$

where $[P]$ is the matrix composed of the permeances from each elements. Some permeance values in the iron core parts vary as the function of the magnetic potentials across the branch when the magnetic saturation effect is taken into account. A formalized introduction about the nodal based PNM is firstly provided by Ostovic [78] [79] to establish the dynamic models about respectively IMs and PMSMs. The saturation effect is taken into consideration by introducing a piecewise parabolic approximation of the BH curve. In order to avoid the iterative solution process for the nonlinear algebraic equations at each time step, a new approach to declare all the machine quantities as state variables is proposed in [80]. However the final differential algebraic equations (DAE) are usually difficult to solve due to the increase of the state variables. Associated with the Bond-graph technique, C.Delforge et al.[81] [82] model the coupling between electric, magnetic and mechanic parts about an IM where the mechanical model is represented by a simple mechanical motion. The same technique is applied in the modeling of an embedded PMSM by W.Kemmetmuller et al.[83] for studying the optimal controller design. And this model is then adopted by D. Faustner et al. for the modeling of a saturated surface mounted PMSM supplied by a pulse width modulation (PWM) inverter. Another nodal based PNM about the IM validated for the asymmetrical excitation is developed in a qd frame to simplify the calculation of the leakage inductance [84]. This model is employed by B.Asghari et al. [85] [86] [87] in the real-time modeling of the IM. The moving band technique is extended in the mesh of the air gap area to simplify the study domain to $\frac{1}{4}$ of the machine. The transmission-line modeling (TLM) [88] is used to solve nonlinear lumped networks whose calculation is accelerated by applying a look-up table method (LUT). Another real-time PNM about a switched reluctance machine is developed later by F.E.Fleming et al.[89]. The normal 2D PNM can also be extended to a simple 3D PNM to describe the electromagnetic dynamic behavior of a claw-pole alternator [90] [91]. In order to detect the stator winding faults, the nodal based PNM is adopted by A.Mahyob. et al [92] and Y.Amara et al [93] to analyze the influence of different stator winding faults in the IM and then it is developed in another IPM [94] [95] for the diagnostic of the stator inter-turn faults. By introducing different air gap eccentricities in the nodal based PNM [96], the gear faults [97] and different bearing defects [1] [98] are investigated in the IM using Motor Current Signal Analysis (MCSA). However, even if a mechanical part is considered in these models [96] [97] [1] [98], its coupling with the electromagnetic models are too weak to consider the complete electro-magneto-mechanic interactions in electrical machines. To achieve a more accurate model, an enhanced PNM is proposed by C. B. Rasmussen et al.[99] for predicting PM motor performance at the design stage. This enhanced permeance network is composed of two types of elements: one is the unidirectional elements applying in tooth and yoke areas and another is the bidirectional elements using in and around the air gap area. This enhanced mesh is adopted by S.A. Randia et al.[100] and D.J. Gomez et al.[101] [102] for respectively the modeling of the surface PMSM and of the embedded PMSM. Based on these elementary blocks, the mesh-based generated reluctance network (MGRN) approach is recently developed by S. Asfirane et al.[103] [104] to provide a generic permeance network meshing method for electric motors. Besides of the previously mentioned machine types, the nodal based

PNM can be applied in the modeling of many other different electrical machines, such as the doubly salient permanent magnet motors [105], the surface PMSM with any pole-slot combinations [106], the linear PMSM [107], the high speed PM traction motor [108], switched-reluctance machine with full pitched windings [109] and different synchronous reluctance machines [110] [111] [112].

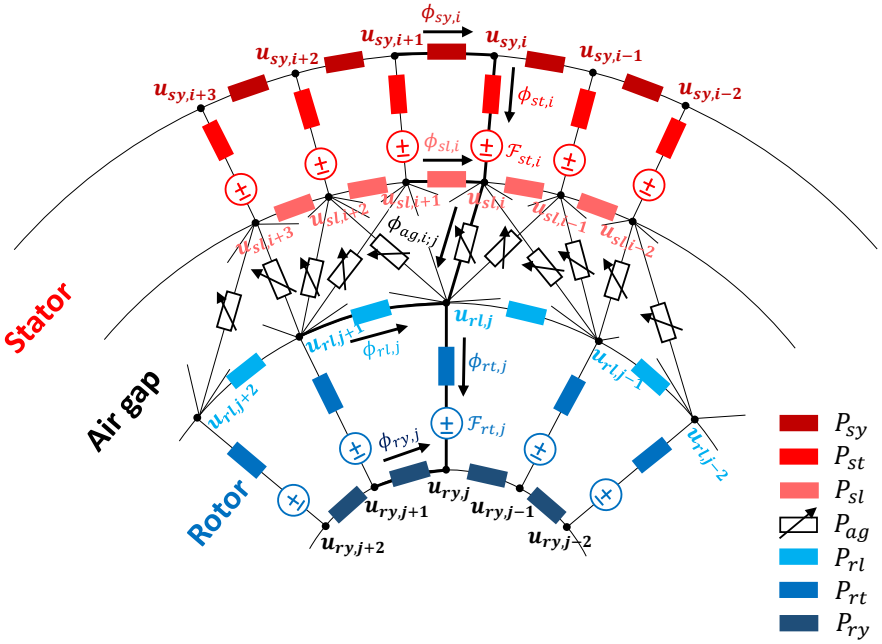

Figure 1.2: Nodal based PNM

As discussed in [113], through the comparison between the nodal and mesh based PNM, it can be seen that the nodal based PNM often fails to converge when dealing with the local nonlinear phenomena in the magnetic field. This is due to the ill-conditioned Jacobian matrices from the nodal formulation. In oder to solve this problem, the **mesh based PNM** attracts more attention of the researchers. In a mesh based PNM shown in FIG.1.3, the magnetic loop flux in each mesh φ are considered as the unknowns to calculate the magnetic potential drop U over each branch. By applying Kirchhoff voltage law (KVL) in each mesh assuming that the algebraic sum of the magnetic potential differences in one loop equal zero $\sum U = 0$, the final reluctance network equations about the mesh based PNM is illustrated as:

$$[\mathcal{R}(\{\varphi\})] \cdot \{\varphi\} = \{U\} \tag{1.3}$$

where the matrix of the reluctance $[\mathcal{R}(\{\varphi\})]$ is variated as the function of the magnetic loop flux in the case with magnetic saturation effect. The first mesh based model is proposed by J.D.Law et al. [114] to study the transient performance of a field regulated reluctance machine. It is indicated that one of the advantages of using the loop equations

allows the whole machine to be represented by one equivalent pole. This model is then improved in [115] to take into account the magnetic saturation effect without convergence problem. A dynamic mesh based PNM about an IM is coupled with a simple mechanical motion to investigate several typical failures in this kind of machine [116]. To the author's acknowledgments, there are fewer applications about the mesh based model due to the meshing problems in the air gap area. First the mesh numbers in the air gap is changed at every rotor position and then the mesh-based algorithm becomes unstable in the presence of a very large reluctance. The two problems are solved by M.L.Bash et al. [117] to introduce a shape algorithm for defining the air gap permeance during the rotor motion and to avoid the large reluctance values by excluding a very narrow range of rotor positions. This model is then employed for the population-based design [118] to create the trade off between various competing performance objectives for the wound rotor synchronous machines. The reluctance network is then enhanced by R.Wang et al. [119] to model the flux distribution around stator tooth tips and damper bar openings. The original magnetic model is extended in the format of state equations by coupling with the electric circuits. similarly, this improved model is later used in the population-based design for the optimization of the damper winding topologies [120]. In order to reduce the computational error, a refined mesh-based PNM is realized by Stefano et al.[121] for calculating the torque and radial forces in PM multiphase bearingless motors. Different from the UMP due to the rotor eccentricity, the radial forces in [121] are generated by one set of windings to produce the radial levitation force.

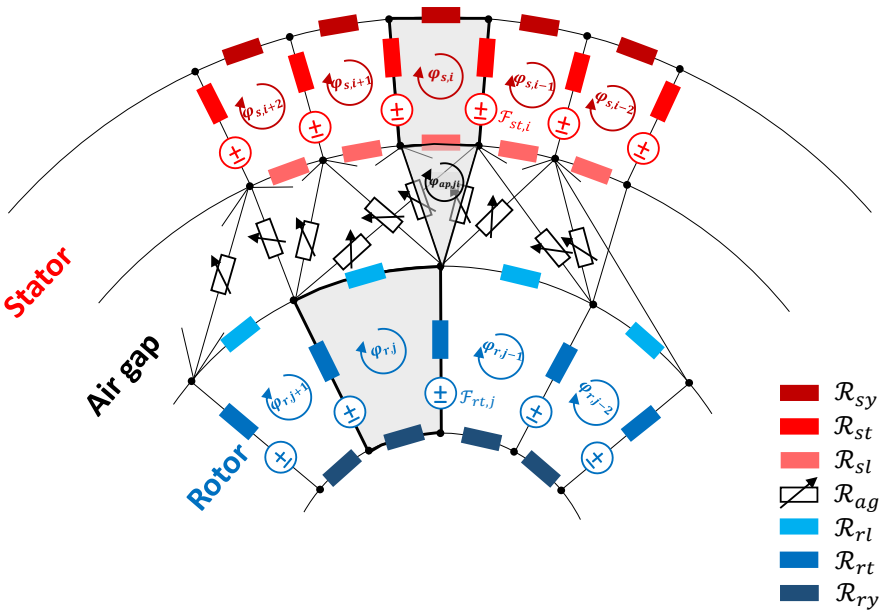

Figure 1.3: Mesh based PNM

Comparing the nodal based PNM with the mesh based PNM, it can be seen that they

each have their own advantages and shortcomings. The nodal based model is less efficient in calculating the system with nonlinear magnetic materials but it is easier to realize the KCL formulation in the air gap area. The mesh based model has a better numerical convergence in solving the nonlinear algebraic equations associated with the magnetic saturation effect however it has a big challenge to calculate the air gap reluctance values during the rotor motion. In order to combine all the advantages but to avoid all the shortcomings from the two types of PNM, a **mesh/nodal mixed PNM** is derived in [122] based on the similar models discussed in [113]. As demonstrated in FIG.1.4, the unknowns for the mesh/nodal mixed PNM are the magnetic loop flux through the nonlinear elements and the magnetic node potentials at the two side of the branches with linear magnetic materials. By applying respectively KVL in the iron core parts (stator and rotor) to include the magnetic saturation effect and KCL around the air gap, the new mixed PNM not only maintains the effective convergence properties of the mesh based PNM but also keeps the simplicity for the air gap mesh from the nodal based model. Furthermore, a scaling technique is applied in the permeance network equations to eliminate the large difference in the magnitude of the mixed matrix composed of both reluctance and permeance values.

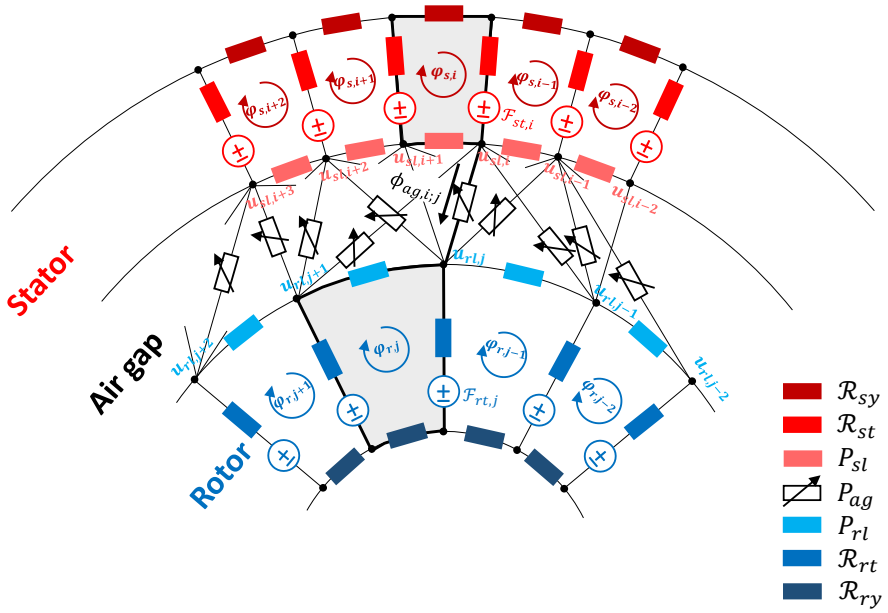

Figure 1.4: Mesh/Nodal mixed PNM

In summary, as one of the traditional numerical methods, FEM is famous for obtaining the relative precise simulation results. Many local phenomena (i.e. nonlinear effect, variation on the geometry) can be taken into consideration naturally since it is designed to solve the Maxwell equations in every mesh of the motor section. The simulation about the transient behavior of the electric motor can be realized by adopting the time-stepping FEM. However as the price of the accurate prediction results, FEM usually needs a large

calculating effort to accomplish the simulation so that it's not convenient to perform the longtime simulation especially in non-stationary operations. In order to overcome this limitation, PNM is proposed to achieve a compromise between the calculation efforts and the accuracy of the simulation results. By comparing the PNMs established from different permeance network equations, the mesh/nodal mixed PNM is finally adopted to describe the magnetic field of the electric motors in this work for its capacity in setting up the saturation effect and calculating the air gap permeance during the rotor motion

1.2.2 Mechanical modeling

When talking about the dynamic behavoir and the vibration phenomena of the electrical machines, the mechanical model should be put forward in the whole system in order to establish the relation between the electromagnetic field and the mechanical structure. The mechanical defects such as different kinds of rotor eccentricities can be introduced naturally in the multiphysics model. There are usually three types of rotor eccentricities defined and studied in literatures: static eccentricity[96], dynamic eccentricity[37] [52] and the mix of the two [123] [124] [125]. However, those three eccentricity types tend to coexist in reality. With the coupling of the mechanical structure, the reactions of the structure under the influence of these eccentricities can be analyzed at the same time. Therefore, once the strong mechanical coupling is taken into account, all of three types of rotor eccentricities mentioned before are reduced to the mixed one with the intervention of the rotor motion. Due to the complex coupling between the two subsystems, different mechanical modelings in the needs of different goals are summarized in this section.

1.2.2.1 Simple mechanical motion equation

The easiest way to include the mechanical motion into the model of electrical machines is to introduce a simple mechanical motion equation about the shaft rotational movement. It is suitable for various electromagnetic models of different types of machines. J.M.Stephenson et al.[126] applies it in an analytical model to calculate the electromagnetic torque and currents in a doubly salient reluctance motor. The other motion-coupled analysis based on the MEC models of switched reluctance machines are developed respectively in [68] and [89]. H.T.DURU et al.[127] includes an additional mechanical terminal in a 2D time-stepping FEM of the PMSM coupled with 3-phase electrical network equations. And the similar modeling process about other PMSMs can be also identified in [65] to combine with a "$\lambda - i$ model" and in [94] to couple with a nodal based PNM. The most common case to add a simple mechanical motion equation in the electromagnetic model is in the IM as discussed in [31] [30] [81] [116] [96] [92] [97] where it is employed to control the system according to the "Torque-Speed" characteristic curve. Among them, the rotor eccentricities are only taken into consideration in [31] [97] [96] to detect their influence on the stator currents pattern and the UMP due to the eccentricities are calculated as the result only in [96]. It is shown that the simple mechanical motion equation is often used to calculate the rotation speed through the rotational equilibrium for the transient

simulation but its addition in the electromagnetic model doesn't bring a strong coupling with the mechanical field.

1.2.2.2 Laval-Jeffcott rotor model

Since one simple mechanical motion equation is not sufficient to introduce the complete electro-magneto-mechanical interaction of the electrical machine, a lumped mechanical model known as the Laval-Jeffcott rotor model is adopted for the deeper study especially in terms of the rotordynamics. The Laval-Jeffcott rotor model often discussed in literatures is composed of a uniform massless flexible shaft with a disc mass installed in the middle of the shaft and supported by two very stiffly bearings. The disc is used to represent the rotor of the electrical machine and only the lateral motions are discussed as the planar problem so that the system is considered to be 2 degree of freedom (DOF) with the equilibrium in the axial rotation. Due to its simplicity, many researchers have adopted this model in their recherches about the stability and vibration analysis in electrical machines.

It is firstly applied by R. Belmans et al. [128] to study the influence of UMP on the radial stability of the induction machines. The UMP expression calculated from the **Airgap permeance approach** [5] is used to identify the coefficients of the electromagnetically induced spring and damping and they are combined with Jeffcott rotor model for the analysis on the rotor radial vibrations. The same electromagnetic model is then developed by Guo et al. [124] to achieve an analytical expression of the UMP for any pole-pair number. The generated UMP is exerted directly on the **Jeffcott rotor model** as an external force and the mass unbalance excitation is also considered to study the effects of the UMP in a 3-phase generator with an eccentric rotor. Based on the model of Guo, Bai et al.[129] study the circular whirling motion and the stability of the rotor due to UMP and eccentric force. Xu et al. [130] extend this model by including the gyroscopic effect to study the dynamic behavoir of an inclined rotor with both static displacement eccentricity and the static angle eccentricity. They also improve this model by considering both dynamic and static eccentricities [125] and by adding a classic rub impact model as well as an approximated function for the saturation effects [131]. On the other hand, the coupled model is also adopted in an eigenvalue-based stability analysis [132] [133] to discover the negative stiffness effect of the UMP in reducing the natural frequency of the rotor system. Different bifurcations due to the asymmetric effect of static radial eccentricity is analyzed in [134] by applying the center minifold theorem and Lyapunov method. The nonlinear restoring force from the bearing clearance, Hertz contact force and the rotor weight are added for the stability analysis in a more complex situation [135].

Although the coupled model based on the Airgap permeance approach and the Jeffcott rotor model provides us with an efficient model to analyze the lateral vibration in electrical machines. It's difficult to include some local phenomena of the magnetic field such as the nonlinear saturation effect and the slotting effect. And the UMP is calculated due to a relatively small eccentricity with the assumption of the spatial linearity of the air gap flux density distribution. Therefore, the electromagnetic model based on the **FEM** is proposed to couple with the **Jeffcott rotor model**. A low order linear model of UMP

deduced in [54] is expressed in the complex form to combine with a simple 2 DOF Jeffcott rotor model by Holopainen TP et al.[136] [137] [138]. The UMP is induced by the circular whirling motion and the nonlinear saturation effect is modeled by a single valued magnetization curve. The coupled model is adopted to investigate the electromechanical interaction effects in induction machines and a form of self-excited vibrations that may leads to the rotor instability is finally identified. In order to avoid the time-consuming parameters identification processes based on FEM, X.Han et al.[139] combines **a refined nodal based PNM** with the Jeffcott rotor model to study the unstable force due to the IM eccentricity in a geared machinery train. Both the radial and tangential force component of UMP are represented as the equivalent negative stiffness in the vibration-stability analysis.

All the methods mentioned before belong to the **direct approaches** which means that each physical domains are described individually from Newton's and Kirchhoff's laws and the electro-mechanical interactions are defined retrospectively. In order to better describe the energetic consistency in the electro-mechanical coupling of electrical machines, an **indirect approach** is proposed recently by Boy et al. [140]. to include all physical domains in one expression based on Lagrange's equations or Hamilton's principle. Different from the previous work, both torsional and lateral rotor oscillations are considered here so that the transient simulations considering a strong electro-mechanical couplings are performed in a natural way. In the frame of the indirect approach, a model based on Airgap permeance approach about a non-salient pole synchronous machine is firstly coupled with Jeffcott rotor model for the analysis about an arbitrary lateral rotor motion [141] [142] and then a similar coupled model is applied on a four poles induction machine to observe both the self-excited oscillations and the modified passage of resonance from the simulation results. A synthesis about the models of the two machines is summarized in Boy's thesis [143]. In addition, the similar co-energy based approach is also employed by N.L.P.Lundstrom et al. [144] [145] to investigate the UMP due to shape deviations of the generator and is adopted by Hyungbin Im et al. [146] to derive the equations of motion about a BLDC motor using Lagrange's equation.

1.2.2.3 Finite element model

Thanks to the development of computer science, many commercial softwares are emerged to analyze the structure and electromagnetic problems based on FEM. Since the Jeffcott rotor model is usually applied to simulate the rotation machine operated below the second critical speed [140], some researchers tend to establish the coupled model of the high speed electrical machines with both the electromagnetic field and the mechanical structure described by FEM. D.Mazur et al.[147] creates a coupled model about IM in ABAQUS for modeling its electrical and mechanical phenomena. The magnetic field model is considered as 2.5D since the skew of rotor bars is included by dividing the rotor into 7 elementary sections along the axial direction. Similarly, Martin et al. analyze the dynamic behavior about the IM [148] [149] and about the asynchronous hydro-power generator [150] in ANSYS. J.Martinez et al.[151] build up the FEM of IMs in Comsol

Multiphysics to project 2D magnetic stress into 3D mechanical mesh. The same method is also employed by Alarcon et al. [152] to study the skin effect and mechanical loads in the cage. To avoid the intense calculation about two different subsystems, the low order parametric force model mentioned in [146,147,148] is adopted to couple with a 3D FEM of the mechanical structure by Antti Laiho et al. [153] in order to study the electromechanical interaction in both induction machines and synchronous generators.

1.2.2.4 Multibody model

Although many assumptions have been realized in the coupled models based on FEM to simplify the simulation, the large computational effort is still hard to avoid especially for the transient simulation. The multibody model for the mechanical structure is appeared as a compromise between the Jeffcott rotor model and the Finite element model. T.J.Kim et al. [158,159] model the rotor-motor system by applying the **finite element transfer matrix**. A typical flexible rotor-bearing system about the PMSM in the cantilever type is described through an FEM formulation with discrete elements. U.Werner et al.[168,169,170] presents **a simplified multibody model** about a soft mounted induction machine for a vibration stability analysis. The model consists of two masses to represent the stator and rotor part. The stiffness and damping values of the oil film from the sleeve bearings are deduced by solving the Reynolds-differential equations. The discussed vibration is limited in the transverse plan for the sake of the simplicity. Hence the moments of inertia of the rotor is neglected as well as the gyroscopic effects. Another **two-mass rotor model** with 2 DOF is proposed by Chen et al.[154] to investigate the torsional vibrations due to the electromechanical coupling effects. Later a **finite beam element model** to describe the mechanical structure is employed by many researchers which is often combined with the electromagnetic model based on the Airgap permeance approach. Pennacchi et al. [155] [156] [157] discrete the rotor into 153 beam elements with 4 DOF per node. Different from the other predefined rotor orbits, the effective airgap distribution is based on the actual rotor position. The dynamic behavoir of the big size generators caused by the UMP is investigated considering both the gravitational force and the mass unbalance. The similar coupled model is also applied in another vertical installed hydropower generator [158]. Afterwards, the finite beam element model is improved by applying the Timoshenko beam theory [159]. Each node has 6 DOF to take into account the heterogeneous assembly of the rotor. Due to its compatibility to the motions in all directions, it is finally chosen in the proposed multiphysics model [160] for modeling the motor shaft in order to analyze the influence of radial eccentricity to the rotational movement. Furthermore, based on the finite beam element model, Zhang et al.[161] introduces the nonlinear bearing force in the coupled model of PMSM and H.Kim et al. [162] [163] construct a coupled model about a centrifugal pump driven by an integrated PMSM to analyze the vibrations caused by the mixed eccentricity, by the axial-varying eccentricity, and by the motor frame vibration. The generated UMP from the analytical model is added on the mechanical structure either as a linear negative stiffness or as an external force. The whole model is simplified by neglecting all the movements in the axial direction.

1.2.3 Angular approach

In most of industrial applications, the rotating machines are not able to operate in the literally stationary state because their rotation speed can't maintain a constant value even in the healthy operations. Many researchers tend to simulate the rotating machine in a steady state with the assumption of a constant rotation speed or to realize a dynamic simulation with a predefined rotation speed variation. These models lose the information associated with their inherent periodic geometry variations. In order to go beyond these limits and to display the angular periodicity relation in the rotating machine, a new modeling method known as the angular approach is proposed to describe the machines in the angular domain [164].

1.2.3.1 Advantages of the angular approach

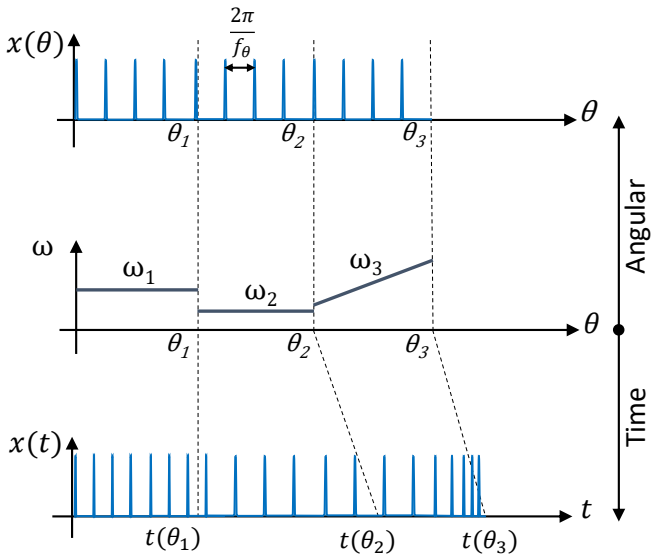

Figure 1.5: Representation of a signal with the cyclic frequency in the angular and time domain from [1].

Rotating machines exhibit periodic geometries in the angular domain. These geometries define the characteristic frequencies of the machine and govern the kinematic relationships between the rotation speeds of its different technological elements. If one of the elements is chosen as the reference, these characteristic frequencies are equivalent to a number of events per revolutions about this rotating reference element. Considering about this fact, it appears to be natural to express the equations of the rotating machine model as the function of the angular displacement of the reference element. In the framework of the angular approach, the DOF of the main rotation angle θ is chosen as the reference variable. FIG.1.5 illustrates the distribution of a signal with the angular periodicity f_θ

in respectively the angular and time domain. The signal is presented in three operating regimes with different rotation speeds where the third one ω_3 is variable in order to highlight the angular periodicity of the signal treated in different cases. Comparing both the temporal and angular distribution of the signal, it is demonstrated that the cyclic phenomena is covered up in the time domain in the non-stationary operation. In the opposite case, if the signal has the time periodicity, it will also lose its periodic characteristics in the angular domain in non-stationary operations. As mentioned before rotating machines never operate at the stationary state in the reality, describing them in a dynamic model based on the angular approach in order to reveal their characteristic frequency in non-stationary operations becomes a necessary. By keeping this characteristic of frequency in the angular domain, the geometric fault frequencies will be invariant and independent of rotation speed variation so that they could be identified easily from the angular spectra and the condition monitoring of rotating machines will be simpler.

Moreover as a multi-frequency system, rotating machines may have characteristic frequencies from two sources: the angular dependent frequencies and the time dependent frequencies. Take the electric motor as an example, the angular dependent frequencies come from the angular periodicity associated with the motor geometry for example the variation of the air gap permeances due to the stator and rotor slots as well as the excitations induced by the defects of the rotating components such as the bearing defects while the time dependent frequencies are brought by those structural resonance and the input power supply frequency. In order to distinguish or to demodulate the two types of characteristic frequencies so as to identify the source of the vibration and noise in electrical machines, the angular approach could be a useful tool.

1.2.3.2 Applications of the angular approach

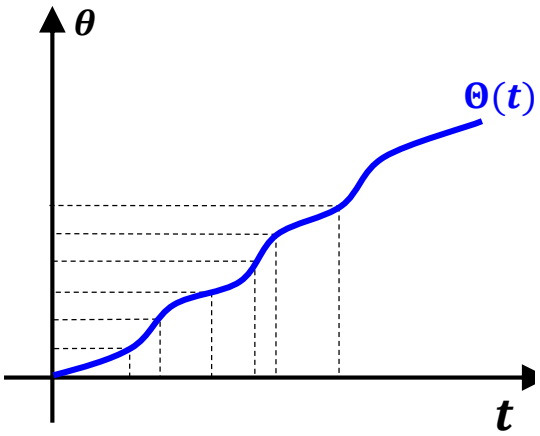

Figure 1.6: The expression of the rotation angle as a function of time.

In the dynamic model of the rotating machine solved in the time domain, the rotational displacement θ is often obtained by integrating the rotation speed over a time span. This rotation speed value could be achieved either by assigning a predefined constant value or through a numerical estimation based on the finite differentiation method. However, this method contradicts to the reality of the non-stationary operation state and it can't take the real fluctuation of the rotation speed into account. In order to overcome this limitation, the fundamental relation "Angle-Time" is introduced. This relation defines two bijective functions to pass from the temporal domain to the angular domain and vice versa. The first function is the expression of the rotation angle as a function of time $\theta = \Theta(t)$ as illustrated in FIG.1.6 and the second is defined as the inverse function of the first $t = \Theta^{-1}(\theta)$. This transformation is mathematically feasible only when θ and t are strictly monotonous and their derivative (which is the rotation speed of the system) is different from zero. The rotation speed is calculated as the derivative of the rotational displacement with respect to the time. By introducing the "Angle-Time" relation, the new definition of the rotation speed is developed as:

$$\omega(t) = \frac{d\Theta(t)}{dt} = \frac{d\theta}{dt} = \frac{d\theta}{d\Theta^{-1}(\theta)} = \hat{\omega}(\theta) \tag{1.4}$$

where $\hat{\omega}(\theta)$ is known as the Instantaneous Angular Speed (IAS) [165] which can be achieved directly from the state vector. Therefore the assumption of the constant rotation speed is unnecessary in the angular approach and simulations in non-stationary operations can be performed directly without any further assumptions. With the IAS and by applying the chain rules, the relation between the derivations in time and in angle is deduced as:

$$\frac{d\bullet}{dt} = \frac{d\bullet}{d\theta} \cdot \frac{d\theta}{dt} = \frac{d\bullet}{d\theta} \cdot \hat{\omega}(\theta) \tag{1.5}$$

This equation allows us to describe the rotating system according the angular variables such as those associated with the geometry of the rotating machine.

The general differential equations in the time domain about a simple rotating machine could be expressed in the form of the state equations as defined in EQ.1.6:

$$\frac{d\{Q\}}{dt} = [A] \cdot \{Q\} + [B] \cdot \{U\} \tag{1.6}$$

where $\{Q\}$ is the state vector. $[A]$ and $[B]$ are the matrices of constant coefficients and $\{U\}$ is the vector of the input excitation. By adopting EQ.1.5, the differential equations can be rewritten in the angular domain as shown in EQ.1.7:

$$\begin{cases} \dfrac{d\{Q\}}{d\theta} = \dfrac{1}{\hat{\omega}(\theta)} \cdot ([A] \cdot \{Q\} + [B] \cdot \{U\}) \\ \dfrac{dt}{d\theta} = \dfrac{1}{\hat{\omega}(\theta)} \end{cases} \tag{1.7}$$

Two coefficients matrices $[A]$ and $[B]$ remain the same. The size of the differential equations is increased by adding one equation in order to take into account the "Angle-Time"

relation. Therefore not only the main DOF of the rotation θ but also the time variable t are both considered as two variables in the state vector. As the result, the state vector can be represented as the function of angle or time $\{Q\} = \{Q(t)\} = \{\hat{Q}(\theta)\}$ so that the dynamic equations can be solved freely in both time and angular domain.

1.2.4 State of the art (Previous model)

Based on the comparison of different modeling methods discussed before, the PNM is adopted to describe the whole magnetic field of the electric motor while the motor shaft is discretized into several beam and node elements based on Timoshenko beam theory. A strong coupling between the electro-magneto-mechanic fields is taken into consideration in this multiphysics model and all the state variables of the electric motor are calculated and analyzed in the frame of the angular approach to simulate the machine's dynamic behavior in non-stationary operating conditions as well as to interpret the transfer path from different angularly-periodic variation field in an electrical machine.

Fourati et al. [1, 4] have presented a simple asynchronous electrical machine model to describe this multiphysics interaction. In this first model, the main coupling with the mechanical part is supposed to be through the speed variation of the shaft. In the framework of angular approach, rotor speed is never considered to be constant. This offers the possibility to obtain the rotor speed as an output of the model so as to perfectly know the relationship between the time and the angle. Therefore, the simulations in non-stationary operating conditions are performed in a natural way. Unfortunately, in this previous work the strong coupling with the mechanical part is only realized on the rotational movement to identify the bearing defects represented by the angularly varying load torque in the model. In order to reinforce this strong coupling and create a more robust model, the relation between the UMP and the rotor radial displacements is set up in this model and several modifications are applied. Before that, in order to get a better understanding about the previous model, a general presentation about the models of three fields and their couplings are provided in this subsection.

1.2.4.1 Mechanical modeling

The mechanical part is consisted of the shaft and the support shown in FIG.1.7. The rotating shaft is divided into five nodes based on the classical Timoshenko model while the quasi-2D IM model is situated on the middle node. The shaft is supported by two bearings which are simplified as two orthogonal springs along x and y directions with two identical stiffness values for each in the present simulation. The vibration differential equation is applied to interpret the dynamic motion of the system as described in EQ.(1.8).

$$[M] \cdot \{\ddot{X}\} + [C] \cdot \{\dot{X}\} + [K] \cdot \{X\} = \{F(t)_{ext}\} + \{F(\{X\}, \{I\})_{mag}\} \tag{1.8}$$

where $[M]$, $[C]$ and $[K]$ are the matrices of mass, damping and stiffness respectively. $\{F(t)_{ext}\}$ is the vector of the global external forces exerted on the mechanical structure and variated as a function of the time like the load torque T_r shown in FIG.1.7, while

$\{F(\{X\},\{I\})_{mag}\}$ are the general magnetic forces generated inside of the motor as the function of the rotor center displacement $\{X\}$ and the electric currents $\{I\}$. Since only the interaction between the electromagnetic torque T_{em} and the shaft rotation angle θ is taken into consideration in the first model, the general magnetic forces term can be simplified as $\{F(\theta,\{I\})_{mag}\}$. The mass and the stiffness matrices $[M]$, $[K]$ are associated with each structural element of the shaft and the support part. Since the stator part of the motor is fixed to the base, only the rotor is taken into account in the modeling with the assumption that the stator part is considered to be rigid and not to vibrate in this model. As it is mentioned in [1], the structural damping is calculated by adopting the modal damping approach while the damping of the rotational rigid mode is added as a damping elementary matrix. Each node has 6 DOF to illustrate their displacements in all directions of the space. For example about the k_{th} node in the shaft, its 6 DOF are shown as $\{X\}_k = \{x,y,z,\theta_x,\theta_y,\theta_z\}^t_k$. From FIG.1.7, it can be seen that the displacement of rotor center θ is represented by the rotation DOF of the middle node in the shaft. By transforming it into a state-space form in EQ.(1.9), one obtains

$$\frac{d\{Q_M\}}{dt} = [A_M]\cdot\{Q_M\} + [B_M]\cdot\{U_M(\{Q_M\},\{I\})\} \tag{1.9}$$

with the state vector of the mechanical part $\{Q_M\} = \{\{X\},\{\dot{X}\}\}^t$ to display the displacements and velocities of each node about all 6 DOF at every iteration step. The force term $\{U_M\}$ is composed of the external applied forces $\{F(t)_{ext}\}$ and the inside generated motor forces $\{F(\theta,\{I\})_{mag}\}$.

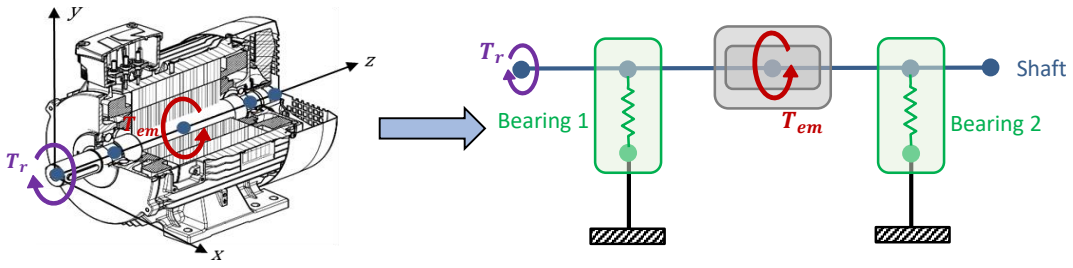

Figure 1.7: Mechanical modeling in the first model (Bearing stiffness only presented in one direction)

1.2.4.2 Magnetic modeling

As discussed before, the PNM [2] is adopted to describe the magnetic field in this multiphysics model of the electric motor. The motor section (the left schema in FIG.1.8) is discretized by a network with various permeance elements ($P_{sy}, P_{st}, P_{sl}, P_{ag}, P_{rl}, P_{rt}, P_{ry}$)

located in each branch with the subscripts indicating the respective belonging areas which are shown in different colors in the right schema of FIG.1.8. The corresponding magnetic flux ($\phi_{sy}, \phi_{st}, \phi_{sl}, \phi_{ag}, \phi_{rl}, \phi_{rt}, \phi_{ry}$) can only pass through the decided path in a defined direction as illustrated in the schema. The induced MMF source ($\mathcal{F}_{st}$ and $\mathcal{F}_{rt}$) are set up on the stator and the rotor tooth area respectively because they are the part to cut off the magnetic induction lines and produce the MMF. Since the saturation of the magnetic field is neglected in the previous work, the permeance values in the stator and rotor iron core part ($P_{sy}, P_{st}, P_{sl}, P_{rl}, P_{rt}, P_{ry}$) are considered to be constant. Their values are considered to be identical in each region that were obtained by the FEM analysis about the motor's magnetic field. However the air-gap permeances (P_{ag}) vary as a function of the shaft rotation angle θ and they are calculated by adopting the Ostovic model [2] in the case without eccentricity. Since the skew of the rotor bars and the steel lamination stack length are taken into consideration in calculating the permeance values, this magnetic model can be considered as $2.5D$. In the first model which is created with the nodal-based PNM, it's easy to deduce the relation between the magnetic flux $\{\phi\}$ and the electric current $\{I\}$ by applying Kirchhoff's current law and Ampere's law. That leads to EQ.(1.10) which indicates the coupling of the magneto-electric fields.

$$\{\phi\} = [Gg] \cdot [XX(\{X\})] \cdot \{F_{md}\} = [Gg] \cdot [XX(\{X\})] \cdot [ZZ] \cdot \{I\} \tag{1.10}$$

where $\{\phi\}$ is the magnetic flux of each phase, $\{I\}$ is the electrical phase currents, $[Gg]$ is a constant matrix that transform the magnetic flux from each branch of the permeance network to those of each phase, $[XX(\{X\})]$ is a permeance matrix in function of the rotor center displacements $\{X\}$ (it is precisely referred to θ in the first model) which implies the coupling between the mechanical field and the magnetic field, $\{F_{md}\}$ is a vector of MMF and $[ZZ]$ is a winding matrix defined by different winding configurations. The details about the construction of each matrix can be found in [4].

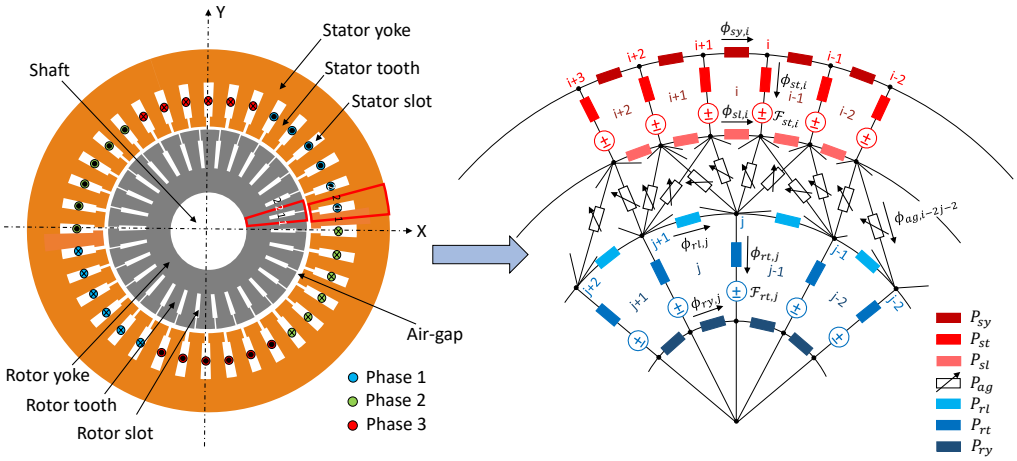

Figure 1.8: Magnetic modeling in the first model

1.2.4.3 Electrical modeling

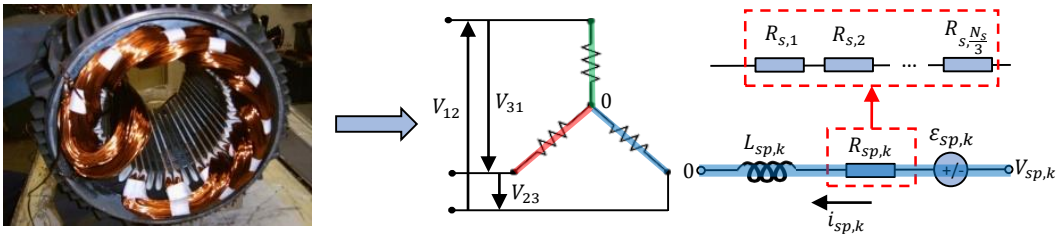

(a) Stator

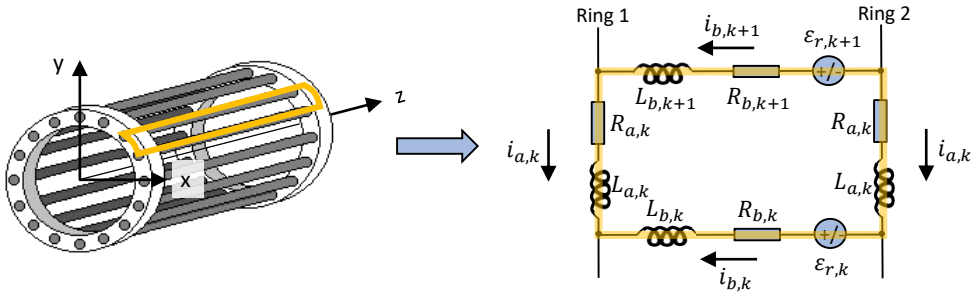

(b) Rotor

Figure 1.9: Electrical modeling in the first model

The electrical model consists of two parts as shown in FIG.1.9. One is the three phase windings in the stator and another is the n_r short circuits formed by the squirrel cage in the rotor. The stator windings in FIG.1.9(a) are fed by three phase star connection voltages (V_{12}, V_{23}, V_{31}) which can also be replaced by the delta connection in the proposed model. Each phase circuit is simplified by a phase resistance R_{sp}, a phase winding leakage reluctance L_{sp} and an electromotive force (EMF) ε_{sp}. Since the stator windings adopted in this model are the distributed windings connected in series, R_{sp} is the sum of the coil resistance R_{s} surround each stator slot in the same phase. The short circuits in the rotor squirrel cage from FIG.1.9(b) are each composed of two ring segments and two adjacent rotor bars. Similar as the stator part, each bar branch is represented by a bar resistance R_b, a bar leakage reluctance L_b and an EMF ε_{r} while each ring branch is composed of a ring resistance R_a and a ring leakage reluctance L_a. There is no EMF source in the ring branch because this part isn't involved in producing the EMFs. In the first model, the stator phases currents i_{sp} and the rotor ring currents i_a are chosen as the state vectors of the electromagnetic modeling. Their dynamic behavior is described in EQ.(1.11).

$$[L] \cdot \frac{d\{I\}}{dt} + [R] \cdot \{I\} + \frac{d\{\phi\}}{dt} = \{V(t)\} \tag{1.11}$$

where $[L]$ is a matrix of leakage reluctance, $[R]$ is a matrix of resistance, $\{I\}$ is the state vector containing 3 stator phase currents $\{i_{sp}\}$ and n_r rotor ring currents $\{i_a\}$, $\{\phi\}$ is a vector of phase magnetic flux and $\{V(t)\}$ is the supply voltage of three phases which variates as a time function. The Faraday law is applied to realize the connection between the magnetic field and the electric field: $E = \triangle\varepsilon_r = -\frac{d\phi}{dt}$.

1.2.4.4 Multiphysics couplings

The multiphysics couplings are realized by solving the global differential equations with a set of global state vectors belonged to the mechanical part (displacements $\{X\}$ and velocities $\{\dot{X}\}$ of all 6 DOF for each node) and to the electrical part (3 stator phase currents and N_r rotor ring currents $\{I\}$). Different from other multiphysics models, this one is considered as a strong coupling which means there is a mutual influence between each of the two fields. As illustrated in FIG.1.10, Magnetic field and Electrical circuit form the Induction Machine model while the mechanical structure is consisted of the Shaft and Support system.

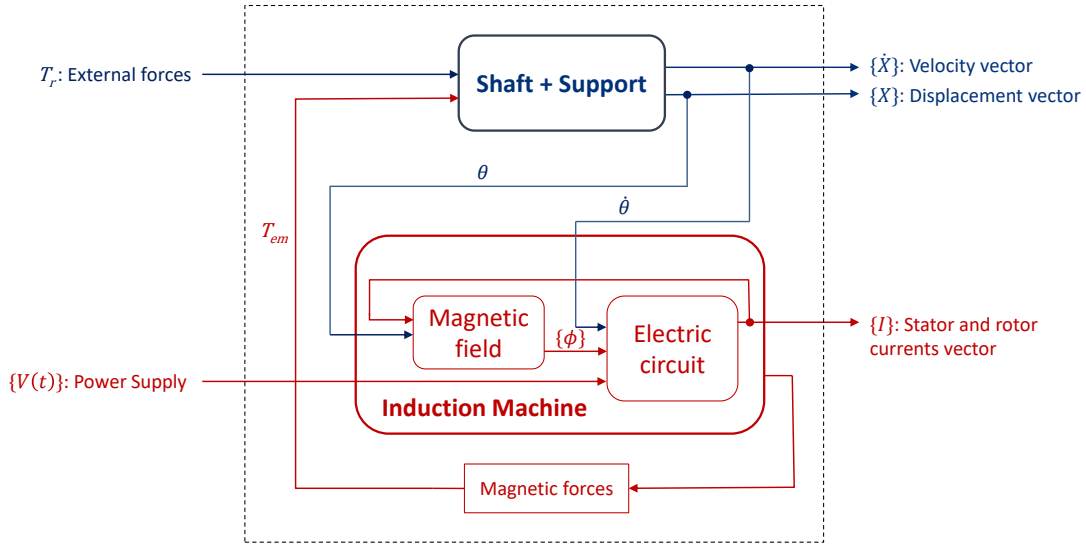

Figure 1.10: Multiphysics couplings in the first model

Inside of the Induction Machine model, the stator and rotor phase currents $\{I\}$ and the shaft position angle θ are used to calculate the magnetic flux $\{\phi\}$ which can be adopted inversely to calculate the electrical phase currents at each moment by combining with the supply voltage $\{V(t)\}$ and the instantaneous rotor center rotation speed $\dot{\theta}$. The strong

coupling between the electromagnetic field can be described by substituting EQ.(1.10) into EQ.(1.11):

$$\begin{aligned}
&[L]\cdot\frac{d\{I\}}{dt}+[R]\cdot\{I\}+\frac{d([Gg]\cdot[XX(\theta)]\cdot[ZZ]\cdot\{I\})}{dt}=\{V(t)\}\\
\Longrightarrow&[L]\cdot\frac{d\{I\}}{dt}+[R]\cdot\{I\}+[Gg]\cdot\frac{d[XX(\theta)]}{dt}\cdot[ZZ]\cdot\{I\}+[Gg]\cdot[XX(\theta)]\cdot[ZZ]\cdot\frac{d\{I\}}{dt}=\{V(t)\}\\
\Longrightarrow&\big([Gg]\cdot[XX(\theta)]\cdot[ZZ]+[L]\big)\cdot\frac{d\{I\}}{dt}=\{V(t)\}-\big([R]+[Gg]\cdot\frac{d[XX(\theta)]}{dt}\cdot[ZZ]\big)\cdot\{I\}
\end{aligned}\tag{1.12}$$

By applying the chain rule, the derivative of the permeance matrix can be deduced in EQ.(1.13).

$$\frac{d[XX(\theta)]}{dt}=\frac{d[XX(\theta)]}{d\theta}\cdot\frac{d\theta}{dt}=\frac{d[XX(\theta)]}{d\theta}\cdot\dot{\theta}\tag{1.13}$$

where the derivative of permeance matrix about the shaft rotation angle $\frac{d[XX(\theta)]}{d\theta}$ can be calculated analytically and the $\dot{\theta}$ is the instantaneous shaft rotation speed which can be achieved directly from the state vectors. In EQ.(1.12) if the sum of matrices before $\frac{d\{I\}}{dt}$ is considered to be $[AAA(\theta)]=[Gg]\cdot[XX(\theta)]\cdot[ZZ]+[L]$ and the sum of the matrices before $\{I\}$ is considered to be $[BBB(\theta,\dot{\theta})]=[R]+[Gg]\cdot\frac{d[XX(\theta)]}{dt}\cdot[ZZ]$, then EQ.(1.12) can be simplified in the form of the state equation:

$$\begin{aligned}
\frac{d\{I\}}{dt}&=-[AAA(\theta)]^{-1}\cdot[BBB(\theta,\dot{\theta})]\cdot\{I\}+[AAA(\theta)]^{-1}\cdot\{V(t)\}\\
&=[A_{EM}(\theta,\dot{\theta})]\cdot\{I\}+[B_{EM}(\theta)]\cdot\{V(t)\}
\end{aligned}\tag{1.14}$$

In the mechanical subsystem, the outputs from the electromagnetic part "Magnetic forces" (T_{em}) are exerted on the mechanical part to change its dynamic behavior and at the same time the variation of these values affected mechanical state values (θ and $\dot{\theta}$) will react on the electromagnetic part to alter the magnetic field distribution so as to influence their output values like currents and magnetic forces. Their interactions can be described by combining EQ.(1.14) and EQ.(1.9) together. Thanks to the global state vector, this mutual influence energy conversion happens simultaneously and automatically in this multiphysics model which is able to describe the real dynamic behavior of electrical machines. The two sets of differential equations are programed and calculated in MATLAB® by adopting directly the Ordinary Differential Equation (ODE) Solvers (ODE15s) in the software to solve the stiff differential equations defined in this model. The time variable t is added in the state vector to save it in the output when the system is solved in the angle domain. The associated state equation is presented as:

$$\frac{dt}{dt}=0\times t+1\tag{1.15}$$

And the global differential equations are assembled by EQ.(1.14), EQ.(1.9) and EQ.(1.15)

as:

$$\begin{cases} \dfrac{d\{I\}}{dt} = [A_{EM}(\{Q_M\})] \cdot \{I\} + [B_{EM}(\{Q_M\})] \cdot \{V(t)\} \\ \dfrac{d\{Q_M\}}{dt} = [A_M] \cdot \{Q_M\} + [B_M] \cdot \{U_M(\{Q_M\}, \{I\})\} \\ \dfrac{dt}{dt} = 0 \times t + 1 \end{cases} \tag{1.16}$$

They can be described in a more compact expression through EQ.(1.17).

$$\frac{d\{Q\}}{dt} = [A(\{Q_M\})] \cdot \{Q\} + [B(\{Q_M\})] \cdot \{U(\{Q\})\} \tag{1.17}$$

where $\{Q\} = \{\{I\} \ \{Q_M\} \ t\}^t$ is the global state vector, $\{U(\{Q\})\} = \{\{V(t)\} \ \{U_M(\{Q\})\} \ 1\}^t$ is global generalized force vector and the two coefficient matrices $[A(\{Q_M\})]$ and $[B(\{Q_M\})]$ are defined respectively as:

$$[A(\{Q_M\})] = \begin{bmatrix} [A_{EM}(\{Q_M\})] & [0] & \{0\} \\ [0] & [A_M] & \{0\} \\ \{0\} & \{0\} & 0 \end{bmatrix} ; \ [B(\{Q_M\})] = \begin{bmatrix} [B_{EM}(\{Q_M\})] & [0] & \{0\} \\ [0] & [B_M] & \{0\} \\ \{0\} & \{0\} & 1 \end{bmatrix} \tag{1.18}$$

Based on the angular approach, EQ.(1.17) is also able to be solved in the angular domain by replacing the time step with the shaft rotation angle step according to EQ.(1.7).

1.2.4.5 Corrections and improvements

The first model developed by Fourati et al. [1, 4] only realized the strong coupling between the electromagnetic subsystem and the mechanical structure in terms of the rotational movement in the case without rotor eccentricity. It is an useful model for analyzing the steady state of a healthy IM. But once the mechanical or the electromagnetic defects are introduced into the system, the original even magnetic field will be distorted and the UMP will be generated to further disturb the whole system. It is obvious that the first model is no longer adapted in the case with mechanical or electromagnetic defects. Considering that the simulation results of the first model are not validated quantitatively and some errors have been identified in the code during the study, the first goal of this research work is to implement some corrections in order to obtain a more robust and efficient model. And then some improvements are realized to develop the capacity of this multiphysics model in simulating the case with rotor eccentricity. As one of the contributions of the study, a summary about all the corrections and improvements that will be effectuated in the model are listed in the followings.

Corrections

- Different from [1], the rotor bar currents i_b are chosen to be the state vectors instead of the rotor ring currents i_a for the surveillance of the rotor bar fault.

- The matrix of the winding leakage inductance $[L]$ in EQ.(1.11) is ignored in the present model since it is small compared to the mutual inductance as discussed in [139]. Thus the matrix $[AAA(\theta)]$ in EQ.(1.14) is modified as $[AAA(\theta)] = [Gg] \cdot [XX(\theta)] \cdot [ZZ]$.

- The original matrix $[AAA(\theta)]$ becomes singular after the remove of the winding leakage inductance matrix because the $n_{ph} + n_r$ lines equations in the electromagnetic modeling are not independent with each other. In the other word, only $n_{ph} + n_r - 2$ current values from the electromagnetic state vector are needed to describe the operation state at each moment for the reason that the sum of n_{ph} stator phase currents and the sum of n_r rotor currents respectively equals to zero. This non invertible problem is resolved by reducing the number of the state vector. More details about the modifications of the corresponding matrices can be consulted in SEC.2.2.2.

- The nodal permeance matrix $[XX]$ was calculated as the product of the fundamental transform matrix and the branch permeance matrix from EQ.(2.51) in [4]. The iron core part permeances from each area are considered as one constant value, Ex: $P_{sy,1} = P_{sy,2} = \cdots = P_{sy,Nns}$. This assumption is no longer validated especially in the case with magnetic saturation effects. Therefore, the nodal permeance matrix $[XX]$ is re-deduced from the nodal PNM and re-programmed in the code considering that the iron core part permeances from each area are independent values. The detailed construction processes are available in SEC.A.1.

- The derivative of the nodal permeance matrix is re-organized in the form of the sub-matrix to accelerate the calculation efficiently.

- Instead of adopting directly the parameters measured from the FEM simulation results, all the motor parameters in the electromagnetic part (like the winding resistance and the iron core part permeances) are calculated automatically according to the motor's geometric dimensions in order to obtain a more closer bond between the motor's behavior and its design. Furthermore, the calculation of the iron core part permeances based on the motor's geometry is also important for setting up the magnetic saturation effect in the model.

- The electromagnetic modeling based on nodal-based PNM is re-developed to obtain a complete system for integrating the magnetic saturation effect. The calculation about the electromagnetic forces (T_{em}, F_{emr}) are reconsidered in respect of magnetic node potentials instead of the magnetic branch flux. The detailed processes will be presented systematically in the second chapter.

Improvements

- The relation between the electromagnetic radial forces F_{emr} also known as UMP and the rotor center radial displacements x_r and y_r is added in the present model to

predict the motor's dynamic behavior in the case with the rotor eccentricity. So that the nodal permeance matrix defined in EQ.(1.10) isn't only the function of the rotor center rotation angle θ but also varies with the evolution of the radial displacements of the rotor center (x_r, y_r) due to the rotor eccentricity. However the rotation angle θ is always considered as the main iteration step for solving the dynamic differential equations due to the bijective "Angle-Time" relation in the rotation machine.

- The modified multiphysics model which is also called as the electro-magneto-mechanical model (Model EMM) is validated in the quasi-static regime by comparing its simulation results with those simulated from another traditional FEM. A model without the coupling of the mechanical structure which is called as the electromagnetic model (Model EM) is separated from the Model EMM to highlight the importance of the strong coupling in the multiphysics modeling of the electric motor and to help with the validation of the proposed model in the quasi-static regime.
- Different winding configurations and power supply connections are applied in the model to study the influence of different electrical architectures.
- Different mechanical structures are established in the model to study the influence of different mechanical architectures.
- The state vector of the electromagnetic part is changed from the phase currents to the phase flux for the simplicity of the calculation and for the preparation of setting up the magnetic saturation effect in the model. The two models with different state vectors are compared in this thesis.
- The electromagnetic modeling based on nodal-based PNM is remodeled by adopting the mixed PNM for a easier integration of the saturation effect. The two models based on different PNM mesh algorithms are described simultaneously in this thesis.
- The whole multiphysics model is developed in a PMSM for the extension analysis in a second electric motor type. The comparison about the dynamic behavior between those two traditional electric motors is discussed in this thesis.
- The mass unbalance excitation is set up in this multiphysics model to study the vibration behavior of the electric motor in the frame of the rotor dynamic motion.

1.3 Model assumptions and thesis outline

Based on the first model about an IM and followed by the needs of the corrections and improvements, a new multiphysics model with strong electro-magneto-mechanical couplings dedicated to investigate the influence of the UMP on the dynamic behavoir of electric motors is proposed in this thesis. This fully coupled model is adopted to describe the performance of both the IM and the PMSM with different winding configurations and in

different mechanical structures. The vibration phenomena excited by the UMP, the mass unbalance force and the rotor gravity are analyzed respectively in two traditional electric motors under the influence of different architectures and in non-stationary operations. Both physical and geometrical nonlinearities are considered in this model to interpret the nonlinear phenomena of UMP. Since the model is supposed to perform the longtime simulations with the reasonable computational effort, several assumptions about the models of different physical fields in electrical machines are put forward to simplify the calculation. They are summarized as follows:

Mechanical model

- All the beam elements involved in the shaft are considered as rigid bodies to keep the same angular velocity for each point of the shaft.
- Both rotor and stator are perfect cylinders and their axes are parallel which means only the translation eccentricity is taken into account and the airgap length is considered to be axially constant.
- Stator is considered to be a rigid body so that deformations of the stator and the housing are neglected.
- Gyroscopic effects are not considered since all lateral motions are assumed planar and the rotor angular velocity is parallel to the principle axis of inertia.
- The supports and bearings are simplified as linear elastic springs (with a constant stiffness k).
- The distribution of magnetic material on the rotor is assumed to be symmetric and homogeneous.

Magnetic model

- Electrical capacitances are neglected compared to magnetic inductances to imply that the electric field energy can be neglected compared to the magnetic field energy.
- Thermal effects are neglected.
- The electromagnetic materials are assumed isotropic. Their nonlinear behavior such as the magnetic saturation effect is considered but no hysteresis.
- The magnetic field is modeled as 2.5D by ignoring the end effects and homopolar fluxes. The skewing is considered in the calculation of the airgap permeances.
- Eddy currents in solid conductive domains are neglected.
- The distribution of the currents in each slot is assumed to be homogeneous so that the skin and the proximity effect are neglected.

- In each divided magnetic tube elements, the flux density is assumed to be distributed homogeneously so that their magnetic flux can be calculated by the isotropic magnetic permeability and the average geometry dimension.
- PMs are assumed to have a constant residual magnetic flux density and a linear magnetic characteristic.

Electrical model

- The electrical circuits are represented by the electrical network composed of constant resistances and nonlinear inductances where the inductances are represented by the derivative of the linkage flux from the magnetic field.
- The winding leakage effects are neglected.
- The electric motor is powered by an ideal balanced three-phase voltage or current source.

The whole thesis is composed of five chapters and three appendices.

CHAP.1 provides the context of this research work. The research motivation is presented firstly by describing an abnormal vibration problem appeared in an integrated PMSM. And then several modeling methods for simulating respectively the electromagnetic field and mechanical structure of the electrical machines are summarized and discussed from the literature in order to choose the most appropriate methods for establishing the models of each subsystems in the proposed model. The angular approach is introduced afterwards to demonstrate its importance to the simulations in non-stationary operating conditions. A brief presentation about the first proposed model is provided to obtain a better understanding about the state of the art in order to better introduce the contributions of this work. The model assumptions about different physical fields and the thesis outlines are summarized at the end of the chapter.

CHAP.2 presents a methodology about the establishment of the multiphysics model for an IM. Different algebraic equations based on the mesh/nodal mixed PNM are developed progressively to achieve the final augmented magnetic equations about the magnetic field. They are coupled with the electrical differential equations deduced from the three-phase stator winding and the rotor cage to obtain the electromagnetic coupled model. From different deductive equations, the state equations of the electromagnetic field can be solved with two different set of state vectors: the phase current or the phase flux. The phase flux model is identified as the better choice through their comparison. By setting up the mass unbalance in the mechanical system, the electromagnetic force is calculated in the mechanical equation. The two differential equations from different subsystems are combined together to construct finally the multiphysics coupled model which is compared with a decoupled model without the mechanical structure in order to demonstrate the significance of the electro-magneto-mechanical couplings in the modeling of electrical machines. This multiphysics model is validated in the quasi-static regime by comparing with a traditional FEM and the industrial reference data. The dynamic simulation results

are finally analyzed respectively in the stationary and non-stationary operations under different eccentricities.

CHAP.3 is dedicated to develop the proposed multiphysics model about an interior PMSM. Based on the model of the IM established in CHAP.2, the same modeling pattern about the three physical fields in the PMSM is repeated to achieve the final fully coupled model. In order to avoid repetition, only the parts different from those in the model of the IM are presented such as the definition of the permeance network mesh in the rotor part, the MMF calculation of the PMs, the single concentric stator winding connection and the current power supply. The establishment of the magnetic saturation effect is introduced in the couplings between the electromagnetic field since the reference PMSM is very sensitive to the magnetic saturation especially in the magnetic bridges from the rotor part. A customized mechanical structure about the reference PMSM is described in the multiphysics couplings where the coupled and non-coupled models are compared to explain how to conduct the simulation in the PMSM model without the control system. Similar as before, the multiphysics model is validated by comparing with the identical model established in the software "Finite element method magnetics (FEMM)". Another equivalent model with a simplified rotor geometry is created and validated for the long-time simulations in non-stationary operations. To the end of the chapter, the characteristic phenomena corresponding to the input static eccentricity is recognized in the stationary operation while the dynamic simulation results under the mass unbalance excitation are analyzed in non-stationary operations.

CHAP.4 investigates the influence of different architectures on the dynamic behavoir of electrical machines. The equivalent model about the reference PMSM created in CHAP.3 is adopted to study the influence of different mechanical structures because some instability phenomena are identified in an integrated PMSM connected with a screw compressor in a cantilever structure as mentioned in CHAP.1. The second study about the influence of different winding configurations are performed in the framework of the IM as discussed in CHAP.2 since the same pole pairs of the modified field winding can be induced automatically in the rotor cage of the IM without modifying its geometry.

CHAP.5 draws the final conclusions of the research work and some suggestions about the future study are proposed toward the end of the chapter.

APPENDIX.A and APPENDIX.B presents the magnetic field modeling about respectively the IM and the PMSM in the frame of nodal based PNM in order to provide the modified version of the first proposed model. A summary of the motor parameters and mechanical model characteristics about different reference electric motors are given respectively in APPENDIX.C.

Chapter 2

Induction motor modeling

Contents

2.1 Introduction

Induction motors (IMs) also known as asynchronous motors are mostly used both for home appliances and in different industrial fields among electric motors [166]. They are popular for their simple but rugged structure at the moderate costs with a good reliability in the working operation. They were firstly invented by Galileo Ferraris (1885) and Nicola Tesla (1886) with a two-phase AC power source supply. Since the three-phase AC power grid is able to transfer the energy from the distance to IMs, those contemporary designs about IMs with the wound rotor and single or double cage rotor were put forward by Dolivo-Dobrovolsky in 1889.

The principle of IMs operation is very simple. Firstly, a rotational magnetic field is produced from the AC circulate in the stator windings. Then this rotational magnetic field passes through the rotor winding to induce the currents in it according to the Faraday's law and afterwards the induced currents in the rotor winding produces the second magnetic field in the rotor. According to Lenz's law, the rotational magnetic field from the stator pulls the induced magnetic field on the rotor side to move with it. Thus finally the rotor begins to rotate and the electromagnetic torque is produced due to the interaction between the two magnetic fields. Since the rotor induced current is generated by the rotor coils cutting the stator magnetic field lines, a relative movement between the stator rotational magnetic field and the rotation of the rotor must exist. That's why it is named as the asynchronous motor since the rotor speed ω_r never reaches the rotation speed of the stator rotational magnetic field which is also known as the synchronous speed of the IM ω_s except for the no-load state. The difference between the two speeds is defined as the slip (s):

$$s = \frac{\omega_s - \omega_r}{\omega_s} \tag{2.1}$$

The asynchronous motor studied in this chapter is a double squirrel cage IM. It has two poles and 36 slots. The stator is equipped with a single layered, distributed three phase winding. For the sake of the simplicity, the double rotor cage is simplified as a single cage with 30 rotor bars to conserve the same rotor slot area. The main characteristic parameters of the this IM "LSES132SM" are available in APPENDIX.C.

This chapter provides a methodology about the establishment of the multiphysics model for the IM. Since the permeance network approach is adopted to describe the magnetic field which is the core part of the electric motor, the permeance network meshing and the calculation of the basic element values are firstly introduced in SEC.2.2. By applying the Kirchhoff electrical laws, the permeance network equations are developed in SEC.2.3 to describe the relation between the chosen unknowns and the MMF sources in the whole cross section of the electrical machine. The flux linkage equations to calculate the magnetic flux in each phase from the tooth flux are worked out in SEC.2.4. The two groups of equations are combined together to build up the augmented magnetic equations in SEC.2.5 in order to obtain a full description about the whole magnetic field. As discussed in SEC.1.2.1.2, the magnetic model can be developed with different PNMs. The nodal based model is adopted in the previous model so that it is reformed in this thesis

with some modifications mentioned in SEC.1.2.4.5. Since the mesh/nodal mixed model combines the advantages of the first two, it is finally employed to establish the magnetic model in the proposed multiphysics model. For a better and clear explanation, the description of the magnetic field in the text will be based on the mesh/nodal mixed model while the one developed in the frame of the nodal based model is referred to APPENDIX.A. The electric model defined by the electrical differential equations is established in SEC.2.6. The coupling between the electromagnetic fields is then conducted in SEC.2.7 to study the performance of the electromagnetic models with different state vectors. The mechanical model of the electric motor is improved later in SEC.2.8 by adding the mass unbalance excitation and calculating the electromagnetic forces. All of the three fields are finally assembled together to realize the strong multiphysics coupling in the proposed model in SEC.2.9. A decoupled model without the mechanical part is also created in this section to compare with the fully coupled model. Before the analysis of the simulations results, this multiphysics model is validated in the quasi-static regime by comparing with a traditional FEM in the software FEMM in SEC.2.10. The dynamic simulation results are finally analyzed respectively in the stationary and non-stationary operations with the final conclusions at the end of this chapter.

2.2 Permeance network mesh

As illustrated in FIG.1.8, a permeance network mesh is realized in the whole section of the reference IM. It is composed of three parts from the outside to the inside: the stator, the air-gap and the rotor. The air-gap branches can be considered as the one-by-one connection between the nodes from the stator and rotor leakage side. FIG.2.1 are plotted to get a clear understanding about the construction of the stator and rotor mesh. Basically, the center nodes of the stator and rotor tooth width ($n_{sl,i}$ or $n_{rl,j}$) are chosen to connect with each evenly distributed nodes on the yoke ring ($n_{sy,i}$ or $n_{ry,j}$) along the radius direction in order to former the stator and rotor tooth branch while the other two curved branches along the periphery are used to represent separately the yoke and leakage flux paths. Those branches are connected together as shown in the right figure form FIG.1.8 to constitute finally n_s stator meshes and n_r rotor meshes. In FIG.2.1(a), the x axis is located at the slot which embraces the stator coil of phase 2 to allow the coil of phase 1 to situate in the first slot above the x axis since we count it in the anti-clock direction. Thus, the first tooth above the x axis is numerated as the tooth 1 while the first slot that embraces the phase 1 coil is considered as the slot 1. The same meshing method is also applied in the rotor part seeing FIG.2.1(b).

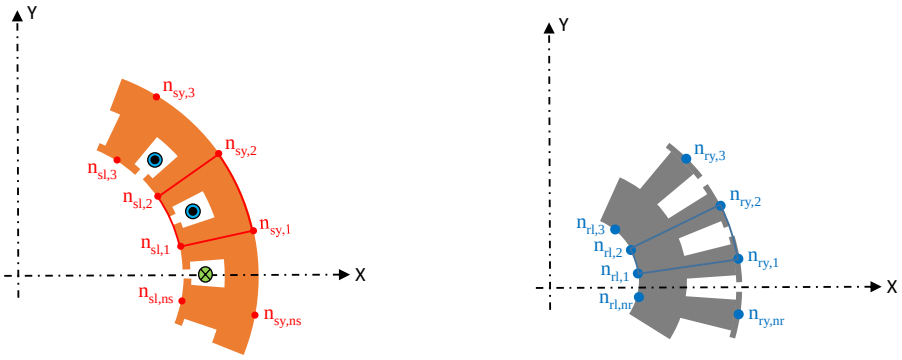

(a) Stator (b) Rotor

Figure 2.1: One of the permeance network mesh in the stator and rotor parts.

The elements appeared in the permeance network can be classified in two categories: the active and the passive. The active ones are referred to the MMF sources induced in the stator and rotor tooth branches ($\mathcal{F}_{st,i}$ and $\mathcal{F}_{rt,j}$) since they are the zones which are embraced by the windings according to Ampére's circuital law. And the passive ones are those reluctances (or the inverse of the permeance: $P_{sy}, P_{st}, P_{sl}, P_{ag}, P_{rl}, P_{rt}, P_{ry}$) in each branch to represent the opposition to the magnetic flux. As mentioned in the first chapter, those two kind of parameters are calculated according to the motor's geometry in the present model. The detailed processes are explained in the following two subsections.

2.2.1 Permeance (Reluctance) calculation

The permeance network defined before is used to describe the magnetic circuit path in the motor cross section. As similar as the resistance in the electric circuit (as discussed in TAB.2.1 from [2]), the reluctance ($\mathcal{R}$) in the magnetic field can be generally calculated as:

$$\mathcal{R} = \int_0^l \frac{dx}{\mu(x) \cdot A(x)} \tag{2.2}$$

where l is the length of the magnetic circuit, μ is the permeability of the material and A is the cross-sectional area of the circuit. It is shown that the magnetic reluctance depends on the geometry and the composition of the support. Since each branch element are assumed to be an uniform magnetic circuit in this model, EQ.(2.2) can be integrated as

$$\mathcal{R}_k = \frac{l_k}{\mu_k \cdot A_k} \tag{2.3}$$

where the subscript k is the integer to present the k-th branch in the defined permeance network. Since the permeance is the inverse of the reluctance, it is defined as:

$$P_k = \frac{\mu_k \cdot A_k}{l_k} \tag{2.4}$$

According to [2], the permeances existed in the magnetic equivalent circuit can be identified in three types: constant, parametrically nonlinear and inherently nonlinear. The last one is due to the influence of the magnetic saturation effect which means that the permeability of the iron core part is not a constant value but varies as the function of the passing magnetic flux or the instantaneous magnetic field density. Since the chosen IM is not so much influenced by the saturation effect, for the simplicity this part is not taken into the consideration in the first stage with the assumption that there is no saturation in the present model. Thus all the permeances in the iron core parts are considered to be constant and the parametrically nonlinear permeances are referred to the permeances in the air-gap that varies in the function of the rotor center instantaneous position.

2.2.1.1 Iron core part permeances

As illustrated in FIG.2.2, a portion of the stator and rotor iron core part are superimposed with each permeance network to present the discretization of each permeance element. Since the motor cross section has been discretized into small parts, each permeance element can be considered as a cuboid by neglecting the deformation of the tooth width and the influence of the curved yoke. The yoke and the tooth permeance situate separately in each yoke and tooth segment. The leakage permeance is located on the segment between the two teeth and closed to the air gap side since the slot area are used to calculate the leakage flux in air. One mesh which is composed of one yoke permeance (P_{sy} and P_{ry}), one leakage permeance (P_{sl} and P_{rl}) and two tooth permeances (P_{st} and P_{rt}) is expanded in the straight form as presented in the right schema. The passing direction of the magnetic flux in each branch can be identified by the filling texture orientation. By applying the EQ.(2.4), each permeance terms in the stator core can be calculated as:

$$\begin{aligned} P_{sy} &= \frac{\mu_{ir} \cdot h_{sy} \cdot L_m}{l_{st} + l_{sl}} \\ P_{st} &= \frac{\mu_{ir} \cdot l_{st} \cdot L_m}{h_{sy} + h_{st}} \\ P_{sl} &= \frac{\mu_0 \cdot h_{st} \cdot L_m}{l_{st}} \end{aligned} \tag{2.5}$$

where μ_{ir} is the permeability of the iron part which can be treated as a constant value in the case without the magnetic saturation. μ_0 is the vacuum permeability. L_m is the core length. h_{sy} is the width of the stator yoke. h_{st} and l_{st} are respectively the length and the average width of the stator tooth. l_{sl} is the average width of the slot. All these parameters are able to be achieved from the stator and rotor sketches of a given motor.

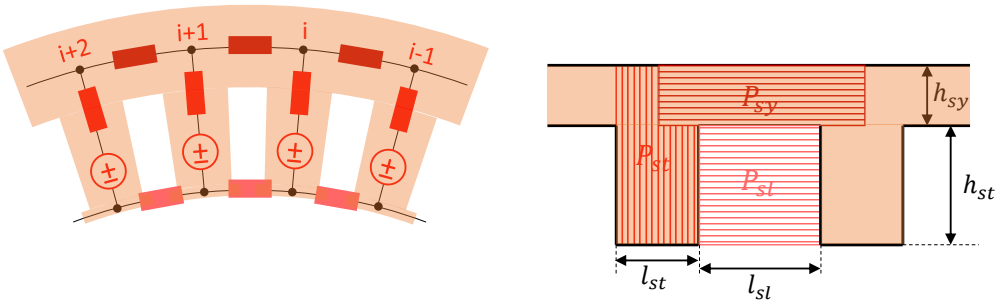

(a) Stator

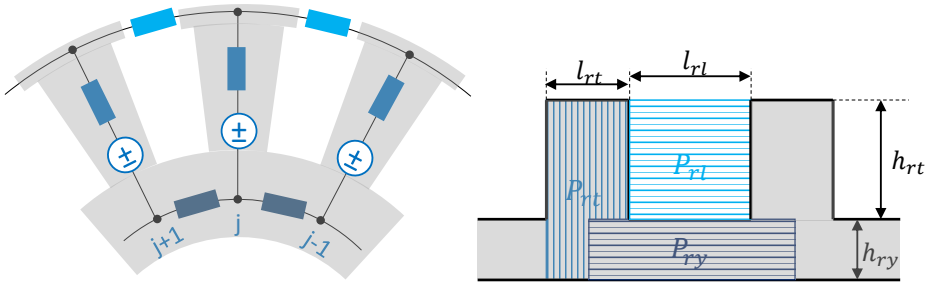

(b) Rotor

Figure 2.2: Permeance calculation in the iron core part

Due to the similar geometrical structure of the stator and rotor iron core part in the squirrel cage IM, the calculation of the permeance in the rotor iron part are realized in the same way.

2.2.1.2 Air gap permeances

General calculation According to the permeance network in FIG.1.8, the air-gap permeances are described as the sum of the permeances between each pair of stator (i) and rotor (j) tooth at each moment where i and j are the integers referred to $i \subseteq [1, n_s]$ and

$j \subseteq [1, n_r]$ with n_s, n_r denote to the stator and rotor teeth number respectively. As mentioned previously in the Magnetic modeling (SEC.1.2.4.2), their values are considered to be parametrically nonlinear and they are described as the function of the rotor instantaneous position. In the previous model without the eccentricity, the rotor instantaneous position only refers to the shaft rotation angle since the air gap length (e_i) are considered to be evenly distributed along the periphery. However in this modified model, the rotor eccentricity is taken into consideration by expressing the instantaneous air gap length as a function of the rotor geometric center coordinates. Therefore, the air gap permeance between each pair of stator and rotor tooth (P_{ij}) in the case of rotor eccentricity is defined as:

$$P_{ij}(x_G, y_G, \theta_{ij}) = \frac{P_{\text{maxc}}}{e_i(x_G, y_G)} \cdot f_p(\theta_{ij}) \tag{2.6}$$

where x_G, y_G are the coordinates of rotor geometric center, θ_{ij} is the relative angle between arbitrary stator tooth i and rotor tooth j which is described in EQ.(2.7) .

$$\theta_{ij} = \theta_{\text{rt},j} + \theta - \theta_{\text{st},i} \tag{2.7}$$

where $\theta_{\text{rt},j}$ is the angular position of rotor tooth j, $\theta_{\text{st},i}$ is the angular position of stator tooth i and θ is the shaft rotation angle at each moment.

EQ.(2.6) is composed of three components which are explained in the following parts.

1. P_{maxc} describes the maximum permeance coefficient between one pair of rotor and stator teeth when the two teeth are directly opposite with each other. The rotor bars skewing angle are taken into account in its calculation.

$$P_{\text{maxc}} = \begin{cases} \mu_0 \cdot L_m \cdot L_{\text{tr}} & \text{if } 0 \leq \tan(\beta) \leq \dfrac{|L_{\text{ts}} - L_{\text{tr}}|}{L_m} \\ \mu_0 \cdot \left(\dfrac{L_m \cdot (L_{\text{ts}} + L_{\text{tr}})}{2} - \dfrac{L_m^2 \tan(\beta)}{4} - \dfrac{(L_{\text{ts}} - L_{\text{tr}})^2}{4\tan(\beta)}\right) & \text{if } \dfrac{|L_{\text{ts}} - L_{\text{tr}}|}{L_m} \leq \tan(\beta) \leq \dfrac{L_{\text{ts}} + L_{\text{tr}}}{L_m} \\ \dfrac{\mu_0 \cdot L_m \cdot L_{\text{tr}}}{\tan(\beta)} & \text{if } \dfrac{L_{\text{ts}} + L_{\text{tr}}}{L_m} \leq \tan(\beta) \end{cases} \tag{2.8}$$

where μ_0 is the air permeability, , L_{ts} and L_{tr} are respectively the effective width of the stator and rotor tooth end and β is the skewed angle of the rotor bar.

2. $f_p(\theta_{ij})$ represents the air-gap permeance scale factor variation between one pair of stator and rotor teeth as shown in FIG.2.3. It is defined in EQ.(2.9) based on the Ostovic model [2]. And then it is developed to the adjacent pair of teeth around the periphery of the air-gap as shown in FIG.2.4 where $\tilde{\theta_{ij}}$ is the abscissa to describe the relative angular position between two pairs of stator and rotor teeth. It can be seen that in the case with eccentricity, the family of the permeances according to i_{th} stator tooth have the same amplitude like $\max(P_{i,j}) = \max(P_{i,j-1})$ but the amplitudes of the permeances according to another stator tooth will vary as $\max(P_{i,j}) \neq \max(P_{i+1,j})$ due to the variation of the effective air-gap length. Here, we assumed that only the amplitude will change when we move to the next stator tooth but there

is no change on the variation form of $f_p(\theta_{ij})$.

$$f_p(\theta_{ij}) = \begin{cases} 1 & \text{if } -\theta_{ij0} \leq \theta_{ij} \leq \theta_1 - \theta_{ij0} \text{ and } 2\pi - \theta_1 - \theta_{ij0} \leq \theta_{ij} \leq 2\pi - \theta_{ij0} \\ \dfrac{1+\cos(\pi\frac{\theta_{ij}-\theta_1}{\theta_2-\theta_1})}{2} & \text{if } \theta_1 - \theta_{ij0} \leq \theta_{ij} \leq \theta_2 - \theta_{ij0} \\ \dfrac{1+\cos(\pi\frac{\theta_{ij}-2\pi+\theta_1}{\theta_2-\theta_1})}{2} & \text{if } 2\pi - \theta_2 - \theta_{ij0} \leq \theta_{ij} \leq 2\pi - \theta_1 - \theta_{ij0} \\ 0 & \text{if } \theta_2 - \theta_{ij0} \leq \theta_{ij} \leq 2\pi - \theta_2 - \theta_{ij0} \end{cases} \tag{2.9}$$

where θ_{ij0} is the initial angular displacement between the defined pair of stator and rotor teeth. Two angle position limits (θ_1, θ_2) are defined in Eq. (2.10) and Eq. (2.11) in consideration of the skewed rotor bars:

$$\theta_1 = \begin{cases} \dfrac{L_{\text{ts}} - L_{\text{tr}} - L_m \tan(\beta)}{D_{\text{ag}}} & \text{if } 0 \leq \tan(\beta) \leq \dfrac{|L_{\text{ts}} - L_{\text{tr}}|}{L_m} \\ 0 & \text{if } \dfrac{|L_{\text{ts}} - L_{\text{tr}}|}{L_m} \leq \tan(\beta) \leq \dfrac{L_{\text{ts}} + L_{\text{tr}}}{L_m} \\ \dfrac{L_m \tan(\beta) - L_{\text{ts}} - L_{\text{tr}}}{D_{\text{ag}}} & \text{if } \dfrac{L_{\text{ts}} + L_{\text{tr}}}{L_m} \leq \tan(\beta) \end{cases} \tag{2.10}$$

where D_{ag} is the average diameter of stator inner ring and rotor outer ring.

$$\theta_2 = \frac{L_{\text{ts}} + L_{\text{tr}} + O_{\text{ss}} + O_{\text{sr}} + L_m \tan(\beta)}{D_{\text{ag}}} \tag{2.11}$$

with O_{ss} and O_{sr} are respectively the stator and rotor slot open length.

3. $e_i(x_G, y_G)$ is the effective air-gap length according to each stator tooth position in consideration of the rotor eccentricity.

The former two terms can be considered as two constant parts because they are decided once the geometry of the reference machine is defined. Consequently the description of the effective air-gap length in the function of the rotor geometric center coordinates is very important to calculate the air-gap permeances in the case with the eccentricity.

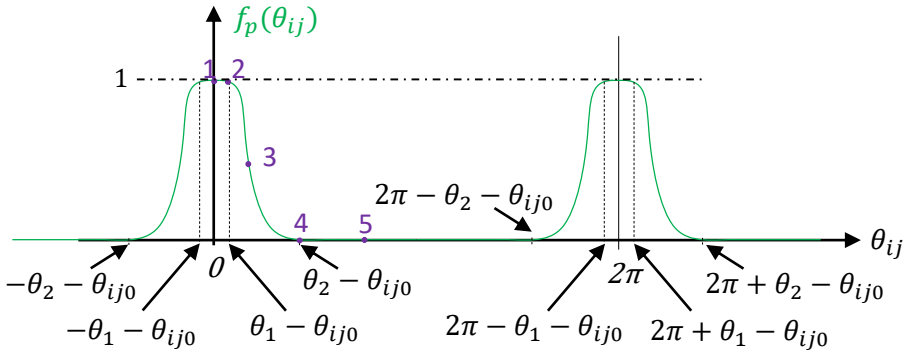

Figure 2.3: The shape function of the air-gap permeance between any two opposite teeth versus their relative angle position

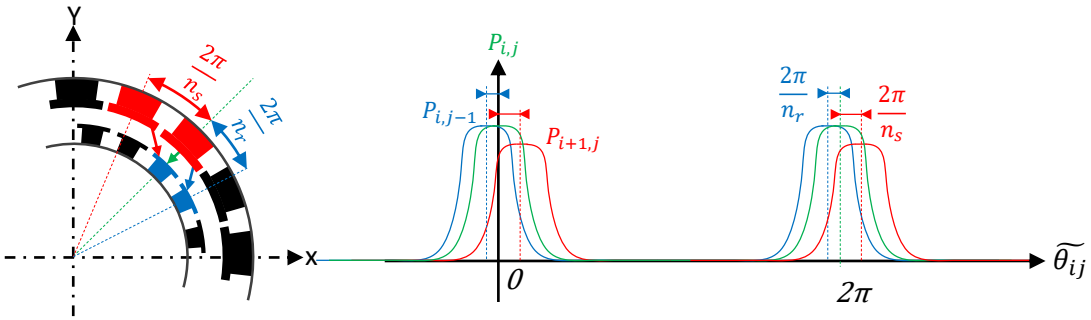

Figure 2.4: Evolution of air-gap permeance of adjacent teeth

Setting up different types of input eccentricities Before calculating the effective air gap length, the way to set up different types of input eccentricities should be discussed firstly. Since the mechanical modeling is based on the rotor part as mentioned in SEC.1.2.4.1, the reference coordinate system xOy in FIG.2.5. is established by taking the initial position of the rotor center as the origin point O. This initial position is defined before the start of the electric machine's operation. At this moment, the coordinate of the stator center $O_S(x_s, y_s)$ is used to present its position and the value of the initial input static eccentricity. Once the motor begins to operate, due to the strong coupling with the mechanical part, the rotor geometric center isn't fixed at its initial point O but moves to another position which is assumed to be the point O_R. Its coordinate (x_r, y_r) in the reference coordinate system is considered as one of the state variables in this multiphysics model so that it is updated at every rotor rotation angle θ under the influence of the UMP generated inside of the electric machine or the effect of the radial external force on the structure.

If the rotor stacks are installed unsymmetrically due to some manufacturing faults, then its geometric center O_G of the middle section doesn't coincide with its rotation center

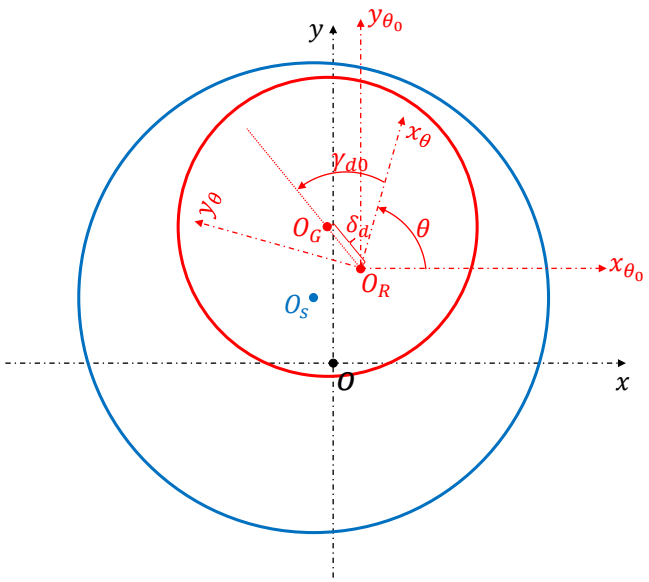

Figure 2.5: Cross-sectional view of an eccentric rotor

O_R but rotates around it in a similar crankshaft movement with the radius δ_d and a constant phase shift angle γ_{d0}. The rotational coordinate $x_\theta O_R y_\theta$ in FIG.2.5 rotates around the rotation center O_R from the initial position presented by the coordinate $x_{\theta_0} O_R y_{\theta_0}$ which is translated parallel to the reference coordinate xOy. The similar synchronism whirling movement of O_G is described by the vector $\mathbf{O_R O_G} = (\delta_d * \cos(\theta + \gamma_{d0}), \delta_d * \sin(\theta + \gamma_{d0}))$ in the coordinate system $x_{\theta_0} O_R y_{\theta_0}$. Considering the vector $\mathbf{OO_R} = (x_r, y_r)$, the position of O_G is calculated in the form of $\mathbf{O_G O}$ as EQ.(2.12) .

$$\mathbf{OO_G} = \mathbf{OO_R} + \mathbf{O_R O_G} = (\delta_d * \cos(\theta + \gamma_{d0}) + x_r, \delta_d * \sin(\theta + \gamma_{d0}) + y_r) \tag{2.12}$$

Then the coordinate of the rotor geometric center position $O_G(x_G, y_G)$ in the reference coordinate system is deduced from EQ.(2.13):

$$\begin{aligned} x_G &= x_r + \delta_d * \cos(\gamma_d) \\ y_G &= y_r + \delta_d * \sin(\gamma_d) \\ \gamma_d &= \gamma_{d0} + \theta \end{aligned} \tag{2.13}$$

This coordinate is adopted to calculate the instantaneous effective air-gap length. It can be seen clearly that by modifying the position of the point O_S and O_G in FIG.2.5, different kinds of eccentricities can be set up in this multiphysics model as described in the following:

- Case 1: If O_S doesn't coincide with O and O_G coincides with O_R, it represents the pure input "static" eccentricity.
- Case 2: If O_S coincides with O and O_G doesn't coincide with O_R, it represents the pure input "dynamic" eccentricity.

- Case 3: If O_S doesn't coincide with O and O_G doesn't coincide with O_R, it represents the input "mix" eccentricity.

Since all the input eccentricities set up in this multiphysics model are based on the instantaneous actual rotor center position, the final rotor center orbit simulated from this model does not strictly follow the trace of the defined eccentricity but is also impacted by the rotor dynamic motion. That's why all the eccentricity types are presented between the quotation marks since they can't present the rotor real motion orbit due to the strong coupling with the mechanical model.

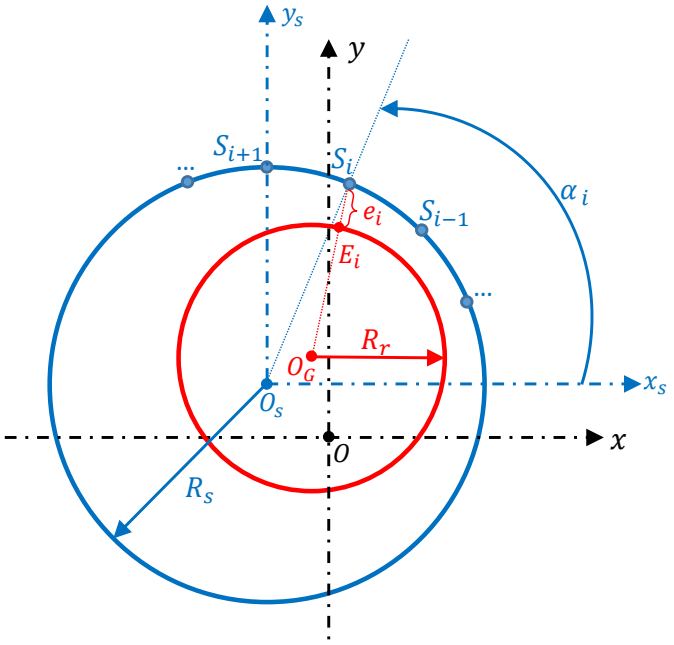

Figure 2.6: Calculation of the instantaneous air-gap length e_i associated with the stator tooth i

Calculation of the effective air-gap length FIG.2.6 shows the distribution of the effective air-gap length around the periphery of the stator inner ring (blue circle) and the rotor outer ring (red circle) with respect to each stator tooth position (blue nodes evenly distributed on the blue circle) at a certain moment. As defined before, O_G is the rotor geometric center and O_S is the stator center which is used to introduce the input static eccentricity. Since the rotation center O_R is used to describe the position of O_G, it is omitted in FIG.2.6. Two different radius R_r and R_s are denoted to the rotor outer ring and the stator inner ring respectively. E_i is the interaction point of the line $O_G S_i$ and the rotor outer ring. Every stator tooth position $\theta_{st,i}$ from EQ.(2.7) is expressed in FIG.2.6 by its

angular position α_i around the stator inner ring which is defined as:

$$\alpha_i = \frac{2\pi}{n_s} * (i-1) \tag{2.14}$$

where i is the integer belonged to $[1, n_s]$.

The effective air-gap length e_i is defined as the minimum distance between the i-th stator tooth and the rotor outer ring. According to each stator tooth position point S_i, the instantaneous effective air-gap length is deduced as

$$e_i = \| E_i S_i \| = \| O_G S_i \| - R_r \tag{2.15}$$

Two sets of coordinate systems are defined in FIG.2.6, one is the $x_s - y_s$ with the origin of the stator center O_S and another is the reference coordinate xOy that is established by taking the initial position of the rotor center as the origin point O. They are parallel to each other. In the coordinate $x_s O_S y_s$, the vector $\mathbf{O_S S_i}$ is defined as $(R_s \cos\alpha_i,\ R_s \sin\alpha_i)$. In the fundamental orthogonal coordinate system xOy, the coordinates of O_G and O_S are identified as (x_G, y_G) and (x_s, y_s) separately. So the vector $\mathbf{O_G S_i}$ appears as:

$$\begin{aligned} \mathbf{O_G S_i} &= \mathbf{O_G O_S} + \mathbf{O_S S_i} \\ &= (x_s - x_G, y_s - y_G) + (R_s \cos\alpha_i, R_s \sin\alpha_i) \\ &= (R_s \cos\alpha_i - (x_G - x_s), R_s \sin\alpha_i - (y_G - y_s)) \end{aligned} \tag{2.16}$$

Substituting EQ.(2.16) into EQ.(2.15), the instantaneous effective air-gap length can be finally expressed as:

$$e_i(x_G, y_G) = \sqrt{R_s^2 - 2R_s \cdot [\cos\alpha_i \cdot (x_G - x_s) + \sin\alpha_i \cdot (y_G - y_s)] + (x_G - x_s)^2 + (y_G - y_s)^2} - R_r \tag{2.17}$$

2.2.2 Magneto-motive force calculation

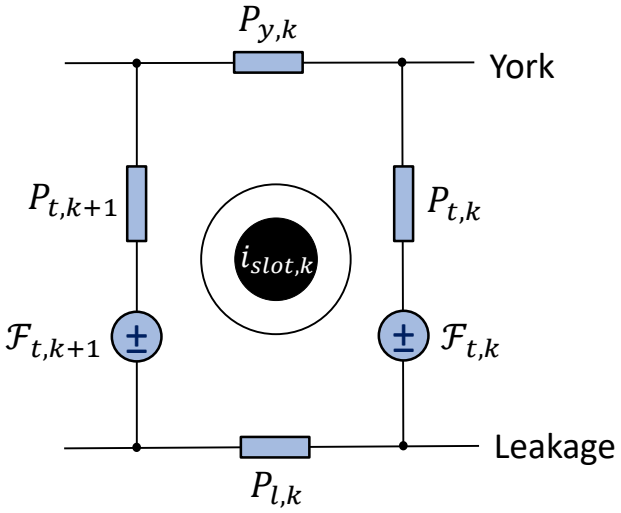

Figure 2.7: One slot mesh from the Permeance Network

One slot mesh from either the stator or the rotor iron core part is extracted from the permeance network in FIG.2.7. By applying the Ampère's law in this mesh, the relation between the MMF and the inner slot current can be described as:

$$\mathcal{F}_{t,k} - \mathcal{F}_{t,k+1} = n_c \cdot i_{slot,k} \tag{2.18}$$

where n_c is the coil turns and $i_{slot,k}$ is the current in the k-th slot. This relation can be developed in both stator and rotor mesh as defined in EQ.2.19.

$$\begin{cases} \mathcal{F}_{st,i} - \mathcal{F}_{st,i+1} = Nnc \cdot i_{ss,i} \\ \mathcal{F}_{rt,j} - \mathcal{F}_{rt,j+1} = i_{b,j} \end{cases} \tag{2.19}$$

with $i_{ss,i}$ refers to the current in each stator slot. By developing this relation in all the iron core part meshes, two set of equations are achieved in the matrix format.

$$\begin{cases} [eas] \cdot \{\mathcal{F}_{st}\} = Nnc \cdot * \{i_{ss}\} \\ [ear] \cdot \{\mathcal{F}_{rt}\} = \{i_b\} \end{cases} \tag{2.20}$$

where the constant coefficient matrix $[eas]_{(n_s * n_s)}$ and $[ear]_{(n_r * n_r)}$ are shown as:

$$\begin{bmatrix} 1 & -1 & 0 & \cdots & \cdots & 0 \\ 0 & 1 & -1 & 0 & \cdots & 0 \\ 0 & 0 & 1 & -1 & \cdots & 0 \\ & & & \ddots & \ddots & \\ 0 & \cdots & \cdots & 0 & 1 & -1 \\ -1 & 0 & \cdots & \cdots & 0 & 1 \end{bmatrix} \tag{2.21}$$

The value of all the MMF can't be worked out directly with EQ.2.20 due to the fact that in each group one of the equation is the linear combination of the rest. Generally, there are two methods to solve this problem. First is to replace one of the equations by the condition that the sum of the MMF around the periphery of the air gap equals to zero.

$$\begin{cases} \sum_{i=1}^{n_s} \mathcal{F}_{st,i} = 0 \\ \sum_{j=1}^{n_r} \mathcal{F}_{rt,j} = 0 \end{cases} \tag{2.22}$$

And the second is to eliminate one of the equations and express the correspond MMF by the others based on the condition defined in EQ.2.22. For example,

$$\begin{cases} \mathcal{F}_{st,n_s} = -\sum_{i=1}^{n_s-1} \mathcal{F}_{st,i} \\ \mathcal{F}_{rt,n_r} = -\sum_{j=1}^{n_r-1} \mathcal{F}_{rt,j} \end{cases} \tag{2.23}$$

The second method is adopted in this model since the first one may introduce numerical errors in the MATLAB calculation. Then the last equation of the stator and rotor parts in EQ.2.20 are removed and those before the last equations are modified as:

$$\begin{cases} \mathcal{F}_{st,n_s-1} - \mathcal{F}_{st,n_s} = Nnc \cdot i_{ss,n_s-1} \\ \mathcal{F}_{rt,n_r-1} - \mathcal{F}_{rt,n_r} = i_{b,n_r-1} \end{cases} \Rightarrow \begin{cases} \mathcal{F}_{st,n_s-1} + \sum_{i=1}^{n_s-1} \mathcal{F}_{st,i} = Nnc \cdot i_{ss,n_s-1} \\ \mathcal{F}_{rt,n_r-1} + \sum_{j=1}^{n_r-1} \mathcal{F}_{rt,j} = i_{b,n_r-1} \end{cases} \tag{2.24}$$

At the same time, the constant coefficient matrix $[eas]_{(n_s * n_s)}$ and $[ear]_{(n_r * n_r)}$ defined in EQ.2.21 should be modified as $[\tilde{eas}]_{((n_s-1)*(n_s-1))}$ and $[\tilde{ear}]_{((n_r-1)*(n_r-1))}$:

$$\begin{bmatrix} 1 & -1 & & & & \\ & 1 & -1 & & & \\ & & 1 & -1 & & \\ & & & \ddots & \ddots & \\ & & & & 1 & -1 \\ 1 & 1 & \cdots & 1 & 1 & 2 \end{bmatrix} \tag{2.25}$$

And the two set of equations defined in EQ.2.20 reduce their dimensions from $n_s + n_r$ to $n_s - 1 + n_r - 1$. In this case, the amount of each MMF can be calculated by inversing the coefficient matrix.

$$\begin{cases} \{\tilde{\mathcal{F}}_{st}\} = Nnc \cdot * [\tilde{eas}]^{-1} \cdot \{\tilde{i_{ss}}\} \\ \{\tilde{\mathcal{F}}_{rt}\} = [\tilde{eas}]^{-1} \cdot \{\tilde{i_b}\} \end{cases} \tag{2.26}$$

where the $\{\tilde{\bullet}\}$ means the vectors that has removed its last term and $[\tilde{\bullet}]$ denotes the matrix that has reduced its dimensions by one.

As mentioned in SEC.1.2.4.3, the stator phase currents are chosen to be part of the state vectors of the electromagnetic model. The relation between the stator slot currents i_{ss} and the stator phases currents i_{sp} should be found out. Their relation can be described according to the position of the stator winding in each slot as illustrated in the right image from FIG.1.8. The three phases currents of the stator are distributed in order in each slot. With the counting order defined in FIG.2.1(a), each stator slot currents can be calculated from the three phases currents:

$$\{i_{ss}\} = [S_{abc}] \cdot \{i_{sp}\} \tag{2.27}$$

where the winding connection matrix $[S_{abc}]_{(n_s * n_{ph})}$ is defined according to the stator winding topology and is given as an example in FIG.2.8.

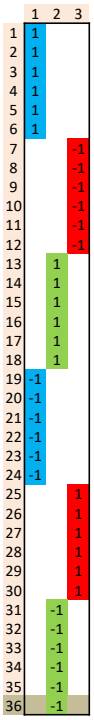

Figure 2.8: Winding current distribution matrix $[Sabc]$

Substituting EQ.2.27 into EQ.2.26, the relation between the induced MMF source and the state vectors of the electromagnetic model could be described as:

$$\begin{cases} \{\tilde{\mathcal{F}}_{st}\} = Nnc \cdot *([\tilde{eas}]^{-1} \cdot [\tilde{S_{abc}}] \cdot \{i_{sp}\}) = [ZZs] \cdot \{i_{sp}\} \\ \{\tilde{\mathcal{F}}_{rt}\} = [\tilde{ear}]^{-1} \cdot \{\tilde{i_b}\} = [ZZr] \cdot \{\tilde{i_b}\} \end{cases} \tag{2.28}$$

where the matrix $[\tilde{S_{abc}}]_{((n_s-1)*n_{ph})}$ is the winding connection matrix $[S_{abc}]$ with the remove of the last line. Let $Nnc \cdot *([\tilde{eas}]^{-1} \cdot [\tilde{S_{abc}}]) = [ZZs]$ and $[\tilde{ear}]^{-1} = [ZZr]$ to get a compact form. The full vector of MMF in the stator and the rotor can be generated from their reduced vector derived in EQ.2.28 by adopting the condition defined in EQ.2.23 .

$$\begin{cases} \{\mathcal{F}_{st}\} = [Mfs] \cdot \{\tilde{\mathcal{F}}_{st}\} \\ \{\mathcal{F}_{rt}\} = [Mfr] \cdot \{\tilde{\mathcal{F}}_{rt}\} \end{cases} \tag{2.29}$$

where the transformation matrix $[Mfs]_{(n_s*(n_s-1))}$ and $[Mfr]_{(n_r*(n_r-1))}$ are organized as:

$$\begin{bmatrix} 1 & 0 & \cdots & 0 \\ 0 & 1 & \cdots & 0 \\ 0 & 0 & \ddots & 0 \\ 0 & 0 & \cdots & 1 \\ -1 & \cdots & -1 & -1 \end{bmatrix} \tag{2.30}$$

Substituting EQ.2.28 into EQ.2.29, one obtains finally the general form:

$$\begin{cases} \{\mathcal{F}_{st}\} = [Mfs] \cdot [ZZs] \cdot \{i_{sp}\} = [MZs] \cdot \{i_{sp}\} \\ \{\mathcal{F}_{rt}\} = [Mfr] \cdot [ZZr] \cdot \{\tilde{i_b}\} = [MZr] \cdot \{\tilde{i_b}\} \end{cases} \tag{2.31}$$

2.3 Permeance network equations

With all the defined parameters and elements in the permeances network, the Kirchhoff electrical laws are adopted to construct the system of equations between the chosen unknowns and the MMF source.

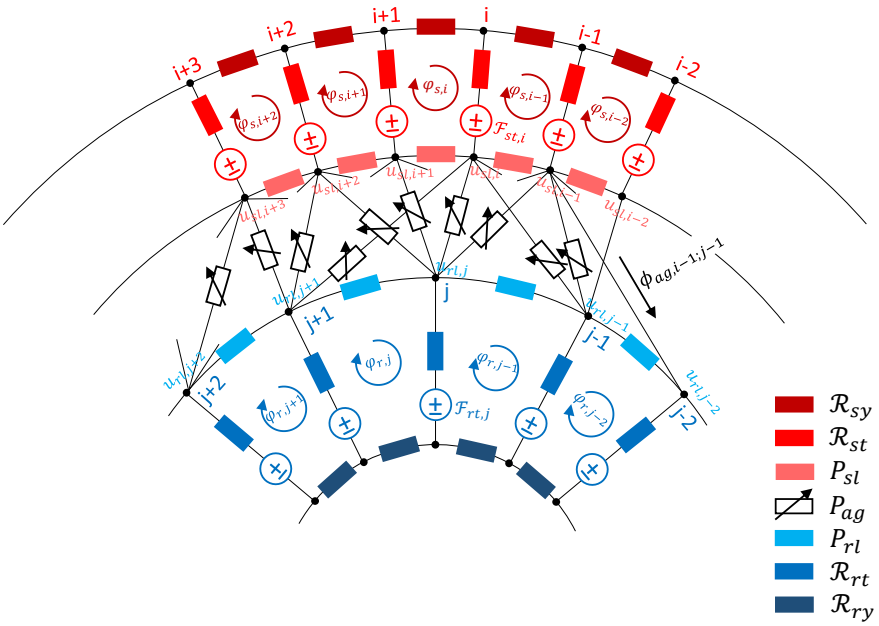

Figure 2.9: Nodal and mesh mixed based PNM for the squirrel cage IM

In the Mesh/Nodal mixed model as illustrated in FIG.2.9, the magnetic loop flux $\{\phi_s\}$, $\{\phi_r\}$ and magnetic node potentials $\{u_{sl}\}$, $\{u_{rl}\}$ in the stator and rotor leakage parts on the two sides of the air gap are considered as the unknowns. Since it is a mixed model, the KVL is applied in all the network meshes of the iron core part and the KCL is used at every node in the leakage part closed to the air gap zone to achieve finally the permeance network equations of the whole motor's cross section.

About a random active branch extracted from the permeance network as depicted in FIG.2.10, similar as the electric circuit, the relation between the magnetic potential (u_a and u_b) and the branch magnetic flux (ϕ) is described as:

$$u_a - u_b - \mathcal{F}_t = U_{ab} - \mathcal{F}_t = \phi \div P = \phi \times \mathcal{R} \tag{2.32}$$

where $U_{ab} = u_a - u_b$ denotes the magnetic potential difference of each branch. It means that the voltage drop across each branch equals to the product between the magnetic flux and the reluctance. Then all the basic elements from the iron core part in the mixed PNM are considered as the reluctance instead of the permeances as shown in FIG.2.9. Considering that the algebraic sum of all the voltages around a closed path is zero and the magnetic voltage drop direction is in the same direction as the defined magnetic loop flux, the first two groups of permeance network equations in the stator and rotor iron core part are respectively deduced as the followings.

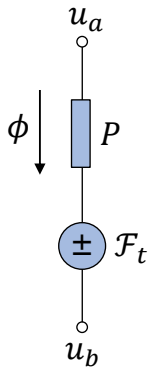

Figure 2.10: An active branch from the PNM

About the mesh k in the stator iron core part:

$$\begin{aligned}
&U_k^{sy} + U_k^{st} + U_k^{sl} - U_{k+1}^{st} = 0 \\
\Rightarrow &\phi_k^{sy} \cdot \mathcal{R}_k^{sy} + (\phi_k^{st} \cdot \mathcal{R}_k^{st} + \mathcal{F}_k^{st}) + u_k^{sl} - u_{k+1}^{sl} - (\phi_{k+1}^{st} \cdot \mathcal{R}_{k+1}^{st} + \mathcal{F}_{k+1}^{st}) = 0 \\
\Rightarrow &\phi_k^{s} \cdot \mathcal{R}_k^{sy} + (\phi_k^{s} - \phi_{k-1}^{s}) \cdot \mathcal{R}_k^{st} + \mathcal{F}_k^{st} + u_k^{sl} - u_{k+1}^{sl} - (\phi_{k+1}^{s} - \phi_k^{s}) \cdot \mathcal{R}_{k+1}^{st} - \mathcal{F}_{k+1}^{st} = 0 \\
\Rightarrow &\underbrace{-\mathcal{R}_k^{st} \cdot \phi_{k-1}^{s} + (\mathcal{R}_k^{sy} + \mathcal{R}_k^{st} + \mathcal{R}_{k+1}^{st}) \cdot \phi_k^{s} - \mathcal{R}_{k+1}^{st} \cdot \phi_{k+1}^{s}}_{[\mathcal{R}_{11}]} + \underbrace{u_k^{sl} - u_{k+1}^{sl}}_{[\mathcal{R}_{13}]} + \underbrace{\mathcal{F}_k^{st} - \mathcal{F}_{k+1}^{st}}_{[\mathcal{R}_{15}]} = 0
\end{aligned} \tag{2.33}$$

This can be presented in the matrix format by developing EQ.2.33 in all the stator iron core meshes.

$$[\mathcal{R}_{11}] \cdot \{\phi_s\} + [\mathcal{R}_{13}] \cdot \{u_{sl}\} + [\mathcal{R}_{15}] \cdot \{\mathcal{F}_{st}\} = \{0\}_{n_s * 1} \tag{2.34}$$

where the reluctance matrix $[\mathcal{R}_{11}]$ is defined as:

$$[\mathcal{R}_{11}]_{(n_s * n_s)}$$
$$\begin{bmatrix}
\mathcal{R}_1^{sy} + \mathcal{R}_1^{st} + \mathcal{R}_2^{st} & -\mathcal{R}_2^{st} & 0 & \cdots & 0 & -\mathcal{R}_1^{st} \\
-\mathcal{R}_2^{st} & \mathcal{R}_2^{sy} + \mathcal{R}_2^{st} + \mathcal{R}_3^{st} & -\mathcal{R}_3^{st} & 0 & \cdots & 0 \\
0 & -\mathcal{R}_3^{st} & \mathcal{R}_3^{sy} + \mathcal{R}_3^{st} + \mathcal{R}_4^{st} & -\mathcal{R}_4^{st} & \cdots & 0 \\
: & 0 & \ddots & \ddots & \ddots & 0 \\
0 & \cdots & 0 & -\mathcal{R}_{n_s-1}^{st} & \mathcal{R}_{n_s-1}^{sy} + \mathcal{R}_{n_s-1}^{st} + \mathcal{R}_{n_s}^{st} & -\mathcal{R}_{n_s}^{st} \\
-\mathcal{R}_1^{st} & 0 & \cdots & 0 & -\mathcal{R}_{n_s}^{st} & \mathcal{R}_{n_s}^{sy} + \mathcal{R}_{n_s}^{st} + \mathcal{R}_1^{st}
\end{bmatrix} \tag{2.35}$$

The constant coefficient matrix $[\mathcal{R}_{13}]_{n_s * n_s} = [\mathcal{R}_{15}]_{n_s * n_s}$ and they are organized in the same way as described in EQ.2.21. As discussed before, the MMF source vector $\{\mathcal{F}_{st}\}$ can be substituted by the first equation defined in EQ.2.31, thus EQ.2.34 is transformed into:

$$[\mathcal{R}_{11}] \cdot \{\phi_s\} + [\mathcal{R}_{13}] \cdot \{u_{sl}\} + [\mathcal{R}_{15}] \cdot [MZs] \cdot \{i_{sp}\} = \{0\}_{n_s * 1} \tag{2.36}$$

About the mesh k in the rotor iron core part: The second group of permeance equations about the rotor iron core part are almost deduced in the same way.

$$\begin{aligned}
&U_k^{rl} + U_k^{rt} + U_k^{ry} - U_{k+1}^{rt} = 0 \\
\Rightarrow &u_{k+1}^{rl} - u_k^{rl} + (\phi_k^{rt} \cdot \mathcal{R}_k^{rt} + \mathcal{F}_k^{rt}) + \phi_k^{ry} \cdot \mathcal{R}_k^{ry} - (\phi_{k+1}^{rt} \cdot \mathcal{R}_{k+1}^{rt} + \mathcal{F}_{k+1}^{rt}) = 0 \\
\Rightarrow &u_{k+1}^{rl} - u_k^{rl} + (\phi_k^{r} - \phi_{k-1}^{r}) \cdot \mathcal{R}_k^{rt} + \mathcal{F}_k^{rt} + \phi_k^{r} \cdot \mathcal{R}_k^{ry} - (\phi_{k+1}^{r} - \phi_k^{r}) \cdot \mathcal{R}_{k+1}^{rt} - \mathcal{F}_{k+1}^{rt} = 0 \\
\Rightarrow &\underbrace{-\mathcal{R}_k^{rt} \cdot \phi_{k-1}^{r} + (\mathcal{R}_k^{ry} + \mathcal{R}_k^{rt} + \mathcal{R}_{k+1}^{rt}) \cdot \phi_k^{r} - \mathcal{R}_{k+1}^{rt} \cdot \phi_{k+1}^{r}}_{[\mathcal{R}_{22}]} + \underbrace{u_{k+1}^{rl} - u_k^{rl}}_{[\mathcal{R}_{24}]} + \underbrace{\mathcal{F}_k^{rt} - \mathcal{F}_{k+1}^{rt}}_{[\mathcal{R}_{25}]} = 0
\end{aligned} \tag{2.37}$$

This can be presented in the matrix format by developing EQ.2.37 in all the rotor iron core meshes.

$$[\mathcal{R}_{22}] \cdot \{\phi_r\} + [\mathcal{R}_{24}] \cdot \{u_{rl}\} + [\mathcal{R}_{25}] \cdot \{\mathcal{F}_{rt}\} = \{0\}_{n_r * 1} \tag{2.38}$$

where the reluctance matrix $[\mathcal{R}_{22}]$ is defined as:

$$[\mathcal{R}_{22}]_{(n_r * n_r)} = \begin{bmatrix}
\mathcal{R}_1^{ry} + \mathcal{R}_1^{rt} + \mathcal{R}_2^{rt} & -\mathcal{R}_2^{rt} & 0 & \cdots & 0 & -\mathcal{R}_1^{rt} \\
-\mathcal{R}_2^{rt} & \mathcal{R}_2^{ry} + \mathcal{R}_2^{rt} + \mathcal{R}_3^{rt} & -\mathcal{R}_3^{rt} & 0 & \cdots & 0 \\
0 & -\mathcal{R}_3^{rt} & \mathcal{R}_3^{ry} + \mathcal{R}_3^{rt} + \mathcal{R}_4^{rt} & -\mathcal{R}_4^{rt} & \cdots & 0 \\
: & 0 & \ddots & \ddots & \ddots & 0 \\
0 & \cdots & 0 & -\mathcal{R}_{n_r-1}^{rt} & \mathcal{R}_{n_r-1}^{ry} + \mathcal{R}_{n_r-1}^{rt} + \mathcal{R}_{n_r}^{rt} & -\mathcal{R}_{n_r}^{rt} \\
-\mathcal{R}_1^{rt} & 0 & \cdots & 0 & -\mathcal{R}_{n_r}^{rt} & \mathcal{R}_{n_r}^{ry} + \mathcal{R}_{n_r}^{rt} + \mathcal{R}_1^{rt}
\end{bmatrix} \tag{2.39}$$

The constant coefficient matrix $[\mathcal{R}_{25}]_{n_r * n_r} = -[\mathcal{R}_{24}]_{n_r * n_r}$ is organized in the same way as described in EQ.2.2.21. Similarly, the MMF source vector $\{\mathcal{F}_{rt}\}$ can be substituted by the second equation defined in EQ.2.31, thus EQ.2.38 is transformed into:

$$[\mathcal{R}_{22}] \cdot \{\phi_r\} + [\mathcal{R}_{24}] \cdot \{u_{rl}\} + [\mathcal{R}_{25}] \cdot [MZr] \cdot \{\tilde{i_b}\} = \{0\}_{n_r * 1} \tag{2.40}$$

The magnetic flux traveled through the branches in the air gap are taken into consideration by applying the KCL on each node of the stator and rotor leakage parts. The similar balance relation discussed in the nodal model is reused here to obtain the rest two groups of permeance equations. They are going to be presented in the followings.

About the node k in the stator leakage circle:

$$\begin{aligned}
&\phi^{sl}_{k-1}+\phi^{st}_{k}-\phi^{sl}_{k}-\sum_{j=1}^{n_r}\phi^{ag}_{k,j}=0\\
\Rightarrow &p^{sl}_{k-1}\cdot U^{sl}_{k-1}+\phi^{s}_{k}-\phi^{s}_{k-1}-p^{sl}_{k}\cdot U^{sl}_{k}-\sum_{j=1}^{n_r}p^{ag}_{k,j}\cdot U^{ag}_{k,j}=0\\
\Rightarrow &p^{sl}_{k-1}\cdot (u^{sl}_{k-1}-u^{sl}_{k})+\phi^{s}_{k}-\phi^{s}_{k-1}-p^{sl}_{k}\cdot (u^{sl}_{k}-u^{sl}_{k+1})-\sum_{j=1}^{n_r}p^{ag}_{k,j}\cdot (u^{sl}_{k}-u^{rl}_{j})=0\\
\Rightarrow &\underbrace{\phi^{s}_{k}-\phi^{s}_{k-1}}_{[\mathcal{R}_{31}]}+\underbrace{p^{sl}_{k-1}\cdot\ u^{sl}_{k-1}-(p^{sl}_{k-1}+p^{sl}_{k}+p^{st}_{k}+\sum_{j=1}^{n_r}p^{ag}_{k,j})\cdot u^{sl}_{k}+p^{sl}_{k}\cdot u^{sl}_{k+1}}_{[\mathcal{R}_{33}]}+\underbrace{\sum_{j=1}^{n_r}p^{ag}_{k,j}\cdot u^{rl}_{j}}_{[\mathcal{R}_{34}]}=0
\end{aligned} \tag{2.41}$$

Similarly, this can be presented in the form of matrix by developing EQ.2.41 around the stator leakage circle.

$$[\mathcal{R}_{31}]\cdot\{\phi_s\}+[\mathcal{R}_{33}]\cdot\{u_{sl}\}+[\mathcal{R}_{34}]\cdot\{u_{rl}\}=\{0\}_{n_s*1} \tag{2.42}$$

where the constant coefficient matrix $[\mathcal{R}_{31}]$ is defined as:

$$[\mathcal{R}_{31}]_{n_s*n_s}=\begin{bmatrix}
1 & 0 & \cdots & \cdots & 0 & -1\\
-1 & 1 & 0 & \cdots & \cdots & 0\\
0 & -1 & 1 & 0 & \cdots & 0\\
0 & 0 & -1 & 1 & \cdots & 0\\
 & & & \ddots & \ddots & \\
0 & \cdots & \cdots & 0 & -1 & 1
\end{bmatrix} \tag{2.43}$$

the permeance matrix $[\mathcal{R}_{33}]$ is described as:

$$[\mathcal{R}_{33}]_{(n_s*n_s)}=\begin{bmatrix}
-(P^{sl}_{n_s}+P^{sl}_{1}+\sum_{j=1}^{n_r}P^{ag}_{1,j}) & 0 & \cdots & 0 & P^{sl}_{n_s} & \\
P^{sl}_{1} & -(P^{sl}_{1}+P^{sl}_{2}+\sum_{j=1}^{n_r}P^{ag}_{2,j}) & P^{sl}_{2} & 0 & \cdots & 0\\
0 & P^{sl}_{2} & -(P^{sl}_{2}+P^{sl}_{3}+\sum_{j=1}^{n_r}P^{ag}_{3,j}) & P^{sl}_{3} & \cdots & 0\\
 & & \ddots & \ddots & \ddots & \\
: & 0 & \ddots & \ddots & \ddots & 0\\
0 & \cdots & 0 & P^{sl}_{n_s-2} & -(P^{sl}_{n_s-2}+P^{sl}_{n_s-1}+\sum_{j=1}^{n_r}P^{ag}_{n_s-1,j}) & P^{sl}_{n_s-1}\\
P^{sl}_{n_s} & 0 & \cdots & 0 & P^{sl}_{n_s-1} & -(P^{sl}_{n_s-1}+P^{sl}_{n_s}+\sum_{j=1}^{n_r}P^{ag}_{n_s,j})
\end{bmatrix} \tag{2.44}$$

and the matrix $[\mathcal{R}_{34}]_{(n_s*n_r)}$ composed of all the air gap permeances is identical to the permeance matrix $[P_{23}]$ defined in EQ.A.13 as described in nodal model.

About the node k in the rotor leakage circle:

$$
\begin{aligned}
&-\phi_{k-1}^{rl}+\phi_{k}^{rt}+\phi_{k}^{rl}+\sum_{i=1}^{n_s}\phi_{i,k}^{ag}=0\\
\Rightarrow &-p_{k-1}^{rl}\cdot U_{k-1}^{rl}+\phi_{k-1}^{r}-\phi_{k}^{r}-p_{k}^{rl}\cdot U_{k}^{rl}+\sum_{i=1}^{n_s}p_{i,k}^{ag}\cdot U_{i,k}^{ag}=0\\
\Rightarrow &-p_{k-1}^{rl}\cdot(u_{k}^{rl}-u_{k-1}^{rl})+\phi_{k-1}^{r}-\phi_{k}^{r}+p_{k}^{rl}\cdot(u_{k+1}^{rl}-u_{k}^{rl})+\sum_{i=1}^{n_s}p_{i,k}^{ag}\cdot(u_{i}^{sl}-u_{k}^{rl})=0\\
\Rightarrow &\underbrace{\phi_{k-1}^{r}-\phi_{k}^{r}}_{[\mathcal{R}_{42}]}+\underbrace{\sum_{i=1}^{n_s}p_{i,k}^{ag}\cdot u_{i}^{sl}}_{[\mathcal{R}_{43}]}+\underbrace{p_{k-1}^{rl}\cdot\ u_{k-1}^{rl}-(p_{k-1}^{rl}+p_{k}^{rl}+p_{k}^{rt}+\sum_{i=1}^{n_s}p_{k,j}^{ag})\cdot u_{k}^{rl}+p_{k}^{rl}\cdot u_{k+1}^{rl}}_{[\mathcal{R}_{44}]}=0
\end{aligned}
\tag{2.45}
$$

Likewise, this can be presented in the form of matrix by developing EQ.2.45 around the rotor leakage circle.

$$
[\mathcal{R}_{42}]\cdot\{\phi_r\}+[\mathcal{R}_{43}]\cdot\{u_{sl}\}+[\mathcal{R}_{44}]\cdot\{u_{rl}\}=\{0\}_{n_r*1} \tag{2.46}
$$

where the constant coefficient matrix $[\mathcal{R}_{42}]_{(n_r*n_r)}$ is defined as the negative version of $[\mathcal{R}_{31}]$ from EQ.2.43, the air gap permeance matrix $[\mathcal{R}_{43}]_{(n_r*n_s)}=[\mathcal{R}_{34}]^T$ and the permeance matrix $[\mathcal{R}_{44}]$ is described in a similar way as EQ.2.44:

$$
[\mathcal{R}_{44}]_{(n_r*n_r)}=
\begin{bmatrix}
-(P_{n_r}^{rl}+P_1^{rl}+\sum_{i=1}^{n_s}P_{i,1}^{ag}) & 0 & \cdots & 0 & P_{n_s}^{rl} & \\
P_1^{rl} & -(P_1^{rl}+P_2^{rl}+\sum_{i=1}^{n_s}P_{i,2}^{ag}) & P_2^{rl} & 0 & \cdots & 0\\
0 & P_2^{rl} & -(P_2^{rl}+P_3^{rl}+\sum_{i=1}^{n_s}P_{i,3}^{ag}) & P_3^{rl} & \cdots & 0\\
: & 0 & \ddots & \ddots & \ddots & 0\\
0 & \cdots & 0 & P_{n_s-2}^{rl} & -(P_{n_s-2}^{rl}+P_{n_s-1}^{rl}+\sum_{i=1}^{n_s}P_{i,n_r-1}^{ag}) & P_{n_s-1}^{rl}\\
P_{n_s}^{rl} & 0 & \cdots & 0 & P_{n_s-1}^{rl} & -(P_{n_s-1}^{rl}+P_{n_s}^{rl}+\sum_{i=1}^{n_s}P_{i,n_r}^{ag})
\end{bmatrix}
\tag{2.47}
$$

As discussed in the nodal model, a reference needs to be chosen for measuring the magnetic potential values for each node. Here, the last nodal potential from the rotor leakage part is chosen as the reference so that its value is considered to be zero $u_{n_r}^{rl}=0$. Therefore, all the sub-matrix associated with this term should be modified. The matrix $[\mathcal{R}_{24}]$, $[\mathcal{R}_{34}]$ and $[\mathcal{R}_{44}]$ are transformed respectively into $[\tilde{\mathcal{R}_{24}}]$, $[\tilde{\mathcal{R}_{34}}]$ and $[\tilde{\mathcal{R}_{44}}]$ by removing the last column of each matrix. And the last row in the matrix $[\mathcal{R}_{42}]$, $[\mathcal{R}_{43}]$ and $[\mathcal{R}_{44}]$ are suppressed to construct new sub-matrix $[\tilde{\mathcal{R}_{42}}]$, $[\tilde{\mathcal{R}_{43}}]$ and $[\tilde{\mathcal{R}_{44}}]$.

Assembling of the permeance network equations: Two sets of equations based on KVL (EQ.2.36 and EQ.2.40) and the other two group of equations according to KCL (EQ.2.42 and EQ.2.46) are combined together to construct the full permeance network equations about the whole motor's cross section based on the mesh/nodal mixed model. These equations are used to describe the relation between the magnetic loop flux in iron core part with the magnetic node potentials from the rotor and stator leakage region $\{\phi u_{sr}\}$

and the stator and rotor phase currents $\{i_p\}$ as defined in EQ.2.48.

$$[Ybus] \cdot \{\phi u_{sr}\} - [AFZ] \cdot \{i_p\} = \{0\}_{(2n_s+2n_r-1)*1} \tag{2.48}$$

where each matrix are defined separately as followings:

$$[Ybus] = \begin{bmatrix} [\mathcal{R}_{11}]_{(n_s*n_s)} & [0]_{(n_s*n_r)} & [\mathcal{R}_{13}]_{(n_s*n_s)} & [0]_{(n_s*(n_r-1))} \\ [0]_{(n_r*n_s)} & [\mathcal{R}_{22}]_{(n_r*n_r)} & [0]_{(n_r*n_s)} & [\tilde{\mathcal{R}}_{24}]_{(n_r*(n_r-1))} \\ [\mathcal{R}_{31}]_{(n_s*n_s)} & [0]_{(n_s*n_r)} & [\mathcal{R}_{33}]_{(n_s*n_s)} & [\tilde{\mathcal{R}}_{34}]_{(n_s*(n_r-1))} \\ [0]_{((n_r-1)*n_s)} & [\tilde{\mathcal{R}}_{42}]_{((n_r-1)*n_r)} & [\tilde{\mathcal{R}}_{43}]_{((n_r-1)*n_s)} & [\tilde{\mathcal{R}}_{44}]_{((n_r-1)*(n_r-1))} \end{bmatrix} \tag{2.49}$$

$$[AFZ] = \begin{bmatrix} -([\mathcal{R}_{15}] \cdot [MZs])_{(n_s*n_{ph})} & [0]_{(n_s*(n_r-1))} \\ [0]_{(n_r*n_{ph})} & -([\mathcal{R}_{25}] \cdot [MZr])_{(n_r*(n_r-1))} \\ [0]_{(n_s*n_{ph})} & [0]_{(n_s*(n_r-1))} \\ [0]_{((n_r-1)*n_{ph})} & [0]_{((n_r-1)*(n_r-1))} \end{bmatrix} \tag{2.50}$$

The vector $\{\phi u_{sr}\}$ includes all the magnetic loop flux in the iron core parts and the magnetic node potentials on the two sides of the air gap.

$$\{\phi u_{sr}\} = \begin{Bmatrix} \{\phi_s\}_{n_s*1} \\ \{\phi_r\}_{n_r*1} \\ \{u_{sl}\}_{n_s*1} \\ \{\tilde{u}_{rl}\}_{(n_r-1)*1} \end{Bmatrix} \tag{2.51}$$

And the vector $\{i_p\}$ is the state vector of the electromagnetic parts as defined in EQ.A.34.

2.4 Flux linkage equations

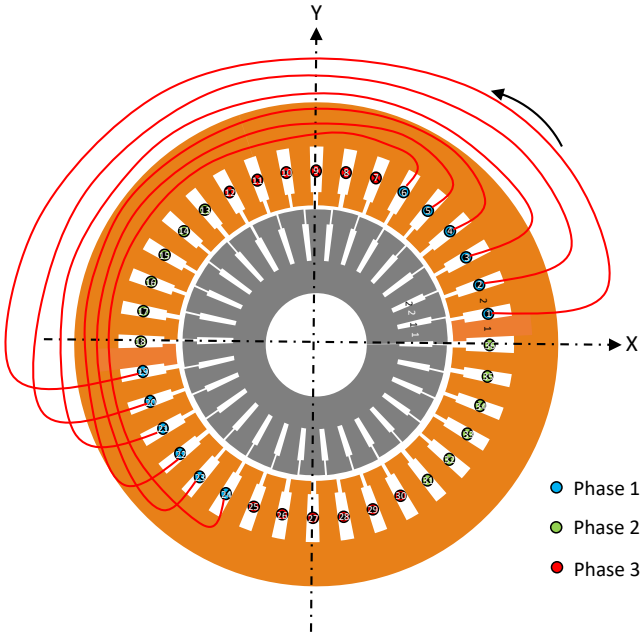

Figure 2.11: Single layer lap winding diagram in the first phase of the stator

The flux linkage equations are introduced by calculating the magnetic flux in each phase from those in each active branches which are particular in the tooth part in this case. If a single stacked winding connection is adopted in the stator of the reference motor, the winding connection in the first phase is illustrated in FIG.2.11. Six coils are constructed by connecting two wires located in two opposite slots in the successive order. For each coil, it covers nearly half of the stator tooth which means that the algebraical sum of the magnetic flux passing through these teeth branches is counted as the magnetic flux passing through this coil. This relation can be describe in EQ.2.52.

$$\{\phi_c\} = [Mcf] \cdot \{\phi_{st}\} \tag{2.52}$$

where $\{\phi_c\}$ is the vector of the magnetic flux in each coil and the transformation matrix $[Mcf]_{n_{co}*n_s}$ is decided by the winding configuration which is organized as shown in FIG.2.12(a). The number of rows n_{co} is referred to the coils number which equals to the half of the stator slot number in the case of a single layer winding. And then, the six coils constructed in each phase are connected in series to form the winding of each phase. EQ.2.53 is used to describe their relation.

$$\{\phi_{sp}\} = [Mpf] \cdot \{\phi_c\} \tag{2.53}$$

where the connection matrix $[Mpf]_{(n_{ph}*n_v)*n_{co}}$ is defined in FIG.2.12(b) with the number of rows decided by the product between the phase number n_{ph} and the winding parallel path number n_v. Since all the coils are connected in series, the parallel path number is considered as $n_v = 1$.

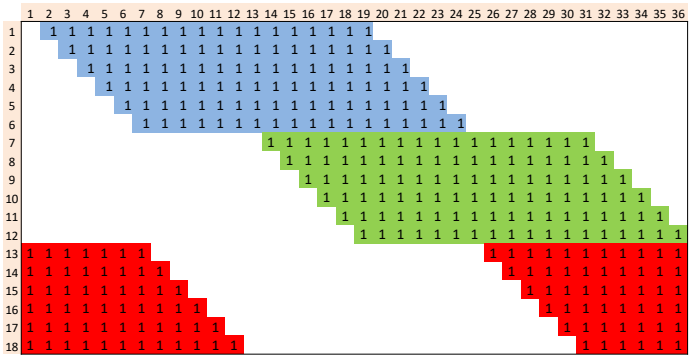

(a) $[Mcf]$

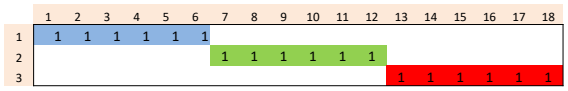

(b) $[Mpf]$

Figure 2.12: Winding matrix distribution about a single layer lap winding

Substituting EQ.2.52 into EQ.2.53, the relation between the stator phase flux and tooth flux is decided as:

$$\{\phi_{sp}\} = [Mpf] \cdot [Mcf] \cdot \{\phi_{st}\} = [ww] \cdot \{\phi_{st}\} \tag{2.54}$$

For the simplicity, the product of the two transformation matrix is considered as $[ww]$. In the rotor part, the rotor magnetic tooth flux are considered as rotor phase flux as described in EQ.2.55.

$$\{\phi_{rp}\} = \{\phi_{rt}\} \tag{2.55}$$

According to Gauss's law for magnetism, the sum of the $\{\phi_{rt}\}$ equals to zero then it is deduced that:

$$\phi^{rt}_{n_r} = -\sum_{j=1}^{n_r-1} \phi^{rt}_{j} \tag{2.56}$$

which means that only $n_r - 1$ terms need to be taken into consideration. In order to conform with the number of the chosen state vectors $\{i_p\}$ for the electromagnetic model, the last term in the two vectors mentioned in EQ.2.55 are also eliminated as for $\{\tilde{\phi_{rp}}\}$ and $\{\tilde{\phi_{rt}}\}$. By combining EQ.2.54 and EQ.2.55, the relationship between the vector of all magnetic phase flux $\{\phi_p\} = \{\{\phi_{sp}\};\{\tilde{\phi_{rp}}\}\}$ and the vector of all magnetic tooth flux $\{\phi_t\} = \{\{\phi_{st}\};\{\tilde{\phi_{rt}}\}\}$ is finally expressed as:

$$\{\phi_p\} = [Gg] \cdot \{\phi_t\} \tag{2.57}$$

where the transformation matrix $[Gg]$ is depicted as the combination of the stator winding matrix $[ww]$ and the identity matrix $[I]$.

$$[Gg] = \begin{bmatrix} [ww]_{(n_{ph}*n_s)} & [0]_{(n_{ph}*(n_r-1))} \\ [0]_{((n_r-1)*n_s)} & [I]_{((n_r-1)*(n_r-1))} \end{bmatrix} \tag{2.58}$$

The relation defined in EQ.2.58 can be applied in both the nodal based model and the nodal/mesh mixed model where the magnetic tooth flux are calculated in different ways from the defined permeance network in each model. The construction of the flux linkage equations in the frame of the nodal/mesh mixed model is going to be presented hereafter.

According to FIG.2.9, the magnetic tooth flux can be easily extracted from the magnetic loop flux which are defined as a part of the unknowns of the permeance network equations in the mesh/nodal based model. About the i-th branch in the stator or the j-th branch in the rotor, the magnetic tooth flux are expressed as:

$$\begin{cases} \phi_i^{st} = \phi_i^s - \phi_{i-1}^s \\ \phi_j^{rt} = \phi_j^r - \phi_{j-1}^r \end{cases} \tag{2.59}$$

By developing EQ.2.59 in all the branches, their relations are organized in the matrix format.

$$\begin{cases} \{\phi_{st}\} = [\mathcal{R}_{31}] \cdot \{\phi_s\} \\ \{\phi_{rt}\} = -[\mathcal{R}_{42}] \cdot \{\phi_r\} \end{cases} \tag{2.60}$$

where the coefficient matrix $[\mathcal{R}_{31}]$ and $[\mathcal{R}_{42}]$ have been defined in EQ.2.43. EQ.2.60 can be expressed in a more compact way by combining the two equations about the stator and rotor part together.

$$\{\phi_t\} = [Dd] \cdot \{\phi_l\} \tag{2.61}$$

where $[Dd]$ is consisted of $[\mathcal{R}_{31}]$ and $[\mathcal{R}_{42}]$ as shown in EQ.2.62:

$$[Dd] = \begin{bmatrix} [\mathcal{R}_{31}]_{(n_s*n_s)} & [0]_{(n_s*n_r)} \\ [0]_{(n_r*n_s)} & -[\mathcal{R}_{42}]_{(n_r*n_r)} \end{bmatrix} \tag{2.62}$$

and the vector of the magnetic loop flux $\{\phi_l\}$ can be calculated from $\{\phi u_{sr}\}$ defined in EQ.2.51.

$$\{\phi_l\} = [Mphi] \cdot \{\phi u_{sr}\} \tag{2.63}$$

where the transformation matrix $[Mphi]$ is composed by the identity matrix $[I]$:

$$[Mphi] = \left[[I]_{((n_s+n_r)*(n_s+n_r))} \quad [0]_{((n_s+n_r)*(n_s+n_r-1))}\right] \tag{2.64}$$

Substituting EQ.2.57 and EQ.2.63 into the EQ.2.61, one obtains finally:

$$\{\phi_p\} = [Gg] \cdot [Dd] \cdot [Mphi] \cdot \{\phi u_{sr}\} = [GDM] \cdot \{\phi u_{sr}\} \tag{2.65}$$

where the product of three constant coefficient matrix $[Gg] \cdot [Dd] \cdot [Mphi]$ is merged into the matrix $[GDM]$.

2.5 Augmented magnetic equations

The permeance network equations and the flux linkage equations deduced in the previous two sections are assembled together in this section in order to construct a set of augmented magnetic equations for the description of the whole magnetic model. At each time instant, they are considered as a linear system in the case without the magnetic saturation effect. However, they are transformed into a set of nonlinear algebraic equations if the saturation effect is taken into consideration. For the sake of the simplicity, the first case is taken into account in this section. Considering about EQ.2.7 and EQ.2.13, the air gap permeances can be finally expressed as a function of the three DOFs about the motor's node like $P_{ij}^{ag}(\theta, x_r, y_r)$. Since the sub-matrix $[PnodU]$ from the nodal based model deduced in EQ.A.31 and the sub-matrix $[Ybus]$ from the mesh/nodal mixed model are separately composed by a group of air gap permeances $\{P_{ag}\}$, the two sub-matrix $[PnodU]$ and $[Ybus]$ also vary as a function of (θ, x_r, y_r). This is important for calculating the derivative of the magnetic flux in the phase current model in SEC.2.7.1.

In the mesh/nodal mixed model, two sets of equations described separately in EQ.2.48 and EQ.2.65 are put in together to form the augmented magnetic equations for the mesh/nodal mixed model which is organized as:

$$\begin{bmatrix} [Ybus(\theta, x_r, y_r)] & -[AFZ] \\ [GDM] & [0] \end{bmatrix} \cdot \begin{Bmatrix} \{\phi u_{sr}\} \\ \{i_p\} \end{Bmatrix} = \begin{Bmatrix} \{0\}_{(2n_s+2n_r-1)*1} \\ \{\phi_p\}_{(n_{np}+n_r-1)*1} \end{Bmatrix} \tag{2.66}$$

By eliminating the vector $\{\phi u_{sr}\}$ in EQ.2.66, the direct relation between the phase currents $\{i_p\}$ and the magnetic phase flux $\{\phi_p\}$ is revealed as:

$$[GDM] \cdot [Ybus(\theta, x_r, y_r)]^{-1} \cdot [AFZ] \cdot \{i_p\} = \{\phi_p\} \tag{2.67}$$

2.6 Electrical differential equations

As mentioned before, the squirrel cage IM contains two physically independent electric circuits. One is made up with electrical wires and set up in the stator slots to connect with the power supply and another is shown in the form of the squirrel cage and installed in the

rotor slots. Both of the two are modeled by the traditional resistor-inductor circuit where the inductance is mainly used to present the stator and rotor winding leakage flux besides of the defined permeance network. Considering that the magnetic leakage flux through the motor's winding part is small compared to those calculated from the permeance network, it is neglected in our model.

2.6.1 Electric circuits in the stator

As illustrated in FIG.1.9(a), all the stator windings belong to three different groups since they are connected to a three phases AC voltage power supply. Therefore, only three electric circuits need to be considered in the stator part. Each of them is depicted in FIG.2.14. It is composed of one resistance R_k^{sp} to present the equivalent resistance value of the phase k in the stator and an induced EMF ε_k^{sp} due to the Faraday's law. Hence, in each electric circuit of the stator, one obtains:

$$\varepsilon_k^{sp} = -\frac{d\phi_k^{sp}}{dt} \tag{2.68}$$

2.6.1.1 Supply voltage connection

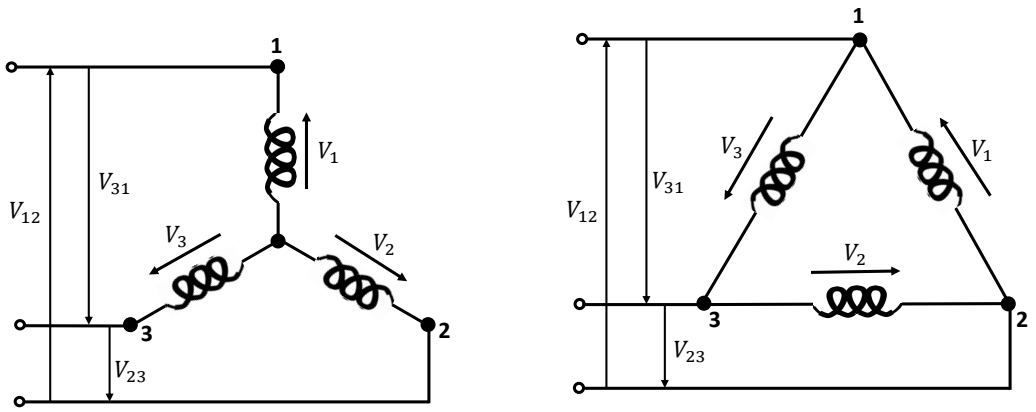

(a) Wye connetion (b) Delta connetion

Figure 2.13: Two types of supply voltage connection

The reference IM is supplied by the AC voltage source. There are generally two kinds of supply voltage connections in industry as illustrated in FIG.2.13. Since it is an AC voltage source, the line voltages on the grid side ($\vec{V_{12}}, \vec{V_{23}}, \vec{V_{31}}$) are usually described by EQ.2.69

when the voltage source is assumed to be perfect.

$$\begin{cases} \vec{V_{12}} = \hat{V} \cdot sin(\omega_s \cdot t) \\ \vec{V_{23}} = \hat{V} \cdot sin(\omega_s \cdot t - \frac{2\pi}{3}) \\ \vec{V_{31}} = \hat{V} \cdot sin(\omega_s \cdot t - \frac{4\pi}{3}) \end{cases} \tag{2.69}$$

where the $\hat{V}$ is the peak value of the voltage which equals to $\sqrt{2}$ times RMS voltage and the ω_s is the supply frequency which is also known as the synchronous speed. FIG.2.13(a) is the Wye connection where the three phase loads are connected together in one end and the other ends are connected respectively to the electric grid. In this case, the relations between the line voltages $(\vec{V_{12}}, \vec{V_{23}}, \vec{V_{31}})$ on the grid side and the phase voltages $(\vec{V_1}, \vec{V_2}, \vec{V_3})$ on the motor's side are defined as:

$$\begin{cases} \vec{V_1} - \vec{V_2} = \vec{V_{12}} \\ \vec{V_2} - \vec{V_3} = \vec{V_{23}} \\ \vec{V_3} - \vec{V_1} = \vec{V_{31}} \end{cases} \tag{2.70}$$

FIG.2.13(b) is known as the Delta connection where the three phase loads are connected in turn between two ends and the three connection points are connected to the three phase power supply. In this situation, the relations between the line voltages $(\vec{V_{12}}, \vec{V_{23}}, \vec{V_{31}})$ and the phase voltages $(\vec{V_1}, \vec{V_2}, \vec{V_3})$ are identified as:

$$\begin{cases} \vec{V_1} = \vec{V_{12}} \\ \vec{V_2} = \vec{V_{23}} \\ \vec{V_3} = \vec{V_{31}} \end{cases} \tag{2.71}$$

The Wye connection is often applied in small power electric motors to avoid the strong impact to the electric grid while the Delta connection is usually employed in the operation of the high power motors. Since the rated power of the reference machine is about 7.5 Kw, the first configuration about the supply connection is adopted. Furthermore in a balanced three-phase Wye connection, it is inferred that the vector sum of the phase currents equals to zero as defined in EQ.2.72

$$i_1^{sp} + i_2^{sp} + i_3^{sp} = 0 \tag{2.72}$$

In the industry, the stator coil resistance is measured between the two terminates of the line voltage. According to FIG.2.13(a), the measured value is actually referred to the sum of the resistance value from the two phases. If the resistances in three phases are considered to be identical, the resistance value of each phase R_{sp} can be achieved easily from the measured data.

2.6.1.2 Derivation of the formula

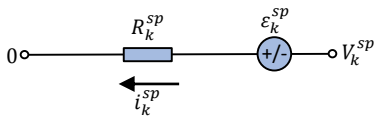

Figure 2.14: The electric circuit of one phase in the stator

According to FIG.2.14, the differential equations to describe the dynamic behavior of electric circuits about all three phases in the stator are defined as:

$$\begin{cases} R_1^{sp} \cdot i_1^{sp} + \varepsilon_1^{sp} = \vec{V}_1 \ ① \\ R_2^{sp} \cdot i_2^{sp} + \varepsilon_2^{sp} = \vec{V}_2 \ ② \\ R_3^{sp} \cdot i_3^{sp} + \varepsilon_3^{sp} = \vec{V}_3 \ ③ \end{cases} \tag{2.73}$$

If they are made to subtract each other in turns as: $① - ②; ② - ③; ③ - ①$, EQ.2.73 is transformed into EQ.2.74 by substituting the relation deduced in EQ.2.70.

$$\begin{cases} R_1^{sp} \cdot i_1^{sp} - R_2^{sp} \cdot i_2^{sp} + \varepsilon_1^{sp} - \varepsilon_2^{sp} = \vec{V}_1 - \vec{V}_2 = \vec{V}_{12} \\ R_2^{sp} \cdot i_2^{sp} - R_3^{sp} \cdot i_3^{sp} + \varepsilon_2^{sp} - \varepsilon_3^{sp} = \vec{V}_2 - \vec{V}_3 = \vec{V}_{23} \\ R_3^{sp} \cdot i_3^{sp} - R_1^{sp} \cdot i_1^{sp} + \varepsilon_3^{sp} - \varepsilon_1^{sp} = \vec{V}_3 - \vec{V}_1 = \vec{V}_{31} \end{cases} \tag{2.74}$$

EQ.2.74 can also be organized in the matrix format as expressed in EQ.2.75.

$$\begin{bmatrix} R_1^{sp} & -R_2^{sp} & 0 \\ 0 & R_2^{sp} & -R_3^{sp} \\ -R_1^{sp} & 0 & R_3^{sp} \end{bmatrix} \cdot \{i_{sp}\} + \begin{bmatrix} 1 & -1 & 0 \\ 0 & 1 & -1 \\ -1 & 0 & 1 \end{bmatrix} \cdot \{\varepsilon_{sp}\} = \begin{Bmatrix} \vec{V}_{12} \\ \vec{V}_{23} \\ \vec{V}_{31} \end{Bmatrix} \tag{2.75}$$

Since one equation among the three defined in EQ.2.75 is the combination of the other two, there is no need to conserve all three equations for describing the state of the system. By adopting the relations from EQ.2.72, EQ.2.75 is simplified by eliminating the third equation.

$$\begin{bmatrix} R_1^{sp} & -R_2^{sp} \\ R_3^{sp} & R_2^{sp} + R_3^{sp} \end{bmatrix} \cdot \begin{Bmatrix} i_1^{sp} \\ i_2^{sp} \end{Bmatrix} + \frac{d}{dt} \begin{Bmatrix} \phi_1^{sp} - \phi_2^{sp} \\ \phi_2^{sp} - \phi_3^{sp} \end{Bmatrix} = \begin{Bmatrix} \vec{V}_{12} \\ \vec{V}_{23} \end{Bmatrix} \tag{2.76}$$

EQ.2.76 can be expressed in a more compact form as described in EQ.2.77.

$$[R_s] \cdot \{\tilde{i_{sp}}\} + \frac{d}{dt}\{\Delta\phi_{sp}\} = \{\tilde{V_s}\} \tag{2.77}$$

As mentioned before, if the three phase resistance are identical and equal to R_{sp}, then the stator resistance matrix $[R_s]$ is depicted as:

$$[R_s] = \begin{bmatrix} R_{sp} & -R_{sp} \\ R_{sp} & 2R_{sp} \end{bmatrix} \tag{2.78}$$

Since all of three terms in the stator phase current vector $\{i_{sp}\}$ are needed for the calculation in the permeance network equations defined before, they can be restored from the modified current vector $\{\tilde{i_{sp}}\}$ by applying EQ.2.79.

$$\begin{Bmatrix} i_1^{sp} \\ i_2^{sp} \\ i_3^{sp} \end{Bmatrix} = \begin{bmatrix} 1 & 0 \\ 0 & 1 \\ -1 & -1 \end{bmatrix} \cdot \begin{Bmatrix} i_1^{sp} \\ i_2^{sp} \end{Bmatrix} \Longrightarrow \{i_{sp}\} = [IMs] \cdot \{\tilde{i_{sp}}\} \tag{2.79}$$

Meanwhile, the vector of the magnetic flux difference between two phases $\{\Delta\phi_{sp}\}$ is generated from the calculated full length flux vector $\{\phi_{sp}\}$ following EQ.2.80.

$$\begin{Bmatrix} \phi_1^{sp} - \phi_2^{sp} \\ \phi_2^{sp} - \phi_3^{sp} \end{Bmatrix} = \begin{bmatrix} 1 & -1 & 0 \\ 0 & 1 & -1 \end{bmatrix} \cdot \begin{Bmatrix} \phi_1^{sp} \\ \phi_2^{sp} \\ \phi_3^{sp} \end{Bmatrix} \Longrightarrow \{\Delta\phi_{sp}\} = [FIMs] \cdot \{\phi_{sp}\} \tag{2.80}$$

2.6.2 Electric circuits in the rotor

As mentioned before, the electric circuits in the rotor of the reference IM is composed of n_r short circuits formed by the squirrel cage. Two of them are presented in FIG.2.16. Each mesh is consisted of two ring segments and two adjacent rotor bars The currents pass through the ring branch are nominated as ring currents i_a while those pass through the bar are known as bar currents i_b. The resistances of each part are considered separately as R_a and R_b which can be calculated according to the geometry of the squirrel cage (seeing the SEC.2.6.2.1). Since the magnetic flux of the rotor tooth ϕ_{rt} pass through each electric mesh in the vertical plane, it induces the EMF ε_r on each rotor bar branches. According to Faraday's law, their relation is defined as:

$$\varepsilon_k^r - \varepsilon_{k+1}^r = \frac{d\phi_{k+1}^{rt}}{dt} \tag{2.81}$$

The electrical potentials at each node V_a are used to derivate the electrical differential equations in the rotor part as explained in SEC.2.6.2.2. All the subscripts k indicate the position of each element.

2.6.2.1 Resistance calculation

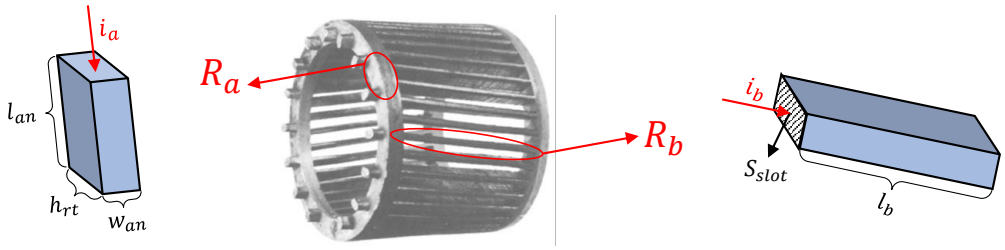

Figure 2.15: Two types of resistance in the rotor squirrel cage

The traditional resistance formula mentioned in EQ.2.82 is adopted to calculate two kinds of resistances in the rotor squirrel cage as illustrated in FIG.2.15.

$$R = \frac{\rho \cdot L}{S} \tag{2.82}$$

where L and S are respectively referred to the length and cross section surface area of the conductor, ρ is the resistivity decided by the material and the ambient temperature which is defined in EQ.2.83.

$$\rho = \rho_0 \cdot (1 + \alpha \cdot T) \tag{2.83}$$

with ρ_0 indicates the resistivity at $0°C$, α is temperature coefficient of the material and T is the ambient temperature in $°C$.

Since EQ.2.82 is used to calculate the resistance of a cylindrical uniform conductor, the two parts from the rotor squirrel cage are simplified in the form of the cuboid on the two sides of the FIG.2.15. The red lines with arrows nearby show the directions of the passing currents. With the defined dimensions in the picture, each resistance are separately calculated in EQ.2.84 with the assumption that there is no defeat in the electrical part. So that all the ring and bar resistances are respectively identical from each mesh.

$$\begin{cases} R_a = \dfrac{\rho_{Al} \cdot l_{an}}{h_{rt} \cdot w_{an}} \\ R_b = \dfrac{\rho_{Al} \cdot l_b}{S_{slot}} \end{cases} \tag{2.84}$$

where ρ_{Al} indicates that this rotor cage is made of aluminum, h_{rt} is the rotor tooth length as defined in FIG.2.2(b), w_{an} is the width of the rotor cage ring and l_{an} is the length of each ring segments which can be represented by the average segment's length between the rotor inner and outer circumference as shown in EQ.2.85

$$l_{an} = (\frac{\pi \cdot D_{ri}}{n_r} + \frac{\pi \cdot D_{ro}}{n_r}) \times 0.5 \tag{2.85}$$

with D_{ri} and D_{r0} are referred separately to the diameters of the rotor inner and outer ring. S_{slot} is the area of the rotor slot while the rotor bar length is calculated in EQ.2.86 by taking into account the skewed angle of the rotor bars.

$$l_b = \frac{L_m}{cos(\beta \cdot \pi \div 180)} \tag{2.86}$$

where β is the rotor skewed angle in degree.

2.6.2.2 Derivation of the formula

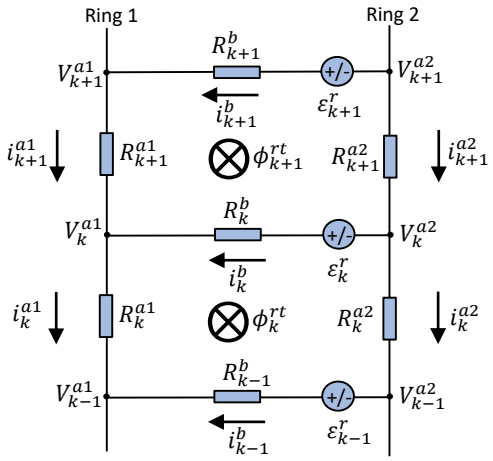

Figure 2.16: The electric circuit of two meshes in the squirrel cage of the rotor

About each ring segment and each bar branch from FIG.2.16, one can deduce respectively EQ.2.87 and EQ.2.88:

$$V^a_k - V^a_{k-1} = R^a_k \cdot i^a_k \tag{2.87}$$

$$V^{a1}_k - V^{a2}_k = R^b_k \cdot i^b_k + \varepsilon^r_k \tag{2.88}$$

EQ.2.87 is firstly applied in the first and second ring part to achieve the relation between the electrical potential voltage and the bar currents. And then the deduced equations are substituted in EQ.2.88 to construct finally the relation between the rotor bar currents and the variation of the induced EMF in each mesh. The detailed derivation processes is available in the followings.

About the part of Ring 1 (or Ring 2): The two ring segments belonged to the part of Ring 1 in FIG.2.16 give us two equations by adopting EQ.2.87 shown as:

$$\begin{cases} V_k^{a1} - V_{k-1}^{a1} = R_k^{a1} \cdot i_k^{a1} \\ V_{k+1}^{a1} - V_k^{a1} = R_{k+1}^{a1} \cdot i_{k+1}^{a1} \end{cases} \tag{2.89}$$

The difference between the two equations in EQ.2.89 is displayed as:

$$2V_k^{a1} - V_{k-1}^{a1} - V_{k+1}^{a1} = R_a \cdot (i_k^{a1} - i_{k+1}^{a1}) \tag{2.90}$$

with the consideration that $R_k^{a1} = R_{k+1}^{a1} = R_a$. The relation between the ring currents and bar currents is obtained by applying the KCL in the node k which is described in EQ.2.91

$$i_k^b = i_k^{a1} - i_{k+1}^{a1} \tag{2.91}$$

Substituting EQ.2.91 into EQ.2.90, the electric equation about the part of Ring 1 is finally revealed as:

$$2V_k^{a1} = V_{k-1}^{a1} + V_{k+1}^{a1} + R_a \cdot i_k^b \tag{2.92}$$

The same processes are realized in the part of Ring 2 to achieve its electric equation shown in EQ.2.93.

$$2V_k^{a2} = V_{k-1}^{a2} + V_{k+1}^{a2} - R_a \cdot i_k^b \tag{2.93}$$

About the part of bar k: In order to substitute EQ.2.92 and EQ.2.93 in EQ.2.88 given by the relation from the bar k, the entire EQ.2.88 is multiplied by two:

$$2V_k^{a1} - 2V_k^{a2} = 2R_k^b \cdot i_k^b + 2\varepsilon_k^r \tag{2.94}$$

After the substitution, EQ.2.94 can be organized as:

$$V_{k-1}^{a2} - V_{k-1}^{a1} + V_{k+1}^{a2} - V_{k+1}^{a1} - 2R_a \cdot i_k^b = 2R_k^b \cdot i_k^b + 2\varepsilon_k^r \tag{2.95}$$

The difference between the two nodal potentials at the two ends of the bar $k-1$ and $k+1$ can be described respectively by adopting EQ.2.88:

$$\begin{cases} V_{k-1}^{a1} - V_{k-1}^{a2} = R_{k-1}^b \cdot i_{k-1}^b + \varepsilon_{k-1}^r \\ V_{k+1}^{a1} - V_{k+1}^{a2} = R_{k+1}^b \cdot i_{k+1}^b + \varepsilon_{k+1}^r \end{cases} \tag{2.96}$$

The corresponding terms in EQ.2.95 are replaced by EQ.2.96 to finally achieve the expression about the electric circuits in the rotor by taking into consideration that $R_{k-1}^b = R_k^b = R_{k+1}^b = R_b$. Therefore, EQ.2.95 is transformed into EQ.2.97.

$$R_{k-1}^b \cdot i_{k-1}^b - (2R_a + 2R_b) \cdot i_k^b + R_{k+1}^b \cdot i_{k+1}^b + (\varepsilon_{k-1}^r - \varepsilon_k^r) - (\varepsilon_k^r - \varepsilon_{k+1}^r) = 0 \tag{2.97}$$

The difference of EMF in each rotor mesh is replaced by adopting EQ.2.81. Then EQ.2.97 is developed as:

$$R_{k-1}^b \cdot i_{k-1}^b - (2R_a + 2R_b) \cdot i_k^b + R_{k+1}^b \cdot i_{k+1}^b + \frac{d\phi_k^{rt}}{dt} - \frac{d\phi_{k+1}^{rt}}{dt} = 0 \tag{2.98}$$

By developing it in all rotor squirrel cage meshes, EQ.2.98 is able to be expressed in the matrix format as shown in EQ.2.99.

$$[R_r] \cdot \{i_b\} + [T_r] \cdot \frac{d\{\phi_{rt}\}}{dt} = \{0\} \tag{2.99}$$

where the rotor resistance matrix $[R_r]$ is defined in EQ.2.100 and the coefficient matrix $[T_r]$ is the same as the matrix $[ear]$ from EQ.2.21.

$$[R_r]_{(n_r * n_r)} = \begin{bmatrix} -(2R_a+2R_b) & R_b & 0 & 0 & \cdots & 0 & R_b \\ R_b & -(2R_a+2R_b) & R_b & 0 & 0 & \cdots & 0 \\ 0 & R_b & -(2R_a+2R_b) & R_b & 0 & \cdots & 0 \\ \cdots & & & & & & \\ R_b & 0 & \cdots & 0 & 0 & R_b & -(2R_a+2R_b) \end{bmatrix} \tag{2.100}$$

The n_r lines of equations defined in EQ.2.99 are not independent with each other since the sum of the rotor bar currents equals to zero which can be deduced from the second equation in EQ.2.20 and the sum of rotor magnetic tooth flux is null according to EQ.2.56. The dimension of EQ.2.99 should be reduced to $(n_r - 1)$ by removing the last term from the rotor bar currents vector $\{i_b\}$ and rotor magnetic tooth flux vector $\{\phi_{rt}\}$. Correspondingly, several modifications should be effectuated in the defined matrix $[R_r]$ and $[T_r]$. As discussed before, $[T_r]$ can be transformed into $[\tilde{T_r}]$ which is identical to the matrix $[\tilde{ear}]$ from EQ.2.25. Since the last row and the last column of the matrix $[R_r]$ should be removed, the associated coefficient multiplied with $i^b_{n_r}$ in the first equation and the one before the last equation needed to be re-distributed to the other terms in the vector of rotor bar currents $\{i_b\}$ by adopting the relation described in EQ.2.101

$$i^b_{n_r} = -\sum_{j=1}^{n_r-1} i^b_j \tag{2.101}$$

Then the first and the last row in the reduced resistance matrix $[\tilde{R_r}]$ are arranged separately as $\{-(2R_a+3R_b)\ 0\ -R_b\ -R_b\ \cdots\ -R_b\}$ and $\{-R_b\ -R_b\ \cdots\ -R_b\ 0\ -(2R_a+3R_b)\}$. The other terms are conserved as the same as described in $[R_r]$.

2.6.3 Combination of the two parts

The electric equations about the stator from EQ.2.77 and those about the rotor defined in EQ.2.99 are combined together to establish the global electric equations about the whole IM. It is described in the matrix format in EQ.2.102.

$$\begin{bmatrix} [R_s] & [0] \\ [0] & [\tilde{R_r}] \end{bmatrix} \begin{Bmatrix} \{\tilde{i_{sp}}\} \\ \{\tilde{i_b}\} \end{Bmatrix} + \begin{bmatrix} [I] & [0] \\ [0] & [\tilde{T_r}] \end{bmatrix} \frac{d}{dt} \begin{Bmatrix} \{\Delta\phi_{sp}\} \\ \{\tilde{\phi}_{rt}\} \end{Bmatrix} = \begin{Bmatrix} \{\tilde{V_s}\}_{(n_{ph}-1)*1} \\ \{0\}_{(n_r-1)*1} \end{Bmatrix} \tag{2.102}$$

This can be expressed in a more compact format as shown in EQ.2.103.

$$[R_p] \cdot \{\tilde{i_p}\} + [T_p] \cdot \frac{d\{\tilde{\phi}_p\}}{dt} = \{V_p\} \tag{2.103}$$

where $\{\tilde{i_p}\}$ and $\{\tilde{\phi_p}\}$ are respectively the reduced version of $\{i_p\}$ and $\{\phi_p\}$ adopted in EQ.A.42 and EQ.2.67. In order to be compatible with this conversion, the transformation relation between the two sets of vectors are described respectively in EQ.2.104 and EQ.2.106.

$$\{i_p\}_{(n_{np}+n_r-1)*1} = [IMp] \cdot \{\tilde{i_p}\}_{(n_{np}+n_r-2)*1} \tag{2.104}$$

where the transformation matrix $[IMp]$ is defined as

$$[IMp]_{(n_{ph}+n_r-1)*(n_{ph}+n_r-2)} = \begin{bmatrix} [IMs]_{n_{ph}*(n_{ph}-1)} & [0]_{n_{ph}*(n_r-1)} \\ [0]_{(n_r-1)*(n_{ph}-1)} & [I]_{(n_r-1)*(n_r-1)} \end{bmatrix} \tag{2.105}$$

with the matrix $[IMs]$ defined in EQ.2.79.

$$\{\tilde{\phi_p}\}_{(n_{np}+n_r-2)*1} = [FIMp] \cdot \{\phi_p\}_{(n_{np}+n_r-1)*1} \tag{2.106}$$

where the transformation matrix $[FIMp]$ is defined as

$$[FIMp]_{(n_{ph}+n_r-2)*(n_{ph}+n_r-1)} = \begin{bmatrix} [FIMs]_{(n_{ph}-1)*n_{ph}} & [0]_{(n_{ph}-1)*(n_r-1)} \\ [0]_{(n_r-1)*n_{ph}} & [I]_{(n_r-1)*(n_r-1)} \end{bmatrix} \tag{2.107}$$

with the matrix $[FIMs]$ defined in EQ.2.80.

Applying EQ.2.104 and EQ.2.106 in EQ.A.42 and EQ.2.66, the augmented magnetic equations based on the relation between $\{i_p\}$ and $\{\phi_p\}$ are transformed into the function of $\{\tilde{i_p}\}$ and $\{\tilde{\phi_p}\}$. The modified equations about EQ.A.42 for the nodal based model and about EQ.2.66 for the mixed model are separately shown as

$$[FIMp] \cdot ([HPW] \cdot [PnodU(\theta, x_r, y_r)]^{-1} \cdot [HPD] + [PnodI]) \cdot [IMp] \cdot \{\tilde{i_p}\} = \{\tilde{\phi_p}\} \tag{2.108}$$

$$[FIMp] \cdot [GDM] \cdot [Ybus(\theta, x_r, y_r)]^{-1} \cdot [AFZ] \cdot [IMp] \cdot \{\tilde{i_p}\} = \{\tilde{\phi_p}\} \tag{2.109}$$

2.7 Couplings between the electromagnetic fields

The couplings between the electromagnetic fields are realized by substituting the relation between $\{\tilde{i_p}\}$ and $\{\tilde{\phi_p}\}$ deduced from the augmented magnetic equations (EQ.2.108 and EQ.2.109) into the global electric differential equations (EQ.2.103). It is obvious that both the currents and the magnetic flux can be chosen as the state vector of the electromagnetic field. This provides us with two options to simulate the dynamic behavior of the electric machine. The two dynamic models are discussed in this section in order to choose the better one for the further UMP analysis. For the sake of the simplicity, the augmented magnetic equations deduced from the two different permeance network models (EQ.2.108 and EQ.2.109) are represented by a simple compact equation defined in EQ.2.110 due to their similar structure.

$$[GW] \cdot [PY(\theta, x_r, y_r)] \cdot [ZZ] \cdot \{\tilde{i_p}\} = \{\tilde{\phi_p}\} \tag{2.110}$$

where $[GW]$ and $[ZZ]$ are the product of several constant coefficient matrix while $[PY(\theta, x_r, y_r)]$ is the permeance matrix mainly including the matrix $[PnodU(\theta, x_r, y_r)]^{-1}$ or $[Ybus(\theta, x_r, y_r)]^{-1}$.

2.7.1 Phase current model

As described in the previous model, the phase currents of the electric machine $\{\tilde{i_p}\}$ are chosen to be the state vector for the electromagnetic field. It means that the magnetic phase flux $\{\tilde{\phi_p}\}$ appeared in EQ.2.103 should be replaced by the function about the $\{\tilde{i_p}\}$ shown in EQ.2.110. The global differential equation about the coupling of electromagnetic model becomes:

$$[R_p]\cdot\{\tilde{i_p}\}+[T_p]\cdot\frac{d([GW]\cdot[PY(\theta,x_r,y_r)]\cdot[ZZ]\cdot\{\tilde{i_p}\})}{dt}=\{V_p\} \tag{2.111}$$

The second term about the derivative of the magnetic flux in EQ.2.111 is developed as:

$$\begin{aligned}&\frac{d([GW]\cdot[PY(\theta,x_r,y_r)]\cdot[ZZ]\cdot\{\tilde{i_p}\})}{dt}\\=&[GW]\cdot\frac{d[PY(\theta,x_r,y_r)]}{dt}\cdot[ZZ]\cdot\{\tilde{i_p}\}+[GW]\cdot[PY(\theta,x_r,y_r)]\cdot[ZZ]\cdot\frac{d\{\tilde{i_p}\}}{dt}\end{aligned} \tag{2.112}$$

Substituting EQ.2.112 into EQ.2.111, the global differential equation can be organized in the traditional form of the state equation as described in EQ.2.113.

$$\frac{d\{\tilde{i_p}\}}{dt}=([T_p]\cdot[GW]\cdot[PY(\theta,x_r,y_r)]\cdot[ZZ])^{-1}\cdot(\{V_p\}-([R_p]+[T_p]\cdot[GW]\cdot\frac{d[PY(\theta,x_r,y_r)]}{dt}\cdot[ZZ])\cdot\{\tilde{i_p}\}) \tag{2.113}$$

Since the permeance matrix $[PY(\theta,x_r,y_r)]$ is mainly composed of the matrix $[PnodU(\theta,x_r,y_r)]^{-1}$ for the nodal based model or of the matrix $[Ybus(\theta,x_r,y_r)]^{-1}$ for the mesh/nodal mixed model, the derivative of the global permeance matrix $\frac{d[PY(\theta,x_r,y_r)]}{dt}$ is mainly determined by the derivative of each inverse local permeance matrix deduced from each permeance network equations $\frac{d[PnodU(\theta,x_r,y_r)]^{-1}}{dt}$ or $\frac{d[Ybus(\theta,x_r,y_r)]^{-1}}{dt}$. Take the one from the nodal based model as an example, its derivative is developed as:

$$\begin{aligned}&\frac{d[PnodU(\theta,x_r,y_r)]^{-1}}{dt}\\=&-[PnodU]^{-1}\cdot\frac{d[PnodU(\theta,x_r,y_r)]}{dt}\cdot[PnodU]^{-1}\end{aligned} \tag{2.114}$$

where the derivative of the local permeance matrix is deduced in EQ.2.115 due to the angular approach.

$$\begin{aligned}&\frac{d[PnodU(\theta,x_r,y_r)]}{dt}\\=&\frac{\partial[PnodU(\theta,x_r,y_r)]}{\partial\theta}\cdot\frac{d\theta}{dt}\\=&(\frac{\partial[PnodU]}{\partial\theta}+\frac{\partial[PnodU]}{\partial x_r}\cdot\frac{dx_r}{d\theta}+\frac{\partial[PnodU]}{\partial y_r}\cdot\frac{dy_r}{d\theta})\cdot\frac{d\theta}{dt}\end{aligned} \tag{2.115}$$

Since the rotor center displacements and their corresponding instantaneous translation speeds are available from the state vectors, their derivative about the rotation angle are calculated in EQ.2.116 by applying again the chain rule :

$$\begin{aligned}\frac{\mathrm{d}x_r}{\mathrm{d}\theta} &= \frac{\mathrm{d}x_r}{\mathrm{d}t}\cdot\frac{\mathrm{d}t}{\mathrm{d}\theta} = \dot{x_r}\cdot\frac{\mathrm{d}t}{\mathrm{d}\theta}\\ \frac{\mathrm{d}y_r}{\mathrm{d}\theta} &= \frac{\mathrm{d}y_r}{\mathrm{d}t}\cdot\frac{\mathrm{d}t}{\mathrm{d}\theta} = \dot{y_r}\cdot\frac{\mathrm{d}t}{\mathrm{d}\theta}\end{aligned} \tag{2.116}$$

Substitution EQ.2.116 into EQ.2.115, the derivative of the local permeance matrix about the time is finally achieved in EQ.2.117.

$$\frac{d[PnodU(\theta,x_r,y_r)]}{dt} = \frac{\partial[PnodU]}{\partial\theta}\cdot\dot{\theta} + \frac{\partial[PnodU]}{\partial x_r}\cdot\dot{x_r} + \frac{\partial[PnodU]}{\partial y_r}\cdot\dot{y_r} \tag{2.117}$$

where $\dot{\theta}$, $\dot{x_r}$ and $\dot{y_r}$ are respectively the instantaneous angular and translation speeds of the rotor center. Considering about the permeance matrix $[PnodU]$ described in EQ.A.31, only the sub matrix $[P_{22}]$, $[P_{23}]$, $[P_{32}]$ and $[P_{33}]$ are composed of the air gap permeances $\{P_{ag}(\theta,x_r,y_r)\}$. So that the partial derivatives about the matrix $[PnodU]$ mentioned in EQ.2.117 should be effectuated on these sub-matrix which can be expressed as:

$$\frac{\partial[PnodU]}{\partial\bullet} = \begin{bmatrix} [0]_{(n_s*n_s)} & [0]_{(n_s*n_s)} & [0]_{(n_s*n_r)} & [0]_{(n_s*(n_r-1))} \\ [0]_{(n_s*n_s)} & \frac{\partial[P_{22}]}{\partial\bullet}_{(n_s*n_s)} & \frac{\partial[P_{23}]}{\partial\bullet}_{(n_s*n_r)} & [0]_{(n_r*(n_r-1))} \\ [0]_{(n_r*n_s)} & \frac{\partial[P_{32}]}{\partial\bullet}_{(n_r*n_s)} & \frac{\partial[P_{33}]}{\partial\bullet}_{(n_r*n_r)} & [0]_{(n_r*(n_r-1))} \\ [0]_{((n_r-1)*n_s)} & [0]_{((n_r-1)*n_s)} & [0]_{((n_r-1)*n_r)} & [0]_{((n_r-1)*(n_r-1))} \end{bmatrix} \tag{2.118}$$

Similarly, the partial derivatives about the local permeance matrix $[Ybus]$ defined in EQ.2.49 from the mixed model is described in EQ.2.119

$$\frac{\partial[Ybus]}{\partial\bullet} = \begin{bmatrix} [0]_{(n_s*n_s)} & [0]_{(n_s*n_r)} & [0]_{(n_s*n_s)} & [0]_{(n_s*(n_r-1))} \\ [0]_{(n_r*n_s)} & [0]_{(n_r*n_r)} & [0]_{(n_r*n_s)} & [0]_{(n_r*(n_r-1))} \\ [0]_{(n_s*n_s)} & [0]_{(n_s*n_r)} & \frac{\partial[\tilde{\mathcal{R}}_{33}]}{\partial\bullet}_{(n_s*n_s)} & \frac{\partial[\tilde{\mathcal{R}}_{34}]}{\partial\bullet}_{(n_s*(n_r-1))} \\ [0]_{((n_r-1)*n_s)} & [0]_{((n_r-1)*n_r)} & \frac{\partial[\tilde{\mathcal{R}}_{43}]}{\partial\bullet}_{((n_r-1)*n_s)} & \frac{\partial[\tilde{\mathcal{R}}_{44}]}{\partial\bullet}_{((n_r-1)*(n_r-1))} \end{bmatrix} \tag{2.119}$$

And the partial derivatives about each sub-matrix appeared in EQ.2.118 and EQ.2.119 are realized by calculating those partial derivatives about each terms in the vector of the air gap permeances. According to the calculation formula about the air gap permeance between each pair of stator and rotor tooth defined in EQ.2.6. Its partial derivatives about the rotor center displacements (θ,x_r,y_r) are deduced respectively in the following parts.

The partial derivative of the air-gap permeance about the rotor center rotation displacement

$$\begin{aligned}
&\frac{\partial P_{ij}(x_G(x_r,\theta),y_G(y_r,\theta),\theta_{ij}(\theta))}{\partial\theta} \\
=&\frac{P_{\text{maxc}}}{e_i(x_G,y_G)}\cdot\frac{\partial f_p(\theta_{ij})}{\partial\theta_{ij}}\cdot\frac{d\theta_{ij}(\theta)}{d\theta}+(\frac{\partial(\frac{1}{e_i(x_G,y_G)})}{\partial x_G}\cdot\frac{dx_G(x_r,\theta)}{d\theta}+\frac{\partial(\frac{1}{e_i(x_G,y_G)})}{\partial y_G}\cdot\frac{dy_G(y_r,\theta)}{d\theta})\cdot P_{\text{maxc}}\cdot f_p(\theta_{ij}) \\
=&\frac{P_{\text{maxc}}}{e_i(x_G,y_G)}\cdot\frac{\partial f_p(\theta_{ij})}{\partial\theta_{ij}}\cdot\frac{d\theta_{ij}(\theta)}{d\theta}+\frac{-1}{e_i^2(x_G,y_G)}\cdot(\frac{\partial e_i}{\partial x_G}\cdot\frac{dx_G(x_r,\theta)}{d\theta}+\frac{\partial e_i}{\partial y_G}\cdot\frac{dy_G(y_r,\theta)}{d\theta})\cdot P_{\text{maxc}}\cdot f_p(\theta_{ij})
\end{aligned} \tag{2.120}$$

where $\frac{\partial f_p(\theta_{ij})}{\partial\theta_{ij}}$ can be deduced from EQ.2.9 which is defined in EQ.2.121 as illustrated in FIG.2.17:

$$\frac{df_p(\theta_{ij})}{d\theta_{ij}}=\begin{cases}0 & \text{if } -\theta_{ij0}\le\theta_{ij}\le\theta_1-\theta_{ij0} \text{ and } 2\pi-\theta_1-\theta_{ij0}\le\theta_{ij}\le 2\pi-\theta_{ij0}\\ -\frac{1}{2}\cdot sin(\pi\frac{\theta_{ij}-\theta_1}{\theta_2-\theta_1})\cdot\frac{\pi}{\theta_2-\theta_1} & \text{if } \theta_1-\theta_{ij0}\le\theta_{ij}\le\theta_2-\theta_{ij0}\\ -\frac{1}{2}\cdot sin(\pi\frac{\theta_{ij}-2\pi+\theta_1}{\theta_2-\theta_1})\cdot\frac{\pi}{\theta_2-\theta_1} & \text{if } 2\pi-\theta_2-\theta_{ij0}\le\theta_{ij}\le 2\pi-\theta_1-\theta_{ij0}\\ 0 & \text{if } \theta_2-\theta_{ij0}\le\theta_{ij}\le 2\pi-\theta_2-\theta_{ij0}\end{cases} \tag{2.121}$$

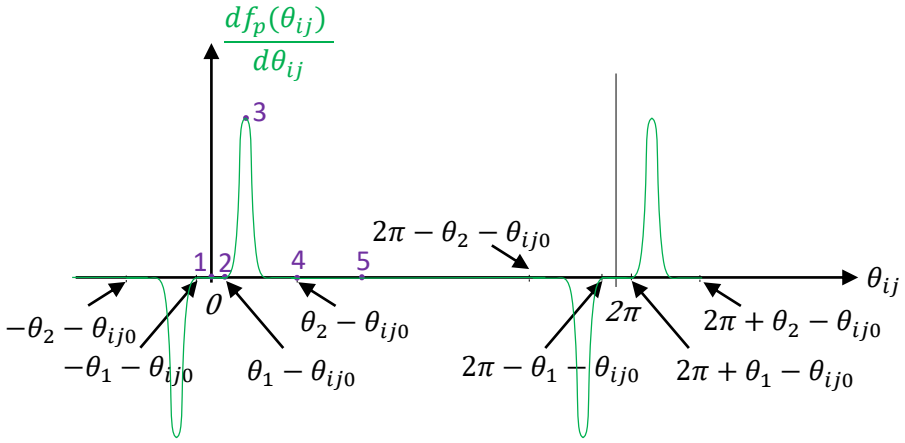

Figure 2.17: Derivative of air-gap permeance between any two teeth versus shaft rotation

According to EQ.2.9 and EQ.2.13, the derivatives of certain terms about the rotation angle θ are calculated as:

$$\begin{aligned}
\frac{d\theta_{ij}(\theta)}{d\theta}&=1\\
\frac{dx_G(x_r,\theta)}{d\theta}&=-\delta_d*\sin(\theta+\gamma_{d0})\\
\frac{dy_G(y_r,\theta)}{d\theta}&=\delta_d*\cos(\theta+\gamma_{d0})
\end{aligned} \tag{2.122}$$

The partial derivatives of the effective air gap length e_i about the rotor geometrical center (x_G, y_G) are deduced in EQ.2.123 from their original equations EQ.2.13.

$$\begin{aligned}\frac{\partial e_i(x_G,y_G)}{\partial x_G} &= \frac{1}{2}\cdot\frac{-2R_s\cos\alpha_i + 2x_G}{\sqrt{R_s^2 - 2R_s(\cos\alpha_i\cdot x_G + \sin\alpha_i\cdot y_G) + x_G^2 + y_G^2}}\\ \frac{\partial e_i(x_G,y_G)}{\partial y_G} &= \frac{1}{2}\cdot\frac{-2R_s\cos\alpha_i + 2y_G}{\sqrt{R_s^2 - 2R_s(\cos\alpha_i\cdot x_G + \sin\alpha_i\cdot y_G) + x_G^2 + y_G^2}}\end{aligned} \tag{2.123}$$

The partial derivative of the air-gap permeance about the rotor center translation displacements

$$\begin{aligned}\frac{\partial P_{ij}(x_G(x_r,\theta),y_G(y_r,\theta),\theta_{ij}(\theta))}{\partial x_r} &= \frac{-1}{e_i^2(x_G,y_G)}\cdot\frac{\partial e_i}{\partial x_G}\cdot\frac{dx_G(x_r,\theta)}{dx_r}\cdot P_{\max c}\cdot f_p(\theta_{ij})\\ \frac{\partial P_{ij}(x_G(x_r,\theta),y_G(y_r,\theta),\theta_{ij}(\theta))}{\partial y_r} &= \frac{-1}{e_i^2(x_G,y_G)}\cdot\frac{\partial e_i}{\partial y_G}\cdot\frac{dy_G(y_r,\theta)}{dy_r}\cdot P_{\max c}\cdot f_p(\theta_{ij})\end{aligned} \tag{2.124}$$

where the derivative of the rotor geometrical center about each rotor center translation displacements are separately deduced in EQ.2.125 according to EQ.2.13.

$$\begin{aligned}\frac{dx_G(x_r,\theta)}{dx_r} &= 1\\ \frac{dy_G(y_r,\theta)}{dy_r} &= 1\end{aligned} \tag{2.125}$$

2.7.2 Phase flux model

Different from the previous model, the magnetic phase flux can also be considered as the state vector of the electromagnetic field. Instead of expressing the global differential equation in the function of the phase currents, in the phase flux model it should be organized in an equation with the variable of the magnetic phase flux. The augmented magnetic equations defined in EQ.2.110 has to be transformed into

$$\{\tilde{i_p}\} = ([GW]\cdot[PY(\theta,x_r,y_r)]\cdot[ZZ])^{-1}\cdot\{\tilde{\phi_p}\} \tag{2.126}$$

Substitution EQ.2.126 into EQ.2.103, the global differential equations from the phase flux model is finally presented in the traditional form of the state equation as described in EQ.2.127:

$$\frac{d\{\tilde{\phi_p}\}}{dt} = [T_p]^{-1}\cdot\left(\{V_p\} - [R_p]\cdot([GW]\cdot[PY(\theta,x_r,y_r)]\cdot[ZZ])^{-1}\cdot\{\tilde{\phi_p}\}\right) \tag{2.127}$$

As mentioned before, since the differential equation is programed and calculated in MATLAB®, all the inverse matrix are obtained directly in the software without any further treatments.

2.7.3 Comparison of the two models

Due to different magnitudes of the phase currents and the phase flux, the absolute tolerances for each state vector are set up with different values (e.g. $1E-3$ for the phase current model and $1E-6$ for the phase flux model) in order to obtain the simulation results with an equivalent precision. Since the ODE solver adopted in MATLAB® to solve these differential equations ODE15s is a variable-step solver, the total iteration numbers over the same simulation time interval are usually not the same for the two models. In order to realize the comparison between the simulation results with the same iteration numbers, the option "MaxStep" is set up in the program to fix the maximum step size taken by the solver. The smallest value among all the variable step values according to the effectuated simulation results is used to describe this input parameter in order to fix the iteration step in the two models with different state vectors. The comparison is based on the simulation at the rated operation point in the case without any eccentricity. Three main simulation results from this multiphysics model: the electromagnetic torque T_{em}, the shaft rotation speed ω_r and the three-phase stator currents I_{sp} are compared respectively in the time domain seeing FIG.2.19 and the frequency domain from FIG.2.20. With the angular approach mentioned in SEC.1.2.3, the differential equations are solved at each shaft rotation angle step instead of the traditional time step. Therefore the variations of each simulation results are presented in the function of the shaft position by default in this thesis while their frequency components are achieved by applying the Fast Fourier Transform (FFT) in the "angle domain" to plot the angular spectrum with the unit defined as "event per shaft revolution ($\mathrm{ev}\cdot\mathrm{rev}^{-1}$) ". This defined angular frequency is equivalent as the order in the rotating terms or is similar to the harmonic in musical terms. The transform relationship between the angular frequency f_θ and the traditional frequency f is defined in EQ.2.128.

$$f_\theta(\mathrm{ev}\cdot\mathrm{rev}^{-1}) = 2*\pi*\frac{f(\mathrm{Hz})}{\omega_r(\mathrm{rad}\cdot\mathrm{s}^{-1})} \tag{2.128}$$

Then the power supply frequency 50 Hz is shown as $1.016\ \mathrm{ev}\cdot\mathrm{rev}^{-1}$ in the angular spectrum at the rated rotation speed 309.2 rad/s.

According to FIG.2.19, it can be seen that there is no large difference between the global variation of the simulation results generated from the two models. The fluctuation shapes about the simulated electromagnetic torque and about the three-phase stator currents from the two models are almost the same except for that of the shaft rotation speed. By comparing FIG.2.19(b) and FIG.2.19(e), although their fluctuation amplitudes are nearly identical, a shift of 0.01 exists between their average values. Since this shift appears also in other simulation case seeing FIG.2.18, this difference is treated as a numerical error. Considering that this shift value is minor compared to its average value, the instantaneous rotation speeds simulated from the the two models are considered to be the same. The comparisons about their frequency components between the two models are illustrated in FIG.2.20. Apart from some noise appeared in the low frequency zone in the angular spectrum of the electromagnetic torque and of the instantaneous rotation speed,

their characteristic frequency peaks can be identified in both of two simulation results. The angular spectrum about the stator first phase current are almost the same from the two models. Their characteristic frequencies are explained in details in SEC.2.11.

Based on the comparisons above, the two models with different state vectors are basically the same. Considering that the phase flux model is simple in the construction of the global differential equations and it is more efficient in the simulation (e.g. To conduct a simulation about 100 shaft revolutions, the phase flux model takes 4.8 hours while the phase current model needs 6.2 hours.), the phase flux model is finally adopted as the main model to perform all the simulations after. Another important reason to choose the magnetic phase flux as the state vector for the electromagnetic part is to prepare for the implementation of the magnetic saturation effect in this multiphysics model. Once the magnetic saturation effect is taken into consideration, the permeance matrix $[PY(\theta, x_r, y_r)]$ defined in EQ.2.110 varies also as the function of magnetic phase flux $\{\tilde{\phi}_p\}$. Then it's impossible to calculate analytically the derivative of the permeance matrix $[PY(\theta, x_r, y_r, \{\tilde{\phi}_p\})]$ as described in EQ.2.115 from the phase current model. The detailed process to set up the magnetic saturation is going to be explained in the modeling of the permanent magnet synchronous motor in CHAP.3.

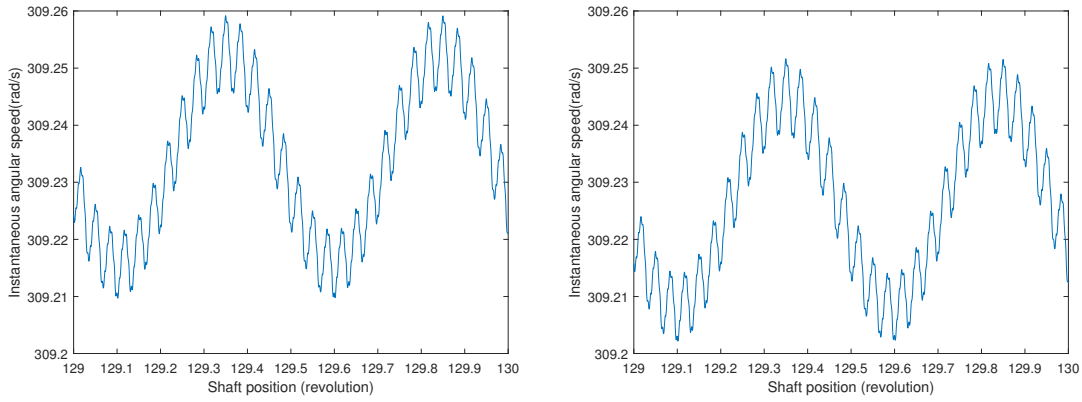

(a) Phase current model

(b) Phase flux model

Figure 2.18: Variation of the instantaneous rotation speed in the last shaft revolution at the rated state with the static eccentricity of $50\%E_e$.

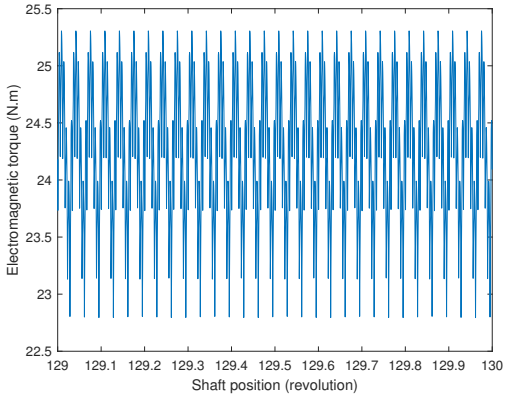

(a) T_{em} from Phase current model

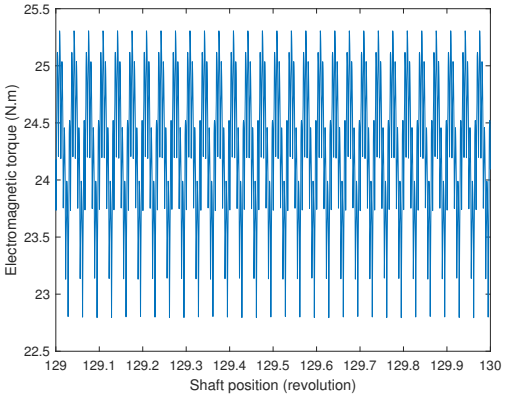

(d) T_{em} from Phase flux model

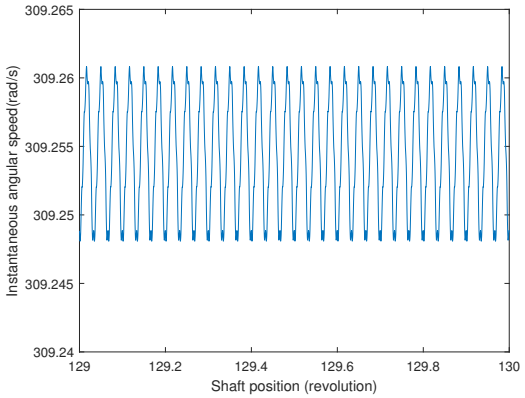

(b) ω_r from Phase current model

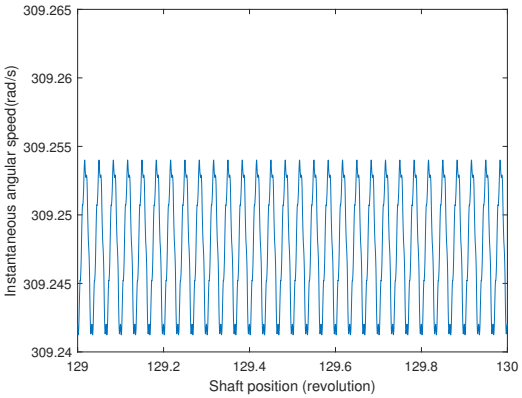

(e) ω_r from Phase flux model

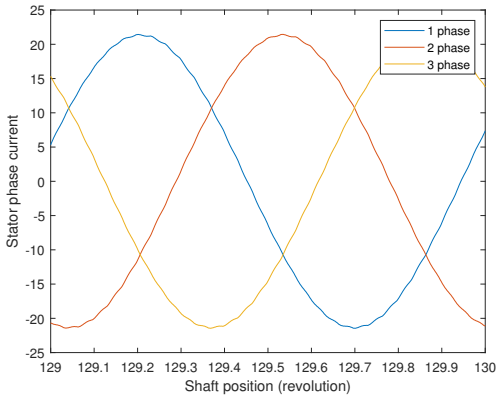

(c) I_{sp} from Phase current model

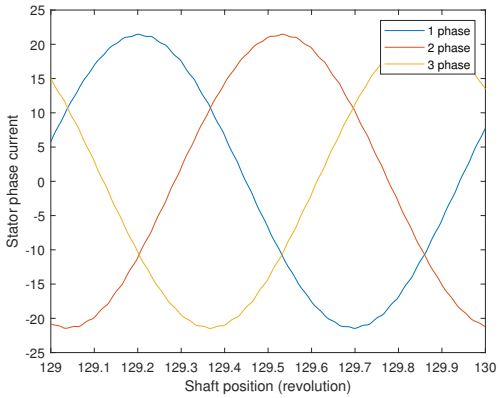

(f) I_{sp} from Phase flux model

Figure 2.19: Variation of different simulation results in the last shaft revolution at the rated state without eccentricity

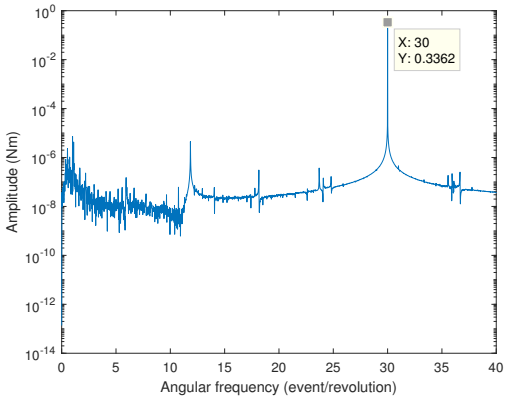

(a) T_{em} from Phase current model

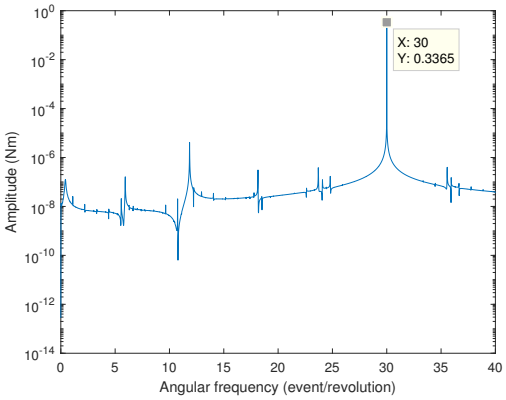

(d) T_{em} from Phase flux model

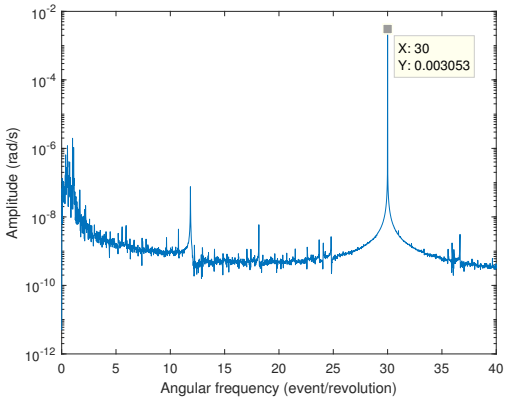

(b) ω_r from Phase current model

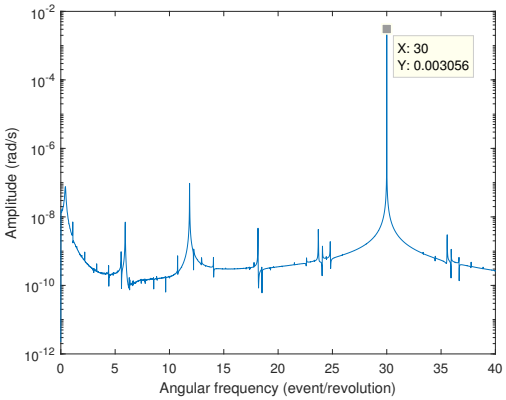

(e) ω_r from Phase flux model

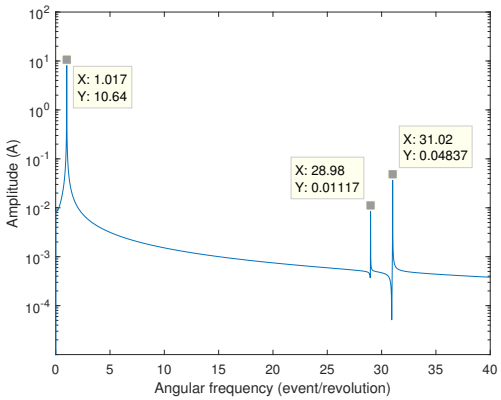

(c) $I_{sp,1}$ from Phase current model

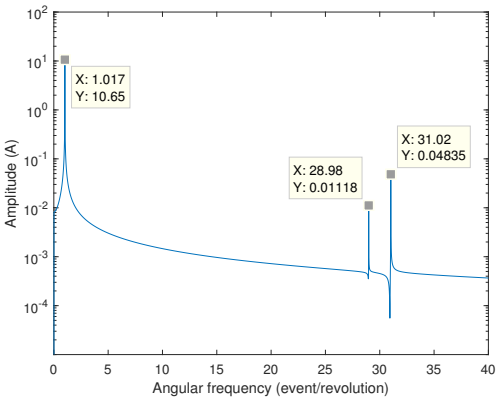

(f) $I_{sp,1}$ from Phase flux model

Figure 2.20: Angular spectrum of different simulation results at the rated state without eccentricity

2.8 Mechanical equations

As mentioned in SEC.1.2.4.1, the mechanical structure of the rotor bearing system in the IM is discretized into several node elements where one of them is used to denote the $2.5D$ electromagnetic field of the electrical machine with the assumption that the effective length of the motor's iron core part is short when comparing to the total shaft length. The shaft segments between the two nodes are represented by the Timoshenko beam elements with a circular cross-section considering the assumptions of the small deformation. According to the right picture in FIG.1.7, the 6 DOF of the two nodes in the support part that are connected to the base are blocked since they are only used to calculate the forces in the bearings so that only the elements in the shaft need to be taken into consideration in the mechanical differential equations.

The UMP is generated mainly due to the misalignment between the rotor and the stator center. The source of this misalignment generally comes from two parts. One is the predefined input eccentricities that have been discussed in SEC.2.2.1.2 for calculating the effective air gap length. Another is the rotordynamics motion such as the mass unbalance excitation, the shaft elastic deformation or the effect of the UMP thanks to the strong coupling between the mechanical structure and the electromagnetic field in this multiphysics model. In the reality, those two sources exist simultaneously in the system. Since the mass unbalance due the manufacturing tolerance is very common in the rotating machine and its excitation becomes harmful with the increase of the rotation speed, the set up of the mass unbalance excitation in the mechanical model is of great importance to the analysis of the rotor dynamic behavior which is discussed in the first subsection. The calculation about the electromagnetic force in the permeance network is going to be developed in the second subsection.

2.8.1 Set up of the mass unbalance excitation

In order to achieve a clear explanation, a modified Jeffcott/Laval rotor model used in [143] is adopted here to develop the kinetic differential equations about the main DOFs related to the node chosen to represent the electric motor. Compared with FIG.2.5, the rotor mass center O_M is added in FIG.2.21 to stand for the implementation of the mass unbalance. Similar as the rotor geometric center O_G, the coordinate of $O_M(x_M, y_M)$ in the reference coordinate system is defined as:

$$\begin{aligned} x_M &= x_r + \delta_m * \cos(\gamma_m) \\ y_M &= y_r + \delta_m * \sin(\gamma_m) \\ \gamma_m &= \gamma_{m0} + \theta \end{aligned} \tag{2.129}$$

with its initial phase angle and mass eccentricity respectively defined as γ_{m0} and δ_m. The mass eccentricity can be assessed by the balancing quality grade G of the rotation machine defined from the industrial norm ISO 1940 [167] provided by our industrial partner

NIDEC Leroy Somer. The magnitude of the mass eccentricity is calculated as:

$$\delta_m = \frac{G}{\Omega * 1000} \tag{2.130}$$

where Ω is considered as the average rotation speed value at each operating point. According to the table in the page 11 from [167], $G = 2.5mm \cdot s^{-1}$ is chosen for the later simulations by default.

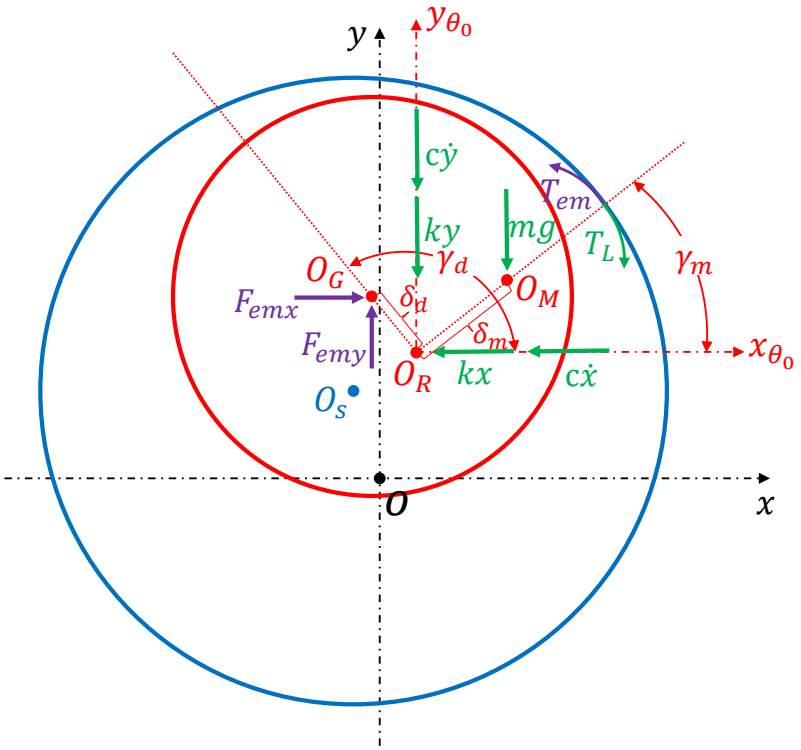

Figure 2.21: Kinetics of the eccentric rotor

There are three DOFs in this simple mechanical model including two translation displacements x, y along the x and y direction and one rotation angle θ around the z-axis. The coordinate of the $O_R(x_r, y_r)$ are simplified as (x, y) for the sake of the simplicity. The model is considered as isotropic then the spring constant k and the damper constant c are respectively identical along the x-axis and y-axis. The spring constant k could be substituted by the equivalent bearing stiffness. By adopting the modal damping approach mentioned in SEC.1.2.4.1, the damper constant c is calculated as:

$$c = 2 \cdot d \cdot m \cdot \omega_0 \tag{2.131}$$

where d is the modal damping ratio, m is the lumped mass of the IM including the rotor iron stack and the aluminum squirrel cage and $\omega_0 = \sqrt{\frac{k}{m}}$ is the natural frequency of

the lumped mechanical structure. As illustrated from FIG.2.21, all the elastic restoring forces kx and ky and the damping forces $c\dot{x}$ and $c\dot{y}$ are exerted on the shaft axis center O_R. The generated UMP F_{emx} and F_{emy} act on O_G since it is also the magnetic center of the rotor stack. The gravity of the rotor disk mg is imposed on the point O_M since it is also considered as the gravity center of the rotor. Furthermore, the electromagnetic torque T_{em} generated in the air gap and the external load torque T_L can be also identified in FIG.2.21 with the counter-clockwise considered as the positive direction of the torques. By applying NEWTON'S law, the motion equations of the rotor are depicted as:

$$\begin{aligned} m\ddot{x_M} &= -c\dot{x} - kx + F_{emx} \\ m\ddot{y_M} &= -c\dot{y} - ky + F_{emy} - mg \\ J\ddot{\gamma_m} &= -T_L + T_{em} + (-c\dot{x} - kx)\cdot\delta_m \cdot sin(\gamma_m) - (-c\dot{x} - kx)\cdot\delta_m \cdot cos(\gamma_m) \\ &\quad + F_{emx}\cdot[\delta_m \cdot sin(\gamma_m) - \delta_d \cdot sin(\gamma_d)] - F_{emy}\cdot[\delta_m \cdot cos(\gamma_m) - \delta_d \cdot cos(\gamma_d)] \end{aligned} \tag{2.132}$$

where J is the inertial moment around the z-axis. Since there is an intrinsic servo loop inside of the asynchronous motor (i.e. the Torque Speed characteristic curve of the IM), it is no need to include the damping term in the rotation direction in order to reach the steady state. Considering about EQ.2.129, the second derivative of each DOF are deduced as:

$$\begin{aligned} \ddot{x_M} &= \ddot{x} - \delta_m * [\ddot{\gamma_m}\cdot\sin(\gamma_m) + \dot{\gamma_m}^2\cdot\cos(\gamma_m)] \\ \ddot{y_M} &= \ddot{y} + \delta_m * [\ddot{\gamma_m}\cdot\cos(\gamma_m) - \dot{\gamma_m}^2\cdot\sin(\gamma_m)] \\ \ddot{\gamma_m} &= \ddot{\theta} \text{ with } \dot{\gamma_m} = \dot{\theta} \end{aligned} \tag{2.133}$$

Substitution EQ.2.133 into EQ.2.132, those three differential equations are transformed in the matrix form.

$$\begin{aligned} &\begin{bmatrix} m & 0 & -m\delta_m\cdot\sin(\gamma_m) \\ 0 & m & m\delta_m\cdot\cos(\gamma_m) \\ 0 & 0 & J \end{bmatrix}\cdot\begin{Bmatrix}\ddot{x}\\ \ddot{y}\\ \ddot{\theta}\end{Bmatrix} + \begin{bmatrix} c & 0 & 0 \\ 0 & c & 0 \\ 0 & 0 & 0 \end{bmatrix}\cdot\begin{Bmatrix}\dot{x}\\ \dot{y}\\ \dot{\theta}\end{Bmatrix} + \begin{bmatrix} k & 0 & 0 \\ 0 & k & 0 \\ 0 & 0 & 0 \end{bmatrix}\cdot\begin{Bmatrix}x\\ y\\ \theta\end{Bmatrix} \\ &= \begin{Bmatrix} m\delta_m\cdot\cos(\gamma_m)\cdot\dot{\theta}^2 + F_{emx} \\ m\delta_m\cdot\sin(\gamma_m)\cdot\dot{\theta}^2 + F_{emy} - mg \\ -T_L + T_{em} + (-c\dot{x} - kx)\cdot\delta_m\cdot sin(\gamma_m) - (-c\dot{x} - kx)\cdot\delta_m\cdot cos(\gamma_m) \\ + F_{emx}\cdot[\delta_m\cdot sin(\gamma_m) - \delta_d\cdot sin(\gamma_d)] - F_{emy}\cdot[\delta_m\cdot cos(\gamma_m) - \delta_d\cdot cos(\gamma_d)] \end{Bmatrix} \end{aligned} \tag{2.134}$$

which can be expressed in a compact format described in EQ.2.135.

$$[M]\cdot\{\ddot{X}\} + [C]\cdot\{\dot{X}\} + [K]\cdot\{X\} = \{U\} \tag{2.135}$$

with all three DOFs of the main node presented by the vector $\{X\} = \{x, y, \theta\}^T$. The set of differential equations defined in EQ.2.135 is then transformed into the state equations as developed in EQ.2.136 for the later solving process.

$$\begin{Bmatrix}\{\dot{X}\}\\ \{\ddot{X}\}\end{Bmatrix} = \begin{bmatrix} [0] & [I] \\ -[M]^{-1}\cdot[K] & -[M]^{-1}\cdot[C] \end{bmatrix}\cdot\begin{Bmatrix}\{X\}\\ \{\dot{X}\}\end{Bmatrix} + \begin{bmatrix}[0]\\ [M]^{-1}\end{bmatrix}\cdot\{U\} \tag{2.136}$$

As mentioned in SEC.1.2.4.1, the combination of the displacements and their first derivative are chosen to be the state vector of the mechanical part $\{Q_m\} = \{\{X\}\{\dot{X}\}\}^T$.

All the modifications associated with the mass unbalance excitation are applied to the main node of the motor illustrated in FIG.1.7 in our complete EF based mechanical model to take into account the centrifugal effect due to the mass unbalance.

2.8.2 Electromagnetic force calculation

There are principally two methods to calculate the electromagnetic force including the electromagnetic torque and UMP due to the air-gap eccentricity. One is obtained by the principle of virtual work or also known as the derivative of the magnetic co-energy method [54, 81, 96]. Another is solved by Maxwell stress tensor method [6, 123]. The latter is often adopted by the researchers who apply the air-gap permeance approach to obtain firstly the radial and tangential flux densities in order to calculate the stress tensor component in normal and tangential direction [139, 156, 168]. The tangential component is often omitted to simplify the calculation according to the assumption that the permeability of the stator and rotor iron is infinite and the motor has smooth poles [139]. In this case, some properties of the UMP cannot be revealed in the simulation results (more details are available in Section 2.11.1.1). In order to achieve a more realistic UMP values, the magnetic co-energy method is adopted in this thesis.

The principle of the co-energy approach is to apply the partial differentiation with respect to the relative displacement in order to achieve the force function. For example, the electromagnetic torque T_{em} is calculated by Eq. (2.137).

$$T_{\mathrm{em}} = \frac{\partial W_m^{'}}{\partial \theta} \tag{2.137}$$

The co-energy $W_m^{'}$ in the electromagnetic system is often defined by Eq. (2.138).

$$W_m^{'} = \int_0^U \phi \cdot \mathrm{d}U \tag{2.138}$$

where ϕ is the linkage magnetic flux and U is the corresponding MMF drop. In the permeance network, the co-energy can be deduced as the sum of co-energies from three parts: the stator and rotor iron part (ir); the leakage part (l) and the air-gap part (a) as described in Eq. (2.139).

$$W_m^{'} = \sum_{iron} \int_0^{U_{\mathrm{ir}}} \phi_{\mathrm{ir}} \cdot \mathrm{d}U_{\mathrm{ir}} + \sum_{leakage} \int_0^{U_{\mathrm{l}}} \phi_{\mathrm{l}} \cdot \mathrm{d}U_{\mathrm{l}} + \sum_{air-gap} \int_0^{U_{\mathrm{a}}} \phi_{\mathrm{a}} \cdot \mathrm{d}U_{\mathrm{a}} \tag{2.139}$$

Every linkage magnetic flux passed through each branch are represented by the product of the permeance and MMF drop of each branch in the permeance network. It is calculated in Eq. (2.140).

$$\phi_k = U_k \cdot P_k \tag{2.140}$$

where ϕ_k is the linkage flux through k_{th} branch in the defined permeance network, U_k is the corresponding MMF drop and P_k is the permeance value of the k_{th} branch. k is all integer from 1 to N denoted to the branch number of each part. Then Eq. (2.139) is transformed into Eq. (2.141):

$$W_m^{'} = \sum_{iron} \int_0^{U_{\mathrm{ir}}} U_{\mathrm{ir}} \cdot P_{\mathrm{ir}} \cdot \mathrm{d}U_{\mathrm{ir}} + \sum_{leakage} \int_0^{U_{\mathrm{l}}} U_{\mathrm{l}} \cdot P_{\mathrm{l}} \cdot \mathrm{d}U_{\mathrm{l}} + \sum_{air-gap} \int_0^{U_{\mathrm{a}}} U_{\mathrm{a}} \cdot P_{\mathrm{a}} \cdot \mathrm{d}U_{\mathrm{a}} \quad (2.141)$$

Substitution Eq. (2.141) into Eq. (2.137), since the MMF drop U_k of each branch is constant at every simulation step, the derivative of Eq. (2.141) are treated as the derivative of the permeance value of each part. Considering that the permeances of the stator and rotor iron part P_{ir} don't depend on the variation of the rotor relative displacements directly and the permeances of the leakage part P_{l} are constant values so that the derivatives of the first two terms in Eq. (2.141) equal to zero. It implies the fact that the energy conversion between the electromagnetic part and the mechanical part only happens in the air-gap area [2]. Therefore Eq. (2.137) is developed into Eq. (2.142) :

$$T_{\mathrm{em}} = 0 + 0 + \sum_{air-gap} \int_0^{U_a} \frac{\partial P_a}{\partial \theta} \cdot U_a \cdot \mathrm{d}U_a = \sum_{air-gap} \frac{U_a^2}{2} \cdot \frac{\partial P_a}{\partial \theta} \quad (2.142)$$

As introduced in the former sections the branches in the air-gap are related to each stator tooth i and rotor tooth j. In this way the air-gap permeances and corresponding MMF drops are defined as $P_a = P_{ij}$ and $U_a = U_{ij}$. Since the relative rotation angle between each stator and rotor teeth is represented by θ_{ij}, the expression of Eq. (2.142) in the whole air-gap area becomes:

$$T_{\mathrm{em}} = \frac{1}{2} \sum_i^{n_s} \sum_j^{n_r} \frac{\partial P_{ij}}{\partial \theta_{ij}} U_{ij}^2 \quad (2.143)$$

The partial derivation of the Eq. (2.6) about the relative rotation angle θ_{ij} appears as:

$$\frac{\partial P_{ij}(x_G, y_G, \theta_{ij})}{\partial \theta_{ij}} = \frac{P_{\mathrm{maxc}}}{e_i(x_G, y_G)} \cdot \frac{df_p(\theta_{ij})}{\mathrm{d}\theta_{ij}} \quad (2.144)$$

The second term $\frac{\mathrm{d}f_p(\theta_{ij})}{\mathrm{d}\theta_{ij}}$ is defined in EQ.2.121. In the same way, magnetic radial forces (UMP) due to the eccentricity are achieved by taking the derivative of the magnetic co-energy about their relative displacement along the x and y directions:

$$\begin{aligned} F_{\mathrm{emx}} &= \frac{1}{2} \sum_i^{n_s} \sum_j^{n_r} \frac{\partial P_{ij}}{\partial \tilde{x}} U_{ij}^2 \\ F_{\mathrm{emy}} &= \frac{1}{2} \sum_i^{n_s} \sum_j^{n_r} \frac{\partial P_{ij}}{\partial \tilde{y}} U_{ij}^2 \end{aligned} \quad (2.145)$$

From FIG.2.6, it can be seen that the effective air-gap length actually depends on the variation of the relative displacements between the stator center O_S and rotor geometric

center O_G. In order to obtain their variation, Eq. (2.17) needs to be transformed into the coordinate of $x_s o_s y_s$ in FIG.2.6 with the relative displacements along two directions $\tilde{x}$ and $\tilde{y}$ defined as:

$$\begin{aligned} \tilde{x} &= x_G - x_s \\ \tilde{y} &= y_G - y_s \end{aligned} \tag{2.146}$$

Therefore the partial differentiation of Eq. (2.6) about the relative displacement $\tilde{x}$ is deduced as:

$$\begin{aligned} \frac{\partial P_{ij}(\tilde{x},\tilde{y},\theta_{ij})}{\partial \tilde{x}} &= \frac{\partial(\frac{1}{e_i(\tilde{x},\tilde{y})})}{\partial \tilde{x}} \cdot P_{\text{maxc}} \cdot f_p(\theta_{ij}) \\ &= -\frac{1}{e_i(\tilde{x},\tilde{y})} \cdot \frac{\partial e_i(\tilde{x},\tilde{y})}{\partial \tilde{x}} \cdot P_{ij}(\tilde{x},\tilde{y},\theta_{ij}) \end{aligned} \tag{2.147}$$

Substitution from Eq. (2.17) in the coordinate of $x_s O_s y_s$, the second term on the right side of Eq. (2.147) is developed as:

$$\frac{\partial e_i(\tilde{x},\tilde{y})}{\partial \tilde{x}} = \frac{1}{2} \cdot \frac{-2R_s \cos\alpha_i + 2\tilde{x}}{\sqrt{R_s^2 - 2R_s(\cos\alpha_i \cdot \tilde{x} + \sin\alpha_i \cdot \tilde{y}) + \tilde{x}^2 + \tilde{y}^2}} \tag{2.148}$$

The partial differentiation of Eq. (2.6) about $\tilde{y}$ can be deduced in the same way.

2.9 Multiphysics couplings

Once the models of all three different physical fields are established, they are combined together to describe the general dynamic behavior of the electrical machine as discussed in SEC.1.2.4.4. Compared with the previous model shown in FIG.1.10, the strong multiphysics couplings are reinforced in this thesis by taking into consideration the electro-magneto-mechanic couplings in the radial movement. The interactions between the UMP (F_{emx} and F_{emy}) and their radial displacements (x_r and y_r) and speeds ($\dot{x_r}$ and $\dot{y_r}$) are added in the Phase current model from FIG.2.22(a) and meanwhile some parameters to introduce the rotor misalignments are set up in the system as a source of the UMP. The Phase flux model is illustrated in FIG.2.22(b). Since the stator and rotor magnetic flux are chosen as the state vector of the electromagnetic subsystem, the radial and the rotational speeds of the rotor center don't need to be shown up explicitly in the whole model. That's why the Phase flux model is more simple than the Phase current model in the terms of the construction as discussed in SEC.2.7.3.

In order to highlight the importance of the strong coupling between the electromagnetic and mechanic subsystems, an electromagnetic model without the coupling of the mechanical structure is isolated from the complete multiphysics model. For the sake of the simplicity, the separated electromagnetic model is known as " Model EM" while the complete coupled model is called as " Model EMM". The detailed information about these two models are provided in the following two subsections while the comparison between two models particularly about their simulation results are discussed in the third subsection.

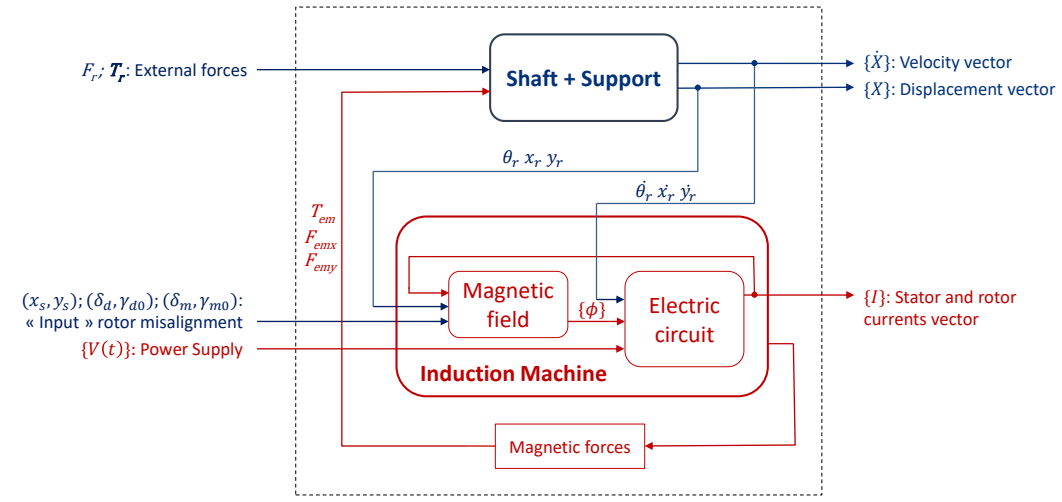

(a) Phase current model

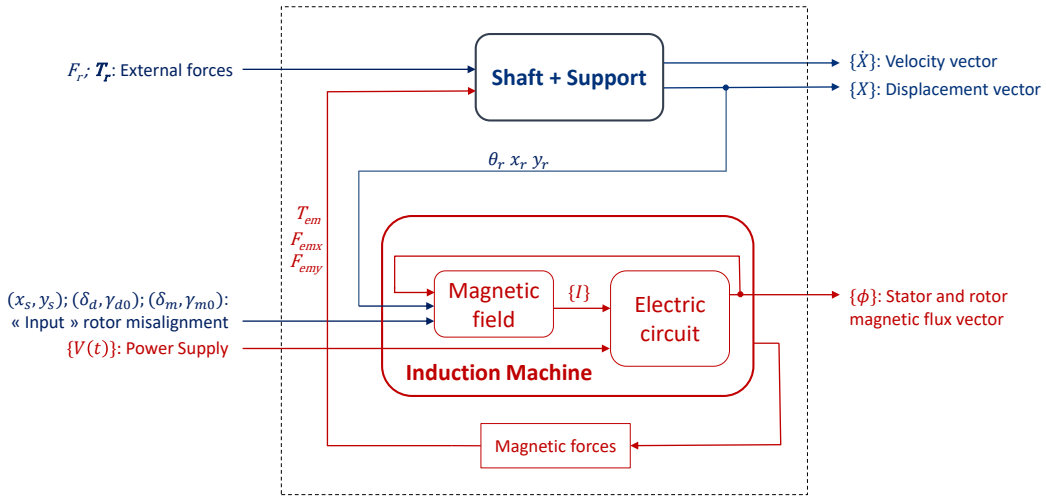

(b) Phase flux model

Figure 2.22: Multiphysics coupling

2.9.1 Model EMM

The image shown in FIG.2.23 is a compact format of the multiphysics model from FIG.2.22. The load torque T_r is used to control the simulation. With a certain input load torque value, the model will generate finally an equal electromagnetic torque value corresponding to a certain rotation speed according to the Torque-Speed characteristic curve of the asynchronous motor. This could realize the simulation at each operation point of the IM. The load torque can be also represented in a variation form in order to conduct a simulation in the non-stationary operation. Since the mechanical structure is

taken into consideration in Model EMM, the rotor misalignment induced by the rotordynamics motion (e.g. the mass unbalance excitation and the rotor displacements generated by the external radial force) are set up in the system as the inputs and the real rotor center orbit and the instantaneous angular speed are considered as the outputs of the model. Besides of these, some intermediate values are also able to be achieved from the model as the magnetic flux, the magnetic potentials, MMF etc. Overall, this is a rather realistic model which can be applied to simulate the real dynamic behavior of the electrical machine under the consideration of the mechanical and the electromagnetic interaction.

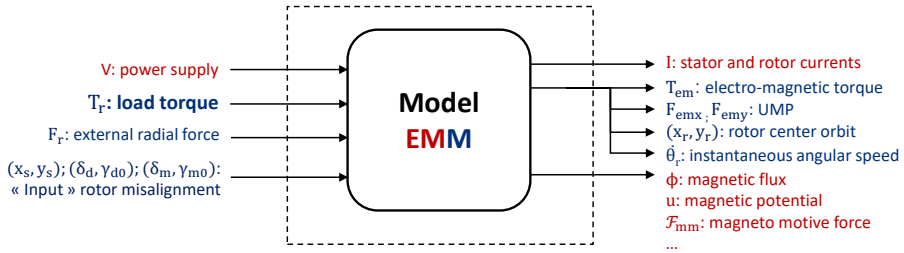

Figure 2.23: Inputs and outputs about the model EMM for the IM

2.9.2 Model EM

Model EM, the one without the coupling with the mechanical model is illustrated in FIG.2.24. Similar as described in Model EMM, it is also supplied by the three phases AC voltage and all the basic electromagnetic variables (those in red) and the electromagnetic forces are achieved as the outputs in Model EM. However since the mechanical structure is eliminated, the state vector is modified as $\{Q\} = \{\{\tilde{\phi}_p\}\ \theta\ t\}^t$ with the two last differential equations expressed as:

$$\begin{aligned} \frac{d\theta}{dt} &= \dot{\theta}_r \\ \frac{dt}{dt} &= 1 \end{aligned} \tag{2.149}$$

and the rotation speed $\dot{\theta}_r$ has to be considered as an input with the assumption that the rotation speed is constant or its variation is predefined in the simulation which means that in Model EM, the rotation speed is used to specify the simulation at a certain operation point. Furthermore, the UMP can only be generated by the geometric predefined rotor misalignment since the rotor center is fixed or its orbit is following a defined trajectory during the simulation in Model EM. Generally, Model EM helps us to study the influence of the electro-magneto-mechanic interaction in the whole system and its simulation results can be adopted to compare with those from other simulation softwares (e.i. FEMM) in order to validate the model since it is suitable for the simulation in a quasi-static regime.

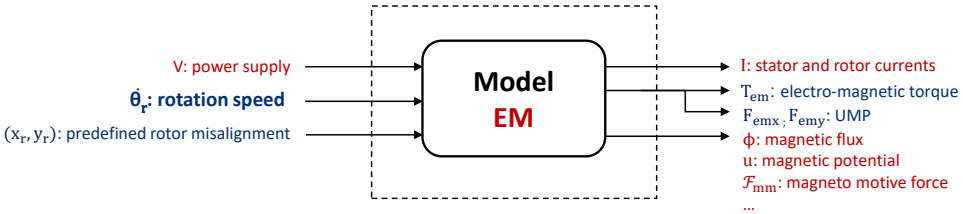

Figure 2.24: Inputs and outputs about the model EM for the IM

2.9.3 Comparison of the two models

In order to analyze the strong couplings between the electromagnetic and the mechanical subsystems, many simulations are realized in several cases either with different input static eccentricity values at the rated operating point or with the same input static eccentricity value but at different operating points. Among all the simulation results, those simulated with the static eccentricity of $50\%E_e$ (here for the simplicity, the eccentricity value is expressed as the percentage of the average air-gap length E_e in this thesis) at the rated operating point are chosen as the examples for the discussion about the comparison of the simulation results at a certain operating point. Then the asynchronous motor characteristic curves plotted according to the simulation results from those two models are compared to study their overall difference.

2.9.3.1 Simulation results at one operating point

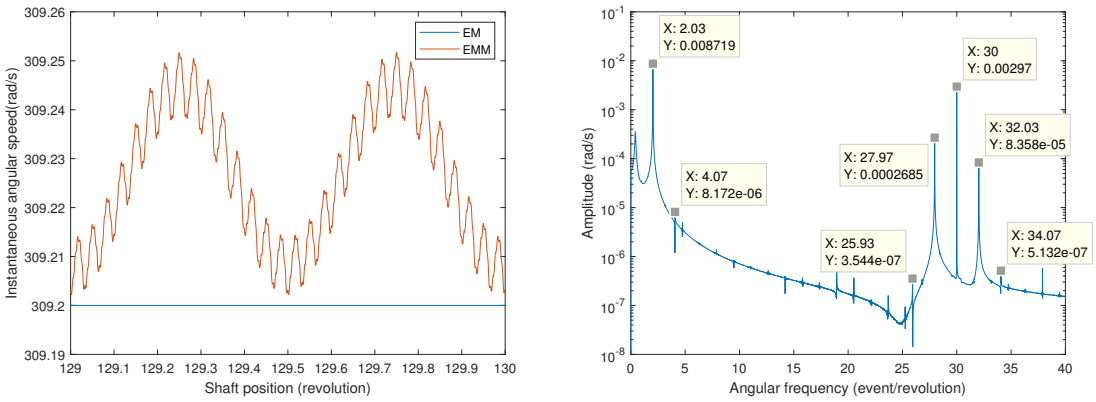

(a) Variation of the rotational speed

(b) Angular spectrum of the rotational speed

Figure 2.25: Instantaneous rotation speed at the rated state with the static eccentricity of $50\%E_e$

As mentioned before, a load torque equal to the rated electromagnetic torque is applied in Model EMM while the shaft rotation speed is fixed at the rated rotation speed value in Model EM to conduct respectively the simulation at the rated operating point. That's why from the comparison about the instantaneous rotation speed in FIG.2.25(a), it can be seen that the one simulated from Model EMM is not a constant value as that from Model EM, but it fluctuates in a modulation form with the variation of the shaft position around an average value close to the rated rotation speed. Its modulation form is generated due to the slot effects and the interaction with the power supply variation in the space because the rotor slot harmonic 30 ev/rev, the double power supply frequency 2.03 ev/rev and its harmonics 4.07 ev/rev and their combinations 27.97 ev/rev ; 32.03 ev/rev and 25.93 ev/rev; 34.07 ev/rev are identified from the angular spectrum about the rotation speed of Model EMM in FIG.2.25(b).

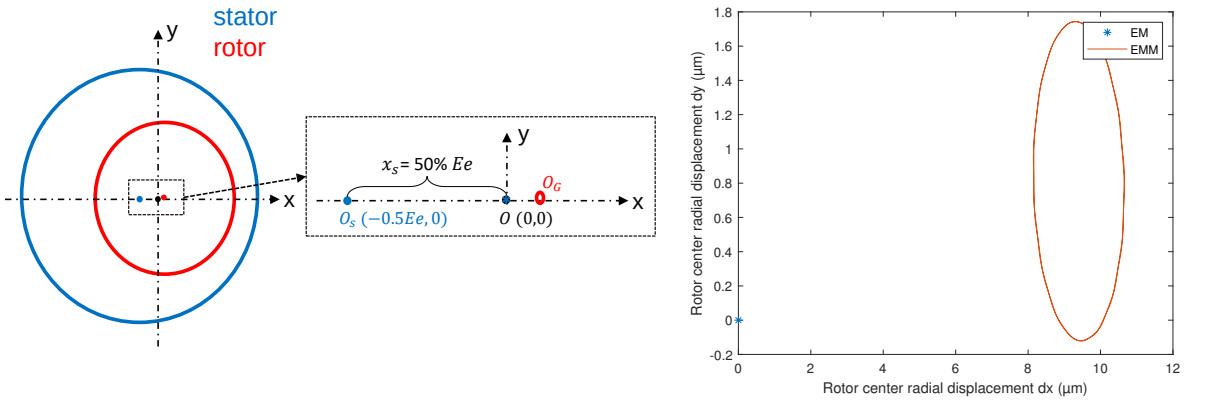

(a) Relative position of the rotor center

(b) Rotor center orbit in the last shaft revolution

Figure 2.26: Rotor center orbit in xoy section with the static eccentricity of 50%E_e

As described in SEC.2.2.1.2, the position of the stator center O_s is used to set up the static eccentricity in the model. Thus from FIG.2.26(a), the distance between the stator center and the origin of the coordinate O equals to the input static eccentricity value. Since the rotor center in Model EM isn't influenced by the generated UMP, it is always fixed at the origin point O. However due to the strong coupling with the mechanical structure in Model EMM, its rotor center O_G will shift from its original position O and it will finally be stabilized in the red circle orbit toward the direction of the minimum air-gap length. The real rotor center orbit simulated from Model EMM is illustrated in FIG.2.26(b). As a reference, a blue star point located at the origin point $(0,0)$ is used to represent the rotor center position of Model EM during the dynamic simulation. It is indicated that the generated UMP due to the initial eccentricity do have some effects on the mechanic structure and the displacement of the rotor center will react on the distribution of magnetic field so as to produce more or less UMP on the structure. It is evident that Model EMM is more precise about the simulation of UMP.

The comparison about other three different simulation results: electromagnetic torque, UMP and stator phase currents are illustrated respectively in FIG.2.27, FIG.2.28 and FIG.2.29. Their variations during the last shaft revolution are compared in the first two sub-figures while their angular spectrum are superposed in the third sub-figure for the comparison of their frequency components. It can be seen that their global fluctuation forms are almost identical however there is an obvious difference in the comparison about their angular spectrum. For the mechanical variables T_{em} and UMP, besides of those common characteristic frequencies exist in both of the two models, the second harmonic of the double power supply frequency 4.07 ev/rev and its combination with the slot harmonics 25.93 ev/rev and 34.07 ev/rev only appear in the results simulated from Model EMM. In the angular spectrum of the first phase stator current shown in FIG.2.29(c), three different characteristic frequencies: power supply frequency 1.02 ev/rev and its combination with the rotor slot harmonic 29.98 ev/rev and 31.02 ev/rev can be identified in both of the two models while the peaks of the third harmonic of the power supply frequency 3.05 ev/rev and of its combinations with the rotor slot harmonic 33.05 ev/rev are very weak but exist only in Model EMM. The difference about their frequency components are also able to be identified in the case with $10\%E_e$ at the operating point but with a large slip. However it can't be detected in the case with a small eccentricity or without the eccentricity.

Since all the characteristic frequencies appeared in the angular spectrum of the instantaneous rotation speed exist also in those of the mechanical variables generated from Model EMM, it is indicated that the difference about their angular spectrum between Model EM and Model EMM is introduced by the variation of the rotation speed and the unfixed rotor center orbit. In the case without the eccentricity or with a small eccentricity, the fluctuation of the rotation speed is so weak that it can be treated as a constant value as defined in Model EM and therefore Model EM and Model EMM are equivalent in this situation. However in the case with a large eccentricity or simulated at the operating point with a large load torque, the variation of the rotation speed becomes larger and more harmonics of the power supply frequency and their combinations with the rotor slot harmonic will be generated in the system to increase the vibration of the IM. It is obvious that Model EMM is more accurate than Model EM in simulating all the dynamic behaviors under that situation.

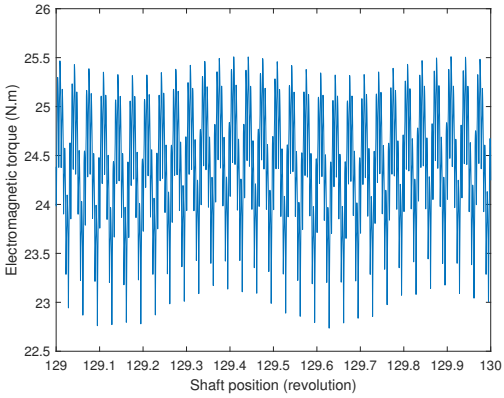

(a) Model EM

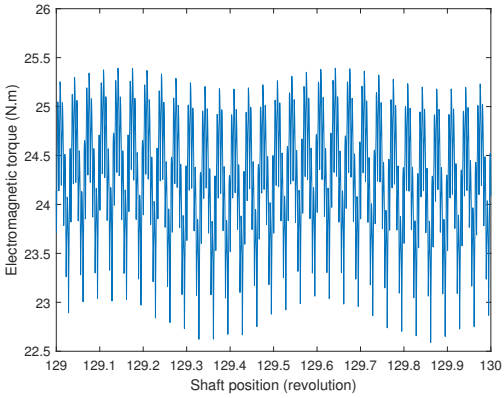

(b) Model EMM

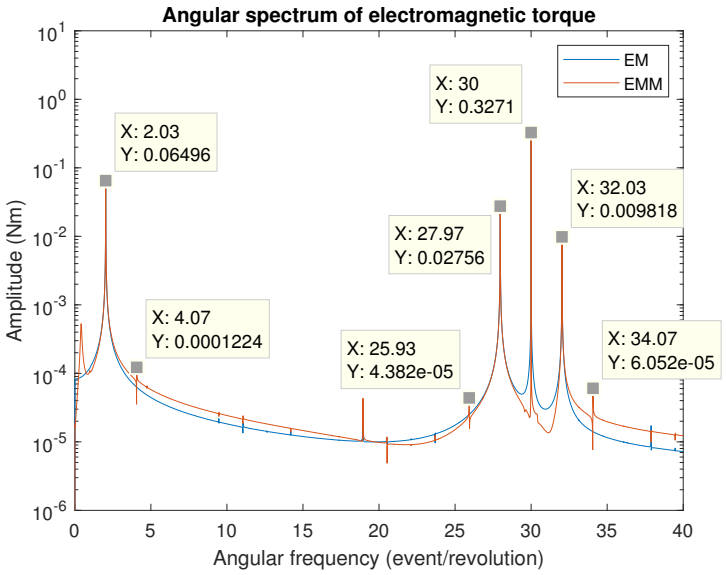

(c) Angular spectrum

Figure 2.27: Electromagnetic torque at the rated state with the static eccentricity of $50\%E_e$

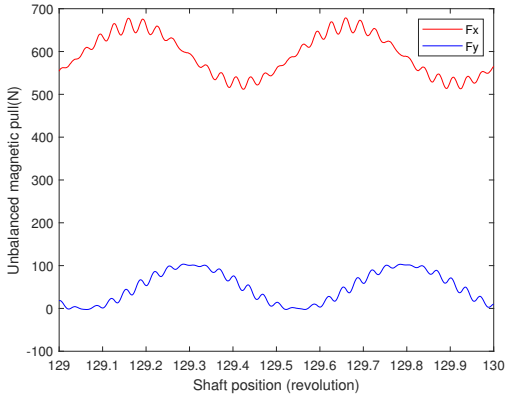

(a) Model EM

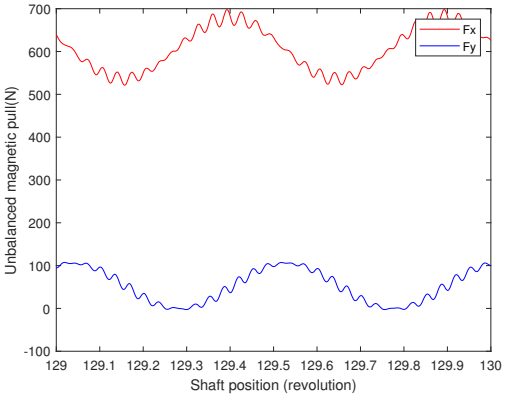

(b) Model EMM

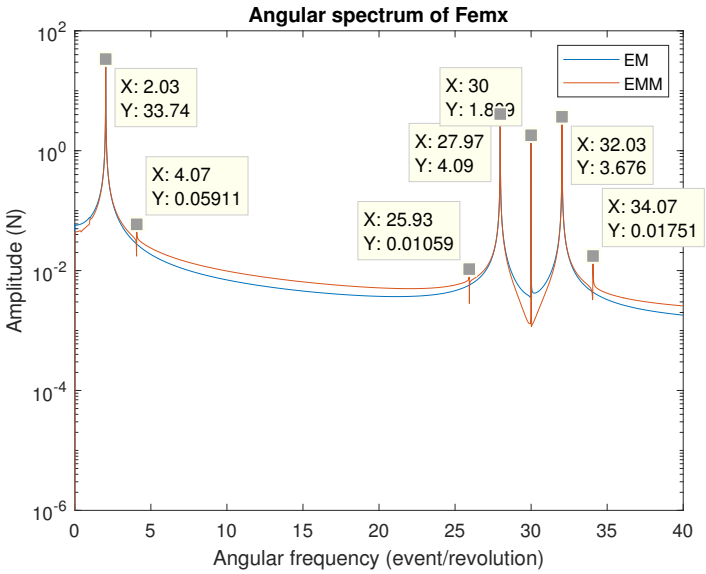

(c) Angular spectrum of F_{emx}

Figure 2.28: UMP force components at the rated state with the static eccentricity of $50\%E_e$

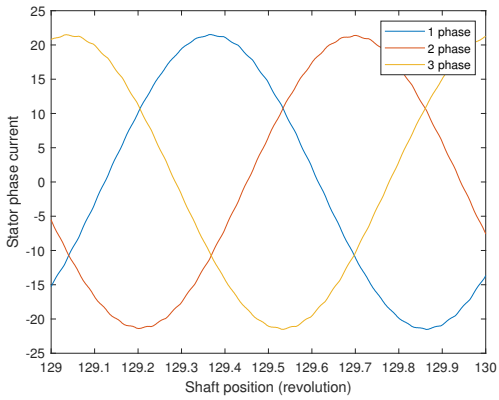

(a) Model EM

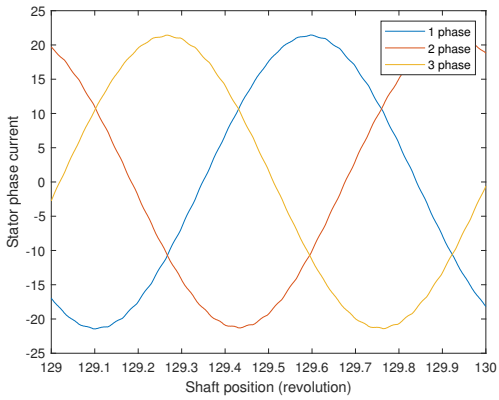

(b) Model EMM

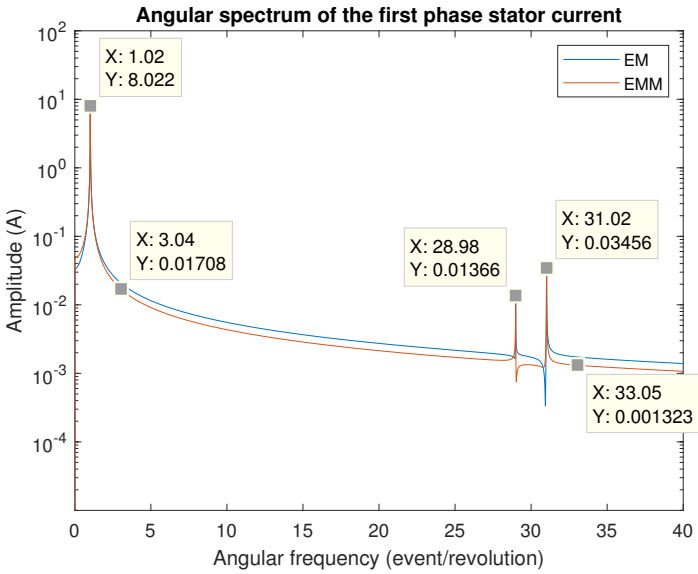

(c) Angular spectrum

Figure 2.29: Stator currents at the rated state with the static eccentricity of 50%E_e

2.9.3.2 Asynchronous motor characteristic curves

The asynchronous motor characteristic curves about "Torque-Speed" and "Current-Speed" plotted according to the simulation results from Model EM and Model EMM are compared separately in FIG.2.30. A series of simulations at different operating points are performed in the case without any input eccentricity in the two models. Each point in the curve of "Torque-Speed" are calculated from the average value of the electromagnetic torque shown in FIG.2.31(a) while those points in the curve of "Current-Speed" are collected from the amplitude of the stator phase currents at every operating points depicted in FIG.2.31(b). According to FIG.2.30, we can see clearly that the common part from Model EM and Model EMM are well superimposed however the curves generated by Model EM

cover all the operating speed range while those simulated from Model EMM only occupy the half of the curve. This is due to different control strategies adopted in Model EM and Model EMM. Since the load torque is used in Model EMM to conduct the simulation at a certain operating point according to the torque equilibrium of the mechanical structure, only the stable operating points can be achieved in Model EMM. That's why the red curves covers the range of the possible speed variation as a motor. In the other word, different from Model EM, Model EMM can only provide us with the simulation results in the stable operating zone of the motor which has more practical significance in the study.

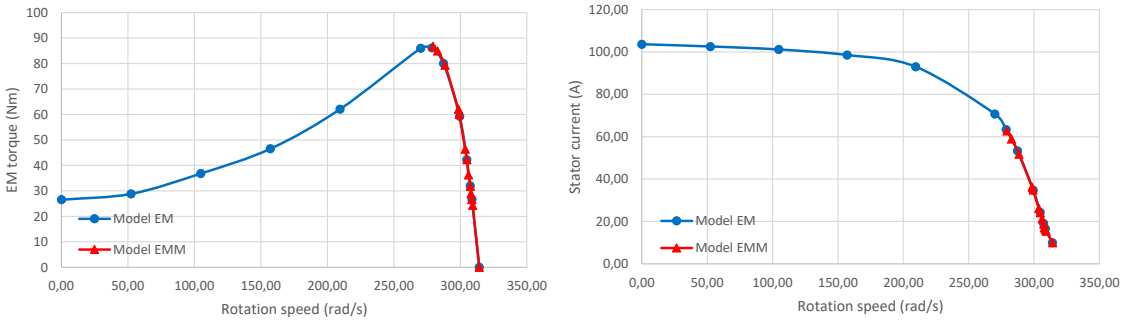

(a) Torque vs Speed (b) Current vs Speed

Figure 2.30: Comparison of asynchronous motor characteristic curves between Model EM and Model EMM

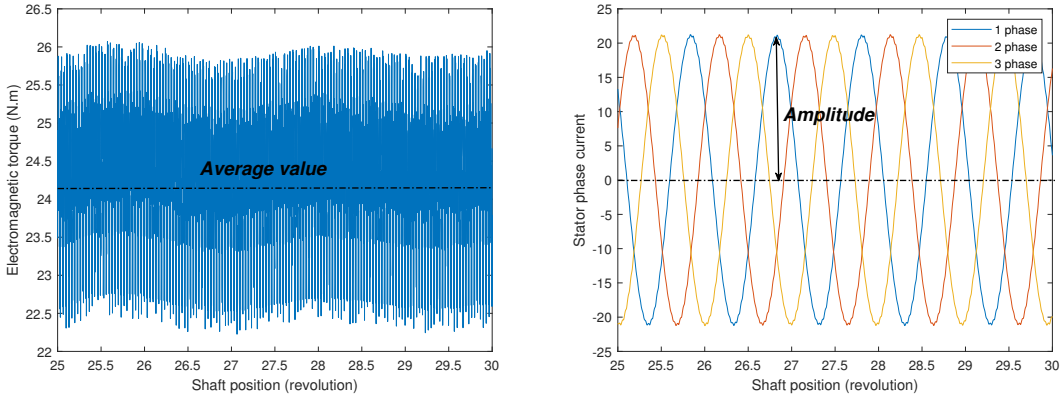

(a) Variation of Electromagnetic torque (b) Variation of stator phase currents

Figure 2.31: Simulation results computed without input eccentricity at the rated state

2.10 Model validation in the quasi-static regime

This multiphysics model is validated in the quasi-static regime in the frame of this thesis which means its validations are realized at each operating point with a constant rota-

tion speed. Therefore, the simulation results from Model EM are adopted to compare with those simulated from other traditional models of the electrical machine. In order to obtain a complete validation, the comparisons are performed receptively with two different reference models in two different aspects. The first comparison between Model EM and another FEM (Model FEMM) is effectuated at the rated operating point to compare the simulation results quantities and their fluctuation form with the variation of the shaft rotation while the second comparison is conducted between the simulation results from Model EM and the reference machine data provided by our industrial partner Nidec-Leroy Somer in order to validate the average value at every operating points according to the asynchronous motor characteristic curve.

The reference machine is a three phases, double squirrel cage IM. All the machine parameters are available in TAB.C.1 and its mechanical characteristics are listed in TAB.C.2 from APPENDIX.C.

2.10.1 Finite Element Method Magnetics Model (Model FEMM)

Before the first comparison, a traditional FEM about this IM needed to be established in an open source software "Finite Element Method Magnetics" (FEMM). It is a set of programs for solving low frequency electromagnetic problems on 2D planar and asymmetric domains [169]. A quarter of the motor's cross section is illustrated in FIG.2.32(a). It is composed of six parts from the outside to the inside: the stator yoke, the stator slot, the air-gap, the rotor yoke, the rotor slot and the shaft. Different materials are distributed in each area. The "Silicon Core Iron" with a modified constant relative permeability value correspond to the reference motor is assigned to the stator and rotor yoke area. It can also be replaced by a nonlinear " B-H curve " to simulate the case with the magnetic saturation. The "Magnetic wire" and "Aluminum, 1100" are separately allocated in the stator slot and the rotor slot to present the material property of the stator winding and the rotor bars. The electrical conductivity of the two materials should be well defined according to their resistivity calculated in EQ.2.83 since they are used to generate the induced rotor bar currents during the simulation. The boundary condition is set up on the stator outer circle and the Maxwell equations are solved in each finite elements discretized by a "Smart mesh" option. The geometric dimensions of each part are created according to the reference machine drawings except for some simplifications about the curved edges in order to accelerate the calculation. FIG.2.32(b) displays the magnetic flux distributions in the whole cross section of the IM at a certain moment. It's shown that it is a 2-pole electrical machine which can also be used to help develop the permeance network mesh discussed in SEC.2.2.

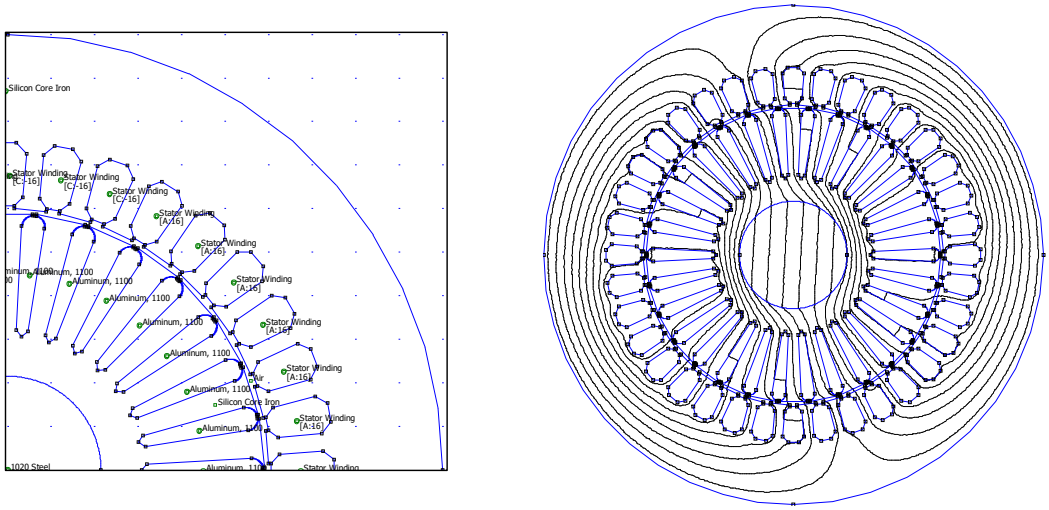

(a) Model FEMM (b) Magnetic flux distribution

Figure 2.32: 2-pole cage induction machine in FEMM.

The Model FEMM is used to calculate electromagnetic forces (T_{em} and UMP) at a certain operating point with a set of given stator phase currents. The operating point of the IM is defined in FEMM by describing the model with a fundamental frequency equaled to the corresponding slip frequency (f_{slip}) shown in EQ.2.150:

$$f_{slip} = \frac{\omega_s - \omega_r}{2 * \pi} \tag{2.150}$$

Since the synchronous rotation speed ω_s and the shaft rotation speed ω_r are considered as two constant values in Model EM and Model FEMM, the slip frequency f_{slip} is fixed for each operating point.

As illustrated in FIG.2.32(a), three-phase stator currents are arranged systematically in each slot according to the real stator winding type. For a simulation at a certain moment, the stator current value in each phase is input in the form of three complex number as depicted in FIG.2.33. The real parts of each current (i.e. $\mathrm{Re}(i_A)$) are achieved from the simulation results of Model EM at the same shaft position as shown in FIG.2.33(a) while the imaginary parts (i.e. $\mathrm{Im}(i_A)$) are used to describe their phase difference which can be calculated in the unit circle from FIG.2.33(b). The peak value of each phase current i_{pic} can be found out from the simulation results in FIG.2.33(a). This kind of simulation can be developed into a "dynamic " simulation if the three-phase stator currents are considered to variate as a sinusoidal function in the complex number form as defined in EQ.2.151:

$$\begin{aligned} i_A &= i_{pic} \cdot e^{(\omega_s \cdot t + \theta_0) * j} \\ i_B &= i_{pic} \cdot e^{(\omega_s \cdot t + \theta_0 - \frac{2*\pi}{3}) * j} \\ i_C &= i_{pic} \cdot e^{(\omega_s \cdot t + \theta_0 - \frac{4*\pi}{3}) * j} \end{aligned} \tag{2.151}$$

where the initial phase angle θ_0 is determined by the angular position of Phase A current vector from the real axis as shown in FIG.2.33(b). In order to perform the "dynamic " simulation at the determined operating point, the rotor part has to rotate according to the function of $\omega_r \cdot t$ at the same time.

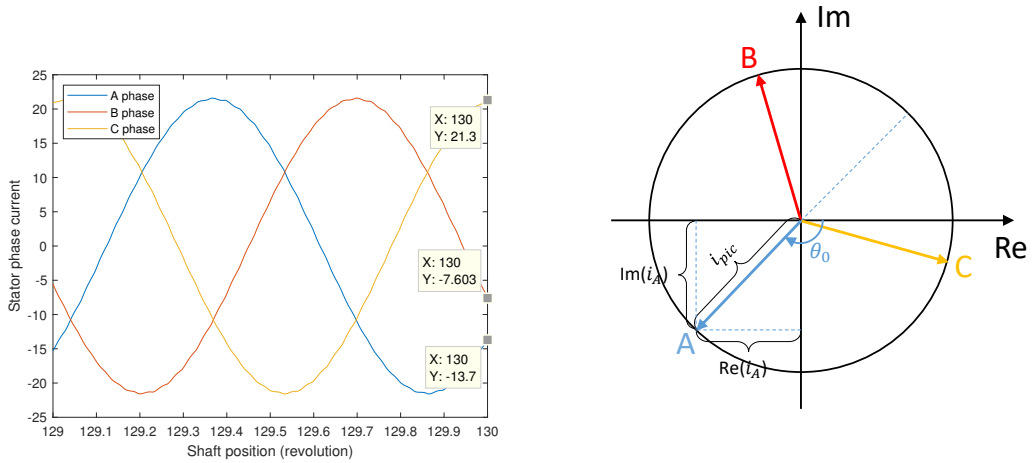

(a) Variation of three-phase currents (b) Spatial distribution of three-phase currents

Figure 2.33: Complex number representation about the stator phase currents.

The chosen IM isn't influenced so much by the magnetic saturation effects and this can be confirmed by comparing the simulation results of Model FEMM between the two cases with and without the magnetic saturation effect. As mentioned before, the difference between the two simulation cases is realized by changing the material of the stator and rotor iron core part. From the simulation results listed in TAB.2.1, it can be seen that at the same operating point and with the identical input stator phase currents and the same static eccentricity of the rotor, the electromagnetic forces (T_{em} and F_{emx}) produced in the case without the saturation effect are a little larger than those generated from the case with the saturation effect. However their difference are not too large to be considered as equivalent results. Since the solution of the nonlinear equations due to the saturation effect consumes too much time in both Model EM and Model FEMM, all the simulation results about the reference IM are going to be discussed in the case without the magnetic saturation in this thesis.

	Without saturation	With saturation
T_{em} (Nm)	25.12	25.02
F_{emx} (N)	93.09	87.19

Table 2.1: Comparison about the simulation results of FEMM between the case with and without the saturation effect.

2.10.2 At the rated operating point

The first validation is realized in the case with the static eccentricity of $10\%E_e$ along the x-axis at the rated operating point. The variation of the electromagnetic torque and the stator first phase current as the function of the shaft rotation position from Model EM are compared respectively with those belonged to Model FEMM as illustrated in FIG.2.34 in order to validate their waveforms. From FIG.2.34(a), it is clearly that the fluctuation forms of the two simulation results are similar even if there is a small difference between their values. The average of their relative error is about 3% so that the two simulation results about the generated electromagnetic torque are assumed to be consistent. Since Model EM is supplied by the three-phase voltage and Model FEMM is controlled by the input three-phase currents, the generated stator first phase current from Model EM is compared with that defined in EQ.2.151 from Model FEMM in FIG.2.34(b). The two current signals are well superposed in the global view however some undulations could be identified in a zoom view from the simulation result's waveform of Model EM. These undulations are introduced due to the interaction between the slot harmonics and the supply frequency according to FIG.2.29(c) which are obviously not taken into consideration in Model FEMM. It indicates that the strong coupling between the electric and the magnetic field are effectuated in Model EM.

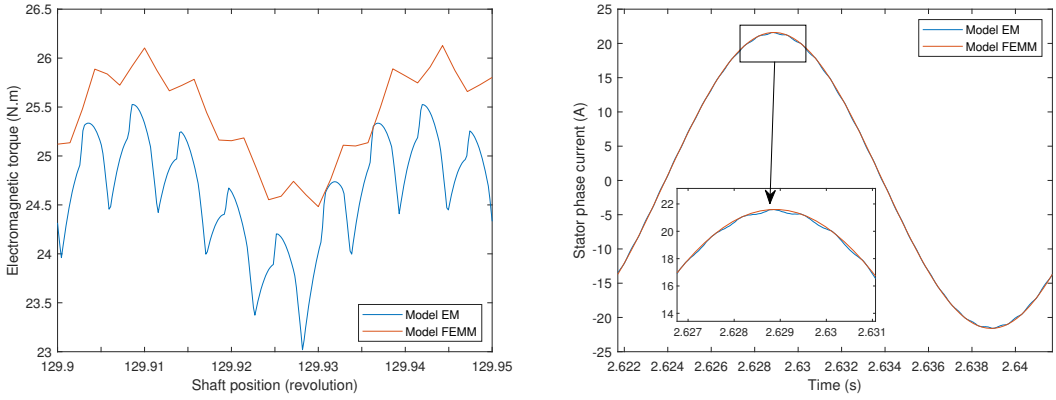

(a) Electromagnetic torque

(b) stator first phase current

Figure 2.34: Comparison about the simulation results between Model EM and Model FEMM at the rated state with $10\%E_e$

Another comparison is performed among several simulations at the rated operating point but with different static eccentricity values. Since the rotor static eccentricity is always set up along the x-axis, the main UMP force component F_{emx} is used to realize the comparison between the two models as shown in FIG.2.35. The average values of F_{emx} calculated from each set of "dynamic" simulation results are plotted with the variation of the eccentricity ratio. In both of the two models, F_{emx} average value increases linearly with the increase of the input eccentricity ratio although there is a discrepancy between

the two curves. The average of their relative error is around 8% and considering about the simplifications on the geometry of Model FEMM, there is an accordance between the two models.

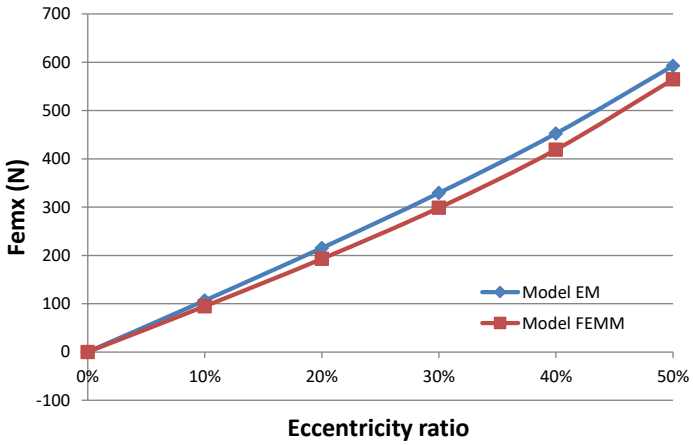

Figure 2.35: Comparison of simulation results about UMP x-axis force at the rated operating point

Based on the previous comparisons about three different simulation results, it is indicated that the waveform of the simulation results and its magnitudes simulated from Model EM are validated in the case with input static eccentricities at the rated operating point through the comparison with the corresponding simulation results from Model FEMM.

2.10.3 At all the operating points

The simulation results from the proposed multiphysics model at other operating points are verified by comparing their values in the case without input eccentricity with the reference machine data provided by our industrial partner Nidec-Leroy Somer. Those reference data are calculated at each operating point from a company internal software based on MEC model while the simulation results of the proposed model (including Model EM and Model EMM) are achieved from the steady state to realize the verification in the quasi-static regime. Therefore two motor characteristic curves about the relation of the Torque-Speed and the Current-Speed are plotted separately in FIG.2.36(a) and FIG.2.36(b). Compared with FIG.2.30, two green curves representing the reference data are added respectively in two sub figures. It can be seen clearly that those three curves have a good consistency in the stable operating range of the motor's operation mode as explained in SEC.2.9.3.2. However there is an obvious difference between Model EM and the reference data in another half of the curves. This difference is due to the simplification of the rotor slot geometry because the real IM has a double cage rotor while it is

simplified as a simple cage rotor by conserving the same slot area. Since the study about the dynamic behavior of the induction machine is focused on the operating range of the electric motor, the simulation results of this multiphysics model at all the operating points can be validated according to their consistency in the common area from the characteristic curves.

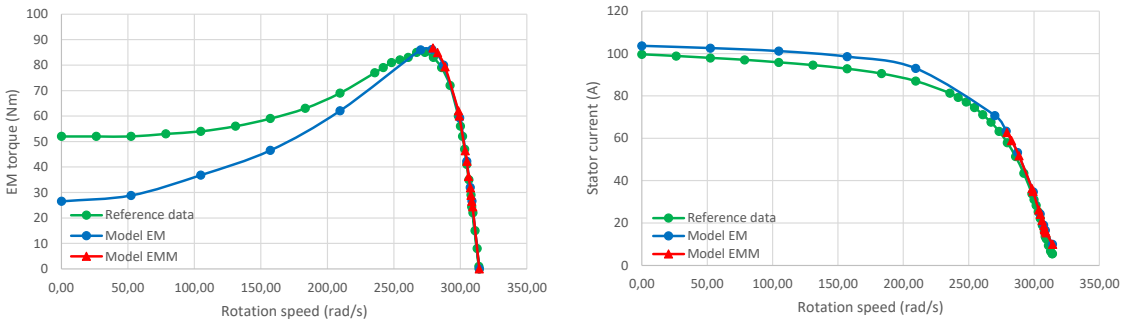

(a) Torque vs Speed

(b) Current vs Speed

Figure 2.36: Asynchronous motor characteristic curves

2.11 Dynamic simulation results analysis

With the validated multiphysics model, different simulation results from Model EMM are analyzed in this section to study the dynamic behavior of the IM under the influence of UMP. It is discussed firstly in the stationary operation and then studied in the non-stationary operation. The machine mentioned in SEC.2.10 is adopted to perform all the simulations.

2.11.1 Analysis in the stationary operation

The simulation in the stationary operation is realized by applying a constant load torque on the mechanical structure to make the system operate at a certain operating point. The simulation results in the steady state are analyzed to study the influence of different rotor eccentricities on the dynamic behavior of the electrical machine. The cases with the rotor eccentricity brought by an input static eccentricity are discussed in the first part and those induced by the rotor dynamic motion (the mass unbalance excitation and the gravity) are studied in the second part.

2.11.1.1 With an input static eccentricity

Simulation results in the stationary operation with an input static eccentricity are discussed in two aspects. The first in focused on the comparison about the simulation results with the same input eccentricity amplitude but at two different operating points and the

second is realized about the study of the simulation results at the rated operating point but with different eccentricity amplitudes.

Influence of different operating points At the first step, the static eccentricity of $10\%E_e$ is set up along the horizontal axis (x-axis) by modifying the coordinate of the stator center O_S into:

$$\begin{aligned} x_s &= -10\%E_e \\ y_s &= 0 \end{aligned} \tag{2.152}$$

Two operating conditions are investigated in this paragraph. The first is at the rated rotation speed 309.26 $\text{rad} \cdot \text{s}^{-1}$ and the second is chosen to be next to the operating point of the maximum torque from FIG.2.36(a) with the average rotation speed equaled to 289.20 $\text{rad} \cdot \text{s}^{-1}$. All the simulations are performed for firstly 50 revolutions to attain the steady state and then the results of the next 1000 revolutions are analyzed to avoid the transient state influence.

The simulation results of UMP in the steady state with the input static eccentricity of $10\%E_e$ for the two operating points are shown separately in FIG.2.37. It can be seen from both two graphs that with an input static eccentricity, two components of UMP are converged to different constant values respectively and fluctuate around them with similar amplitudes. These results conform to the first conclusion in [168]: The UMP includes the constant component and oscillatory components that fluctuated at double supply frequency. Their amplitudes are increased with the increase of the motor slip. Since F_{emx} is the main UMP component force generated from the input eccentricity, its average value in this direction is also increased. This is due to that as the motor slip increases, the induced current in the magnetic field becomes larger as well as the magnetic flux through the air gap, resulting in an increase in the generated electromagnetic forces according to SEC.2.8.2. Some other phenomena about UMP can be investigated and are going to be discussed hereafter in two parts: physical characteristics and frequency analysis.

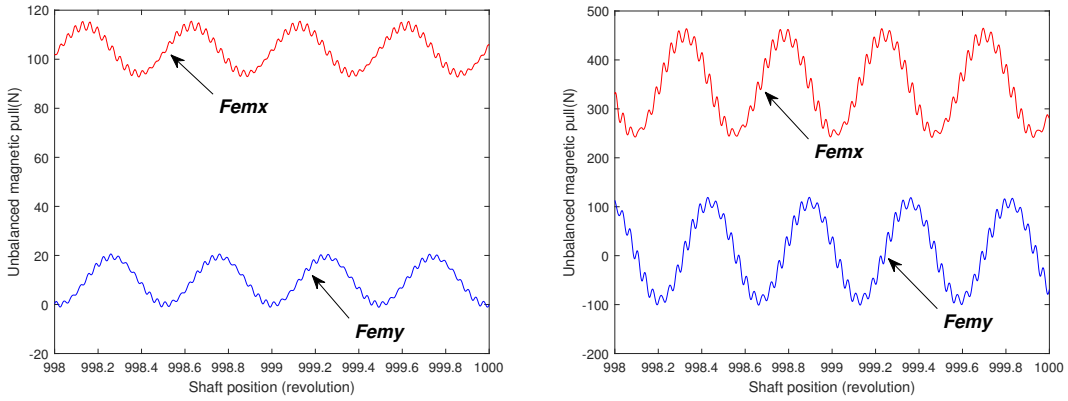

(a) $\omega_r = 309.26\ \mathrm{rad \cdot s^{-1}}$ (b) $\omega_r = 289.20\ \mathrm{rad \cdot s^{-1}}$

Figure 2.37: Variation of UMP with the static eccentricity of $10\%E_e$ in the last two revolutions

Physical characteristics From FIG.2.37, the average value of F_{emx} is larger than that of F_{emy} because the input eccentricity is placed on x-axis. However it is also found that the steady component of UMP projected to the vertical direction F_{emy} isn't zero. This means the UMP resultant force doesn't act along the direction of the initial smallest air-gap as we usually considered but it rotates slightly from the narrowest air-gap position with a certain offset angle. This angle can be identified more clearly in the polar diagram of UMP shown in FIG.2.38(a) by plotting the variation of F_{emy} as a function of F_{emx} in a polar coordinate. Since the UMP variation has some oscillation components, the arrow in FIG.2.38(a) is plotted by the average value of UMP to show its average magnitude and the small orbit at the top of the arrow illustrates the arrow's end trajectory during one shaft revolution in order to display the variation of the UMP magnitude and offset angle in the xoy section. This phenomenon is generated by the effects of equalizing currents induced in the rotor cage due to the eccentricity. As explained in [55] based on a FEM, these currents reduce the amplitude of the force and change the direction of the force from the direction of the minimum air gap. Thus, our multiphysics model can be confirmed by displaying this phenomenon in the simulation results of UMP. Comparing the polar diagrams of UMP at different operating points in FIG.2.38(b), it is shown that the UMP resultant force magnitude increases and the orbit becomes larger in two directions simultaneously with the increase of the motor slip but meanwhile its average offset angle decreases. It demonstrates that the variation range of the UMP magnitude and of its offset angle are increased at the same time. And it indicates that the UMP generated in the case with a larger motor slip tends to fluctuate around the position of the set-up eccentricity with larger oscillations in the vertical direction.

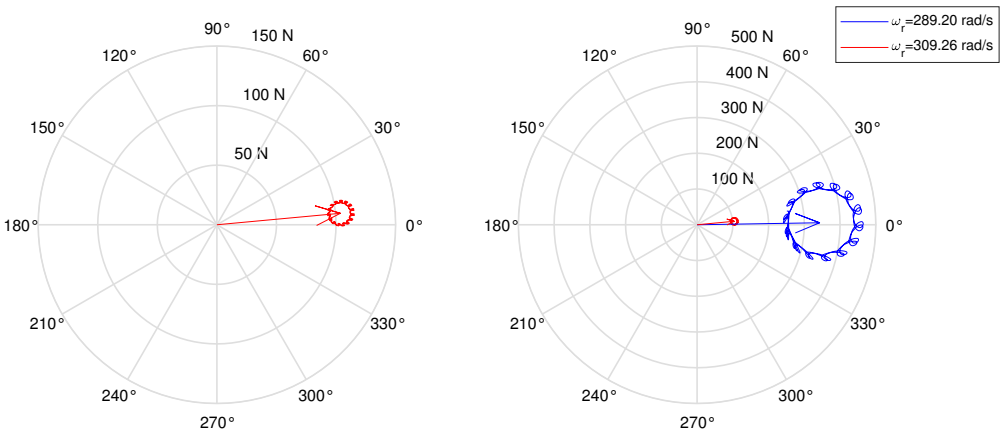

Figure 2.38: Polar diagram of UMP with the static eccentricity of $10\%E_e$ in the last shaft revolution

Due to the UMP fluctuations in its magnitude and direction, the generated radial displacements of the rotor geometric center can be described as an orbit. The simulation result about this rotor center orbit at the rated operation state during the last shaft revolution is plotted in FIG.2.39(a). It is shown that the rotor center rotates in two slightly circumferential shifted orbits that are plotted in two different colors. There are about 15 ripple waveforms as displayed in the zoom part of FIG.2.39(a) around each orbit and they are almost evenly distributed around the entire circumference which means that during the last shaft revolution there are totally 30 ripple waveforms corresponding to the number of the rotor bars. It reflects how slot effects act on the dynamic behavior of the induction machine. Start and end points of this last revolution don't coincide. Their distance and the shift between the two orbits are introduced by the motor slip. The comparison of two orbits simulated at two operating points is illustrated in FIG.2.39(b). Thanks to the strong coupling in this multiphysics model, the nonlinear variation of the rotor center radial displacements under the UMP generated from the cases with the same input eccentricity but at different operating points are achieved naturally from the simulation results.

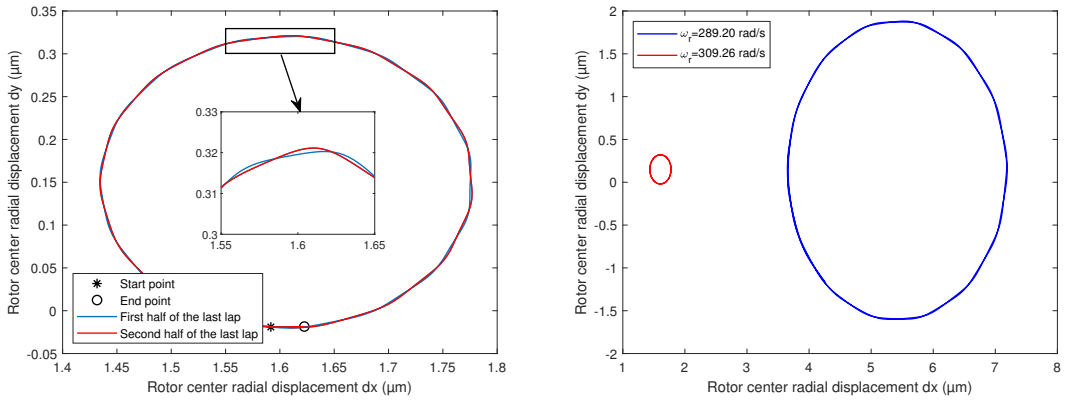

(a) $\omega_r = 309.26\ \mathrm{rad}\cdot\mathrm{s}^{-1}$ (b) Comparison of two orbits

Figure 2.39: Rotor center orbit in xoy section with the static eccentricity of $10\%E_e$

Frequency analysis Frequency responses presented in this section are obtained by applying the Fast Fourier Transform analysis on the results over 1000 revolutions in order to achieve the frequency value with a high precision. The UMP along x direction is chosen to perform the frequency analysis since F_{emx} is the main UMP component force. As defined in EQ.2.128, an order analysis is adopted here to illustrate the frequency component in the angular domain. Therefore the power supply frequency 50 Hz is shown as $1.016\ \mathrm{ev}\cdot\mathrm{rev}^{-1}$ and $1.0863\ \mathrm{ev}\cdot\mathrm{rev}^{-1}$ respectively in the angular spectrum for the two operating points.

Their frequency spectrum in the angular and time domain at two rotation speeds are illustrated separately in FIG.2.40 and FIG.2.41. Four characteristic frequencies could be evidently recognized from all of the four spectrum. Taken the rated state in FIG.2.40 as an example, they are: the double supply frequency $2f_s = 2.032\ \mathrm{ev}\cdot\mathrm{rev}^{-1}$; slot harmonic equals to the rotor teeth number $f_{\mathrm{sh}} = 30\ \mathrm{ev}\cdot\mathrm{rev}^{-1}$ and the other two sideband frequencies on either side of the slot harmonic $f_{\mathrm{sh}} \pm 2f_s$. According to the conclusion stated in [128], a homo-polar flux due to the rotor static eccentricity is generated in the two pole squirrel cage induction machine and this homo-polar component will cause a vibration component of UMP with double supply frequency $2f_s$. Therefore, the existence of this characteristic frequency due to the input static eccentricity allows us to further validate our model.

Comparing the two angular spectrum at different rotation speeds from FIG.5.6(a) and FIG.2.41(a), the frequency peak corresponded to f_{sh} appear at the same place $30\ \mathrm{ev}\cdot\mathrm{rev}^{-1}$ however the others associated with $2f_s$ displaced with the variation of the rotation speed. In contrary, the frequency peak referred to $2f_s$ are identified at the same position $100\ Hz$ in the two traditional spectrum from FIG.5.6(b) and FIG.2.41(b) while the others change their values with the augmentation of the rotation speed. It implies that the slot harmonic f_{sh} is an angular cyclic phenomenon while the double supply frequency $2f_s$ is a temporal cyclic phenomenon and the frequency combinations between the two $f_{\mathrm{sh}} \pm 2f_s$ are assumed to be the modulation between the angular and temporal phenomena.

Since the rotor eccentricity is the disturbance in the electrical machine, this similar signal modulation demonstrates that UMP produced by the input static eccentricity is generally acted as a steady pull to the whole system. The second harmonic of the double supply frequency and its modulation with the slot harmonic arise in FIG.2.41 with the increase of the motor slip and it indicates that the modulation is amplified with the increase of the load torque. This will also be revealed in SEC.2.11.2.1.

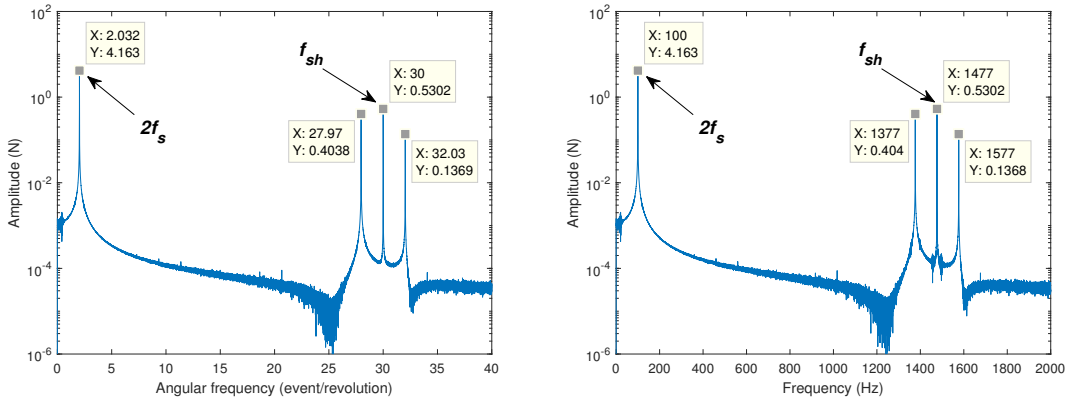

(a) Angular spectrum (b) Traditional spectrum

Figure 2.40: Frequency spectrum of UMP along x direction with 10%E_e eccentricity at $\omega_r = 309.26\ \mathrm{rad} \cdot \mathrm{s}^{-1}$.

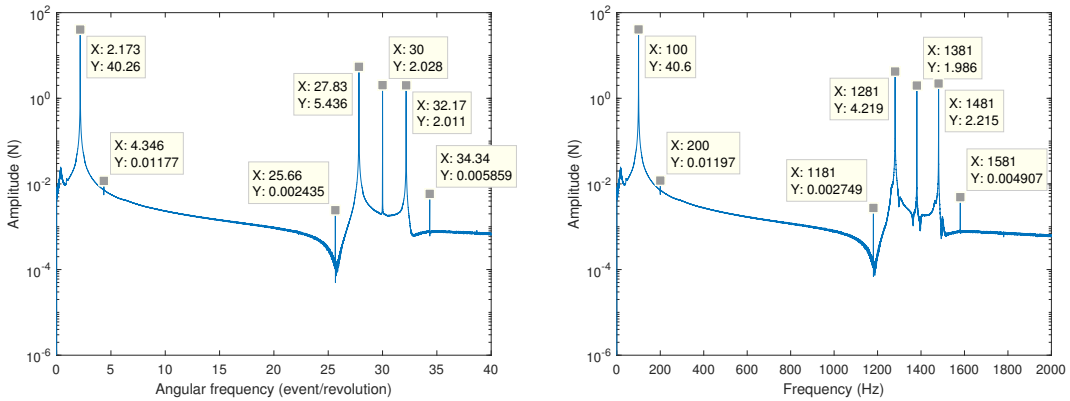

(a) Angular spectrum (b) Traditional spectrum

Figure 2.41: Frequency spectrum of UMP along x direction with 10%E_e eccentricity at $\omega_r = 289.20\ \mathrm{rad} \cdot \mathrm{s}^{-1}$.

Similarly these characteristic frequencies can also be detected in the corresponding electromagnetic torque by comparing its angular spectrum simulated in the case with

and without eccentricity shown in FIG.2.42. Double supply frequency 2.032 $ev \cdot rev^{-1}$ and its modulation with the slot harmonic 27.97 $ev \cdot rev^{-1}$ are only identified in the case with $10\%E_e$ eccentricity. It reflects that the rotor radial displacements also influence its rotational movement. And it provides us with an evidence that the rotor eccentricity could be detected from the generated electromagnetic torque signal.

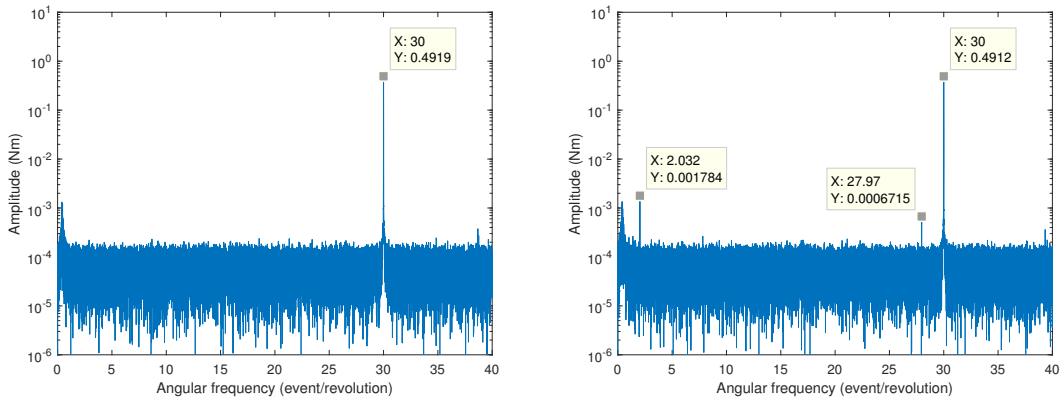

(a) Without eccentricity

(b) With $10\%E_e$ eccentricity

Figure 2.42: Angular spectrum of electromagnetic torque at $\omega_r = 309.26\ rad \cdot s^{-1}$.

Influence of different input eccentricity amplitudes The polar diagrams of UMP with 3 different input static eccentricities at the rated operating point are plotted in FIG.2.43. As introduced in FIG.2.38, the arrows represent the average value of each UMP magnitude while the orbits at the end of each arrow illustrate the variation of the UMP and its offset angle during one shaft revolution. It is shown that at the rated operating point ($\omega_r = 309.26\ rad \cdot s^{-1}$), the magnitude and the fluctuation range of UMP and its offset angle increase proportionally with the augmentation of the input static eccentricity values while their average offset angles remain the same.

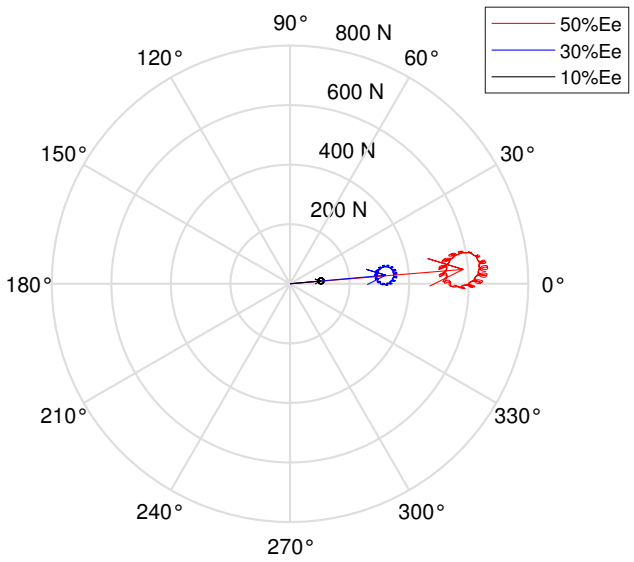

Figure 2.43: Polar diagram of UMP with different eccentricities at the rated state

The variation of the instantaneous rotation speeds simulated with those three eccentricity values are compared with the simulation result from the case without eccentricity in FIG.2.44. Although the rotation speeds all converge to almost the same constant value, it can be seen clearly that some undulations become more and more obvious in their variation waveforms with the increase of the input eccentricity amplitudes. In order to identify this fluctuation component, their angular spectrum are compared in FIG.2.45. As discussed in the previous paragraph, the four characteristic frequencies identified in UMP spectrum can also be recognized in all of three rotation speed spectrum in the case with the eccentricity. However only the slot harmonic $f_{\mathrm{sh}} = 30$ exists in the case without eccentricity which indicates that the double supply frequency and its combinations with the slot harmonic are the three characteristic frequencies associated with the input static eccentricity. Comparing between the three spectrum in the case with the eccentricity, the amplitudes of the three frequency components increase evidently with the augmentation of the input eccentricity value. It signifies that the radial eccentricity do have the influence on the rotation speed variation and this impact becomes more evident with the increase of the eccentricity value. Relatively, the amplitude increase of the double supply frequency and of the sideband frequencies in the rotation speed spectrum reflects the increase of the eccentricity amplitudes. Furthermore, similar as the finding in FIG.2.41, some more harmonics of the double supply frequency and its combination with the slot harmonics appear in the case with $50\%E_e$ eccentricity which means that the vibration becomes more obvious due to a larger eccentricity.

Considering about the strong couplings between the electromagnetic subsystem and the mechanical subsystem taken into account in the proposed model, it can be seen that more UMP is generated inside of the motor with a larger input eccentricity value to increase the vibration in the radial displacement so as to induce more fluctuations in the

distribution of the magnetic field. According to EQ.2.143, these fluctuations are introduced in the generated electromagnetic torque due to the variation in the magnetic field and therefore these fluctuations are finally transfered to the rotation speed and are revealed in its waveform.

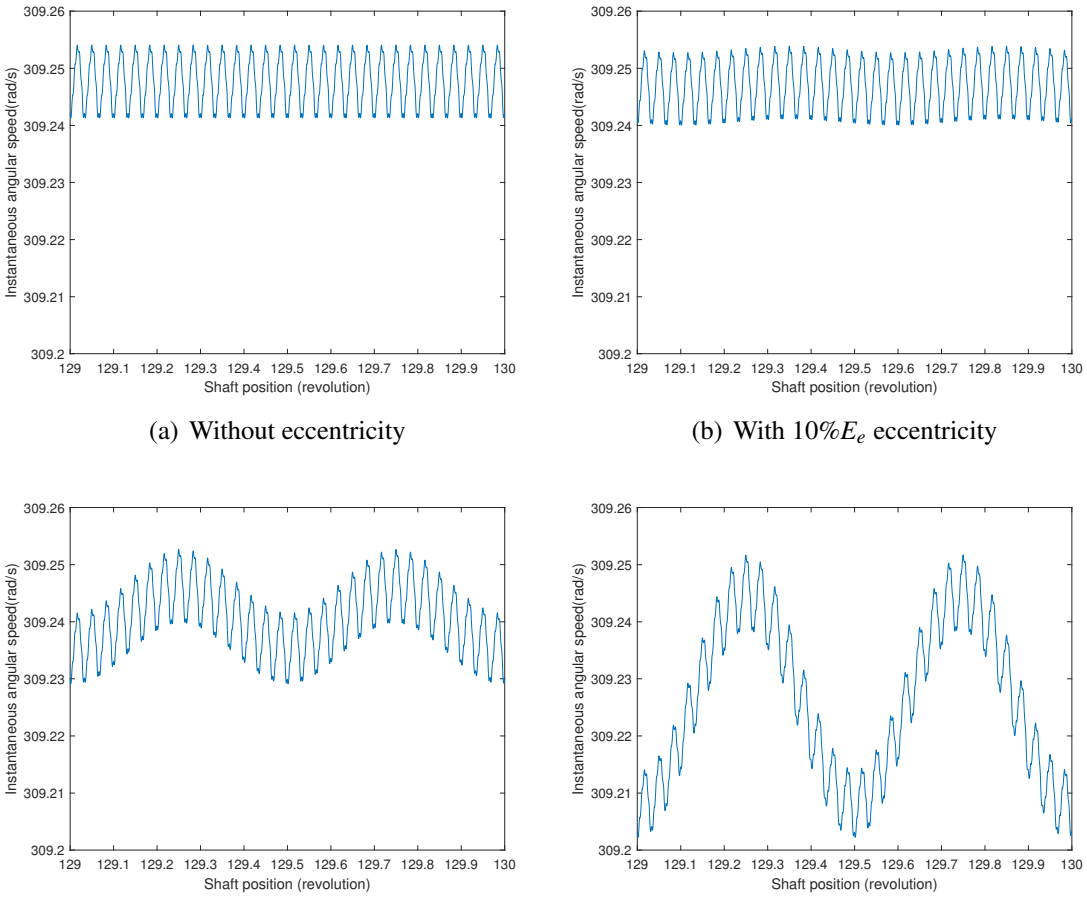

(a) Without eccentricity

(b) With 10%E_e eccentricity

(c) With 30%E_e eccentricity

(d) With 50%E_e eccentricity

Figure 2.44: Variation of instantaneous rotation speed at the rated operation state

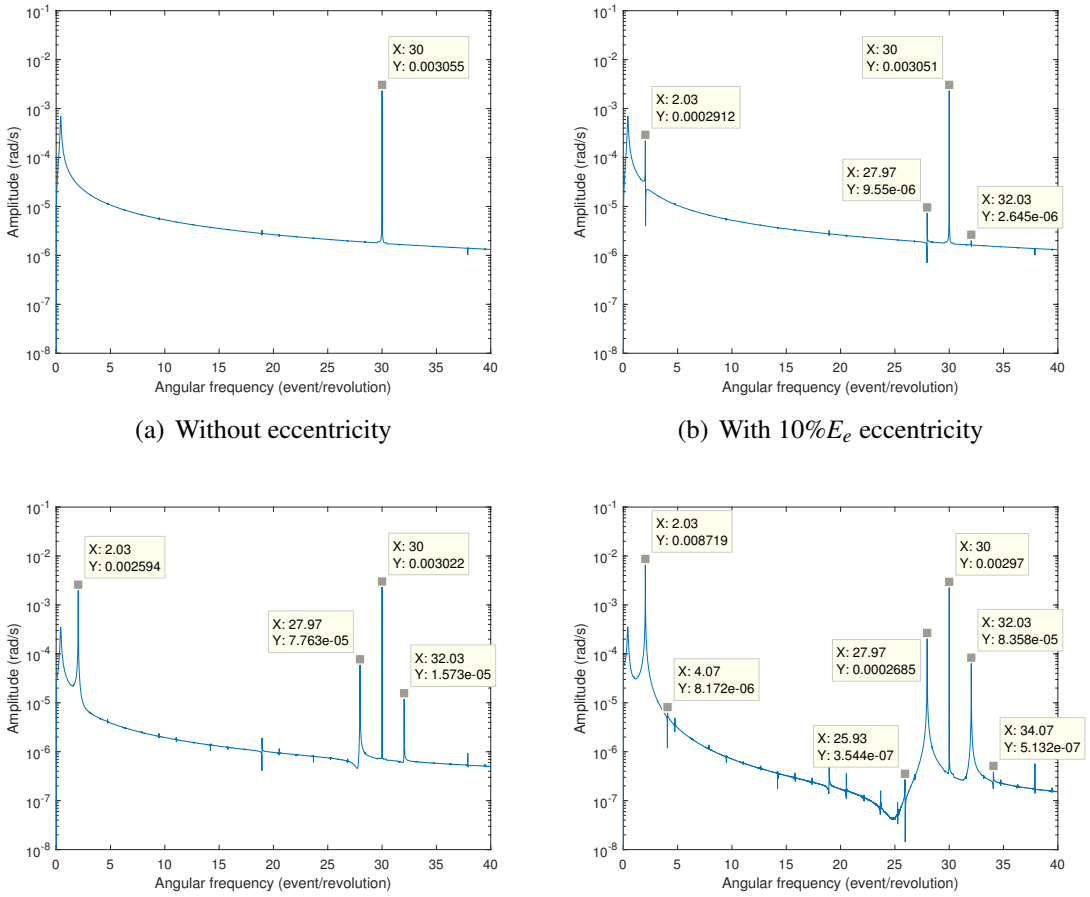

(a) Without eccentricity

(b) With 10%E_e eccentricity

(c) With 30%E_e eccentricity

(d) With 50%E_e eccentricity

Figure 2.45: Angular spectrum of instantaneous rotation speed at the rated operation state

2.11.1.2 With the rotordynamic motion

The simulation results generated under the rotordynamic motion are analyzed at the rated operating state in this section. The effects of two different kinds of rotordynamic motion: the mass unbalance excitation and the gravity on the mechanic structure are compared through the simulation results of UMP and the rotor center orbit.

The variation of UMP simulated in the case with only the mass unbalance excitation is illustrated in FIG.5.9(a). It can be seen that the two UMP force components due to the mass unbalance excitation are identical and fluctuate around zero with a small undulation. It is similar as a synchronous whirling motion and the rotor synchronous frequency 0.9974 ev/rev (which is close to 1 ev/rev) and its combinations with the slot harmonics are detected from the angular spectrum of F_{emx} in FIG.2.47(a). This situation is changed if the gravity effect of the whole rotor part is taken into account in the simulation as shown in FIG.5.9(b). Compared with the results in FIG.5.9(a), it is clearly that both the two UMP force components fluctuate with the similar waveform and they have almost

the same amplitude as that in the left case. However their average values are converged to respectively two different numbers displaced from zero. This is evidently due to the influence of the gravity. A rotor center displacement along the y-axis is introduced naturally in the structure by the gravity then this displacement will produce the similar UMP as the input static eccentricity did. This phenomena could be confirmed by the angular spectrum of F_{emx} shown in FIG.2.47(b), apart from the three frequencies associated with the mass unbalance excitation existed in FIG.5.9(a), the three characteristic frequencies referred to the static eccentricity mentioned before also appear in this case. The effects of the two kinds of rotordynamic motion on the system can be identified more directly from their rotor center orbit during the last shaft revolution displayed in FIG.2.48. Due to the mass unbalance excitation, the two rotor center orbits are both revealed as a circle. Under the effect of the gravity, the orbit center point is displaced toward to a point located on the negative vertical axis shown in FIG.5.10(b) from the origin point $(0,0)$ appeared in FIG.5.10(a).

It is concluded that the effect of the mass unbalance excitation can be treated as a rotor synchronous whirling motion while the influence of the gravity is equivalent to an input static eccentricity.

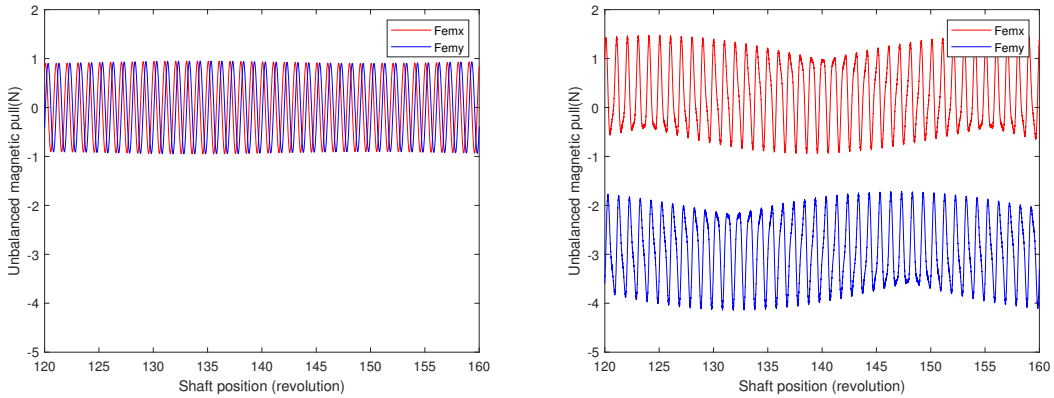

(a) With only the mass unbalance excitation

(b) With the mass unbalance excitation and the gravity

Figure 2.46: Variation of UMP under the rotordynamic motion at the rated operation state.

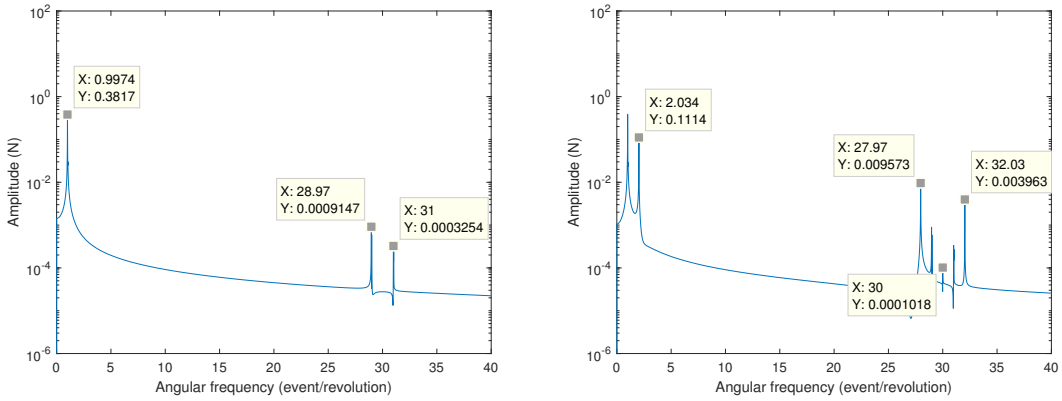

(a) With only the mass unbalance excitation

(b) With the mass unbalance excitation and the gravity

Figure 2.47: Angular spectrum of UMP x-axis force component under the rotordynamic motion at the rated operation state.

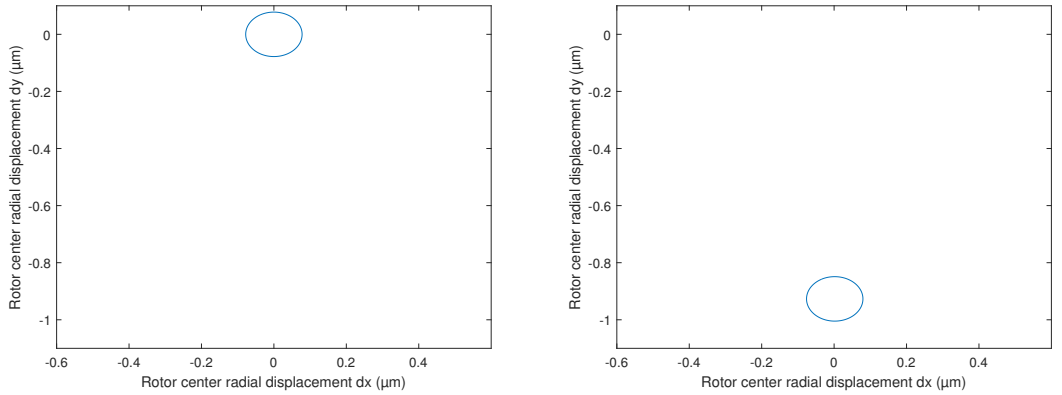

(a) With only the mass unbalance excitation

(b) With the mass unbalance excitation and the gravity

Figure 2.48: Rotor center orbit under the rotordynamic motion at the rated operation state.

2.11.2 Analysis in the non-stationary operation

Different from the simulations in the stationary operation, the non-stationary state is effectuated by applying a changing load torque on the structure. As mentioned in the previous section, a constant load torque is adopted to conduct a simulation at a given operating point from the motor characteristic curve in FIG.2.36(a). In this section, a load torque that increases linearly with the shaft revolution as shown in FIG.2.49(a) is set up in this

multiphysics model to perform respectively the simulation with $10\%E_e$ input eccentricity and the simulation with the mass unbalance excitation in the non-stationary operation.

2.11.2.1 With an input static eccentricity

Under the variable load torque, the simulation results about the variation of the electromagnetic torque, the instantaneous angular speed and the three-phase stator currents are illustrated separately in FIG.2.49(b), FIG.2.49(c) and FIG.2.49(d) as the function of the shaft position. The average value of the electromagnetic torque always equals to the applied load torque but meanwhile its fluctuation amplitude is increased gradually with the augmentation of the load torque due to the increase of the motor slip as explained in SEC.2.11.1.1. The average value of the instantaneous angular speed decreases and the amplitude of the stator phase currents increases due to the movement of the operating point according to the motor's characteristic curves from FIG.2.36.

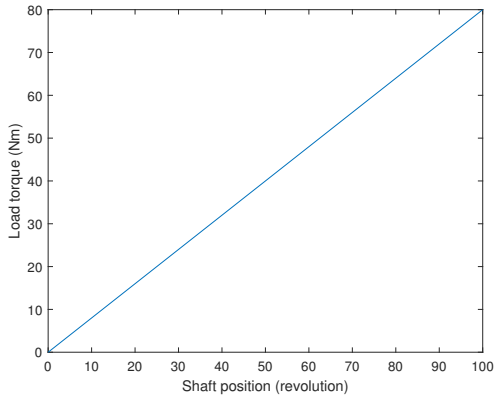

(a) Load torque

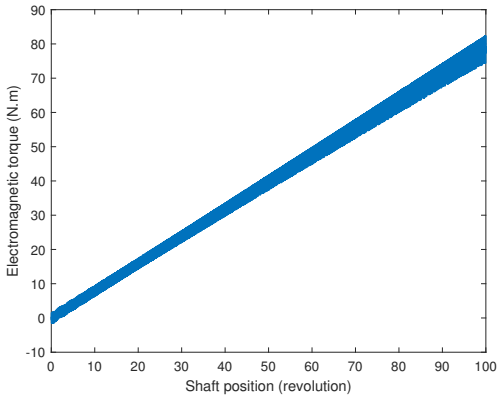

(b) Electromagnetic torque

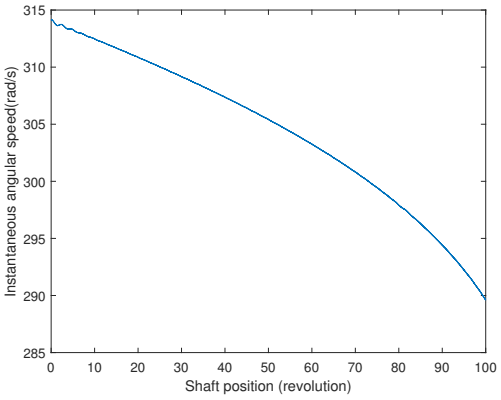

(c) Instananous angular speed

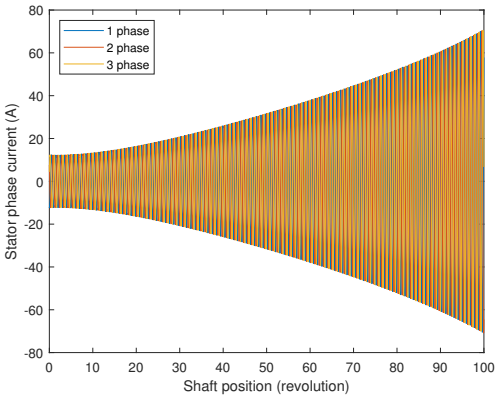

(d) Stator phase currents

Figure 2.49: Simulation results variation with the static eccentricity of $10\%E_e$ in non-stationary operating conditions

The increased fluctuation amplitude shown in the electromagnetic torque appears more evident in the generated UMP x-axis component displayed in Fig. 5.11(a). By applying a short-angle Fourier transform, its angular spectrogram is shown in Fig. 5.11(b). The four characteristic frequencies discussed in SEC.2.11.1.1 are identified clearly in the spectrogram of F_{emx}. With the increase of the motor slip, the amplitudes of each frequency components increased and some more harmonics about the $2f_s$ and their modulations with f_{sh} begin to appear in the case with the large motor slip (see arrows pointing parts in Fig. 5.11(b)) corresponding to the phenomenon presented in Fig. 2.41. It indicates that the same input eccentricity value will have more evident impact on the mechanical system at the operating point of a larger motor slip. In an other word, with the increase of the load torque, the generated UMP not only increases its magnitude but also induces more harmonics in the whole structure which potentially increases the risk of the resonance.

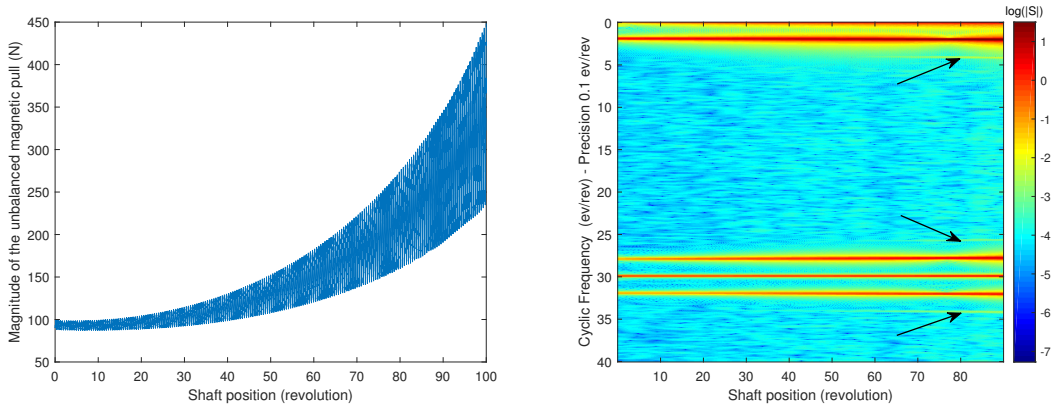

(a) Variation of UMP

(b) Short angle spectrum of UMP

Figure 2.50: UMP x-axis force component with the static eccentricity of $10\%E_e$ in non-stationary operating conditions

2.11.2.2 With the mass unbalance excitation

Most of the simulation results in the case with the mass unbalance excitation and driven by the same variable load torque have the similar global variation forms as described in the previous case so that they are not illustrated here to avoid the repeat. However, the variation of the simulated UMP is an exception as depicted in FIG.2.51(a). It is reasonable that the amplitude of UMP tends to decrease with the reduce of the rotation speed because the centrifugal effect produced by the mass unbalance excitation is proportional to the rotation speed and that's why the rotor synchronous frequency (1 ev/rev) and the two sideband frequencies about its combinations with the slot harmonics (30 ± 1 ev/rev) are recognized clearly in its angular spectrogram as shown in FIG.2.51(b). In addition, some strong undulations appear with the increase of the load torque. This could be explained by plotting the variation of UMP x-axis force component at three different operating points as depicted in FIG.2.52. These undulations appear evidently with the augmentation of

the load torque and meanwhile the angular period of the undulations reduce from 30 tr for the case with $T_r = 24.3$ Nm to 6 tr for the case with $T_r = 80$ Nm. Therefore in their angular spectrum from FIG.2.53, all three characteristic frequencies associated with the mass unbalance excitation discussed in FIG.2.47(a) appear in all three cases but more frequencies correspond to the modulations with the undulation frequencies can be also detected in the zoom parts from the case with the non-zero load torque. This reflects the interaction between the mechanical field and the electromagnetic field. The mass unbalance excitation produces an equivalent rotor synchronous whirling motion in the IM, there is no difference between the power supply synchronous speed and the rotor rotation speed in the case at no load so that there is no undulation in FIG.2.52(a). With the increase of the difference between the two speeds which is also called as the motor slip, a modulation phenomena begins to appear so that the undulations emerge in their waveforms and their frequencies increase with the increase of the motor slip.

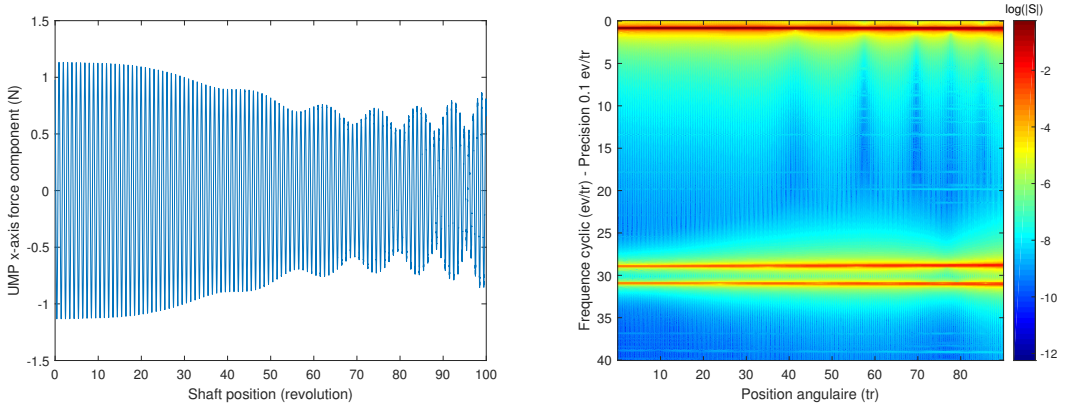

(a) Variation of UMP (b) Short angle spectrum of UMP

Figure 2.51: UMP x-axis force component in non-stationary operating conditions under the mass unbalance excitation

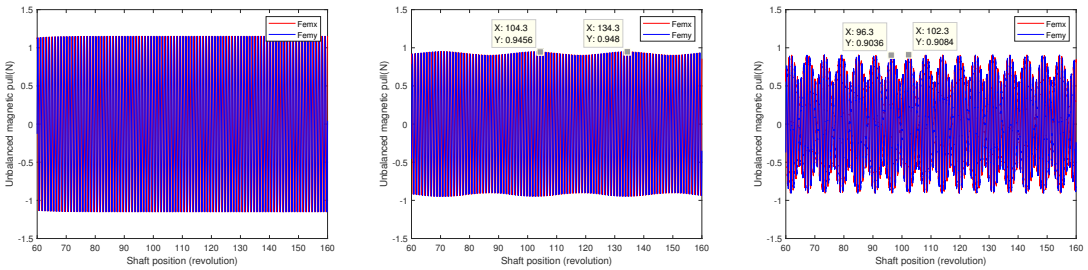

(a) $T_r = 0$ Nm (b) $T_r = 24.3$ Nm (c) $T_r = 80$ Nm

Figure 2.52: Variation of UMP x-axis force component at different operation states under the mass unbalance excitation.

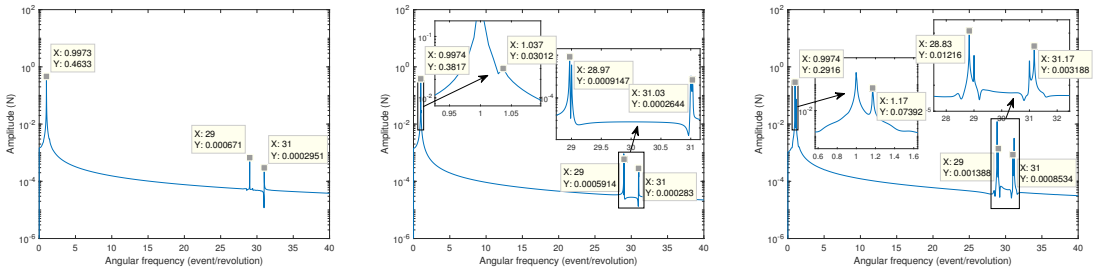

(a) $T_r = 0$ Nm (b) $T_r = 24.3$ Nm (c) $T_r = 80$ Nm

Figure 2.53: Angular spectrum of UMP x-axis component at different operation states under the mass unbalance excitation.

2.12 Conclusions

A multiphysics model with the strong electro-magneto-mechanical couplings about the IM has been established in this chapter. Three different physical fields in the electrical machine: the magnetic field, the electrical circuits and the mechanical structure are described in details by several algebraic or differential equations. The magnetic field is modeled in the frame of the mesh/nodal mixed PNM with all the permeances calculated according to the geometry of the actual machine. The air gap permeance is defined as the function of the rotor center rotational and transversal displacements in order to simulate the case with different rotor eccentricities. The reference IM is supplied by the three-phase voltage source in the Y connection and the two sets of electrical circuits in the stator winding and the rotor squirrel cage are represented by the traditional resistor-inductor circuits. The Faraday's law is adopted to combine the magnetic and the electric model. The modeling of the mechanical structure is based on the discretized Timoshenko beam theory. The mass unbalance excitation is added to analyze the rotor dynamic behavior in the IM. The electromagnetic forces (T_{em} and UMP) are calculated by applying the principle of virtual work method in the defined permeance network. Those three sub-models are coupled together to achieve the final multiphysics model of the IM.

The global differential equations of the proposed model are expressed in the form of state-space equations which can be solved in terms of two different state vectors. The one taking the magnetic phase currents as the state vector is called as phase current model while the other one solved as the function of the magnetic phase flux is named as phase flux model. Through the comparison about their solving expressions and simulation results, it confirms that the two models with different state vectors are basically identical but the phase flux model is both more efficient in the simulation and is ready to set up the magnetic saturation effect in the system. Hence the phase flux model is finally employed in the thesis.

An electromagnetic model (Model EM) without the coupling to the mechanical structure is extracted from the coupled model (Model EMM) in order to illustrate the importance of the electro-magneto-mechanical interaction and to be adopted in the validation of

the proposed model in the quasi-static regime. From the comparison about their simulation results at a certain operating point, it proves that the two models are equivalent in the case without the eccentricity or with a small eccentricity but once the large eccentricity is involved or at the operating point with a large load torque, the results from Model EMM is more accurate than those from Model EM. Due to the coupling with the mechanical structure, the proposed model is controlled by the external load torque to simulate only the operating points in the stable operating zone of the motor.

The proposed model is validated in the quasi-static regime through the comparison of the simulation results between Model EM and Model FEMM at the rated operating point and at all the operating points through the asynchronous motor characteristic curves.

Different simulation results from the proposed model are analyzed firstly in the stationary operation and then in the non-stationary operation with the rotor eccentricity either set up by the input static eccentricity or induced by the rotordynamic motion.

The simulations in the stationary operation with an input static eccentricity are performed in two cases. In the first case, from the simulation results with the same eccentricity value but at two different operating points, the offset angle of the resultant UMP from the narrowest air gap length is firstly discovered from the polar diagram of UMP. This is due to the effect of the equalizing currents induced in the rotor cage from the eccentricity which is in agreement with the reports from other literature. The slot effects in the system are then revealed by plotting the orbit of the rotor center. In the terms of the physical characteristics, it is demonstrated that the UMP generated at the operating point with a larger slip tends to fluctuate around the position of the set-up eccentricity with larger oscillations in the vertical direction. And then in their frequency analysis, several characteristic frequencies associated with the static eccentricities like the double supply frequency and its modulation with the rotor slot harmonics are identified from the angular spectrum of UMP which indicates the modulation between the angular and temporal phenomena. The same characteristic frequencies are also emerged in the spectrum of the electromagnetic torque to reflect that the rotor radial perturbation also influences its rotational movement. In the second case, by comparing the simulation results at the rated operating point but with three different eccentricity values, it is shown that the variations of UMP magnitudes and their offset angles increase linearly with the increase of the input eccentricity value. And at the same time, the undulations in the waveforms of the instantaneous rotation speed become more and more evident therefore more harmonics of the double supply frequency appear gradually in their spectrum. Those identified characteristic frequencies referred to the static eccentricity appear also in the spectrum of the rotation speed in the cases with eccentricities.

The simulations in the stationary operation with the rotor eccentricity induced by the rotordynamic motion are conducted under the mass unbalance excitation. The simulation results about the UMP and the rotor center orbit are compared between the cases with or without the rotor gravity. It can be concluded from the results that the effect of the mass unbalance excitation can be treated as a rotor synchronous whirling motion while the influence of the gravity is equivalent to an input static eccentricity.

The simulations in the non-stationary operation are performed naturally by applying

a linearly increased load torque. Through the analysis of the simulation results with the static eccentricity of $10\%E_e$, it implies that more harmonics about the double supply frequency will be induced in the system with the increase of the load torque which may potentially increases the risk of structural resonance. And the similar simulation under the mass unbalance excitation is studied to find out that the undulations due to the motor slip appear more evident in the waveform of the UMP with the increase of the load torque.

Overall, the proposed multiphysics model of the asynchronous machine based on angular approach is able to simulate its dynamic behavior in the case with different types of rotor eccentricity during the stationary and non-stationary operating conditions in a simple and natural way. Strong couplings of different physical fields inside of the electrical machine are highlighted from the analysis of different simulation results. The same model with multiphysics strong couplings is going to be developed about a PMSM in the next chapter for the dynamic performances analysis in the synchronous machine and to prepare for the study about the influence of different mechanical structures in CHAP.4.

Chapter 3

Permanent magnet synchronous motor modeling

Contents

3.1 Introduction

Permanent magnet synchronous motor (PMSM) is one of the most popular machine type in the synchronous electrical machine. As introduced in [170], the first PM excitation system was adopted in the electrical machines in the 19th century. The early applications in the DC commutator machines appeared with the usage of the simple ferrite PMs and Alnico PMs in 1932. And then with the development of the rare earth PMs, the PM brushless motors attracted more attention than the IMs due to their reliability in the steady-state performance and to their high power density. Afterwards the improvements of different electromechanical drive systems has extended the applications of PMSMs in the domain where the stable dynamic behavior and the wider operating range are of great interest.

The working principle of PMSMs is less complicated than IMs due to the difference in the rotor. They are the same both in the stator structure and in the mechanism of producing the rotational magnetic field in the stator. However in PMSMs since the PMs installed in the rotor have already established a magnetic field, there is no need to induce currents in the rotor part so as to generate another magnetic field attached to the rotor. Finally, the rotational magnetic field generated in the stator pulls the static magnetic field given by PMs in the rotor to move at the same speed and the electromagnetic torque is produced by the attraction between the two magnetic fields. As the name suggests, the synchronous motor has the same angular speed between the rotor and the stator rotating field so that the rotation speed of the synchronous motor (ω_r) is defined by the ratio of power supply frequency (f_s) to the number of pole pairs (P) in the steady-state.

$$\omega_r = \omega_s = \frac{2 \cdot \pi \cdot f_s}{P} \tag{3.1}$$

where the rotor speed is defined in " rad/s" which is also equal to the synchronous speed of the rotating magnetic field (ω_s) produced in the stator.

PMSMs are generally classified in two categories according to the magnet positions in the rotor as shown in FIG.3.1: the surface PM motors (SPM) and the interior PM motors (IPM) [39]. The SPM is divided into the projecting type and the insert type while the IPM is composed of the interior magnets with radial magnetization (RM-IPM) and those with tangential magnetization (TM-IPM). The RM-IPM illustrated in FIG.3.1(c) is chosen as the reference machine type since it is well protected from the centrifugal force when compared to the SPM and it doesn't need a magnetic isolation material between the rotor and the shaft in order to prevent the magnetic flux leakage comparing to the TM-IPM. Therefore, the synchronous machine studied in this thesis is a 4 poles, PMs embedded with radial magnetization synchronous motor. Its stator is equipped with a single layered, distributed 3-phase winding with 48 slots and its rotor is consisted with 8 PMs in the rectangle form. The main characteristic parameters of the motor can be consulted in APPENDIX.C.

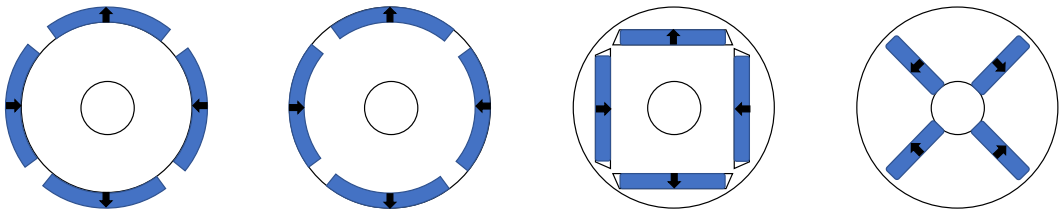

(a) SPM: Projecting type (b) SPM: Insert type (c) RM-IPM (d) TM-IPM

Figure 3.1: Different rotor configurations.

This chapter is dedicated to develop the proposed multiphysics model on the reference PMSM. Based on the model of the IM established in CHAP.2, the same pattern about modeling three sub-systems in the PMSM is repeated in this chapter from SEC.3.2 to SEC.3.8. In order to avoid the repetition, only the parts different from those in the model of the asynchronous machine are presented. Since the two types of the electrical machines have the same structure in the stator part, the magnetic field modeling among the SEC.3.2, SEC.3.3 and SEC.3.4 is focused on the description about the newly defined permeance network in the rotor part. And a new set of distributed concentric winding is introduced in SEC.3.4. Similar as before, the magnetic model is developed based on the mesh/nodal mixed PNM and its nodal based model is available in APPENDIX.B. However, the two models are both illustrated and compared in SEC.3.7 to explain the reason why the mixed model is better for setting up the magnetic saturation effect. Different from the series connected winding in the IM, SEC.3.6 presents the stator parallel winding supplied by the 3-phase current sources. Afterwards, the magnetic field and the electric circuits are coupled in SEC.3.7 and they are discussed respectively in the case with and without the magnetic saturation effect in order to set it up in the PMSM model. A customized mechanical structure about the reference PMSM is described in the multiphysics couplings from SEC.3.8 where the coupled and non-coupled models are compared to explain how to conduct the simulation in the PMSM model without the control system. The multiphysics model is validated by comparing with the identical model established in FEMM from SEC.3.9 where another equivalent model is created and is also validated in order to prepare for the later simulations in the non-stationary operation. Towards the end of the chapter, the identical model is firstly adopted to recognize the characteristic phenomena associated with the input static eccentricity in the stationary operation and then the equivalent model is employed to analyze the dynamic simulation results in the non-stationary operation under the mass unbalance excitation in SEC.3.10.

3.2 Permeance network mesh

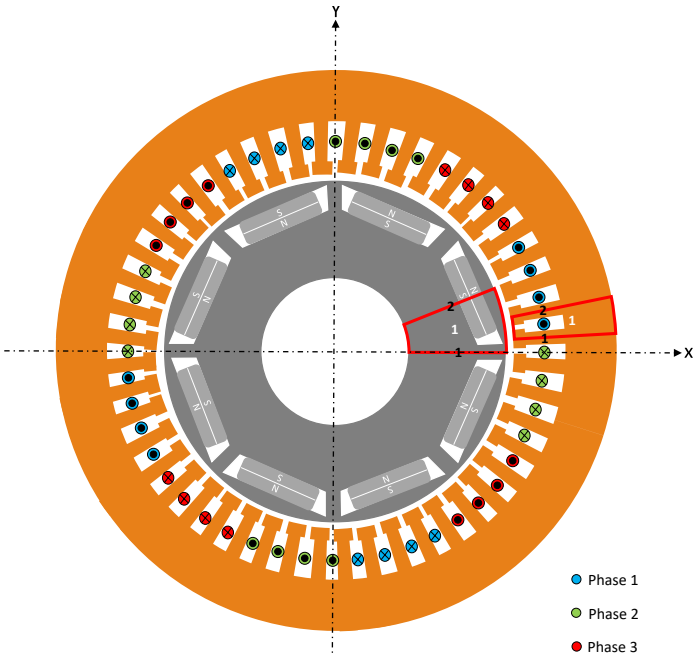

Figure 3.2: The cross sectional view of the reference PMSM.

The cross sectional view of the reference PMSM is illustrated in FIG.3.2. It has a similar structure in the stator part but a different topology in the rotor part when comparing with the IM described in the previous chapter. As before, a set of permeance network mesh has to be firstly realized in the whole section of the PMSM. One mesh of the permeance network in the stator and in the rotor are shown respectively in two red angular sectors from FIG.3.2 with the numbers on them to identify the order of different branches and meshes in the global network. The numbers in white are used to represent the order of the mesh (stator and rotor slots) and the black numbers are referred to orders of tooth branches. The orders of tangential branches in the yoke and air gap areas are correspond to each mesh order. In reference to the x-axis, the orders are counted in the anti-clock direction. The permeance network meshes in the stator are achieved in the same way as described in FIG.2.1(a) while those in the rotor part are determined according to the magnetic field distribution from the FEMM model. At the present stage, the whole rotor is discretized into eight meshes (equal to the number of the PMs) for the sake of the simplicity and each mesh is composed of four branches to represent separately two radial flux path which are considered as the rotor tooth located respectively at the PM part and at the radial iron bridge part and two tangential flux path via respectively the rotor yoke and another tangential iron bridge. Since there is no winding in the rotor part, no MMF will be generated in the rotor tooth branches. However according to [90], PMs can be modeled as an association of a MMF and a magnetic permeance in series. Therefore, the MMF sources in the rotor only exist in the rotor tooth branches with PMs. The magnetic flux

path in the air-gap are established between each pair of stator and rotor tooth branches in the same way as described before. The detailed information about how to calculate the newly defined active and passive elements in this permeance network are explained in the following two subsections.

3.2.1 Permeance (Reluctance) calculation

EQ.2.4 is adopted here to calculate the permeance value of each element. Since the PMs are placed inside the rotor of the electrical machine, this leads to two slender bar structures in the rotor iron core which are called respectively as " rotor tangential iron bridge" and " rotor radial iron bridge". As mentioned before, these two iron bridges are defined separately as two independent branches in the permeance network so that they are very sensitive to the magnetic saturation due to their special forms. Hence the magnetic saturation effect should be considered in the modeling of the reference PMSM. Actually, all the permeances in the iron core parts are possible to be affected by the magnetic saturation effect and this will be reflected in their permeability μ_k. In consideration of the magnetic saturation, their magnetic permeability values are no longer constant but vary as the function of the passed magnetic flux density $\mu_k(B_k)$ or about the magnetic field intensity of each branch $\mu_k(H_k)$. The air-gap permeances are considered as the parametrically nonlinear permeances so that they are not influenced directly by the magnetic saturation effect.

3.2.1.1 Iron core part permeances

The permeances in the iron core part are consisted of two parts respectively from the stator and the rotor. Since the reference PMSM has the similar structure for the stator sheet steel as used in the IM, those permeances in the stator part (P_{sy}, P_{st}, P_{sl}) are calculated in the same way as defined in EQ.2.5. Thus the attention should be paid to the description about the calculation of the permeances in the rotor part. A permeance network is plotted in the real sketch of the rotor sheet steal as illustrated in FIG.3.3. One mesh is marked in red with four different permeance elements located in four branches around. Those permeance elements in different colors are used to represent different magnetic flux travel paths in the rotor which are identified separately as: the light blue for the tangential iron bridge permeance in the rotor leakage branch P_{rl}, the blue for the radial iron bridge permeance in the rotor tooth branch P_{rtb}, the dark blue for the permeance in the rotor yoke branch P_{ry} and the gray for the PM permeance in the rotor tooth branch P_{rtm}. With the geometric dimensions displayed in FIG.3.3, those permeances could be calculated by simplifying them in the cuboid shapes as illustrated in EQ.3.2.

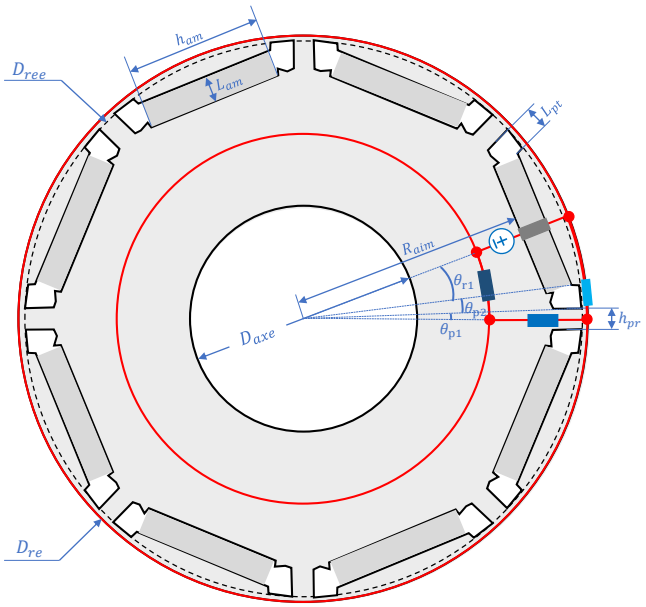

Figure 3.3: Permeance calculation in the rotor part

$$
\begin{aligned}
P_{rl} &= \frac{\mu_{ir} \cdot \left(\frac{D_{re}-D_{ree}}{2}\right) \cdot L_m}{L_{pt}} \\
P_{rtb} &= \frac{\mu_{ir} \cdot h_{pr} \cdot L_m}{\frac{D_{re}}{2} - R_{aim}} \\
P_{ry} &= \frac{\mu_{ir} \cdot \left(R_{aim} - \frac{D_{axe}}{2}\right) \cdot L_m}{\left(\frac{R_{aim}}{4} - \frac{D_{axe}}{2}\right) \cdot \frac{\pi}{8}} \\
P_{rtm} &= \frac{\mu_m \cdot h_{am} \cdot L_m}{L_{am}}
\end{aligned}
\tag{3.2}
$$

where μ_{ir} is the permeability of the iron core part, L_m is the core length as defined before and μ_m is the permeability of the PM material which is about 1.5 times of the vacuum permeability μ_0. All the geometric dimensions mentioned in EQ.3.2 can be extracted from the sketch of the rotor sheet steel. For the sake of simplicity in the later construction of the permeance network equations, the two set of permeance vectors from the rotor tooth branch $\{P_{rtb}\}$ and $\{P_{rtm}\}$ need to be combined together according to their order defined in

PNM from FIG.3.3 in order to form a new permeance vector $\{P_{rt}\}$ as depicted in EQ.3.3.

$$\{P_{rt}\}_{(2*n_m)*1} = \left\{\begin{array}{c} P_1^{rtb} \\ P_1^{rtm} \\ \hline P_2^{rtb} \\ P_2^{rtm} \\ \hline \vdots \\ \vdots \\ \hline P_{n_m}^{rtb} \\ P_{n_m}^{rtm} \end{array}\right\} = [MPP] \cdot \{P_{rtb}\} + [MPD] \cdot \{P_{rtm}\} \tag{3.3}$$

where $[MPP]$ and $[MPD]$ are two constant coefficient matrix composed of 0 and 1 with the dimension of $(2*n_m)*n_m$ to help to establish the new permeance vector.

3.2.1.2 Air gap permeances

The air gap permeances in the model of the PMSM are described in the same way as mentioned in the modeling of the IM in the previous chapter. EQ.2.6 is adopted here to define the air gap permeance between each pair of stator and rotor tooth (P_{ij}) in the case of the rotor eccentricity. The differences about the air gap permeances modeling between the two types of electrical motors reveal in three aspects. Firstly, due to the inhomogeneity of the rotor tooth width in PMSM, the air gap permeances should be calculated in two groups: one is between the stator tooth and the rotor magnet tooth $\{P_{i,l}^m\}$ and another is between the stator tooth and the rotor iron bridge tooth $\{P_{i,l}^b\}$ (where i and l are the integers referred to $i \subseteq [1, n_s]$ and $l \subseteq [1, n_m]$) as illustrated respectively in FIG.3.4 and FIG.3.5. Secondly, the maximum permeance coefficient between one pair of rotor and stator teeth P_{maxc} could be simplified since the rotor step-skew isn't taken into account in the reference PMSM. According to EQ.2.8, when $\beta = 0$ and the effective width of the stator tooth L_{ts} is smaller than those of the rotor tooth, the maximum permeance coefficient between one pair of rotor and stator teeth P_{maxc} could be expressed as:

$$P_{maxc} = \mu_0 \cdot L_m \cdot L_{\text{ts}} \tag{3.4}$$

Thirdly, since the rotor magnet tooth width is much wider than that of the stator tooth, the air gap permeance scale factor variation function $f_p(\theta_{ij})$ should be modified especially regarding to the definition about the two angle limits θ_1 and θ_2 from FIG.2.3.

The three sub-figures from FIG.3.4 and FIG.3.5 depict three important angular positions in the shape function of the air-gap permeances. (a), (b) and (c) are corresponding respectively to the point 1, 2 and 4 in FIG.2.3. In the group of the air-gap permeance between a certain pair of stator tooth and rotor magnet tooth, the first angular position θ_1 is determined when their right borders are radially aligned seeing FIG.3.4(b). Therefore,

$$\theta_1 = \theta_{r1} - \theta_{s1} \tag{3.5}$$

where θ_{r1} can be calculated from FIG.3.3 as shown in EQ.3.6:

$$\theta_{r1} = \arctan\left(\frac{h_{am}}{2 \cdot (R_{aim} + L_{am})}\right) \tag{3.6}$$

and θ_{s1} is the radian corresponding to the half of the stator top tooth width as defined in EQ.3.7:

$$\theta_{s1} = \frac{L_{stt}}{D_{si}} \tag{3.7}$$

where L_{stt} is the stator top tooth width and D_{si} is the stator inner diameter. According to the magnetic flux distribution from the simulation results of the corresponding FEMM model, the second angular position θ_2 is defined when the center line of the next rotor iron bridge tooth is aligned with that of the previous stator slot as illustrated in FIG.3.4(c). Therefore,

$$\theta_2 = \theta_{r2} + \theta_{s2} = \frac{\pi}{n_m} + \frac{\pi}{n_s} \tag{3.8}$$

where n_m is the number of the PMs.

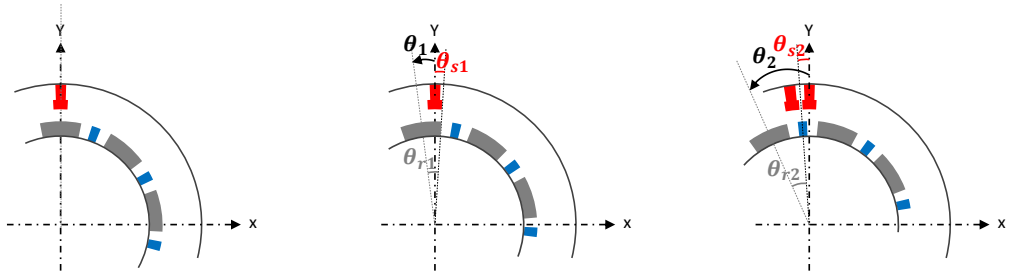

(a) (b) (c)

Figure 3.4: Evolution of air-gap permeance between a certain pair of stator tooth and rotor magnet tooth.

Similarly, in the group of the air-gap permeance between a certain pair of stator tooth and rotor iron bridge tooth, the first angular position is obtained as the difference between θ_{s1} and θ_{p1} as depicted in FIG.3.5(b):

$$\theta_1 = \theta_{s1} - \theta_{p1} \tag{3.9}$$

where θ_{p1} can be achieved from FIG.3.3 as shown in EQ.3.10:

$$\theta_{p1} = \arcsin\left(\frac{h_{pr}}{D_{ree}}\right) \tag{3.10}$$

However, different from FIG.3.4(c) the second angular position presented in FIG.3.5(c) is determined when the center axis of the stator and rotor slot part coincide with each other. Then:

$$\theta_2 = \theta_{p2} + \theta_{s2} = \theta_{p2} + \frac{\pi}{n_s} \tag{3.11}$$

where $\theta_{p2} = \frac{\pi}{n_m} - \theta_{r1} - \theta_{p1}$ according to FIG.3.3.

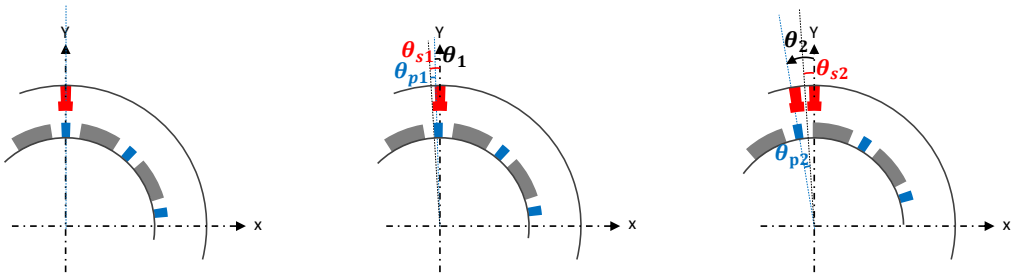

(a) (b) (c)

Figure 3.5: Evolution of air-gap permeance between a certain pair of stator tooth and rotor iron bridge tooth.

The complete air-gap permeance vector $\{P_{i,j}\}$ (where j is the integer referred to $j \subseteq [1, 2 * n_m]$) employed to establish the permeance network equations is made up by the assemblage of the two groups of air-gap permeances $\{P^m_{i,l}\}$ and $\{P^b_{i,l}\}$ defined before. According to the rotor tooth branch order defined in FIG.3.2, the complete air-gap permeance vector is depicted in EQ.3.12:

$$\{P_{i,j}\} = \begin{Bmatrix} P^b_{1,1} \\ P^m_{1,1} \\ P^b_{1,2} \\ P^m_{1,2} \\ \vdots \\ P^b_{1,n_m} \\ P^m_{1,n_m} \\ \hline P^b_{2,1} \\ P^m_{2,1} \\ \vdots \\ \vdots \\ \hline P^b_{n_m,1} \\ P^m_{n_m,1} \\ \vdots \\ \vdots \end{Bmatrix} = [MPYP] \cdot \{P^b_{i,l}\} + [MPY] \cdot \{P^m_{i,l}\} \tag{3.12}$$

where $[MPYP]$ and $[MPY]$ are the coefficient matrix made up with 0 and 1 with the dimension of $(2*n_m*n_s)*(n_m*n_s)$ to help to construct the complete permeance vector.

3.2.2 Magneto-motive force calculation

The MMF source in the PMSM is consisted of two parts: one is from the stator part which is induced by the stator slot currents as described in FIG.2.7 and another is from the rotor part which is brought by the buried PMs as depicted in FIG.3.3. They are going to be explained in the following two subsections.

3.2.2.1 MMF in the stator

Since the stator slot mesh structure of the PMSM model is identical to that of the IM, the relation between the MMF source $\{\mathcal{F}_{st}\}$ located in each stator tooth branch and their slot currents $\{i_{ss}\}$ is described in the same way as defined in EQ.2.26. The stator windings are connected in 4 parallel paths in each phase as illustrated in FIG.3.10. The currents in each parallel $\{i_{sv}\}$ are independent so that they could be chosen as the state vector for the electromagnetic subsystem. According to the slot currents order defined in FIG.3.8, they can be calculated from 12 stator parallel path currents:

$$\{i_{ss}\} = [S_{abc}] \cdot \{i_{sv}\} \tag{3.13}$$

where the winding current distribution matrix $[S_{abc}]$ is expressed in FIG.3.6 according to the stator winding topology.

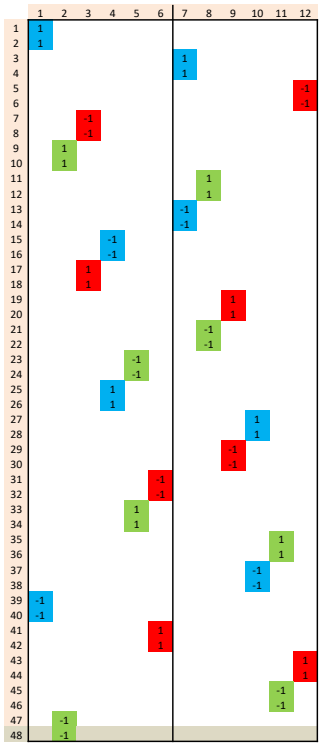

Figure 3.6: Winding current distribution matrix $[S_{abc}]$

Substitution EQ.3.13 into EQ.2.26 and considering about EQ.2.29, the relation between the stator MMF source and the stator path currents is finally achieved as:

$$\{\mathcal{F}_{st}\} = [Mfs] \cdot [ZZs] \cdot \{i_{sv}\} = [MZs] \cdot \{i_{sv}\} \tag{3.14}$$

Since the reference PMSM is powered directly by three phases currents (more details are available in SEC.3.6) and in each phase the sum of the four path currents equals to the corresponding phase current, only the first three path currents in each phase need to be conserved as the state vector $\{\tilde{i_{sv}}\}$ and the full stator path currents $\{i_{sv}\}$ can be expressed by the combination of the state vector and stator phase currents vector $\{I_{sp}\}$ as described in EQ.3.15.

$$\{i_{sv}\} = [MIS] \cdot \{\tilde{i_{sv}}\} + \{I_{sp}\} \tag{3.15}$$

where each term on the right side of the equal sign are expressed respectively as:

$$[MIS] = \begin{bmatrix} 1 & 0 & 0 & 0 & 0 & 0 & 0 & 0 & 0 \\ 0 & 1 & 0 & 0 & 0 & 0 & 0 & 0 & 0 \\ 0 & 0 & 1 & 0 & 0 & 0 & 0 & 0 & 0 \\ 0 & 0 & 0 & 1 & 0 & 0 & 0 & 0 & 0 \\ 0 & 0 & 0 & 0 & 1 & 0 & 0 & 0 & 0 \\ 0 & 0 & 0 & 0 & 0 & 1 & 0 & 0 & 0 \\ 0 & 0 & 0 & 0 & 0 & 0 & 1 & 0 & 0 \\ 0 & 0 & 0 & 0 & 0 & 0 & 0 & 1 & 0 \\ 0 & 0 & 0 & 0 & 0 & 0 & 0 & 0 & 1 \\ -1 & 0 & 0 & -1 & 0 & 0 & -1 & 0 & 0 \\ 0 & -1 & 0 & 0 & -1 & 0 & 0 & -1 & 0 \\ 0 & 0 & -1 & 0 & 0 & -1 & 0 & 0 & -1 \end{bmatrix}; \{\tilde{i_{sv}}\} = \begin{Bmatrix} i_{s1} \\ i_{s2} \\ i_{s3} \\ i_{s4} \\ i_{s5} \\ i_{s6} \\ i_{s7} \\ i_{s8} \\ i_{s9} \end{Bmatrix}; \{I_{sp}\} = \begin{Bmatrix} 0 \\ 0 \\ 0 \\ 0 \\ 0 \\ 0 \\ 0 \\ 0 \\ 0 \\ i_{sp1} \\ i_{sp2} \\ i_{sp3} \end{Bmatrix} \tag{3.16}$$

Furthermore, in order to create a matrix for setting up the magnetic saturation effect in SEC.3.7.2, the input power source $\{I_{sp}\}$ should be moved to the right side of the equal sign, then the full stator path currents need to be represented by the combination of the state vector $\{\tilde{i_{sv}}\}$ and the rest part of the path currents $\{\tilde{i_{svs}}\}$:

$$\{i_{sv}\} = [M1] \cdot \{\tilde{i_{sv}}\} + [M2] \cdot \{\tilde{i_{svs}}\} \tag{3.17}$$

where the two transformation matrix $[M1], [M2]$ and the rest of the stator path currents vector $\{\tilde{i_{svs}}\}$ are expressed as:

$$[M1]_{(12*9)} = \begin{bmatrix} [I]_{(9*9)} \\ [0]_{(3*9)} \end{bmatrix}; [M2]_{(12*3)} = \begin{bmatrix} [0]_{(9*3)} \\ [I]_{(3*3)} \end{bmatrix}; \{\tilde{i_{svs}}\} = \begin{Bmatrix} i_{s10} \\ i_{s11} \\ i_{s12} \end{Bmatrix} \tag{3.18}$$

with the identity matrix $[I]$.

3.2.2.2 MMF in the rotor

Since the MMF source in the rotor are provided directly by the buried PMs, $\{\mathcal{F}_{rt}\}$ is considered as a constant MMF vector according to the arrangement of the PMs in the

rotor from FIG.3.2.

$$\{\mathcal{F}_{rt}\} = \begin{Bmatrix} 0 \\ -\mathcal{F}_m \\ \hline 0 \\ -\mathcal{F}_m \\ \hline 0 \\ \mathcal{F}_m \\ \hline 0 \\ \mathcal{F}_m \\ \hline 0 \\ -\mathcal{F}_m \\ \hline 0 \\ -\mathcal{F}_m \\ \hline 0 \\ \mathcal{F}_m \\ \hline 0 \\ \mathcal{F}_m \end{Bmatrix} \tag{3.19}$$

where the different signs represent different magnetic orientations of the PMs and the MMF value $\mathcal{F}_m$ given by each PMs can be calculated according to the residual flux density B_r of each magnet as illustrated in EQ.3.20.

$$\begin{cases} H_c = \dfrac{B_r}{\mu_m} \\ \mathcal{F}_m = H_c \cdot L_{am} \end{cases} \tag{3.20}$$

where H_c is the coercive force if the magnet induction curve of the PM is considered to be linear and L_{am} is the thickness of the PM which can be achieved from FIG.3.3.

3.3 Permeance network equations

Similar as the discussion in the previous chapter, the permeance network equations to describe the relation between the chosen unknowns and the defined MMF source are established in the PMSM model by applying different Kirchhoff laws. Comparing with the descriptions in SEC.2.3, the identical parts are not repeated for the sake of the simplicity and only the variated parts are presented in the following subsection.

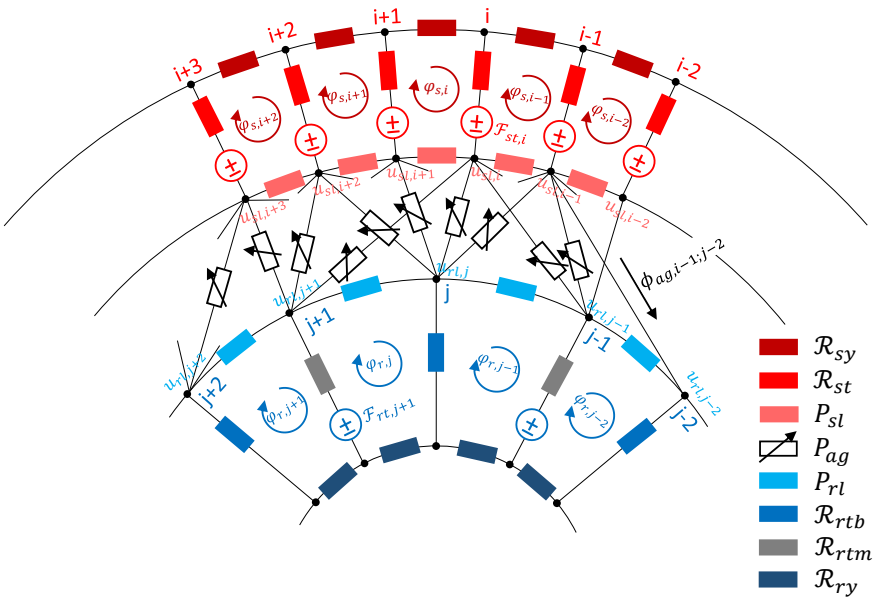

Figure 3.7: Nodal and mesh mixed based PNM for the embedded PMSM

A PNM established in the mesh/nodal mixed model about the reference PMSM is depicted in FIG.3.7. As discussed in the previous section, if the two reluctances vectors in the rotor tooth branch $\{\mathcal{R}_{rtb}\}$ and $\{\mathcal{R}_{rtm}\}$ are merged as the same vector $\{\mathcal{R}_{rt}\}$ as defined in EQ.3.3, the similar deduction process to achieve the permeance network equations in four different parts of the motor's cross section as presented in SEC.2.3 could be reused by applying some corresponding modifications mentioned in the following.

About the mesh k in the stator iron core part: By substituting EQ.3.14 into EQ.2.34, one obtains:

$$[\mathcal{R}_{11}]\cdot\{\phi_s\}+[\mathcal{R}_{13}]\cdot\{u_{sl}\}+[\mathcal{R}_{15}]\cdot[MZs]\cdot\{i_{sv}\}=\{0\}_{n_s*1} \tag{3.21}$$

Since $[\mathcal{R}_{15}]$ is a constant coefficient matrix as defined in EQ.2.21, the linear and nonlinear equations are identical in the mixed model which can be obtained by substitution EQ.3.15 into EQ.3.21:

$$[\mathcal{R}_{11}]\cdot\{\phi_s\}+[\mathcal{R}_{13}]\cdot\{u_{sl}\}+[\mathcal{R}_{15}]\cdot[MZs]\cdot[MIs]\cdot\{\tilde{i_{sv}}\}=-[\mathcal{R}_{15}]\cdot[MZs]\cdot\{I_{sp}\} \tag{3.22}$$

About the mesh k in the rotor iron core part: With the substitution of EQ.3.19 into EQ.2.38, since MMF vector in the rotor part $\{\mathcal{F}_{rt}\}$ and the coefficient matrix $[\mathcal{R}_{25}]$ are constant, EQ.2.38 is transformed into EQ.3.23 for the PMSM model.

$$[\mathcal{R}_{22}]\cdot\{\phi_r\}+[\mathcal{R}_{24}]\cdot\{u_{rl}\}=-[\mathcal{R}_{25}]\cdot\{\mathcal{F}_{rt}\} \tag{3.23}$$

Assemblage of the permeance network equations: Since there is no terms associated with MMF sources appeared in the equations deduced from **the stator and rotor leakage circle**, EQ.2.42 and EQ.2.46 are adopted directly to create the complete permeance network equations in the mesh/nodal mixed model. Therefore, the relation between the magnetic loop flux in iron core part with the magnetic node potentials from the rotor and stator leakage region $\{\phi u_{sr}\}$ and the stator path currents $\{\tilde{i_{sv}}\}$ is finally defined in EQ.3.24.

$$[Ybus]\cdot\{\phi u_{sr}\}-[AFT]\cdot\{\tilde{i_{sv}}\}=\{IFIR\}_{(2n_s+2n_r-1)*1} \tag{3.24}$$

where $[Ybus]$ and $\{\phi u_{sr}\}$ are available separately in EQ.2.49 and EQ.2.51 while the coefficient matrix $[AFT]$ and the vector $\{IFIR\}$ are defined respectively as followings:

$$[AFT]=\begin{bmatrix}-([\mathcal{R}_{15}]\cdot[MZs]\cdot[MIs])_{n_s*(n_{ph}*(n_v-1))}\\ [0]_{n_r*(n_{ph}*(n_v-1))}\\ [0]_{n_s*(n_{ph}*(n_v-1))}\\ [0]_{(n_r-1)*(n_{ph}*(n_v-1))}\end{bmatrix} \tag{3.25}$$

$$\{IFIR\}=\begin{Bmatrix}-([\mathcal{R}_{15}]\cdot[MZs]\cdot\{I_{sp}\})_{n_s*1}\\ -([\mathcal{R}_{25}]\cdot\{\mathcal{F}_{rt}\})_{n_r*1}\\ \{0\}_{n_s*1}\\ \{0\}_{(n_r-1)*1}\end{Bmatrix} \tag{3.26}$$

3.4 Flux linkage equations

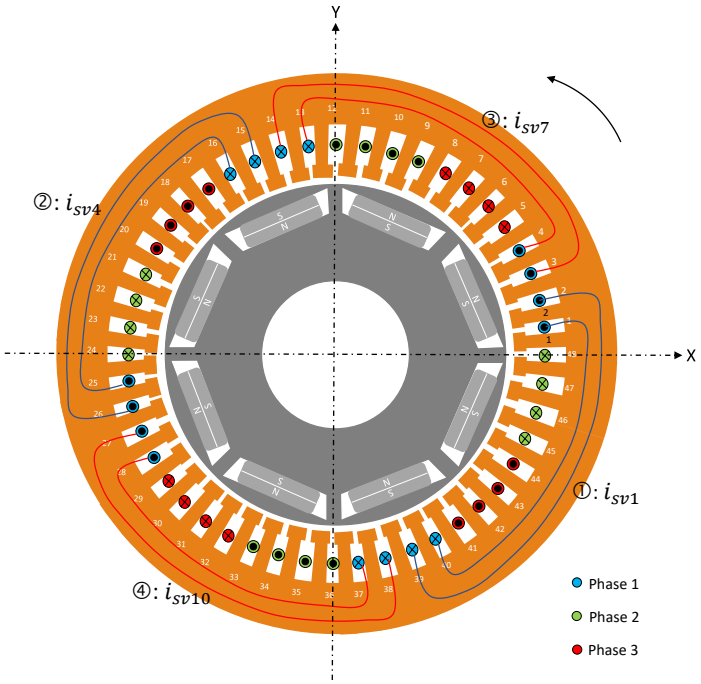

Figure 3.8: Single concentric winding connection in the first phase of the stator

Since the stator windings are connected in 4 parallel paths in each phases and there is no winding in the rotor part, the flux linkage equations established in the model of the reference PMSM are introduced to calculate the magnetic flux in each path of the stator $\{\phi_{sv}\}$ from those in each active stator tooth branches $\{\phi_{st}\}$. Different from the winding connection realized in the IM, a single concentric winding connection is employed in the reference PMSM. Eight coils in each phase are constructed by connecting two conductors located in two slots as illustrated in FIG.3.8. Two concentric coils are joined together to become a stator path and finally the four paths in each phase are connected in parallel as shown in FIG.3.10 from SEC.3.6.1. Therefore, EQ.2.52 is adopted to describe the relation between the magnetic flux in the stator tooth branches $\{\phi_{st}\}$ and the magnetic flux in each coil $\{\phi_c\}$. The order of each coil is numerated by the order of the path defined in FIG.3.10. The new transformation matrix $[Mcf]$ for the PMSM is organized in FIG.3.9(a) according to the arrangement of the stator teeth covered by each coil. It should be noted that the four path coils are marked in two colors in FIG.3.8 according to their different currents circulating directions where the red ones are defined as positive while the blue ones are considered as negative and these are reflected in the matrix $[Mcf]$. The relation between the magnetic flux in each stator path $\{\phi_{sv}\}$ and the magnetic flux in each

coil $\{\phi_c\}$ is described by modifying EQ.2.53 into EQ.3.27.

$$\{\phi_{sv}\} = [Mpf] \cdot \{\phi_c\} \tag{3.27}$$

with the new matrix $[Mpf]$ arranged in FIG.3.9(b). Substitution EQ.2.52 into EQ.3.27, the relation between the magnetic path flux and magnetic tooth flux is finally expressed as:

$$\{\phi_{sv}\} = [ww] \cdot \{\phi_{st}\} \tag{3.28}$$

where the matrix $[ww] = [Mpf] \cdot [Mcf]$ as defined before.

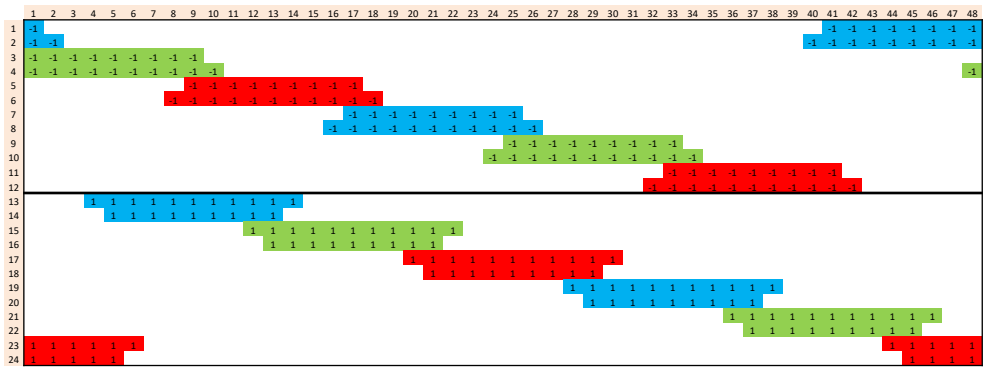

(a) $[Mcf]$

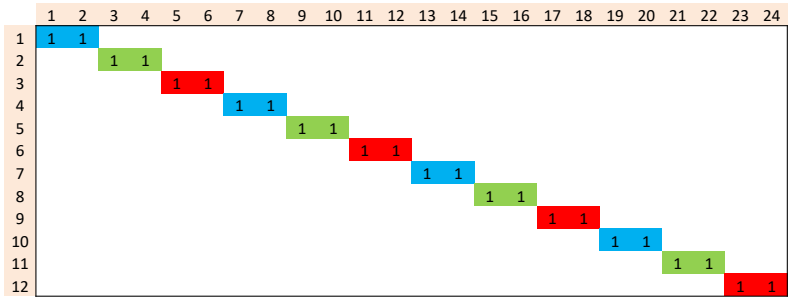

(b) $[Mpf]$

Figure 3.9: Winding matrix distribution about a single stacked winding connection

In the mesh/nodal mixed model, the magnetic tooth flux are calculated from the magnetic loop flux as described in EQ.2.60. Since the windings only exist in the stator part for the PMSM, the stator magnetic loop flux $\{\phi_s\}$ are achieved as:

$$\{\phi_s\} = [Mphis] \cdot \{\phi u_{sr}\} \tag{3.29}$$

where the transformation matrix $[Mphis]$ is made up with the identity matrix $[I]$:

$$[Mphis] = \begin{bmatrix} [I]_{(n_s * n_s)} & [0]_{(n_s * (n_s + 2 * n_r - 1))} \end{bmatrix} \tag{3.30}$$

Substitution EQ.3.29 into the first equations from EQ.2.60 and replacing the magnetic tooth flux by the relation defined in EQ.3.28, one obtains:

$$\{\phi_{sv}\} = [ww] \cdot [\mathcal{R}_{31}] \cdot [Mphis] \cdot \{\phi u_{sr}\} = [WRM] \cdot \{\phi u_{sr}\} \tag{3.31}$$

where the product of three constant coefficient matrix $[ww] \cdot [\mathcal{R}_{31}] \cdot [Mphis]$ is merged into the matrix $[WRM]$.

3.5 Augmented magnetic equations

As mentioned in the previous chapter, in order to create a set of magnetic equations to describe completely the whole magnetic model of the electrical machine, the permeance network equations and the flux linkage equations deduced in the previous two sections are combined together in this section. These augmented magnetic equations are often used to describe the behavior of the magnetic field at each moment with a set of given unknowns.

Two sets of equations described separately in EQ.3.24 and EQ.3.31 are put in together to form the augmented magnetic equations for the mesh/nodal mixed model which is organized as:

$$\begin{bmatrix} [Ybus] & -[AFT] \\ [WRM] & [0] \end{bmatrix} \cdot \begin{Bmatrix} \{\phi u_{sr}\} \\ \{\tilde{i_{sv}}\} \end{Bmatrix} = \begin{Bmatrix} \{IFIR\}_{(2n_s + 2n_r - 1) * 1} \\ \{\phi_{sv}\}_{(n_{np} * n_v) * 1} \end{Bmatrix} \tag{3.32}$$

Furthermore, by eliminating the vector $\{\phi u_{sr}\}$ in EQ.3.32, the direct relation between the path currents $\{\tilde{i_{sv}}\}$ and the magnetic path flux $\{\phi_{sv}\}$ is revealed as:

$$[WRM] \cdot [Ybus]^{-1} \cdot (\{IFIR\} + [AFT] \cdot \{\tilde{i_{sv}}\}) = \{\phi_{sv}\} \tag{3.33}$$

3.6 Electrical differential equations

Different from the IM, there is only one set of electric circuit in the reference PMSM. It is the stator windings installed in each stator slots and connected to the outside power supply. It is also modeled by the traditional resistor-inductor circuit by neglecting the leakage inductance associated with the magnetic leakage flux through the motor's winding part.

3.6.1 Current-Fed Machine

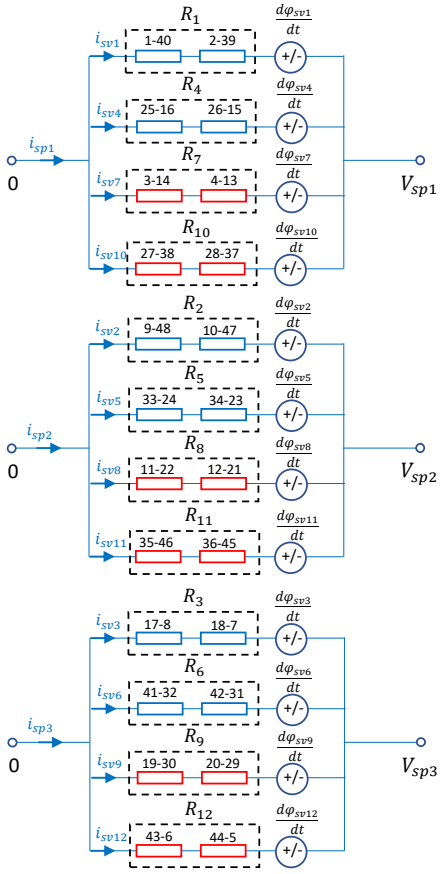

Figure 3.10: Stator winding connections in each phase

The synchronous motor is usually powered by the current source which means that instead of the three-phase voltages ($V_{sp1}, V_{sp2}, V_{sp3}$), the three-phase currents ($i_{sp1}, i_{sp2}, i_{sp3}$) are considered as the input in the PMSM model. If the power supply is connected in Wye connection as shown in FIG.2.13(a), the stator winding connections in each phase with four parallel paths are illustrated in FIG.3.10. The input three-phase stator currents are supposed to be perfect and vary in a sinusoidal wave as described in EQ.3.34:

$$\begin{cases} \vec{i_{sp1}} = \hat{i_{sp}} \cdot cos(\omega_s \cdot t) = \hat{i_{sp}} \cdot cos(\theta_r \cdot P) \\ \vec{i_{sp2}} = \hat{i_{sp}} \cdot cos(\omega_s \cdot t - \frac{2\pi}{3}) = \hat{i_{sp}} \cdot cos(\theta_r \cdot P - \frac{2\pi}{3}) \\ \vec{i_{sp3}} = \hat{i_{sp}} \cdot cos(\omega_s \cdot t - \frac{4\pi}{3}) = \hat{i_{sp}} \cdot cos(\theta_r \cdot P - \frac{4\pi}{3}) \end{cases} \tag{3.34}$$

where the $\hat{i_{sp}}$ is the peak value of the phase currents which equals to its $\sqrt{2}$ times RMS value and the ω_s is the supply frequency. The electrical rotation angle of the stator mag-

netic rotation field ($\omega_s \cdot t$) is replaced by the mechanical rotation angle of the shaft multiplied by the pole pair number ($\theta_r \cdot P$) in order to fix the torque angle ψ so as to perform the simulation at a certain operating point. The torque angle is generally defined for the synchronous motor to describe the electrical angle between the rotor flux and the stator flux [171]. It should be noted that the rotor flux axis always lags the stator axis by the torque angle ψ in the synchronous motor. As illustrated in FIG.3.11, the mechanical torque angle ψ_m in the initial state for the reference PMSM is identified in the motor's section. It is defined as the angle between the rotor flux axis ($+d$) and the stator flux axis (i_{sp1}) in one pair of pole from FIG.3.11(b) since the stator resultant flux axis at the beginning (when $t = 0$) is along the direction of the first phase current i_{sp1} as shown in FIG.3.11(a). Thus in this case the torque angle is calculated as:

$$\psi = \psi_m \cdot P = 18.75^\circ \cdot 2 = 37.5^\circ \tag{3.35}$$

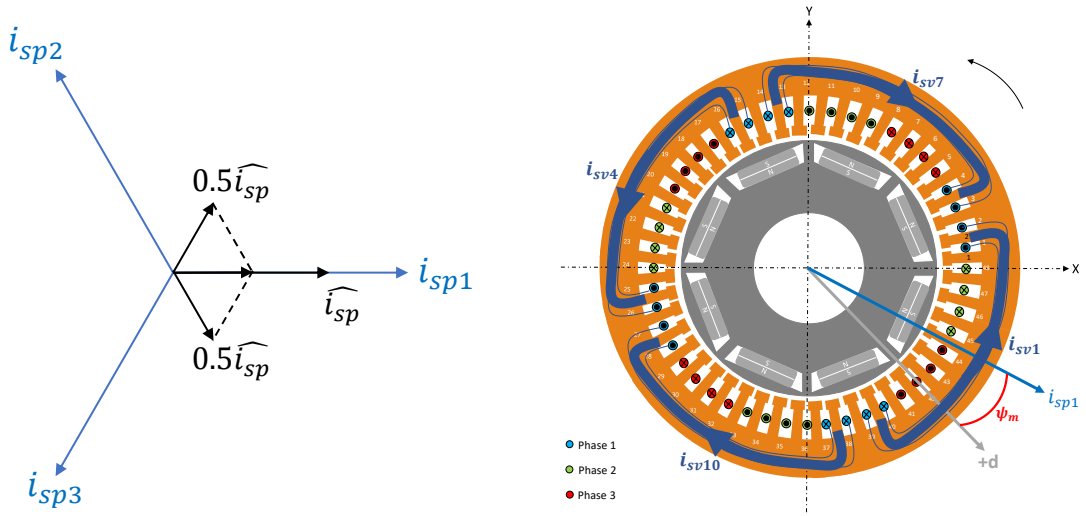

(a) Stator resultant flux axis

(b) Torque angle in the motor's cross section

Figure 3.11: Identification of the torque angle in the reference PMSM model in the initial state.

For the sake of the simplicity, if the current position of the rotor part in FIG.3.11(b) is assumed to be the reference position and the anticlockwise direction is considered as positive then the other initial rotor angular position θ_{r0} with respect to this specified reference position can be used to represent the torque angle so as to indicate different operation points in the further study.

According to the electric circuits in phase 1 illustrated in FIG.3.10, a set of four equa-

tions could be achieved in EQ.3.36

$$\begin{cases} i_{sv1} \cdot R_1 + \dfrac{d\phi_{sv1}}{dt} = V_{sp1} \\ i_{sv4} \cdot R_4 + \dfrac{d\phi_{sv4}}{dt} = V_{sp1} \\ i_{sv7} \cdot R_7 + \dfrac{d\phi_{sv7}}{dt} = V_{sp1} \\ i_{sv10} \cdot R_{10} + \dfrac{d\phi_{sv10}}{dt} = V_{sp1} \end{cases} \tag{3.36}$$

Since the synchronous motor is supplied directly by the three-phase currents, the first phase voltage V_{sp1} should be eliminated from EQ.3.36 by making the four equations subtract each other in turns. If the resistances of each path are considered to be identical as $R_1 = R_4 = R_7 = R_{10} = R_{sv}$, one obtains:

$$\begin{cases} (i_{sv1} - i_{sv4}) \cdot R_{sv} + \dfrac{d(\phi_{sv1} - \phi_{sv4})}{dt} = 0 \\ (i_{sv4} - i_{sv7}) \cdot R_{sv} + \dfrac{d(\phi_{sv4} - \phi_{sv7})}{dt} = 0 \\ (i_{sv7} - i_{sv10}) \cdot R_{sv} + \dfrac{d(\phi_{sv7} - \phi_{sv10})}{dt} = 0 \end{cases} \tag{3.37}$$

Considering that the sum of the four path currents equal to the first phase current, the current in the fourth path can be expressed by the phase current and the rest three path currents in EQ.3.38.

$$i_{sv10} = i_{sp1} - i_{sv1} - i_{sv4} - i_{sv7} \tag{3.38}$$

Substitution EQ.3.38 into the third equation from EQ.3.37 and represent the difference of two path flux by their corresponding flux difference vector $\{\Delta\phi_{sv}\}$, EQ.3.37 is transformed into EQ.3.39 which is expressed in the matrix format as:

$$\frac{d}{dt}\begin{Bmatrix} \Delta\phi_{sv1} \\ \Delta\phi_{sv4} \\ \Delta\phi_{sv7} \end{Bmatrix} = \begin{Bmatrix} 0 \\ 0 \\ R_{sv} \cdot i_{sp1} \end{Bmatrix} - \begin{bmatrix} R_{sv} & -R_{sv} & 0 \\ 0 & R_{sv} & R_{sv} \\ R_{sv} & R_{sv} & 2R_{sv} \end{bmatrix} \cdot \begin{Bmatrix} i_{sv1} \\ i_{sv4} \\ i_{sv7} \end{Bmatrix} \tag{3.39}$$

The similar equations like EQ.3.39 about the electric circuits in the other two phases from FIG.3.10 are deduced in the same way. By combining the three sets of equations together in the defined path order, the global differential equations to describe the relation between the magnetic path flux difference $\{\Delta\phi_{sv}\}$ and the modified stator path currents $\{\tilde{i_{sv}}\}$ are expressed in EQ.3.40.

$$\frac{d\{\Delta\phi_{sv}\}}{dt} = [R_{s1}] \cdot \{\tilde{I_{sp}}\} - [R_{s2}] \cdot \{\tilde{i_{sv}}\} \tag{3.40}$$

where the vector of the magnetic flux difference between each two path $\{\Delta\phi_{sv}\}$ can be calculated from the magnetic flux in each path $\{\phi_{sv}\}$.

$$\{\Delta\phi_{sv}\} = [MFI] \cdot \{\phi_{sv}\} \tag{3.41}$$

with the transformation matrix $[MFI]$ organized as:

$$[MFI] = \begin{bmatrix} 1 & 0 & 0 & -1 & 0 & 0 & 0 & 0 & 0 & 0 & 0 & 0 \\ 0 & 1 & 0 & 0 & -1 & 0 & 0 & 0 & 0 & 0 & 0 & 0 \\ 0 & 0 & 1 & 0 & 0 & -1 & 0 & 0 & 0 & 0 & 0 & 0 \\ 0 & 0 & 0 & 1 & 0 & 0 & -1 & 0 & 0 & 0 & 0 & 0 \\ 0 & 0 & 0 & 0 & 1 & 0 & 0 & -1 & 0 & 0 & 0 & 0 \\ 0 & 0 & 0 & 0 & 0 & 1 & 0 & 0 & -1 & 0 & 0 & 0 \\ 0 & 0 & 0 & 0 & 0 & 0 & 1 & 0 & 0 & -1 & 0 & 0 \\ 0 & 0 & 0 & 0 & 0 & 0 & 0 & 1 & 0 & 0 & -1 & 0 \\ 0 & 0 & 0 & 0 & 0 & 0 & 0 & 0 & 1 & 0 & 0 & -1 \end{bmatrix} \tag{3.42}$$

And the other terms in EQ.3.40 are respectively defined as followings:

$$[R_{s1}] = R_{sv} \cdot * [I]_{(n_{ph} * (n_v - 1)) * (n_{ph} * (n_v - 1))};$$

$$\{\tilde{I_{sp}}\} = \begin{Bmatrix} 0 \\ 0 \\ 0 \\ 0 \\ 0 \\ 0 \\ i_{sp1} \\ i_{sp2} \\ i_{sp3} \end{Bmatrix}; [R_{s2}] = \begin{bmatrix} R_{sv} & 0 & 0 & -R_{sv} & 0 & 0 & 0 & 0 & 0 \\ 0 & R_{sv} & 0 & 0 & -R_{sv} & 0 & 0 & 0 & 0 \\ 0 & 0 & R_{sv} & 0 & 0 & -R_{sv} & 0 & 0 & 0 \\ 0 & 0 & 0 & R_{sv} & 0 & 0 & -R_{sv} & 0 & 0 \\ 0 & 0 & 0 & 0 & R_{sv} & 0 & 0 & -R_{sv} & 0 \\ 0 & 0 & 0 & 0 & 0 & R_{sv} & 0 & 0 & -R_{sv} \\ R_{sv} & 0 & 0 & R_{sv} & 0 & 0 & 2 * R_{sv} & 0 & 0 \\ 0 & R_{sv} & 0 & 0 & R_{sv} & 0 & 0 & 2 * R_{sv} & 0 \\ 0 & 0 & R_{sv} & 0 & 0 & R_{sv} & 0 & 0 & 2 * R_{sv} \end{bmatrix} \tag{3.43}$$

3.7 Couplings between the electromagnetic fields

The geometric relationship between the stator path currents and the magnetic path flux is deduced from the augmented magnetic equations while their dynamic behaviors are described from the electrical differential equations, therefore the couplings between the electromagnetic fields are achieved by combining the algebraic equations from the magnetic field with the differential equations from the electric field. The detailed coupling process is discussed in the cases with and without the magnetic saturation effect in the following subsections.

3.7.1 In the case without magnetic saturation effect

Since the magnetic saturation effect in the iron core part is not taken into account, all the matrices associated with the permeances are considered to be constant at each moment and the augmented magnetic equations deduced in EQ.B.27 for the nodal based model and in EQ.3.32 for the mesh/nodal mixed model are assumed to be a set of linear algebraic equations which can be solved directly by inversing the global coefficient matrix. The

conventional method to deal with the electromagnetic coupling in the linear model is to express the stator path current vector as the function of the magnetic flux vector and substitute it in the differential equations in order to unify the state vector.

3.7.1.1 Nodal based model

By substituting EQ.B.28 into EQ.3.41, one obtains:

$$\begin{aligned}\{\tilde{i_{sv}}\} = &\left([MFI]\cdot([HPP]\cdot[PnodU]^{-1}\cdot[HPT]+[PnodV])\right)^{-1}\\ &\cdot\left(\{\Delta\phi_{sv}\}-[MFI]\cdot[HPP]\cdot[PnodU]^{-1}\cdot\{IFI\}+[MFI]\cdot[ww]\cdot[P_{12}]\cdot[MZs]\cdot\{I_{sp}\}\right)\end{aligned} \tag{3.44}$$

According to the discussion in SEC.2.7.3, the magnetic flux vector $\{\Delta\phi_{sv}\}$ should be chosen as the final state vector for the electromagnetic model in the PMSM model. Then the stator path current vector $\{\tilde{i_{sv}}\}$ in EQ.3.40 is replaced by the relation deduced in EQ.3.44 to achieve the final electromagnetic differential equation as defined in EQ.3.45.

$$\begin{aligned}\frac{d\{\Delta\phi_{sv}\}}{dt} =&[R_{s1}]\cdot\{\tilde{I_{sp}}\}-[R_{s2}]\cdot\left([MFI]\cdot([HPP]\cdot[PnodU]^{-1}\cdot[HPT]+[PnodV])\right)^{-1}\\ &\cdot\left(\{\Delta\phi_{sv}\}-[MFI]\cdot[HPP]\cdot[PnodU]^{-1}\cdot\{IFI\}+[MFI]\cdot[ww]\cdot[P_{12}]\cdot[MZs]\cdot\{I_{sp}\}\right)\end{aligned} \tag{3.45}$$

where only the permeance matrix $[PnodU(\theta,x_r,y_r)]$ vary as the function of the instantaneous rotor center position due to the variation of the air-gap permeances while the other matrix are considered to be constant in every iteration steps.

3.7.1.2 Mesh/Nodal mixed model

Similarly, with the substitution of EQ.3.33 into EQ.3.41, one obtains:

$$\{\tilde{i_{sv}}\} = \left([MFI]\cdot[WRM]\cdot[Ybus]^{-1}\right)^{-1}\cdot\left(\{\Delta\phi_{sv}\}-[MFI]\cdot[WRM]\cdot[Ybus]^{-1}\cdot\{IFIR\}\right) \tag{3.46}$$

Replacing the stator path vector shown in the EQ.3.40 by the relation deduced in EQ.3.46, the differential equations to describe the electromagnetic behavior taken the magnetic path flux difference $\{\Delta\phi_{sv}\}$ as the state vector are depicted as:

$$\begin{aligned}&\frac{d\{\Delta\phi_{sv}\}}{dt}\\ =&[R_{s1}]\cdot\{\tilde{I_{sp}}\}-[R_{s2}]\cdot\left([MFI]\cdot[WRM]\cdot[Ybus]^{-1}\right)^{-1}\cdot\left(\{\Delta\phi_{sv}\}-[MFI]\cdot[WRM]\cdot[Ybus]^{-1}\cdot\{IFIR\}\right)\end{aligned} \tag{3.47}$$

where only the permeance matrix $[Ybus(\theta,x_r,y_r)]$ which includes the air-gap permeances vary at every iteration steps and is considered as the parametric nonlinear terms in the case without magnetic saturation effect.

3.7.2 In the case with magnetic saturation effect (Setting up the magnetic saturation effect)

Magnetic saturation effect is actually composed of two behaviors: the magnetic nonlinearity and the magnetic hysteresis. As most researchers did, only the magnetic nonlinearity is taken into account in this model by representing the permeability variation of each permeance element in the iron core part as the function of the magnetic field intensity (H) or the magnetic flux density (B) over them. A set of data points shown in FIG.3.12(a) was used to describe the B-H curve for the iron material M400P-50 applied in the fabrication of the stator and rotor steel. This curve is then adopted to construct separately the μ-H curve and μ-B curve as illustrated in FIG.3.12(b) and FIG.3.12(c) according to EQ.3.48.

$$\mu_n = \frac{B_n - B_{n-1}}{H_n - H_{n-1}} \tag{3.48}$$

where n is the order of the data points and the value of μ_1 is assumed to equal μ_2 in order to maintain the continuity.

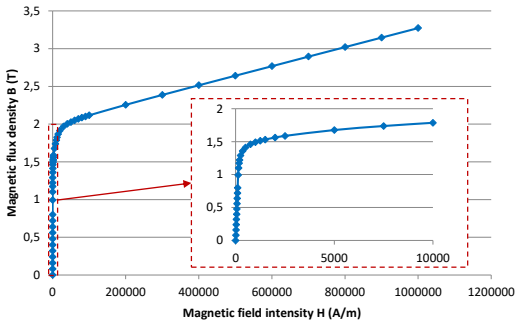

(a) B-H curve

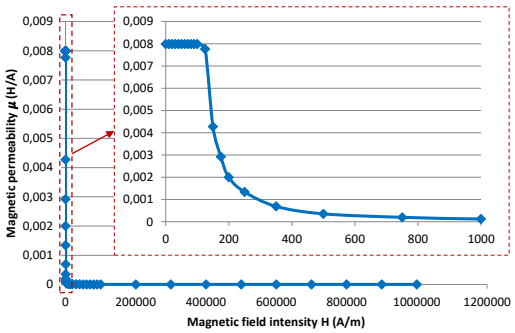

(b) μ-H curve

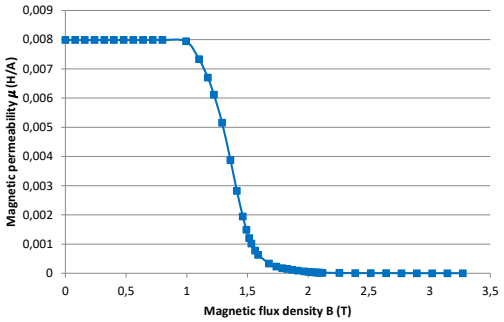

(c) μ-B curve

Figure 3.12: The magnetization curves about the iron material M400P-50.

Once the magnetic saturation effect is taken into consideration, the augmented magnetic equations deduced from the PNM are transformed into a set of nonlinear algebraic equations. All the permeance related matrices are no longer constant at each moment but vary with the variation of their defined magnetic unknowns ($\{u_{sr}\}$ or $\{\phi u_{sr}\}$) due to the variation of the permeance values in the iron core part. As mentioned in [86, 172], the nonlinear magnetic equations should be solved iteratively to achieve the converged results. The whole nonlinear augmented magnetic equations are often organized in the following form:

$$[A(\{X\})] \cdot \{X\} = \{B\} \tag{3.49}$$

where $[A(\{X\})]$ includes all the permeances related matrices especially those composed by the variated permeances in the iron core part; $\{X\}$ is the vector consisted of the unknowns of PNM and the stator path currents and $\{B\}$ is the vector composed of the input excitations. The traditional Newton-Raphson method is often adopted to solve this kind of nonlinear algebraic equations under a set of given excitations. However, for the sake of the simplicity the nonlinear equations solver in MATLAB® "fsolve" is employed directly in this model to solve the augmented magnetic equations at each moment (or inside of each iteration step of the global differential equations). Afterwards, the stator path currents from the converged result of the nonlinear equations $\{X\}$ are transferred in the differential equations in order to calculate the state vectors in the next moment.

Since the magnetic path flux difference vector $\{\Delta\phi_{sv}\}$ is chosen as the state vector for the electromagnetic model, it is allocated as one part of the vector $\{B\}$. The construction of the nonlinear algebraic equations and the relations between their coefficient matrix and the unknowns $[A(\{X\})]$ in different PNMs are explained respectively in the following sub-sections.

3.7.2.1 Nodal based model

Since the permeance matrix $[P_{12}]$ defined in EQ.A.5 is composed of the stator tooth permeance $\{P_{st}\}$ which is variated with the variation of the $\{u_{sr}\}$, EQ.B.27 is only designed for the linear model. All the relevant terms are then moved into the right side of the equal sign to form the nonlinear model in EQ.B.29 in order to prepare for the set-up of the magnetic saturation effect. As mentioned before, the state vector of the electromagnetic field $\{\Delta\phi_{sv}\}$ is one part of the vector $\{B\}$, it should be revealed on the right side of the EQ.B.29 by substituting EQ.3.41. Meanwhile another n_{ph} line equations about the full stator path currents vector $\{i_{sv}\}$ as defined in EQ.3.50 should be added into EQ.B.29 in order to keep the global coefficient matrix as a square matrix.

$$[PnodIs] \cdot \{i_{sv}\} = \{i_{sp}\} \tag{3.50}$$

where the matrix $[PnodIs]$ is organized as:

$$[PnodIs] = \begin{bmatrix} 1 & 0 & 0 & 1 & 0 & 0 & 1 & 0 & 0 & 1 & 0 & 0 \\ 0 & 1 & 0 & 0 & 1 & 0 & 0 & 1 & 0 & 0 & 1 & 0 \\ 0 & 0 & 1 & 0 & 0 & 1 & 0 & 0 & 1 & 0 & 0 & 1 \end{bmatrix} \tag{3.51}$$

Then the final nonlinear algebraic equations in the form of EQ.3.49 for setting up the saturation effect in the nodal based model are illustrated as:

$$\begin{bmatrix} [PnodU] & -[HPTs] \\ [MFI]\cdot[HPPs] & [MFI]\cdot[PnodVs] \\ [0]_{n_{np}*(2*n_s+2*n_r-1)} & [PnodIs] \end{bmatrix} \cdot \begin{Bmatrix} \{u_{sr}\} \\ \{\tilde{i_{sv}}\} \\ \{\tilde{i_{svs}}\} \end{Bmatrix} = \begin{Bmatrix} \{IFIs\}_{(2n_s+2n_r-1)*1} \\ \{\Delta\phi_{sv}\}_{(n_{np}*(n_v-1))*1} \\ \{i_{sp}\}_{n_{np}*1} \end{Bmatrix} \tag{3.52}$$

where the matrices $[PnodU], [HPTs], [HPPs], [PnodVs]$ are all variated as the function of the vector $\{\{u_{sr}\}\{\tilde{i_{sv}}\}\{\tilde{i_{svs}}\}\}^T$ since they are composed of the permeance elements from the iron core part.

As mentioned in SEC.A.1, the magnetic potential of each node defined in EQ.A.33 are chosen as the unknowns in the nodal based model so that μ-H curve described in FIG.3.12(b) is adopted to update the permeability value μ of each permeance element from the iron core part. About a random branch from this area depicted in FIG.2.10, the magnetic field intensity over it H_{ab} could be calculated as:

$$H_{ab} = \frac{(u_a - u_b - \mathcal{F}_t)}{l_{ab}} \tag{3.53}$$

where l_{ab} is the length of this branch. Since the cross-sectional area A_k and the length l_k of each branch from EQ.2.4 are determined by the geometry of the reference motor, their ratio can be considered as a constant value "permeance coefficient" $cP_k = \frac{A_k}{l_k}$ (while the "reluctance coefficient" is similarly defined as $c\mathcal{R}_k = \frac{l_k}{A_k}$) in the program. According to the nodal based PNM illustrated in FIG.B.1, the permeance values from the iron core part are expressed as the functions of the relevant unknowns in EQ.3.54.

$$\begin{cases} P_i^{sy} = \mu_i^{sy}(\dfrac{u_{i+1}^{sy} - u_i^{sy}}{l_i^{sy}}) \cdot cP_i^{sy} \\ P_i^{st} = \mu_i^{st}(\dfrac{u_i^{sy} - u_i^{sl} - \mathcal{F}_i^{st}}{l_i^{st}}) \cdot cP_i^{st} \\ P_j^{rl} = \mu_j^{rl}(\dfrac{u_{j+1}^{rl} - u_j^{rl}}{l_i^{rl}}) \cdot cP_j^{rl} \\ P_k^{rt} = \mu_k^{rt}(\dfrac{u_k^{rl} - u_k^{ry} - \mathcal{F}_k^{rt}}{l_k^{rt}}) \cdot cP_k^{rt} \\ P_j^{ry} = \mu_j^{ry}(\dfrac{u_{j+1}^{ry} - u_j^{ry}}{l_j^{ry}}) \cdot cP_j^{ry} \end{cases} \tag{3.54}$$

where k equals to the order of P_{rtb} in the vector $\{P_{rt}\}$ defined in EQ.3.3 since the PM permeance P_{rtm} are considered as constant values in this PMSM model. The stator MMF $\mathcal{F}_{st}$ are available in EQ.3.55 by substituting EQ.3.17 into EQ.3.14,

$$\{\mathcal{F}_{st}\} = [MZs] \cdot ([M1] \cdot \{\tilde{i_{sv}}\} + [M2] \cdot \{\tilde{i_{svs}}\}) \tag{3.55}$$

and the rotor MMF are revealed in EQ.3.19. The relation about μ-H curve can be taken into account through the simple linear interpolation about the data points but this lacks

the representation about the continuous smooth variation tendency of the curve. In order to set up this relation in a better way, an approximation formula about the B-H curve to describe it as the function of the magnetic field intensity H is available in [173]. Since the nodal based model is not the final choice for performing the simulations in this thesis, the set-up of the exact approximation formula is not presented here.

3.7.2.2 Mesh/Nodal mixed model

Similarly, in order to display the state vector of the electromagnetic field $\{\Delta\phi_{sv}\}$ in the vector $\{B\}$, EQ.3.41 should be substituted into EQ.3.32. Therefore, the final nonlinear algebraic equations in the mixed model for installing the saturation effect are organized in the same form of EQ.3.49:

$$\begin{bmatrix} [Ybus] & -[AFT] \\ [MFI]\cdot[WRM] & [0] \end{bmatrix} \cdot \begin{Bmatrix} \{\phi u_{sr}\} \\ \{\tilde{i_{sv}}\} \end{Bmatrix} = \begin{Bmatrix} \{IFIR\}_{(2n_s+2n_r-1)*1} \\ \{\Delta\phi_{sv}\}_{(n_{np}*(n_v-1))*1} \end{Bmatrix} \tag{3.56}$$

where only the matrix $[Ybus]$ varies as the function of the vector $\{\phi u_{sr}\}$.

Since the magnetic loop flux in the iron core parts and the magnetic node potentials on the two sides of the air gap $\{\phi u_{sr}\}$ defined in EQ.2.51 are chosen as the unknowns in the mixed model, the μ-B curve depicted in FIG.3.12(c) is adopted to update most of the permeability value μ of each permeance element in the iron core part according to the magnetic flux density B flowing through each branch. About a random branch illustrated in FIG.2.10, the magnetic flux density over it B_{ab} could be calculated as:

$$B_{ab} = \frac{\phi}{A_{ab}} \tag{3.57}$$

where A_{ab} is the cross-sectional area of this branch and ϕ represents the magnetic flux passing through this branch. Those magnetic branch flux could be extracted from the defined loop flux according to the mixed based PNM shown in FIG.3.7. Then, the reluctance or permeance values from the iron core part are expressed receptively as the functions of the relevant unknowns in EQ.3.58.

$$\begin{cases} \mathcal{R}_i^{sy} = c\mathcal{R}_i^{sy} \cdot (\mu_i^{sy}(\dfrac{\phi_i^s}{A_i^{st}}))^{-1} \\ \mathcal{R}_i^{st} = c\mathcal{R}_i^{st} \cdot (\mu_i^{st}(\dfrac{\phi_i^s - \phi_i^s}{A_i^{st}}))^{-1} \\ P_j^{rl} = \mu_j^{rl}(\dfrac{u_{j+1}^{rl} - u_j^{rl}}{l_i^{rl}}) \cdot cP_j^{rl} \\ \mathcal{R}_k^{rt} = c\mathcal{R}_k^{rt} \cdot (\mu_k^{rt}(\dfrac{\phi_k^r - \phi_{k-1}^r}{A_k^{rt}}))^{-1} \\ \mathcal{R}_j^{ry} = c\mathcal{R}_j^{ry} \cdot (\mu_j^{ry}(\dfrac{\phi_i^r}{A_j^{ry}}))^{-1} \end{cases} \tag{3.58}$$

It can be seen that most of the permeability are updated by the function of $\mu(B)$ except for those permeance in the rotor leakage part where the relation of $\mu(H)$ is still taken into consideration. In order to achieve a continuous $\mu(B)$ function, an approximation about the discretized $\mu - B$ curve is realized according to the Marrocco formula [174]:

$$\mu = \frac{\mu_0}{\varepsilon + (c - \varepsilon) \cdot \frac{B^{2\cdot\alpha}}{B^{2\cdot\alpha} + \tau}} \tag{3.59}$$

where the parameters $\varepsilon, c, \alpha, \tau$ are determined through the real curve fitting by applying the least square method. The fitted curves about the iron material M400P-50 are compared with those plotted by the original discretized data in FIG.3.13 to demonstrate the good agreement about the fitted curves.

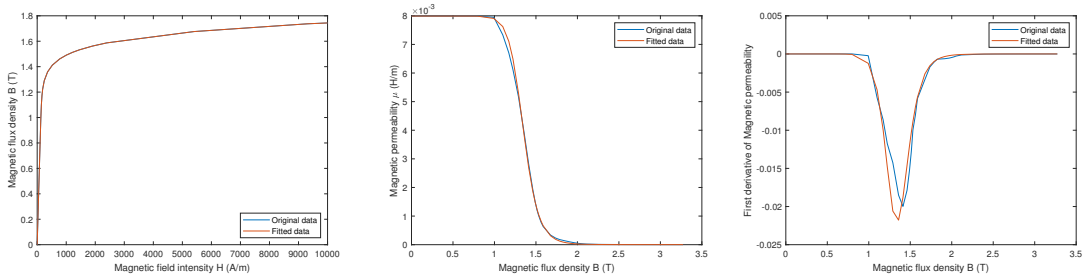

(a) (b) (c)

Figure 3.13: Comparison about the BH curves between the original data and the fitted data.

Furthermore, a high condition number will be achieved in this mixed model due to the large disparity in the magnitudes of the reluctances and permeances appeared in the Jacobian matrix. The ill-conditioned Jacobian matrix may lead to the divergence of the nonlinear equations. In order to avoid this problem when solving the nonlinear algebraic equations defined in EQ.3.56, a scaling is applied to the whole system by applying a per-unitization type of variable transformation as mentioned in [175]. The detailed process is available in the following.

If the flux density value near the knee of the saturation curve shown in FIG.3.12(a) is chosen as a base value ($B_{base} \approx 1.5T$) and the maximum airgap permeance area between each pair of stator and rotor tooth adopted in EQ.3.4 is selected as the base area ($A_{base} = L_m \cdot L_{ts}$), other base values for the scaling are defined correspondingly as:

$$\begin{cases} P_{base} = \dfrac{\mu_0 \cdot A_{base}}{E_e} \\ \mathcal{R}_{base} = \dfrac{1}{P_{base}} \\ \phi_{base} = B_{base} \cdot A_{base} \\ \mathcal{F}_{base} = \phi_{base} \cdot \mathcal{R}_{base} \end{cases} \tag{3.60}$$

Making the both sides of EQ.3.24 divide by $\mathcal{F}_{base}$ and those of EQ.3.31 divide by ϕ_{base}, the nonlinear algebraic equations defined in EQ.3.56 after the scaling becomes:

$$\begin{bmatrix} [\check{Ybus}] & -[AFT] \\ [MFI]\cdot[WRM] & [0] \end{bmatrix} \cdot \begin{Bmatrix} \{\check{\phi u}_{sr}\} \\ \{\check{\tilde{i}}_{sv}\} \end{Bmatrix} = \begin{Bmatrix} \{\check{IFIR}\}_{(2n_s+2n_r-1)*1} \\ \{\Delta\check{\phi}_{sv}\}_{(n_{np}*(n_v-1))*1} \end{Bmatrix} \tag{3.61}$$

where $\check{\bullet}$ represent the scaled parts. They are illustrated respectively as:

$$[\check{Ybus}] = \begin{bmatrix} [\mathcal{R}_{11}]./\mathcal{R}_{base} & [0] & [\mathcal{R}_{13}] & [0] \\ [0] & [\mathcal{R}_{22}]./\mathcal{R}_{base} & [0] & [\tilde{\mathcal{R}}_{24}] \\ [\mathcal{R}_{31}] & [0] & [\mathcal{R}_{33}]./P_{base} & [\tilde{\mathcal{R}}_{34}]./P_{base} \\ [0] & [\tilde{\mathcal{R}}_{42}] & [\tilde{\mathcal{R}}_{43}]./P_{base} & [\tilde{\mathcal{R}}_{44}]./P_{base} \end{bmatrix} \tag{3.62}$$

$$\{\check{\phi u}_{sr}\} = \begin{Bmatrix} \{\phi_s\}./\phi_{base} \\ \{\phi_r\}./\phi_{base} \\ \{u_{sl}\}./\mathcal{F}_{base} \\ \{\tilde{u}_{rl}\}./\mathcal{F}_{base} \end{Bmatrix} \tag{3.63}$$

$$\{\check{IFIR}\} = \begin{Bmatrix} -[\mathcal{R}_{15}]\cdot[MZs]\cdot(\{I_{sp}\}./\mathcal{F}_{base}) \\ -[\mathcal{R}_{25}]\cdot(\{\mathcal{F}_{rt}\}./\mathcal{F}_{base}) \\ \{0\} \\ \{0\} \end{Bmatrix} \tag{3.64}$$

$$\{\check{\tilde{i}}_{sv}\} = \{\tilde{i_{sv}}\}./\mathcal{F}_{base};\ \{\Delta\check{\phi}_{sv}\} = \{\Delta\phi_{sv}\}./\phi_{base} \tag{3.65}$$

3.7.2.3 Discussion

The main difference between the nodal based model and the mesh/nodal mixed model about the set-up of the magnetic saturation effect is to express the variation of the material permeability as the function of the magnetic field intensity (H) or of the magnetic flux density (B). The different curve forms about the relation of $\mu(H)$ and the relation of $\mu(B)$ illustrated respectively in FIG.3.12(b) and FIG.3.12(c) introduce the Jacobian matrix with two different condition numbers as discussed in [176, 177]. It was indicated that when saturation is included, the mesh based formulation brings a model that is more efficient numerically. Since the mesh formulation is largely applied in the iron core part for the mesh/nodal mixed model, it is evident that nonlinear algebraic equations are solved with lower iteration number and better convergence in the mixed model when comparing to the nodal based model. Therefore, the mesh/nodal mixed model of PNM is finally adopted for the further analysis about the reference PMSM model.

The distribution of the simulated permeability values in the iron core part under the magnetic saturation effect are compared with those constant values considered in the linear model in FIG.3.14. It can be seen clearly that the permeability values decrease when the branch is saturated and this saturation effect can be identified in all the iron core regions. The distribution of permeability in the case without eccentricity is symmetrical in

each stator and rotor region and the 4 poles of the reference PMSM are reflected from their variation forms. The rotor yoke part is less saturated as mentioned in [178] due to its geometrical dimension and its position in the PNM so that the smallest permeability values shown in FIG.3.14(e) are bigger than those in the other regions.

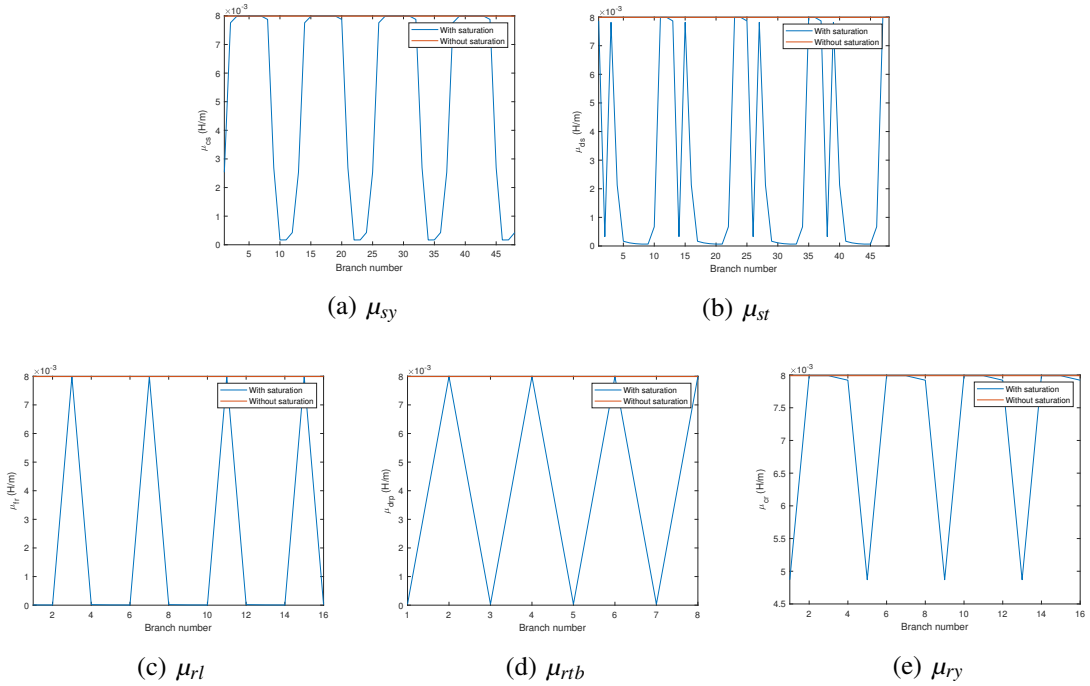

(a) μ_{sy} (b) μ_{st}

(c) μ_{rl} (d) μ_{rtb} (e) μ_{ry}

Figure 3.14: Variation of the permeability from the iron core part in the case without eccentricity during the last iteration.

3.8 Multiphysics couplings

The mechanical structure and its simplified mechanical modeling about the reference PMSM are illustrated in FIG.3.15. Different from the IM discussed before, the reference PMSM is a customized product especially designed for the future experimental part. Thus the motor cage is removed for the set-up of sensors and the stator core is fixed to the frame through four steel rods along four parallel edges in order to input the static eccentricity by adjusting the position of the stator. The 2.5D modeling about the electrical motor could be maintained since the shaft length is long enough compared to the iron core effective length. The shaft is supported by two identical roller bearings on the two sides of the motor to constitute a classical mechanical structure. And this structure is represented by a simplified mechanical model composed of several node and beam elements as depicted in the bottom schema from FIG.3.15 by adopting the similar discretized mechanical model employed in the IM in order to analyze the dynamic behavior of the reference PMSM under the excitation of UMP due to the rotor eccentricity.

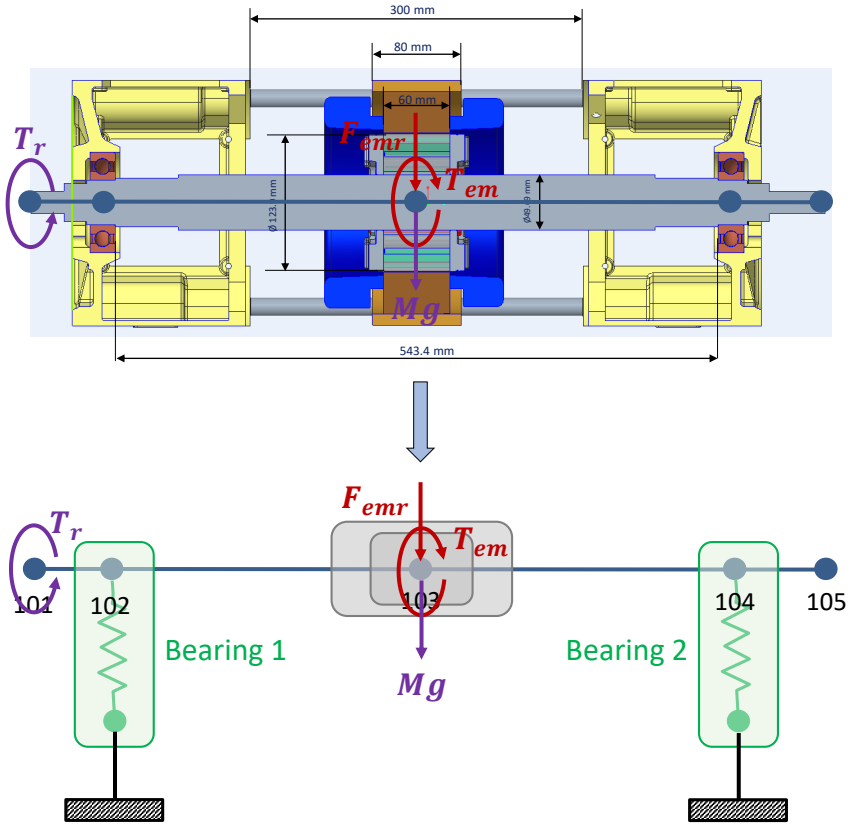

Figure 3.15: Mechanical modeling about the reference PMSM in a classical mechanical structure (Bearing stiffness only presented in one direction).

Similarly as described in the IM, the mechanical eccentricity is either introduced by a geometrical imposed eccentricity (seeing SEC.2.2.1.2) or generated automatically as the result of the rotordynamic motion (seeing SEC.2.8.1). Combined with the magnetic model and the electrical model established before, the strong couplings between different fields are also realized in the PMSM through the interactions between the electromagnetic forces (T_{em} and UMP) and the corresponding displacements with the associated instantaneous speeds (θ, x_r, y_r and $\dot{\theta}, \dot{x_r}, \dot{y_r}$) in both the rotational and radial movement. Their relations in the strong multiphysics couplings about the PMSM model are expressed in FIG.3.16. There are two differences about the multiphysics couplings when comparing with the model of the IM shown in FIG.2.22. Firstly, the PMSM model is supplied by the three-phase currents $\{i_{sp}\}$ with a determined current amplitude value $\hat{i_{sp}}$ and it varies in the synchronism rotational movement of the rotor $\theta_r * P$ to conserve the same torque angle during the simulation as explained in SEC.3.6.1. Secondly, the operating point of the PMSM model is determined by the initial rotor angular position θ_{r0} in the case with a fixed stator phase current amplitude $\hat{i_{sp}}$.

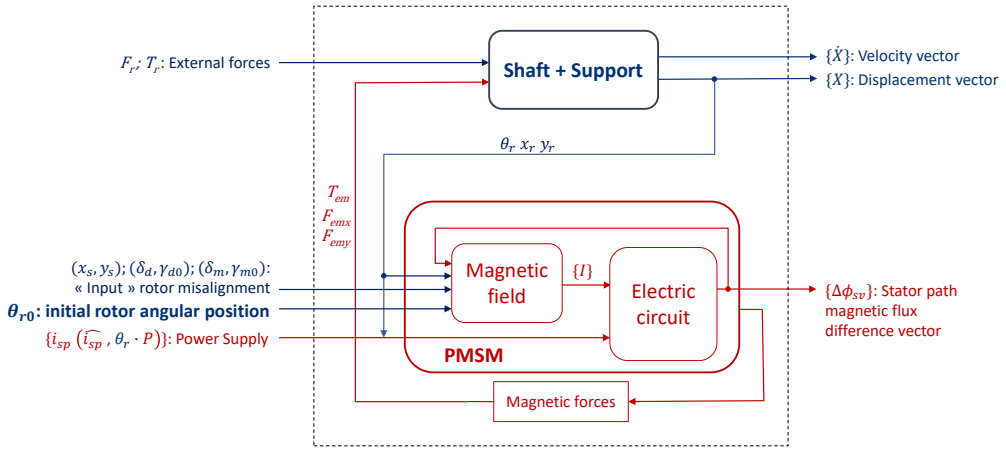

Figure 3.16: Multiphysics coupling about PMSM in the terms of Phase flux model.

In order to validate the proposed model with the corresponding FEM in SEC.3.9, an electromagnetic model without the coupling of the mechanical subsystem is also created in the frame of the reference PMSM model. The two names defined in SEC.2.9 to describe the two models for the IM are re-adopted here. The detailed informations about the two models for the reference PMSM are presented in the following subsections.

3.8.1 Model EMM

A compact format of the multiphysics model from FIG.3.16 is illustrated in FIG.3.17. Different from the IM, the initial rotor angular position θ_{r0} is used to identify the operating point in the PMSM so as to determine the electromagnetic torque because there is no negative feedback relationship in the PMSM between the electromagnetic torque and the angular speed as described in Torque-Speed characteristic curve for the asynchronous motor. The relation between the applied load torque and the produced electromagnetic torque at each moment decides the instantaneous angular speed. However since the generated electromagnetic torque is not a constant value due to the slot effect, it's hard for the angular speed to reach the permanent state naturally with a given constant load torque value. Just as mentioned in [143], the lack of the control system in the synchronous motor will introduce strong torsional oscillations during the operation. Since there is no control system considered in this work (which is not the objective of this thesis), the angular speed needs to be prescribed in each simulation for the PMSM model in order to achieve a clearly comprehensible analysis about its dynamic behavior. There are two methods to realize it. One is to define the load torque value to equal to the generated electromagnetic torque value at each moment in order to maintain the equilibrium of the rotational movement as described in EQ.3.66:

$$T_r(t,\theta) = T_{em}(t,\theta) \tag{3.66}$$

Another is to add a mechanical viscous damping c_T in the applied load torque to make it vary as function of the instantaneous angular speed as defined in EQ.3.67:

$$T_r = T_0 + c_T \cdot \dot{\theta}_r \tag{3.67}$$

where the parameters T_0 and c_T should be chosen correctly through the variation of the simulated electromagnetic torque at each operating point. And in this case, the simulated angular speed converges gradually to the synchronous speed. The variation of the simulated angular speeds from these two methods are going to be presented in SEC.3.10.2.1.

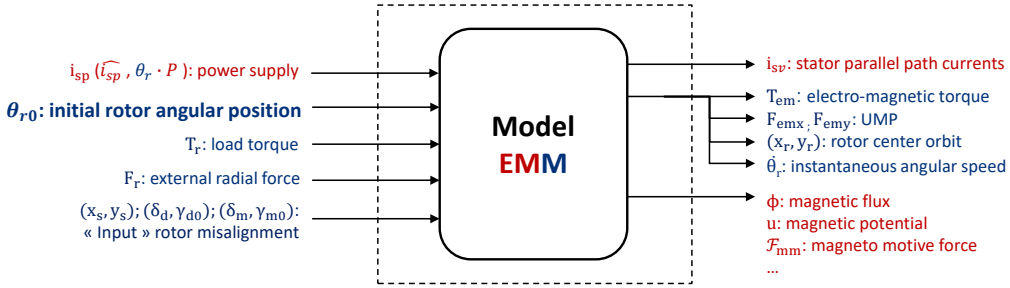

Figure 3.17: Inputs and outputs of the model EMM for the PMSM

3.8.2 Model EM

By decoupling with the mechanical model, Model EM about the reference PMSM is isolated from the coupled model and its inputs and outputs are illustrated clearly on the two sides of FIG.3.18. Since there is no direct relation between the electromagnetic torque and the motor angular speed in the synchronous motor, Model EM is able to simulate the electromagnetic torque independently at a known torque angle. Therefore, Model EM of the reference PMSM is still controlled by the initial rotor angular position. Similarly as described in the Model EM of the IM, the UMP is generated here from a predefined rotor misalignment and the rotation speed is predefined to calculate the motor rotation angle θ_r so as to define the variation of the three-phase stator currents. As mentioned before, the main objective of creating Model EM is to help us validate the proposed model in the quasi-static regime through the comparison with the simulation results of the corresponding FEMM model which is explained in the next section.

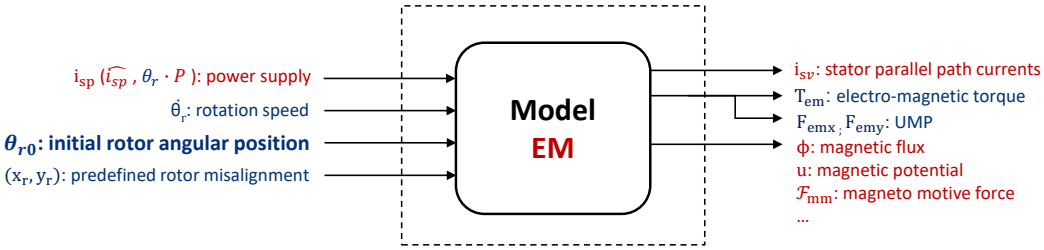

Figure 3.18: Inputs and outputs of the model EM for the PMSM

3.9 Model validation in the quasi-static regime

The multiphysics model about the reference PMSM is also validated in the quasi-static regime. As discussed before, the simulation results from Model EM are adopted to compare with those simulated from the corresponding model established in the software FEMM. Different from the original model established according to the identical geometry of the reference PMSM, another equivalent model referring to the same geometry but without the iron bridge parts is created and validated in this section to prepare for the longtime simulation in the non-stationary operation. The two models with different geometries are both established in the software FEMM and MATLAB in the case with and without the magnetic saturation effect as well as based on the model with or without the mechanical coupling. To achieve a simple and clear expression, different models with different properties about the reference PMSM created in different softwares are named in different abbreviations which can be consulted in TAB.3.1. These models are adopted for the validation of the proposed model in this section and for generating the simulation results in SEC.3.10.

Geometry	Identical		Equivalent
Saturation	With	Without	Without
No mechanical coupling	Model FEMM1	Model FEMM1_L	Model FEMM2
	Model EM1	/	Model EM2
With mechanical coupling	Model EMM1	/	Model EMM2

Table 3.1: Abbreviations of different model names about the reference PMSM.

The three models created in the software FEMM are firstly compared together about their characteristic Torque-Angle curves. The comparison between Model FEMM1 and Model FEMM1_L demonstrates that the magnetic saturation effect must be considered in the original model based on the identical geometry. The other comparison between Model FEMM1 and Model FEMM2 indicates that the equivalent model is a good alternative choice for simulating the original machine in the case without the magnetic saturation effect. Afterwards, the comparisons between the models from two softwares are mainly

performed among the simulation results about the two electromagnetic forces (T_{em} and UMP) in two aspects since one goal of this thesis is to study the vibration of the electric machine. The first is to compare their variation waveforms at a certain operating point between Model EM1 and Model FEMM1 to verify the frequency components in the case with magnetic saturation effect. And then the average values of electromagnetic torque are compared at all operating points between the two models in both groups of identical geometry and of equivalent geometry to check the characteristic Torque-Angle curve of the reference PMSM. The validation about the generated UMP is generally realized by comparing the average values of the x-axis force with different input static eccentricities at a certain operation point.

The description about the modeling of the identical model and the equivalent model about the reference PMSM in the software FEMM is presented in the first subsection and the comparisons in different aspects are explained respectively in the next two subsections.

3.9.1 Finite Element Method Magnetics Model (Model FEMM)

Two models with different geometries about the reference PMSM are established separately in the software FEMM. One is the identical model as illustrated in FIG.3.19 and another is the equivalent model as depicted in FIG.3.20. The second one is created to provide an alternative choice for the later analysis about the dynamic behavior in the non-stationary operation due to its efficiency in the calculation. Both of the two models are explained in the following parts.

3.9.1.1 Identical model

As described by its name, the identical model is created according to the actual geometric dimension from the sketch of the reference machine. Since it is a four poles motor, a quarter of the motor's cross section is illustrated in FIG.3.19(a). It is also composed of six parts as described in the IM model and the difference between the two mostly appears in the rotor part. Eight rectangle PMs are sequentially inserted in the rotor slot with the magnetic isolation air slot on the two sides of each PM to prevent the magnetic flux of the PM from short-circuiting. This kind of the structure forms a radial and a tangential magnetic bridge in the rotor sheet steel. The two bridge structures not only reinforce the mechanical strength of rotor but also limit the magnetic leakage flux of the PMs through the magnetic saturation in this region. Their effects could be recognized evidently in the magnetic flux distribution shown in FIG.3.19(b). By allocating the material "$M400P\_50$" with the nonlinear BH curve to the stator and rotor iron core parts, the obvious saturation phenomena are identified in almost all the bridge regions. The identical model in the case without saturation effect (Model FEMM1_L) is constructed by replacing the nonlinear material "$M400P\_50$" with a material with the linear BH curve.

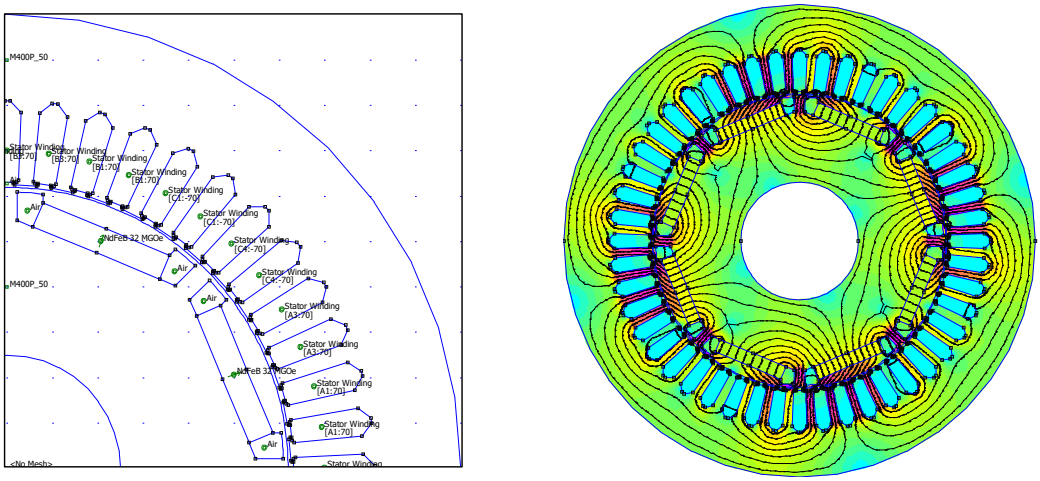

(a) Model FEMM1 (b) Magnetic flux distribution

Figure 3.19: Identical model about the reference PMSM in FEMM.

3.9.1.2 Equivalent model

Although the identical model is able to simulate the machine performance with a complete motor geometry close to the reality, the large time cost calculation due to the consideration of the magnetic saturation effect becomes a big obstacle when performing a simulation in the non-stationary operation during a long time span. In order to solve this problem, an equivalent model is established from the simplification of the identical model. As discussed before, since the bridge regions are highly suffered from the magnetic saturation, they are removed in this equivalent model as shown in FIG.3.20(a) to avoid the necessary nonlinear calculation about the magnetic saturation effect in this part. The rest iron core pieces above each PMs are conserved to maintain the same air gap average length along the periphery of the rotor. The material with the nonlinear BH curve in the iron core parts are replaced by the material "Silicon Core Iron" with a constant permeability value. Its magnetic flux distribution is displayed in FIG.3.20(b). Four poles are also formed even with some large flux density revealed in the rest rotor iron core pieces.

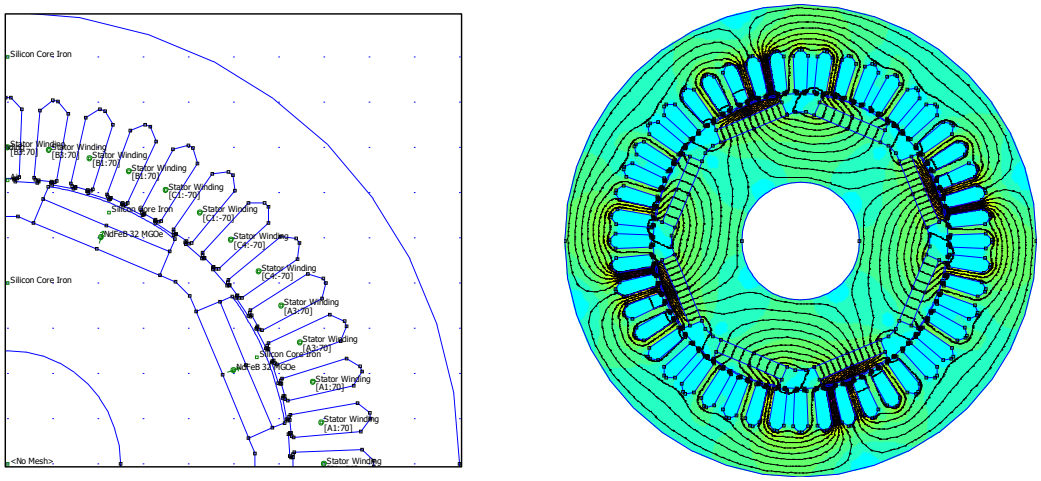

(a) Model FEMM2 (b) Magnetic flux distribution

Figure 3.20: Equivalent model about the reference PMSM in FEMM.

In order to obtain the equivalent model in the proposed model with no mechanical coupling (Model EM2), the nonlinear iron permeability μ_{ir} applied to calculate the permeances of the two rotor bridges should be replaced by the vacuum permeability μ_0 as defined in EQ.3.68:

$$\begin{aligned} P_{rl} &= \frac{\mu_0 \cdot \left(\frac{D_{re}-D_{ree}}{2}\right) \cdot L_m}{L_{pt}} \\ P_{rtb} &= \frac{\mu_0 \cdot h_{pr} \cdot L_m}{\frac{D_{re}}{2} - R_{aim}} \end{aligned} \tag{3.68}$$

Meanwhile the nonlinear iron permeability to calculate the other permeances in the iron core parts are considered as a constant value. Then Model EM2 can be expressed in the form of the state-space equation as described in SEC.3.7.1 in order to effectively accelerate the simulation.

3.9.1.3 Discussion

The simulation settings in the FEMM models about the reference PMSM is less complex than that about the IM since there is no need to set up the motor slip frequency in the PMSM to induce the currents in the rotor bars. Since the reference PMSM is supplied by the stator three-phase currents, only the instantaneous current values in each stator slot are needed as the inputs to simulate the motor behavior in a quasi static regime with a given rotor position. According to the four parallel paths winding connection in each stator phase illustrated in FIG.3.10, the stator phase current is considered to be equally distributed in each path for the sake of the simplicity. The input three-phase stator currents

vary as the functions defined in EQ.3.34 with the synchronous rotation movement of the rotor at the same time to obtain the "dynamic behavior" composed of a set of static simulation results. As mentioned before, the initial rotor angular position θ_{r0} is used to change the operating point of each simulation. The average values of the electromagnetic torque calculated at different operating points are compared between Model FEMM1 and Model FEMM2 in FIG.3.21. It is seen that except for some differences appeared in the operating points with large electromagnetic torque values, the overall profile of the brown and purple curve are well consistent. It proves that the equivalent model can serve as a good alternative choice for the identical model in the case without magnetic saturation effect. A third red curve about Model FEMM1_L is added into FIG.3.21 to display the simulation results from the identical model but without magnetic saturation effect. There is nearly no electromagnetic torque value generated at each operating point since all the magnetic flux tend to be conserved inside of the rotor through the iron bridge structures and no flux will pass through the airgap to generate the electromagnetic torque if the magnetic saturation effect isn't taken into consideration. It indicates that the identical model can't be simulated directly in the case without the saturation effect.

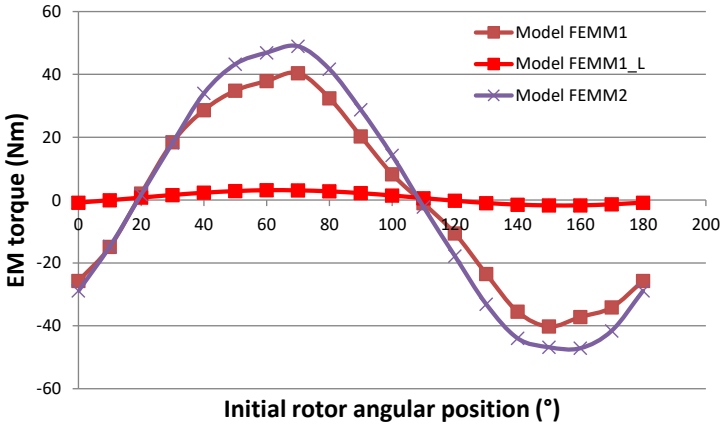

Figure 3.21: Comparison of the electromagnetic torque average value simulated from different FEMM models at different operating points.

3.9.2 At the rated operating point

The operating point at the initial rotor angular position equaled to 65° is chosen as the rated operating point since it produces the largest electromagnetic torque value according to FIG.3.21. The variation of the simulation results at this rated state are compared between Model FEMM1 and Model EM1 in the case with saturation to study their variation waveforms. The comparisons about the stator first path current and about the electromagnetic torque simulated in the case without eccentricity are illustrated separately in

FIG.3.22 as function of the shaft position. There is a good accordance between the predefined stator first path current from Model FEMM1 and that simulated from Model EM1. Although the profile of the two curves about the simulated electromagnetic torque are not completely corresponded with each other due to the different meshing method, they have at least the same period and the similar ripple torque value. The comparison about the generated UMP x-axis force between the two models in the case with the static eccentricity of $10\%E_e$ is displayed in FIG.3.23. It is obvious that the two F_{emx} values fluctuate around two different average values however they have the similar variation waveforms. Considering that there is no big difference between the simulation results from Model EM and Model EMM as discussed in SEC.2.9.3.1, Model EM1 is employed later to study the characteristic frequencies of different simulation results in the case with different input eccentricity values in SEC.3.10.1.

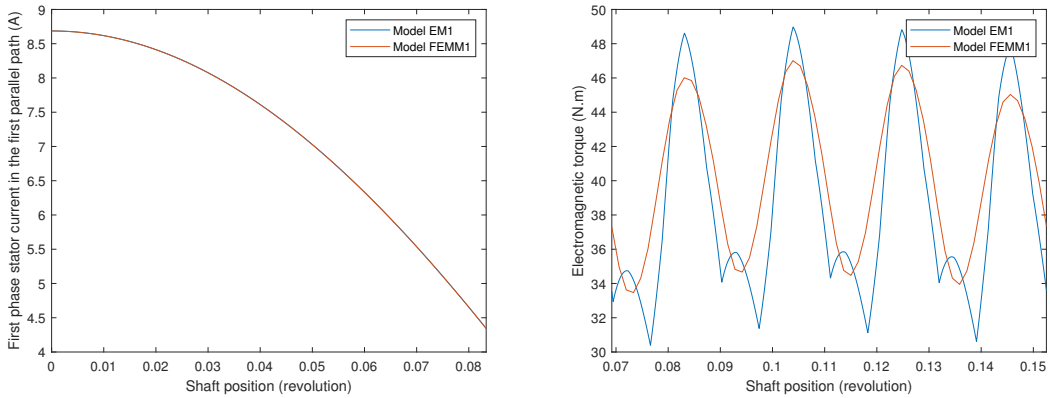

(a) Stator first path current

(b) Electromagnetic torque

Figure 3.22: Comparison about the variation of simulation results from the identical model between Model EM and Model FEMM at the rated state ($\theta_{r0} = 65°$) in the case without eccentricity.

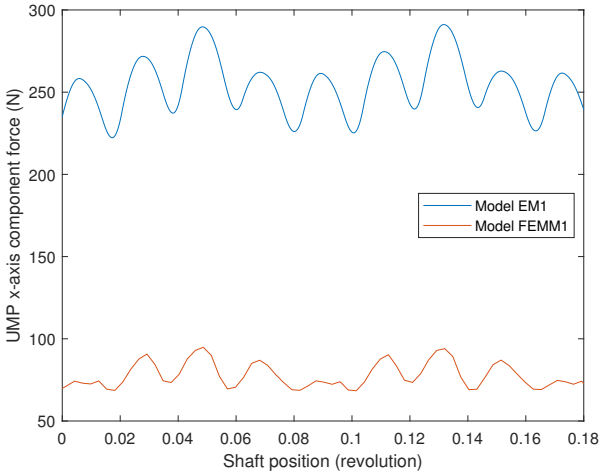

Figure 3.23: Comparison about the variation of the UMP x-axis force from the identical model between Model EM and Model FEMM at the rated state ($\theta_{r0} = 65°$) in the case with the static eccentricity of $10\%E_e$.

The difference between the average values of F_{emx} in the case with the static eccentricity of $10\%E_e$ becomes more evident with the increase of the input static eccentricity values as illustrated in FIG.3.24(a). However their differences become relatively smaller when comparing the same values between Model EM2 and Model FEMM2 in the frame of the equivalent model as displayed in FIG.3.24(b). It seems that there are still some inconsistencies in the meshing method between the proposed model and the FEM established in FEMM especially in the modeling of the air gap part (which is important for calculating the electromagnetic forces.). It should be recognized that the permeance network meshes applied in the proposed model for the PMSM are much more rough than those generated in the FEMM at the present stage. It will not introduce large difference in the simulated electromagnetic torque value since T_{em} is calculated from the derivation of the co-energy about the periphery of the global air gap region while each UMP component force are respectively calculated from the derivation about each translation displacement which is sensitive to the variation of local permeance mesh. Furthermore, the assumption made about the variation form of $f_p(\theta_{ij})$ by adopting the Ostovic model in SEC.2.2.1.2 maybe not valid in the modeling of the PMSM due to the evident difference between the stator tooth width and the equivalent rotor tooth width (the width of the PM). Overall, this part needs to be improved in the future study but according to the similar results of F_{emx} achieved in FIG.3.24(b), the equivalent model could be used to perform the simulation with a variated eccentricity value.

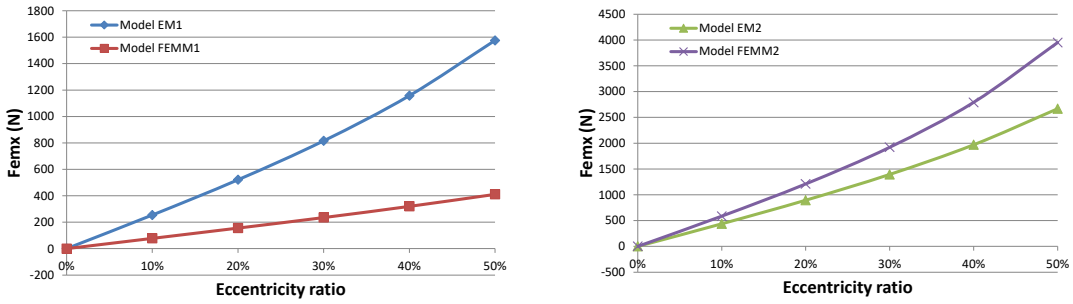

(a) Identical model (b) Equivalent model

Figure 3.24: Comparison about the average value of UMP x-axis force at the rated operating point ($\theta_{r0} = 65°$) with different input static eccentricities.

3.9.3 At all the operating points

The average values about the electromagnetic torque at each operating point are compared in FIG.3.25 between the proposed model and the FEM created in FEMM. The comparison about the simulation results are realized separately in the identical model and in the equivalent model. It can be seen that the two curves in each comparison are correspondent with each other in the general profiles and there is a better agreement between those obtained in the equivalent model which confirms its availability in the simulation of the non-stationary state. Therefore, the coupled proposed model based on the equivalent model is adopted to generate the simulation results in the non-stationary operation during a long time span in SEC.3.10.2.

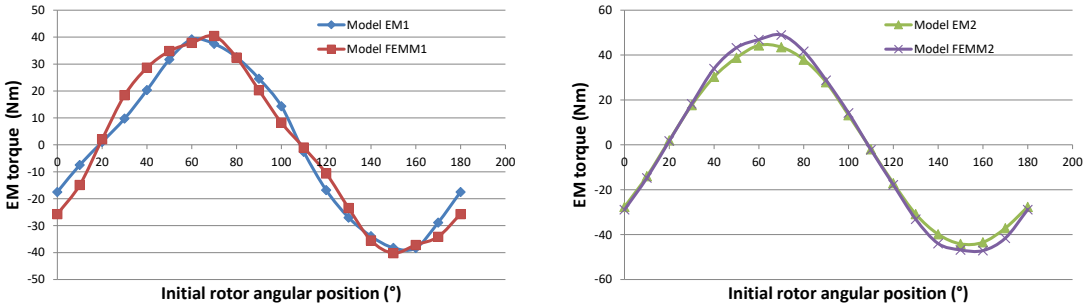

(a) Identical model (b) Equivalent model

Figure 3.25: Comparison of the electromagnetic torque average values at different operating points between Model EM and Model FEMM.

3.10 Dynamic simulation results analysis

Since the proposed multiphysics model is validated separately in two models with different settings, their simulation results are analyzed in this section to study the dynamic behavior of the reference PMSM in consideration of the UMP. As mentioned before, the simulation results from Model EM1 are firstly studied in the case without and with the input static eccentricity in order to find out the characteristic phenomena associated with the input static eccentricity. And then those simulated from Model EMM2 in the non-stationary operation are used to study the vibration performance of the reference PMSM under the mass unbalance excitation.

3.10.1 Analysis of simulation results from Model EM1

All the simulation results analyzed in this subsection are simulated from Model EM1 at the rated operating point (with the initial rotor angular position $\theta_{r0} = 65°$) during one shaft revolution since the model with the magnetic saturation effect is very time cost (e.i. the average calculating time for one shaft revolution is about 11 hours). The simulation results are compared in three cases with different input static eccentricity values in order to study the characteristic phenomena due to these eccentricities in different variables.

The first comparison is focused on the first three stator path currents of the first phase. Their variations as function of the shaft position are illustrated in FIG.3.26. In the case without eccentricity from FIG.5.14(a), all the path currents coincide with each other and each of them vary in a sinusoidal function with the amplitude value equal to the $\frac{\hat{i_{sp1}}}{4}$ since there are totally four parallel paths in each stator phase. However some imbalance between the path currents in the same phase appear in the case with eccentricity and this imbalance becomes larger with the increase of the input eccentricity value when comparing FIG.5.14(b) with FIG.5.14(c). Reflecting in their angular spectrum shown in FIG.3.27, only the power supply frequency 2 ev/rev is recognized in the case without eccentricity from FIG.3.27(a) because the reference PMSM has two pole pairs and more harmonics about the power supply frequency are revealed in the case with the input static eccentricity.

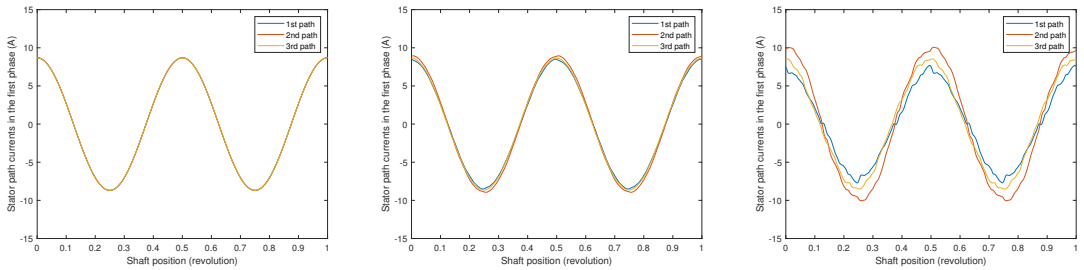

(a) Without eccentricity (b) With 10%E_e (c) With 50%E_e

Figure 3.26: Variation of the first three stator path currents in the first phase as the function of the shaft position.

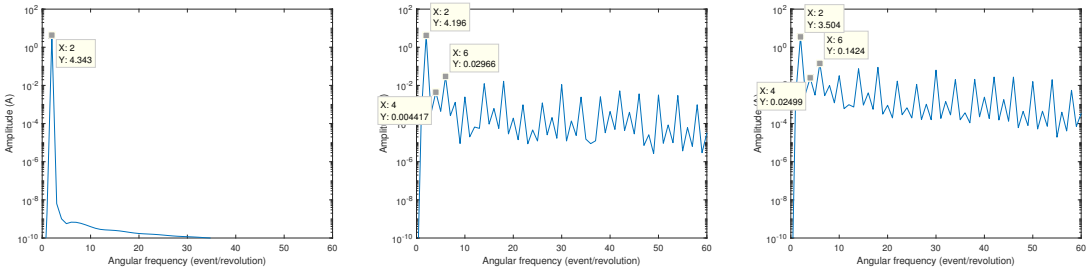

(a) Without eccentricity (b) With 10%E_e (c) With 50%E_e

Figure 3.27: Angular spectrum of the stator first path current in the first phase.

The second comparison is realized in the simulation results about the electromagnetic torque. Their variation versus the shaft position and corresponding angular spectrum are illustrated respectively in FIG.3.28 and in FIG.3.29. There is no obvious difference in their fluctuation waveforms between the case without and with the static eccentricity of 10%E_e so that they are also similar in their angular spectrum. The frequency components like 12 ev/rev and its harmonics are identified in both FIG.3.29(a) and FIG.3.29(b) since $12 = N_{ns} \div 4$ is the number of the stator slots in each poles. Besides some small peaks like 62 ev/rev from the combination between the stator slot frequency harmonics and the power supply frequency are also exhibited in FIG.3.29(b) due to the input static eccentricity. This modulated frequencies become more evident in the angular spectrum of the case with the static eccentricity of 50%E_e shown in FIG.3.29(c). Apart from these, more frequency components like the double supply frequency 4 ev/rev and its modulations with the harmonics of the stator slot frequency are shown up in its spectrum. It indicates that more harmonics about the power supply frequency and their combinations with the harmonics of the stator slot frequency will be induced in the rotational movement of the system with the increase of the input eccentricity value. As a consequence, the variation amplitude of the electromagnetic torque generated in the case with 50%E_e illustrated in FIG.3.28(c) is a little larger than the former two. Similarly as discovered in the IM,

the radial eccentricity will effectively influence the rotational movement. Therefore the dynamic behavior in both the radial movement and the rotational movement should be considered at the same time in the model of the electrical motor.

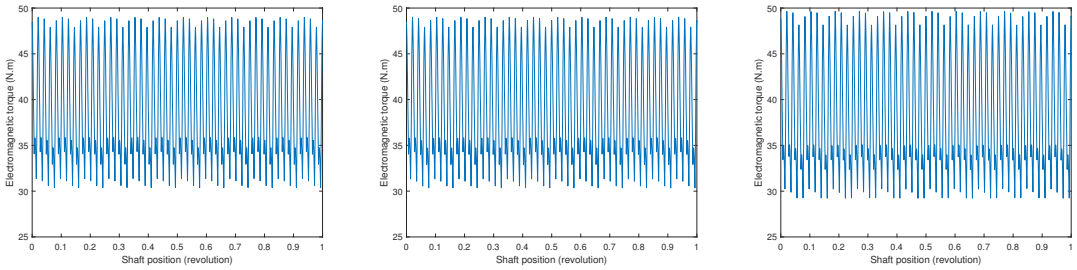

(a) Without eccentricity (b) With $10\%E_e$ (c) With $50\%E_e$

Figure 3.28: Variation of the electromagnetic torque as the function of the shaft position.

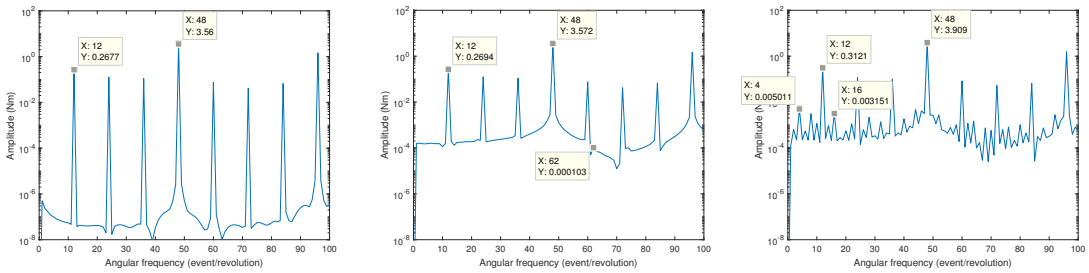

(a) Without eccentricity (b) With $10\%E_e$ (c) With $50\%E_e$

Figure 3.29: Angular spectrum of the electromagnetic torque.

The last comparison is concentrated on the simulated UMP in the reference PMSM model. Since there is no UMP generated in the case without eccentricity, only the simulation results in the two cases with different input static eccentricity values are presented respectively in FIG.3.30. Since the input static eccentricity value is set up on the x-axis, the UMP x-axis component force F_{emx} is fluctuated around a non-zero value. Different from the UMP offset angle obtained in the IM, the UMP y-axis component force F_{emy} simulated from the PMSM model varies around zero because there is no windings existed in the rotor part of the reference PMSM so that no UMP offset angle will be generated due to the equalizing currents effects. It is obvious that the waveform of the F_{emx} simulated from the case with $50\%E_e$ is more fluctuated than that generated in the case with $10\%E_e$. Therefore, when comparing their angular spectrum illustrated in FIG.3.31, the double power supply frequency 4 ev/rev and its combinations with the harmonics of the stator slot frequency are emerged in the case with a larger eccentricity value. Apart from these, the power supply frequency 2 ev/rev, the harmonics of the stator slot frequency 12

ev/rev and the combinations between the two are also existed in the two angular spectrum of F_{emx}.

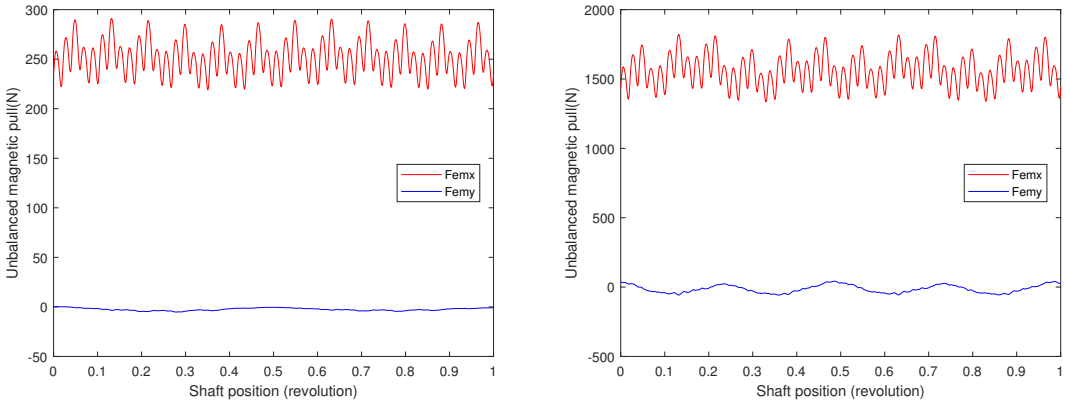

(a) With 10%E_e (b) With 50%E_e

Figure 3.30: Variation of the UMP as the function of the shaft position.

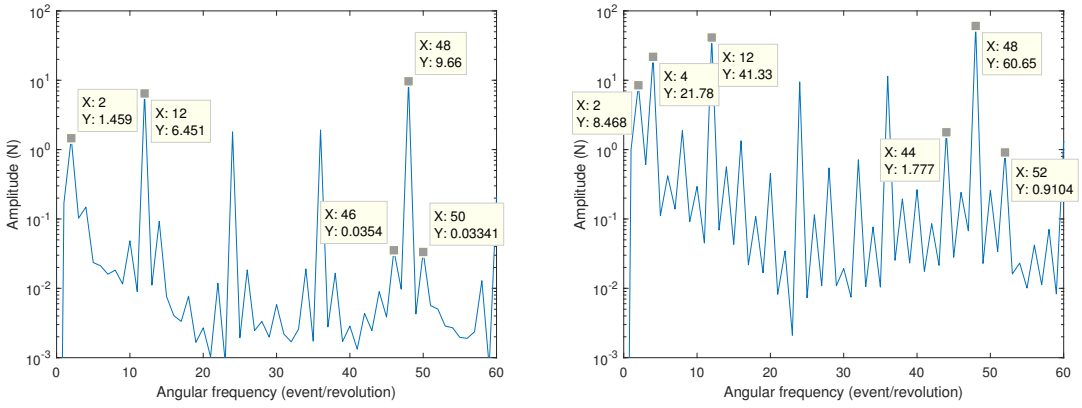

(a) With 10%E_e (b) With 50%E_e

Figure 3.31: Angular spectrum of the UMP x-axis force.

3.10.2 Analysis of simulation results from Model EMM2

Model EMM2 is adopted to perform the simulations in this subsection. It is firstly used to verify the two setting methods about the load torque proposed in SEC.3.8.1 by analyzing the generated instantaneous rotation speed in the stationary operation. Then it is employed in the non-stationary operation with a mass unbalance excitation to study the dynamic behavior of the reference PMSM in three different aspects.

3.10.2.1 In the stationary operation

As mentioned before, the two simulations are realized here at the rated operating point in the case without any eccentricity. EQ.3.66 is firstly applied to achieve the instantaneous angular speed in FIG.3.32. It is reasonable that the simulated rotation speed is almost a constant value with a small variation during all the simulation thanks to the rotational equilibrium at each moment. The small variation is due to the slot effects because the harmonics of the stator slot frequency are also identified in the angular spectrum of the instantaneous angular speed.

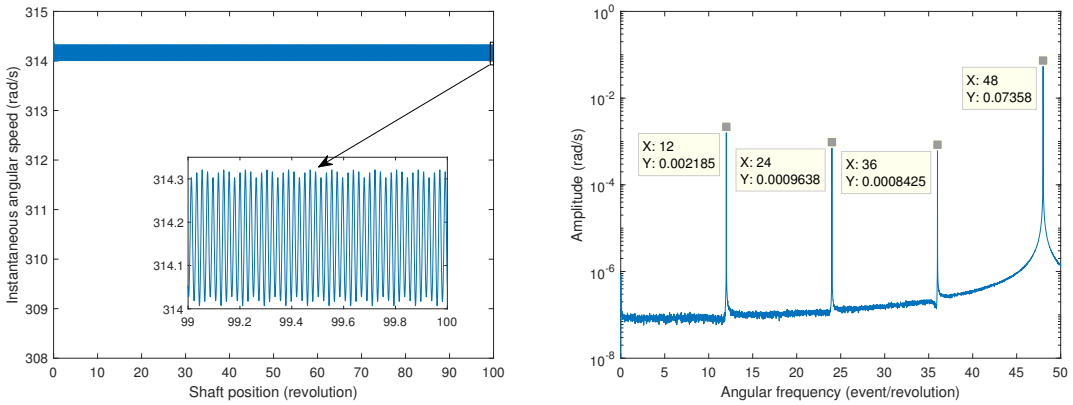

(a) Variation waveform

(b) Angular spectrum

Figure 3.32: Variation of the instantaneous angular speed and its angular spectrum by applying $T_r(t) = T_{em}(t)$.

Secondly, a viscous damping is added in the load torque to reach the steady state by adopting EQ.3.67. Its simulation result about the instantaneous rotation speed is displayed in FIG.3.33. With two appropriate coefficient values, the rotation speed increases gradually from an initial value to the synchronous speed as shown in FIG.3.33(a). The same characteristic frequencies are also revealed in its angular spectrum from FIG.3.33(b).

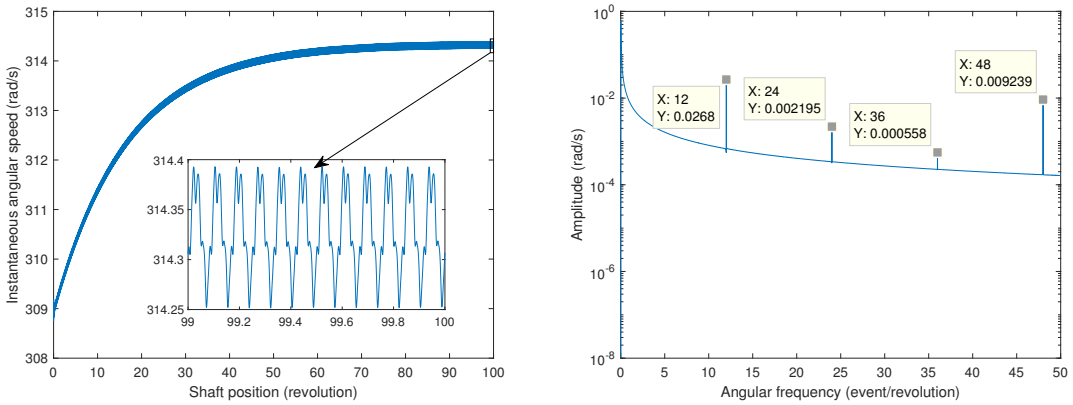

(a) Variation waveform (b) Angular spectrum

Figure 3.33: Variation of the instantaneous angular speed and its angular spectrum by adding a viscous damping.

3.10.2.2 In the non-stationary operation

Since the PMSM is designed to operate at a fixed load torque, the simulations in the non-stationary operation are realized always at the rated state ($\theta_{r0} = 65°$) but with the sweep of the rotation speed value. In order to get a clear and comprehensible analysis, the shaft rotation speed is designed to increase linearly as function of the time from the initial value zero by defining the external force of the rotational DOF about the node of the motor with a constant value. The angular acceleration value $\ddot{\theta}_r$ could be changed by modifying this constant value. The mass unbalance excitation with the same balancing class adopted in the IM ($G = 2.5mm \cdot s^{-1}$) is applied in the simulation to study the dynamic behavior of the reference PMSM under the influence of the mass unbalance excitation in the non-stationary operation. The analysis are going to be discussed in three different aspects hereafter.

Simulation results at a certain angular acceleration By increasing linearly the shaft rotation speed from 0 Hz to 228.8 Hz during 20 s as shown in FIG.5.17(a), the variation of the other simulation results [1] about the simulated stator path currents i_{sv} and the calculated electromagnetic forces T_{em} and UMP in the case with $\ddot{\theta}_r = 71.81\ (rad/s^2)$ are presented respectively as function of the instantaneous angular speed in FIG.3.34. A disturbance appears at almost the same angular speed around 50 Hz in the waveforms of all three simulation results mentioned before. From the zoom view of the perturbation part in the variation of the stator path currents shown in FIG.5.17(b), a large disequilibrium between the four path currents in the same phase are identified in this region. A second

[1] Here only the first critical speed is under consideration and the simulation results may be overestimated due to the assumption of linearized iron core materials.

amplification of the waveform emerges at about 107 Hz in the variation of UMP from FIG.5.17(d) but the amplitude of this second amplification is smaller than the first one.

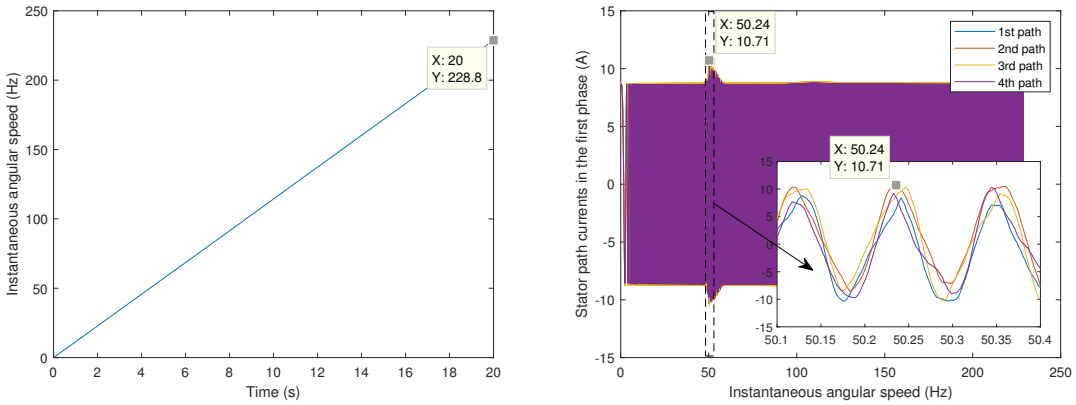

(a) $\dot{\theta}_r$ (b) i_{sv}

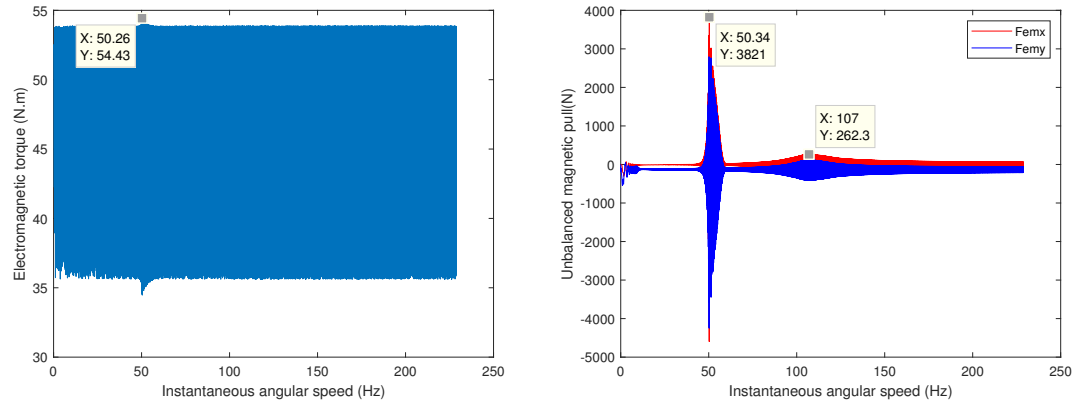

(c) T_{em} (d) UMP

Figure 3.34: Variation of different simulation results in the case with $\ddot{\theta}_r = 71.81\ (rad/s^2)$.

It is reasonable that the similar two peaks arise also in the variation of the simulated rotor center displacements as illustrated in FIG.5.18(a) since there is a positive correlation between the UMP and the radial displacements of the rotor center. The radial displacements along the x and y direction have nearly the same variation form except for a shift between their global values due to the rotor gravity effect in the y direction. The spectrogram of the radial displacements along the x direction is displayed in FIG.5.18(b) and a critical speed at mode 2 is observed at 100 Hz in the dangerous vicinity of the nominal shaft speed 3000 rpm. It is similar to the severe vibration problem appeared in the ARES motor® according to its experimentally measured vibration response spectrum as a function of the shaft's rotation speed from FIG.5.18(c). It is indicated that the proposed model is capable to reproduce the similar vibration phenomena discovered from the real machine.

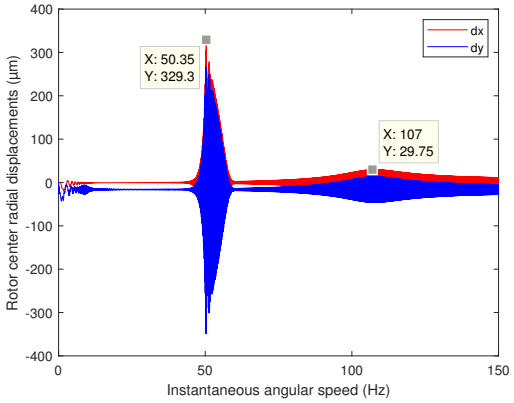

(a) Rotor center displacements

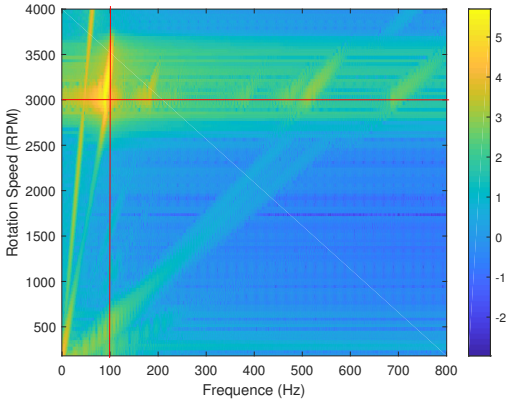

(b) Spectrogram of dx

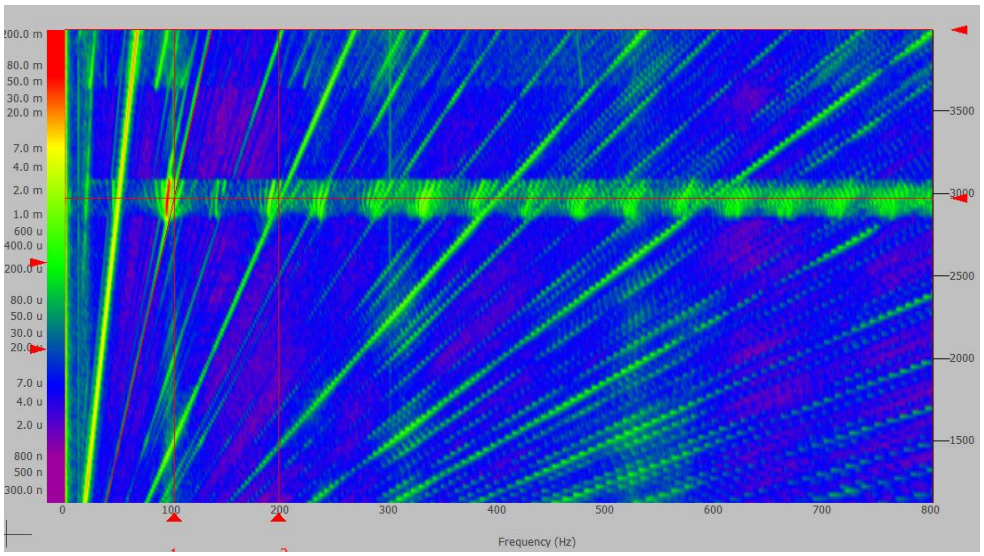

(c) Radial vibration about ARES motor® from NIDEC Leroy Somer

Figure 3.35: Comparison between the simulation result and measuring result about the radial vibration.

UMP effect in the system with mass unbalance excitation The UMP effect in the system with mass unbalance excitation is investigated in the case with the same angular acceleration ($\ddot{\theta}_r = 71.81\ rad/s^2$). The rotor center radial displacements generated in the case without UMP effect are illustrated in FIG.5.19(a) to compare with that simulated in the case excited also by the generated UMP from FIG.5.19(b). There is only one peak appeared around 150.9 Hz in the case with only mass unbalance excitation which corresponds to the first natural frequency of the mechanical structure. However as discussed before two peaks emerge in the simulation result when UMP is taken into consideration. The amplitude of the second peak and that of the peak from the case without UMP are

in the similar size so that they are considered as the response of the mass unbalance excitation. Since the two peaks induced by the mass unbalance excitation arise at different shaft oscillation frequencies and the frequency obtained in the case with UMP (107 Hz) is smaller than the other one (150.9 Hz), it indicates that UMP acting on the rotor system displays a negative stiffness effect so as to reduce the system global stiffness and the natural frequency as discovered in many other literature [128, 132, 133, 135, 158, 168]. Therefore, in some researches about the analysis of the electromagnetic vibration in the electrical machine, UMP is often appeared as an equivalent negative spring in the rotor system [139, 163, 179].

Another peak with a higher amplitude arises at around 50.35 Hz in the case with UMP from FIG.5.19(b). According to the magnetic field harmonic analysis mentioned in [143], it turned out that in a PMSM self-excited rotor vibrations related to stator parallel branches may occur around the critical speed ω_c:

$$\omega_c \approx \frac{\tilde{\omega}_0}{P} \tag{3.69}$$

where $\tilde{\omega}_0$ is the reduced natural frequency under the UMP effect. Hence in the reference PMSM with two pole pairs, the critical speed due to the self-excited rotor vibration is calculated as $\omega_c = 107 \div 2 \approx 53.5$ Hz which is close to the 50.35 Hz where the higher peak emerges. By comparing the two peak amplitudes appeared in the case with UMP, it is also demonstrated that the self-excited rotor vibrations induced by the UMP excitation are more risky than the normal vibrations excited by the mass unbalance in the electrical machine.

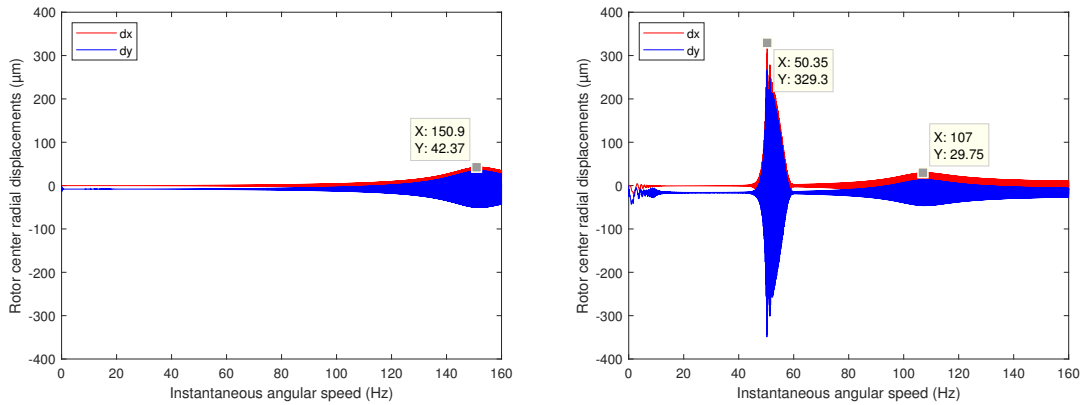

(a) Without UMP (b) With UMP

Figure 3.36: Comparison of the rotor center radial displacements between the cases without and with the UMP.

Influence of different angular accelerations After finishing the analysis of the simulation results in the case with the angular acceleration equaled to 71.81 rad/s^2, the other

simulations with four different angular acceleration values are realized to study their influence on the mechanical behavior of the reference PMSM. Among the four selected angular accelerations, two of them are bigger than the discussed one while the other two are smaller [2]. The simulation results about the rotor center radial displacements are chosen to perform the comparison between the five cases. It is found that the rotor-stator contact happens in the cases with the smaller angular accelerations. The instantaneous shaft rotation speed value when the contact occurs is saved as the contact speed. The contact speeds in different cases are available in TAB.3.2 and it can be seen clearly that no rotor-stator contact happens in the cases with larger angular accelerations while the contact speed tends to decline with the decrease of the angular acceleration. The variation of the rotor center displacements as a function of the shaft rotation speed in the three cases without the rotor-stator contact are illustrated respectively in FIG.3.37. The two peaks analyzed before exist in all of three images. The one excited by the mass unbalance emerges almost at the same shaft oscillation frequency (107 Hz) with the same amplitude (29.7 μm) since the mass unbalance eccentricity isn't modified in three cases. However those induced by the UMP vary with the variation of the angular acceleration: with the decrease of the angular acceleration values, the amplitude of this peak increases while their frequency reduces. In this trend, if the angular acceleration continues to drop from 71.81 rad/s^2, the maximum rotor radial displacement will be increased to touch the stator inner ring at a frequency smaller than 50.35 Hz considering that the air-gap average length of the reference PMSM is just 550 μm. Therefore the influence of different angular acceleration values on the dynamic behavior of the PMSM under the mass unbalance excitation could be explained as: if the shaft rotation speed varies with a high angular acceleration, it will pass the potential resonance region quickly enough to avoid the amplification of the rotor radial displacements at the critical speed. Otherwise, il will have enough time to stay in the resonance region in order to excite a larger amplitude at the critical speed. However it should be noted that the variation of the angular accelerations doesn't change the value of the critical speed.

Angular acceleration $\ddot{\theta}_r$ (rad/s^2)	753.95	100.53	71.81	62.83	50.27
Contact speed (Hz)	NO	NO	NO	49.01	47.46

Table 3.2: Rotor-stator contact speed at different angular accelerations.

[2]Here, the largest angular acceleration 753.95 rad/s^2 is unrealistic which is chosen only to simulate the comparison result.

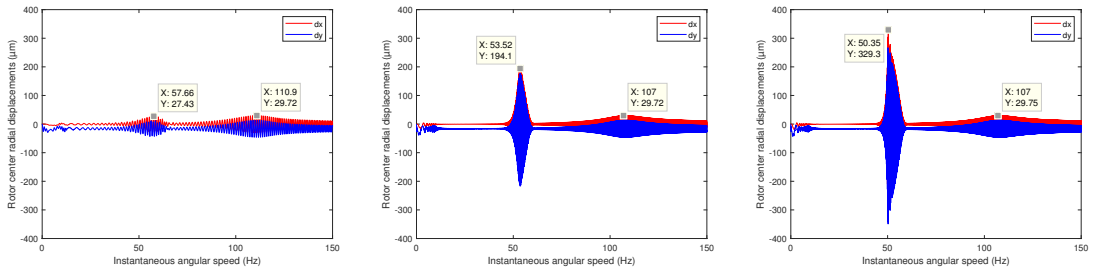

(a) $\ddot{\theta}_r = 753.98\ (rad/s^2)$ (b) $\ddot{\theta}_r = 100.53\ (rad/s^2)$ (c) $\ddot{\theta}_r = 71.81\ (rad/s^2)$

Figure 3.37: Rotor center radial displacements at different angular accelerations.

3.11 Conclusions

Extended from the asynchronous motor model established in CHAP.2, two models with different geometries about the reference PMSM are developed in this chapter for the analysis of the dynamic behaviors of the synchronous motor respectively in the case with and without the magnetic saturation effect. Three different physical fields in the PMSM are re-described according to the differences between the asynchronous and the synchronous motor. In the magnetic model, the permeance network associated with the rotor part are redefined according to the geometry of the rotor with the buried PMs so that all the active and passive elements in the permeance network are re-calculated such as the permeances in the rotor part and the MMF brought by the PMs. Two sets of air gap permeance are defined to better describe the magnetic flux distribution in the air gap of the PMSM. And then in the electrical model, a new winding configuration with two branches connected in parallel is set up in each stator phase and the whole machine is supplied by the 3-phase current source. Thirdly in the mechanical model a customized mechanical structure is introduced to adapt to the assumption of 2.5D electromagnetic model and to prepare for the future experimental part. With a given stator phase current amplitude, the torque angle is identified in the proposed model. By making the 3-phase current vary in the synchronism motion of the rotor, the initial angular position θ_{r0} is chosen as the alternative expression of the torque angle in the PMSM to control the operating point. This strategy is adopted in both the multiphysics coupled model and in the model decoupled with the mechanical part because there is no negative feedback relationship in the PMSM between T_{em} and ω_r as described in the Torque-Speed curve of the asynchronous motor. Since no control system is considered in the present PMSM model, the rotation speed should be predefined through the allocation of the load torque.

The proposed model is able to perform simulations in the case without and with the magnetic saturation effect by considering the permeances in iron core parts as the constant or variables. When these permeances vary as the function of the passing magnetic flux, the original linear augmented magnetic equations become nonlinear which should be solved by the iteration method at each step of the global differential equations. This

will evidently increase the simulation time. In order to overcome this difficulty for the required longtime simulation in the non-stationary operation, an equivalent model is created by removing the two rotor iron bridges in the original identical model. Different models with different setting properties based on the identical model and the equivalent model are established in both FEMM and MATLAB softwares. The abbreviations of their names are available in TAB.3.1. By comparing the Torque-Angle curve between Model FEMM1 and Model FEMM2, the later is confirmed as a good alternative choice for the simulation without the magnetic saturation effect. The proposed models are validated in two aspects by comparing Model EM with the corresponding Model FEMM in the quasi-static regime. The first is effectuated at the rated operating point through the comparison between Model EM1 and Model FEMM1 about the waveforms of electromagnetic torque and of the UMP x-axis force. It is demonstrated that there are differences between their variation amplitude or their average value but their fluctuation profiles are similar. The difference could be caused by the rough permeance network mesh in the air gap and the similarity in their waveforms confirm the reliability of studying the frequency components with Model EM1. Since the difference about the average value of F_{emx} becomes smaller in the equivalent model, it proves that adopting the equivalent model in the analysis of radial vibration under the mass unbalance excitation may not be accurate enough but is still reliable. The second comparison is realized at all the operating points by comparing their Torque-Angle curves in respectively the identical model and the equivalent model. They all correspond with each other in the general profile and the better agreement between the two curves in the equivalent model proves it as the good choice to perform the simulations in the non-stationary operation.

Since there is no big difference between Model EM and Model EMM as discussed in CHAP.2, Model EM1 is employed firstly to study the characteristic phenomena of the simulation results at the rated operating point but with different input eccentricity values. More imbalance between the parallel paths appear in the waveform of the stator path currents in the same phase with the increase of the input eccentricity value and this introduces more harmonics of the power supply frequency in the system. The increase of the static eccentricity value doesn't have much influence on the waveform of the electromagnetic torque but it generates the double supply frequency and the combination of its harmonics with the stator slot harmonics in the rotational movement. Different from the UMP offset angle identified in the IM, the average value of the UMP y-axis force is zero in the PMSM because there is no equalizing currents induced in the rotor part. More evident undulations emerges in the UMP waveforms with the increase of the eccentricity value and meanwhile similar as identified in the electromagnetic torque, more harmonics of the double supply frequency and their modulations with the stator slot harmonics arise in their spectrum.

Model EMM2 is then adopted to study the waveform of the predefined instantaneous angular speed in the stationary operation and to analyze the vibration performance under the mass unbalance excitation and the rotor gravity in the non-stationary operation. The two methods to allocate the load torque parameters in order to maintain the rotation speed in the permanent state are validated in the case without any eccentricity. Some fluctua-

tions appear in the variation of rotor instantaneous speed due to slot effects because stator slot harmonics are identified in its spectrum. The simulations in the non-stationary operation are performed at the rated operating point but with a linearly increased rotation speed. They are analyzed in respectively three different aspects. First is about the analysis of all simulation results at a certain angular acceleration. By plotting the simulation results as function of the instantaneous rotation speed, two disturbances are identified in the variation of UMP and of the rotor center radial displacements while the first one also appears in the other simulation results like the stator path currents and the electromagnetic torque. The amplitude of the first disturbance is bigger than that of the second one but the first occurs at about 50 Hz while the second arises at 107 Hz. The spectrogram of the simulated radial displacements is similar to the severe vibration problem happened in the actual motor which means that the proposed model is capable to reproduce the similar vibration phenomena discovered from the actual machine. The second analysis is about the UMP effects in the system with mass unbalance excitation. By removing the generated UMP from the original simulation and comparing the two simulated radial displacements in the case with and without UMP, it is observed that the UMP displays a negative stiffness effect in the motor system and it will induce a self-excited rotor vibration at the critical speed $\omega_c \approx \frac{\tilde{\omega}_0}{P}$. The influence of different angular accelerations is analyzed thirdly. Through the simulations with different angular accelerations, it is indicated that the amplitude of the first disturbance increases with the decrease of the angular acceleration until the occur of the rotor-stator contact while the second disturbance always appears at the same rotation speed and has the same amplitude size which confirms that it is induced by the modified natural frequency.

In general, the extended multiphysics model based on angular approach for the PMSM is capable to simulate its dynamic behaviors in both the cases with and without the magnetic saturation effects for respectively the analysis of the frequency components in the case with magnetic saturation effects and for the study of the vibration performance in the case without magnetic saturation effects. The two studies are considered to combine together in the future. And the equivalent model with the mass unbalance excitation is adopted to investigate the influence of different mechanical structures in CHAP.4.

Chapter 4

Influence of different architectures

Contents

4.1 Introduction

As one of the main goals of this research, the influence of different architectures on the dynamic behavior of the electrical machines are analyzed in this chapter by adopting the proposed model. Since it is a multiphysics model with the strong electro-magneto-mechanic couplings, the architecture influences could be studied in two aspects: about different mechanical structures and with different winding configurations. To avoid the repetitive, the former is discussed in the frame of the reference PMSM model while the latter is realized in the model of the IM.

4.2 Different mechanical structures

The equivalent linear model about the reference PMSM (Model EMM2) established in CHAP.3 is adopted to study the influence of different mechanical structures. The reason to chose the PMSM for this study is because some instability phenomena are identified in an integrated PMSM connected with a screw compressor in a cantilever structure as mentioned in SEC.1.1. In order to obtain a global view about the influence of mechanical structures, the analysis is firstly effectuated in the classical structure to discuss the influence of different mechanical parameters and then switched to the cantilever structure of the same shaft length in order to study the influence of different length arrangements. All the researches in this section are based on the simulations with a fixed angular acceleration $\ddot{\theta}_r = 71.81\ rad/s^2$ in consideration of the rotor gravity and the mass unbalance excitation.

4.2.1 Classical structure

The classical structure means that the two bearings are set up on the two sides of the electrical machine to support the whole system. The mechanical structure described in FIG.3.15 is employed to realize the following researches about the influence of three different mechanical parameters.

4.2.1.1 Influence of different bearing stiffness

As mentioned in SEC.1.2.4.1, the bearing is represented by two identical orthogonal stiffnesses in the current mechanical structure. The equivalent bearing stiffness k is assigned with three different values arranged in the ascending order: 1e7, 5e7 and 1e8. The middle one is the reference value since it is used in the reference PMSM model as discussed before. The modification of the stiffness value leads to the variation of the first natural frequency of the mechanical structure. The increase of the equivalent bearing stiffness increases the first natural frequency as displayed in TAB.4.1. As the consequence of the natural frequency variation, the rotor-stator contact occurs at the beginning of the simulation in the case with a relative soft stiffness according to TAB.4.2. The variation of the rotor center radial displacements as a function of the shaft rotation speed in the other

two cases are illustrated respectively in FIG.4.1. One can see that the critical speeds of the two peaks increase a little with the increase of the natural frequency but the relation between the two critical speeds remains the same since the number of the pole pairs of the electric motor doesn't change. Furthermore, it is obvious that the relative rigid stiffness could reduce the amplitude of the resonance excited by the UMP.

Equivalent bearing stiffness k $(N \cdot m^{-1})$	1e7	5e7	1e8
F1 (Hz)	113.48	150.91	157.94

Table 4.1: First natural frequency of the mechanical structure with different bearing stiffness.

Equivalent bearing stiffness k $(N \cdot m^{-1})$	1e7	5e7	1e8
Contact speed (Hz)	0.3925	NO	NO

Table 4.2: Rotor-stator contact speed with different bearing stiffness.

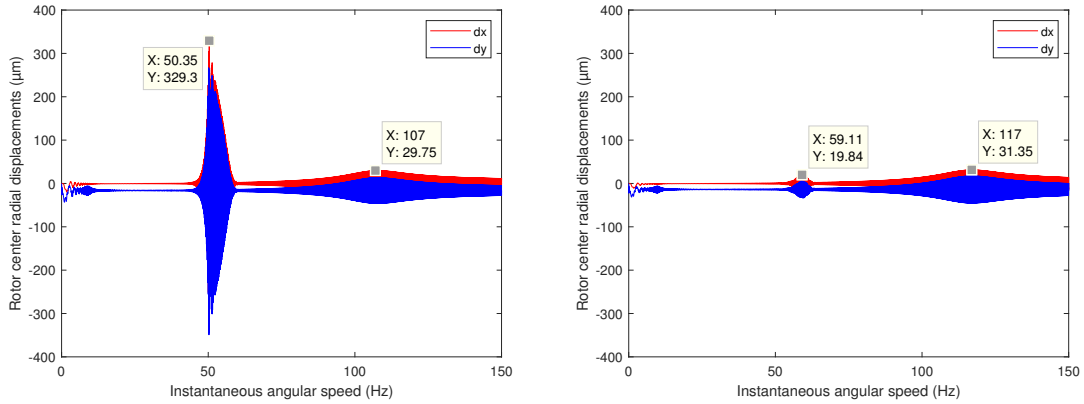

(a) $k = 5e7\ N \cdot m^{-1}$ (b) $k = 1e8\ N \cdot m^{-1}$

Figure 4.1: Rotor center radial displacements with different bearing stiffness.

4.2.1.2 Influence of different structural damping

The second mechanical parameter needs to be studied is the modal damping ratio d. It was chosen to be 0.07 in the original mechanical structure. The other two values of d that one is bigger and another is smaller than the reference value are applied to the structure. It should be known that the variation of the damping factor doesn't modify the natural frequency of the mechanical system but it will affect the vibration amplitude. Therefore, the rotor-stator contact emerges in a less buffered system from TAB.4.3 and the resonance peak excited by the UMP is obviously reduced in the structure with a larger modal damping ratio according to the comparison illustrated in FIG.4.2. It demonstrated

that increasing the structural damping of the system is an efficient way to reduce the risk of the rotor-stator contact due to the UMP.

Modal damping ratio d	0.01	0.07	0.1
Contact speed (Hz)	46.44	NO	NO

Table 4.3: Rotor-stator contact speed with different structural damping.

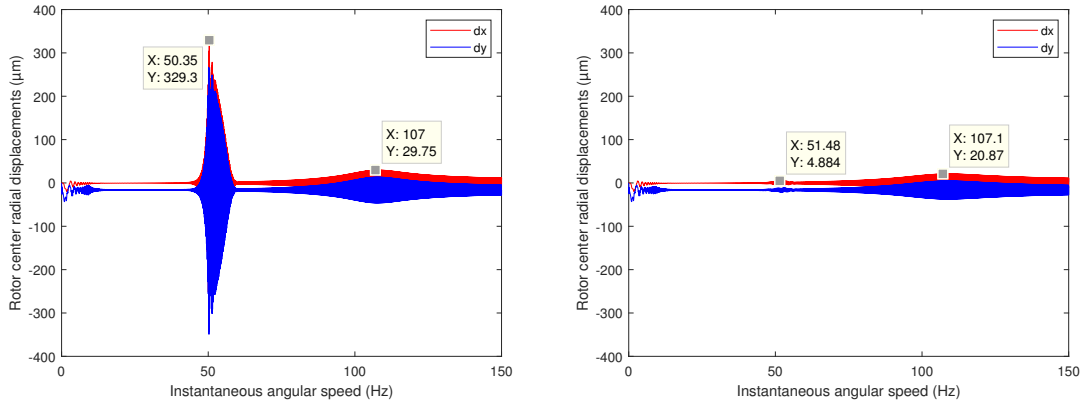

(a) $d = 0.07$ (b) $d = 0.1$

Figure 4.2: Rotor center radial displacements with different structural damping.

4.2.1.3 Influence of different mass eccentricity

The third analysis is focused on the influence of different mass eccentricity. By adopting EQ.2.130, the reference magnitude of the mass eccentricity is calculated as $\delta_m = 8e^{-6}\ m$ at the synchronous speed equal to 314.2 rad/s. Similarly, the other two mass eccentricity values that is bigger and smaller than the reference magnitude are set up in the simulation. The alterations in their simulation results about the rotor center radial displacements are compared in FIG.4.3. There is not so much changes about the first peak excited by the UMP with the variation of the mass eccentricity magnitudes. However, the amplitudes of the second peak are increased linearly with the increase of the mass eccentricity magnitudes even if they all appear at the same shaft rotation speed. It confirms the conclusion deduced in SEC.3.10.2.2: the lower peak emerged at 107 Hz is excited by the mass unbalance excitation so that its amplitude is linearly related to the magnitude of the mass eccentricity.

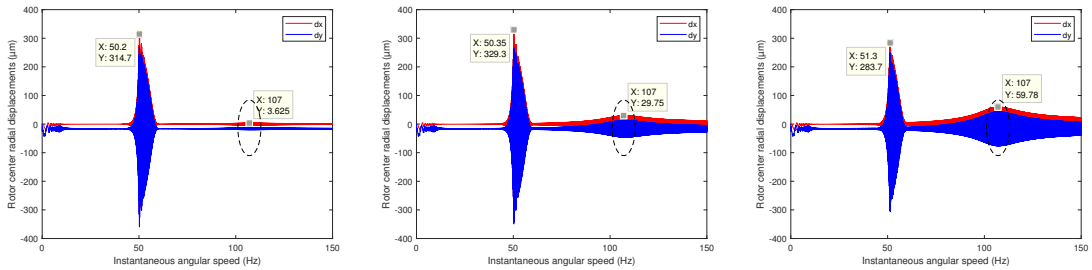

(a) $\delta_m = 1e^{-6}\ m$ (b) $\delta_m = 8e^{-6}\ m$ (c) $\delta_m = 16e^{-6}\ m$

Figure 4.3: Rotor center radial displacements with different mass eccentricity.

4.2.2 Cantilever structure

As illustrated in FIG.4.4, the cantilever structure describes the situation that the electrical machine is installed at the end of the shaft with two supported bearings set up on the same side of the electric motor. Based on the traditional Timoshenko beam theory, this structure is discretized into several beam and node elements. The load torque T_r is set on the node of the screw compressor while the electromagnetic forces T_{em}, F_{emr} and the gravity of the rotor part Mg are applied on the node of the electric motor. The disturbance induced by the screw compressor is also one of the excitation sources in the whole system but it isn't taken into consideration in this study. This kind of structure is potentially unstable. By modifying the length arrangement of each part, the similar cantilever structure in two versions are created to study their influence in the mechanical behavior of the reference PMSM.

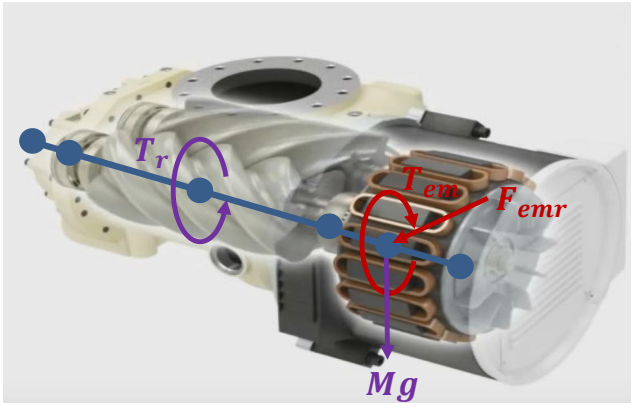

Figure 4.4: A discretized cantilever structure extracted from a screw compressor with an integrated PMSM.

4.2.2.1 Influence of different length arrangement

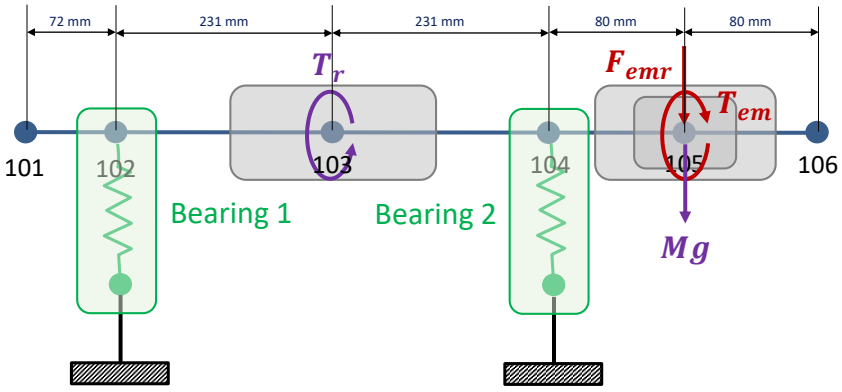

(a) Cantilever structure V1

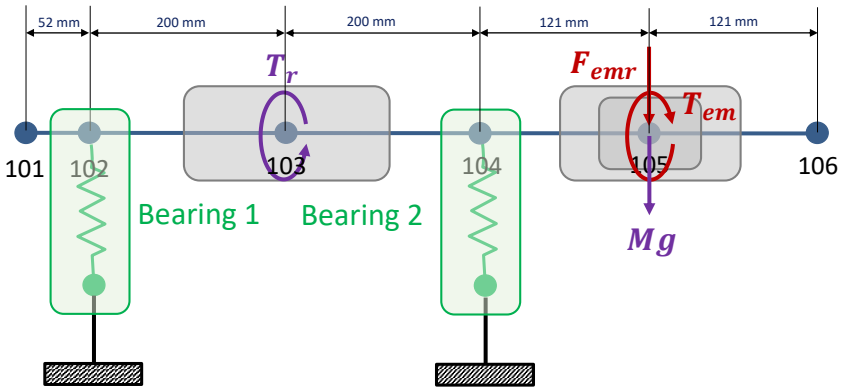

(b) Cantilever structure V2

Figure 4.5: Discretized cantilever structure in two versions with different length arrangement.

The two versions of the cantilever structure are illustrated separately in FIG.4.5. Their shaft entire lengths are designed to be the same as that of the classical structure from FIG.3.15 to conduct the comparison between those three mechanical structures. Their first natural frequencies are available in TAB.4.4. It turned out that the natural frequency decreases in the structure with more shaft length arranged on the electrical machine side as shown in FIG.5.24(b). As the consequence, the rotor-stator contact occurs at the beginning of the simulation in the structure "Cantilever V2" from TAB.4.5. The comparison about the rotor center displacements between the classical structure and the first version

of the cantilever structure is displayed in FIG.4.6. It can be seen that the first peak excited by the UMP is nearly vanished in the Cantilever structure V1 who has a larger first natural frequency and its second peak induced by the mass unbalance excitation arises at the modified natural frequency (148.1 Hz) larger than that identified in the classical structure (107 Hz). It proves that increasing the first natural frequency value is also an efficient method to avoid the rotor-stator contact in the specific motor operation.

Mechanical structure	Classical	Cantilever V1	Cantilever V2
F1 (Hz)	150.91	184.64	137.62

Table 4.4: First natural frequency of the mechanical structure with different mechanical structures.

Mechanical structure	Classical	Cantilever V1	Cantilever V2
Contact speed (Hz)	NO	NO	1.6547

Table 4.5: Rotor-stator contact speed with different mechanical structures.

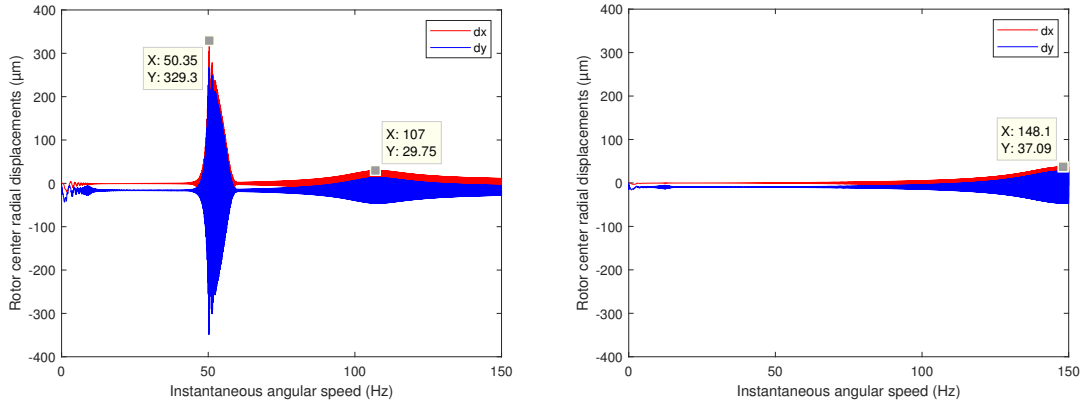

(a) Classical structure

(b) Cantilever structure V1

Figure 4.6: Rotor center radial displacements with different mechanical structures.

4.3 Different winding configurations

The winding in the electrical machine can be classified in two types: the armature winding and the field winding. The armature winding is used for the electromechanical energy conversion while the field winding produces a rotating magnetic field to change the distribution of the magnetic field in the air gap. Since the armature winding is appeared as the rotor squirrel cage in the studied IM with its configuration decided by the geometry of the rotor slots, different winding configurations about the field winding located in the

stator are going to be investigated in this section. Before the investigation, it's important to understand how to construct a 3-phase winding in the stator. As illustrated in FIG.4.7, a 3-phase winding is usually built up in five steps. The basic component of a winding is the wire. A conductor stayed in each slot is composed of several strands of wires connected in parallel. The conductors from two slots are connected in series to form a coil. The number of turns of a coil can be one turn or multiple turns and several coils in one phase band are connected in series to establish a pole phase coil group. The pole phase coil is the basic unit to constitute the winding. There may be one or several pole phase coil in a motor and each of them has a common feature that the induced EMF potentials produced from the pole phase coil in the same phase is equal in size with the same or the opposite phase. The individual pole phase coil of each phase can be connected in series, in parallel or in series-parallel according to the needs of the electromagnetic design in order to create a phase winding. Each phase winding are joined together in the Y or the delta connection to finally obtain the 3-phase winding which is prepared to connect to the external power supply.

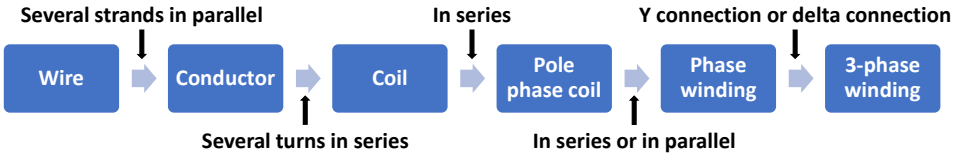

Figure 4.7: The composition of 3-phase winding.

The study about different winding configurations in this section is mainly focused on two steps from the winding composition in FIG.4.7: one is about different coil arrangements (lap winding and concentric winding) in series to form the pole phase coil and another is about different pole phase coil group connections (in series or in parallel) to develop the phase winding. The influence of different winding configurations on the dynamic behavior of the electrical machine are investigated in the frame of the IM because the same pole pairs from the modified field winding can be induced automatically in the rotor cage of the IM without modifying its geometry. The first case study is performed by adopting the 36 slots, 2 pole and 3-phase IM discussed in CHAP.2 while the second is realized by employing another larger IM which has 48 slots, 4 pole and 3-phase.

4.3.1 Comparison between lap windings and concentric windings

Compared with the lap winding displayed in FIG.2.11, the concentric winding is realized in the same IM as illustrated in FIG.4.8. The difference between the two winding patterns is easily to be recognized from their distribution schema. The lap winding is also called as the equal winding since the pitch of two single coils is equal. It is named as lap winding

because the coil ends are stacked from each other in a successive order. Therefore it has more neat and better organized coil ends. This kind of winding configuration is beneficial to the fabrication because all the coils are identical in their shape. The concentric winding is composed with the coils with different coil pitches and these coils are combined together in the form of the concentric circles. Due to its geometry, the concentric windings are usually more convenient for the mechanical wire embedding. More specially, in order to save the copper consumption by reducing the total coil span, the concentric windings realized in our case are evenly divided into two concentric circles as illustrated in FIG.4.8. In order to accommodate with these modifications in the concentric winding, only the magnetic flux transformation matrix $[Mcf]$ should be modified as shown in FIG.4.9. As mentioned in SEC.3.4, the -1 and 1 from matrix $[Mcf]$ are used to present the coils with different current circulating directions.

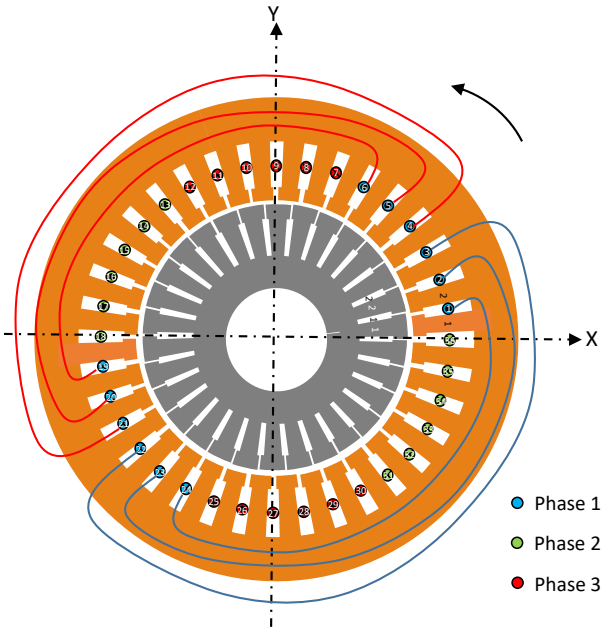

Figure 4.8: Single layer concentric winding diagram in the first phase of the stator

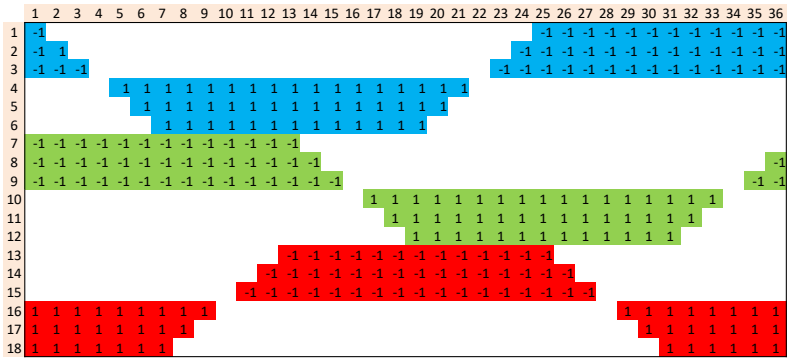

Figure 4.9: Winding matrix $[Mcf]$ distribution about a single layer concentric winding

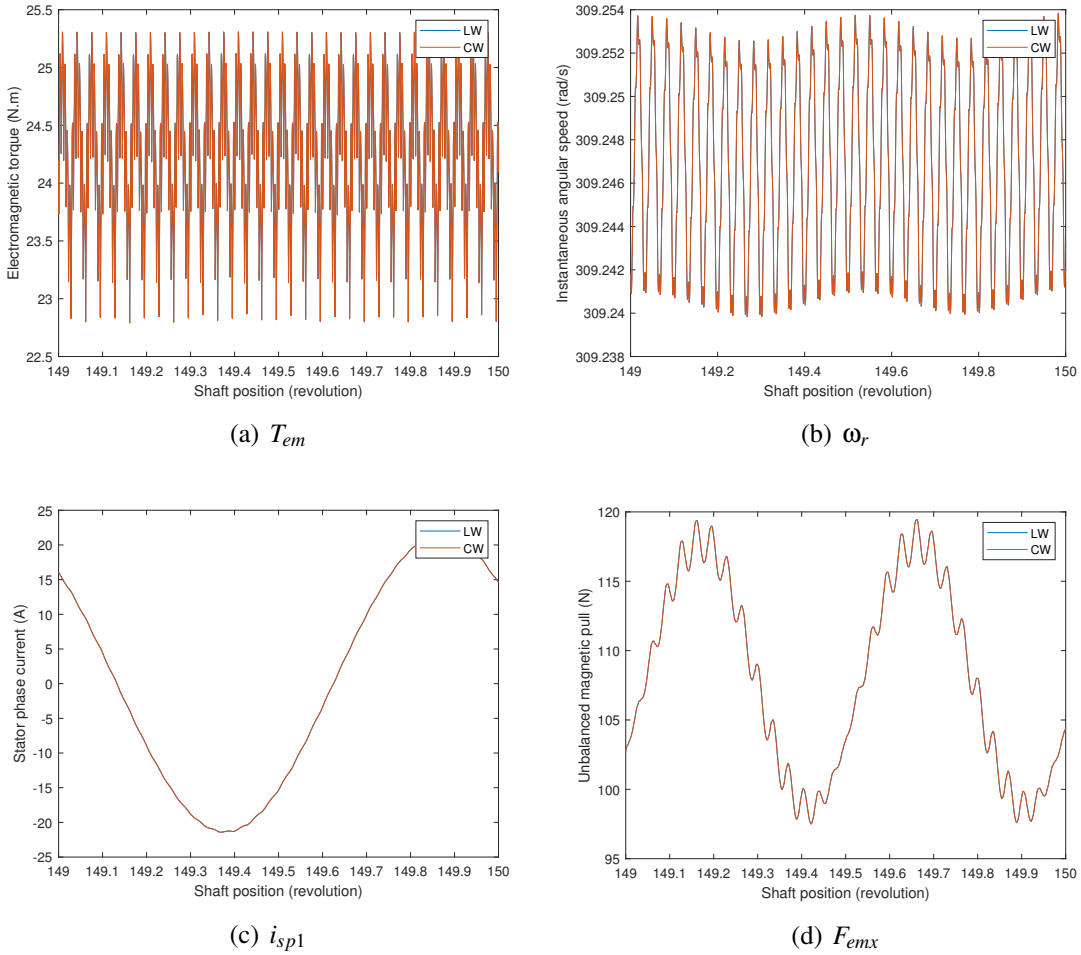

(a) T_{em} (b) ω_r

(c) i_{sp1} (d) F_{emx}

Figure 4.10: Comparison of different simulation results between lap winding (LW) and concentric winding (CW).

The simulations with two different winding arrangements are performed respectively at the rated operation point with the static eccentricity of $10\%E_e$. The comparison of their simulation results are illustrated separately in FIG.4.10. The blue curves represent the simulation results from the lap winding while the red ones refer to those simulated from the concentric winding. It can be seen clearly that the two results are almost identical which indicates that different coil arrangements (lap winding and the concentric winding) don't have any influence on the dynamic behavior of the electric motor.

4.3.2 Comparison between series and parallel windings

The second comparison is conducted between the series and parallel connections about the pole phase coil groups in each phase. Since the lap winding and the concentric winding are equivalent as discussed before, the latter is adopted in this section to adapt to more winding arrangements as illustrated in FIG.4.11. A new IM "LSES180LUR" with more poles and more slots is employed to develop more complex winding configurations. The characteristic parameters about its electromechanical part and the mechanical structure are available respectively in TAB.C.3 and TAB.C.4. Four pole phase coil groups are identified in FIG.4.11 so that totally four winding patterns could be achieved with these concentric windings as mentioned in [180, 181]. They are:

- Four pole phase coils connected in series.
- Two parallel paths with the opposite pole coils (coils with the same color) connected in series and the adjacent pole coils connected in parallel.
- Two parallel paths with the adjacent pole coils (coils with different colors) connected in series and the opposite pole coils connected in parallel.
- Four pole phase coils connected in four parallel paths.

For the sake of the simplicity, only the first three patterns are adopted and are discussed in this research to compare between the series and parallel windings. To apply three different winding patterns in the new IM, the winding current distribution matrix $[S_{abc}]$ should be developed respectively as shown in FIG.4.12 according to the currents' order distributed in each stator slot displayed in FIG.4.11. As defined before, the number of rows corresponds to the number of the stator slots while the number of columns is referred to the number of the state vectors. Three stator phase currents are chosen as state vectors in the series windings however the six path currents are considered as state vectors in the parallel windings because there could be an unbalance between the two path currents in the same phase due to the rotor eccentricity or other defeats. The set-up of different winding configurations in the proposed model is then realized through the modification of two winding matrix $[Mpf]$ and $[Mcf]$. They are going to be explained in details hereafter for the different winding configurations.

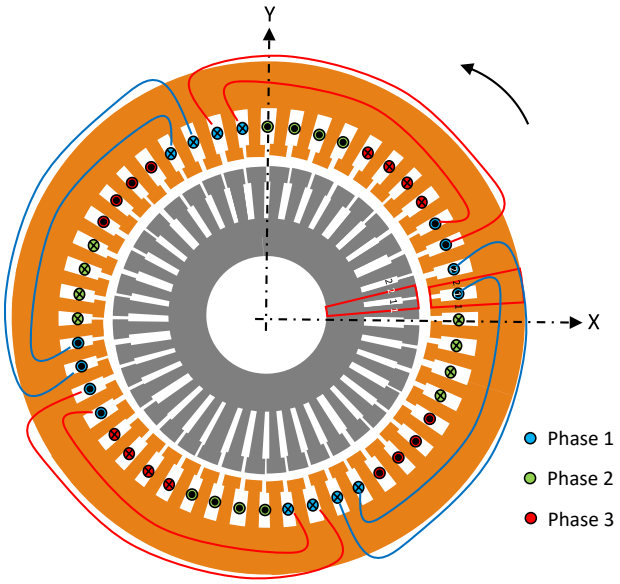

Figure 4.11: Concentric winding diagram in the first phase of the stator about the IM "LSES180LUR".

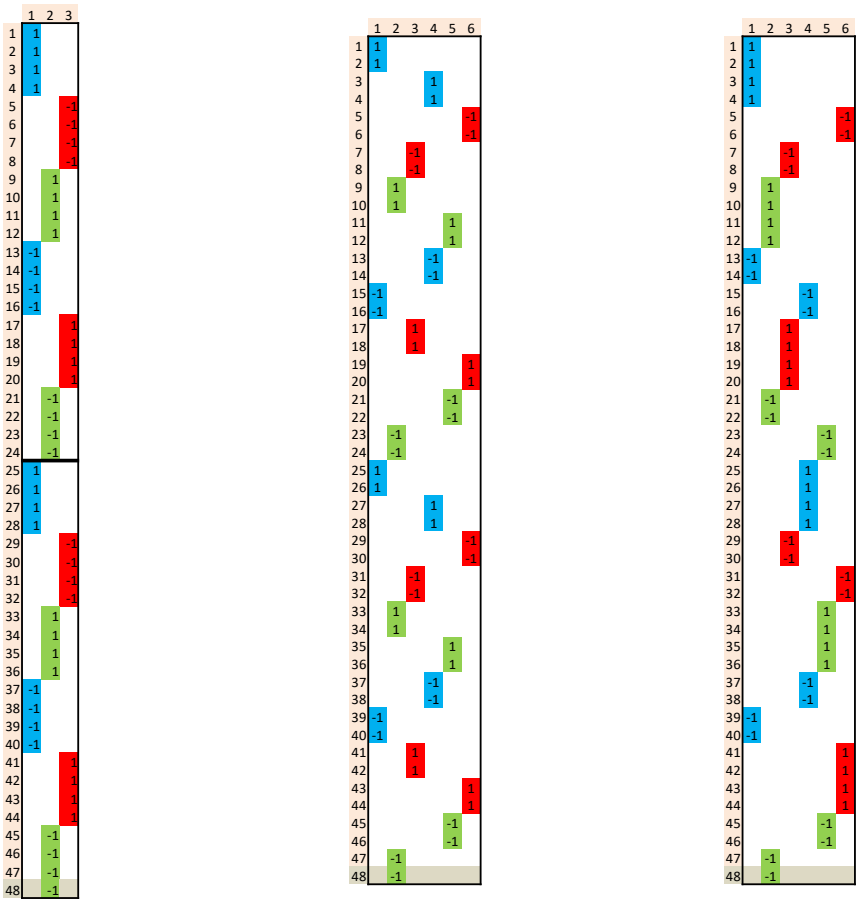

(a) Series (b) Parallel with OCS (c) Parallel with ACS

Figure 4.12: Winding current distribution matrix $[S_{abc}]$ with different winding patterns.

4.3.2.1 Series winding

Since the electrical potential and the magnetic potential generated by the AC winding and its final electromagnetic performance are only related to the connected conductors but are not influenced by their connection order, the opposite pole phase coils are chosen to connect with each other firstly and then connect with the other adjacent pole coils in series. This can be reflected in the winding matrix distribution as illustrated in FIG.4.13. The pole phase coils with the negative current orientation (the coils in blue from FIG.4.11) in each phase forms the first pole pair as displayed in the top half part of the matrix $[Mcf]$ while its bottom half part are used to present the second pole pair established by the other pole phase coils with the positive current orientations. Afterwards, the four pole phase

coils groups in each phase are connected together in series as shown in the matrix $[Mpf]$ from FIG.4.13(b).

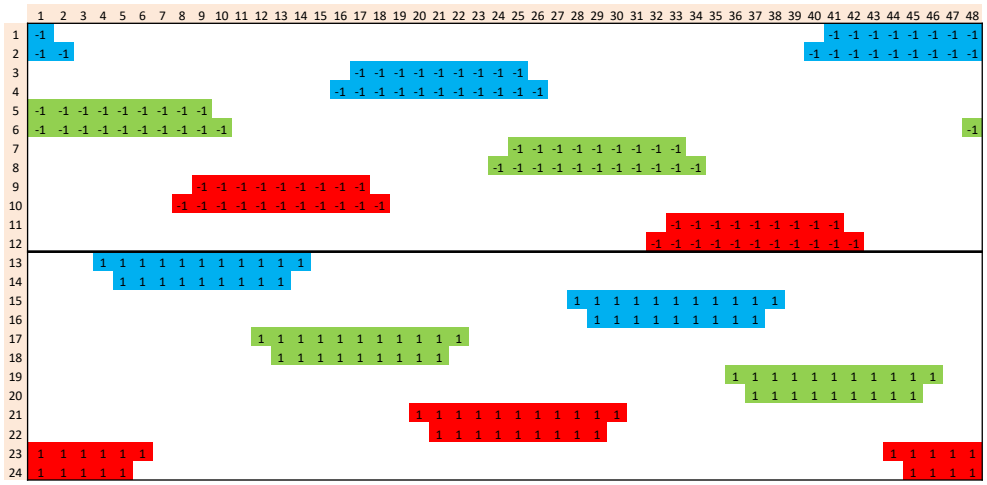

(a) $[Mcf]$

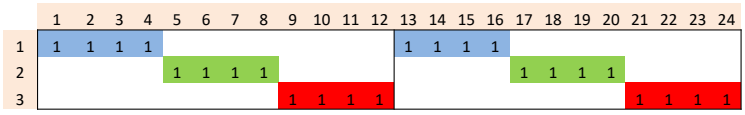

(b) $[Mpf]$

Figure 4.13: Winding matrix distribution about a single lap winding connection

4.3.2.2 Parallel winding

The 3-phase stator winding with two parallel paths in each phase is displayed in FIG.4.14. Since the Wye connection is adopted to connect the 3-phase winding to the supply voltage, the electrical differential equations deduced in SEC.2.6.1 to describe the electric circuits in the stator should be developed in the second pole pair in the case with the parallel winding. According to [2], in the Wye voltage-fed machine without common neutral line, only $(n_{ph}-1)\cdot n_v$ independent differential equations are needed to describe the whole system in consideration that the sum of currents in each parallel circuit has to be equal to zero: $i_{sv1}+i_{sv2}+i_{sv3}=i_{sv4}+i_{sv5}+i_{sv6}=0$. Therefore, the set of new electrical differential equations of the stator part as shown in FIG.4.14 based on EQ.2.76 is developed in EQ.4.1.

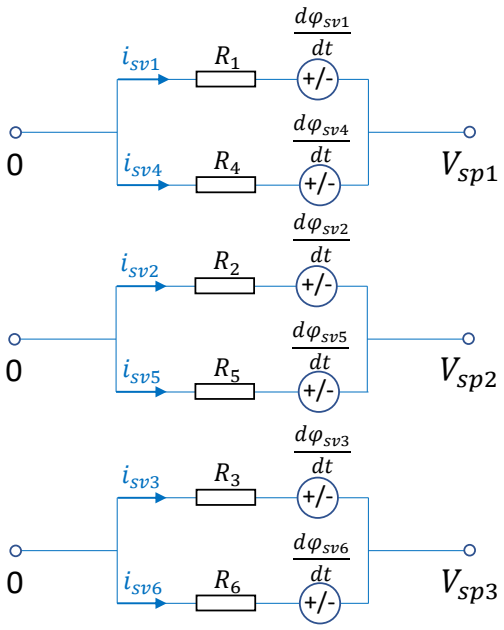

Figure 4.14: Stator parallel winding connections in three phases.

$$\begin{bmatrix} R_1 & -R_2 & 0 & 0 \\ R_3 & R_2+R_3 & 0 & 0 \\ 0 & 0 & R_4 & -R_5 \\ 0 & 0 & R_6 & R_5+R_6 \end{bmatrix} \cdot \begin{Bmatrix} i_{sv1} \\ i_{sv2} \\ i_{sv4} \\ i_{sv5} \end{Bmatrix} + \frac{d}{dt} \begin{Bmatrix} \phi_{sv1}-\phi_{sv2} \\ \phi_{sv2}-\phi_{sv3} \\ \phi_{sv4}-\phi_{sv5} \\ \phi_{sv5}-\phi_{sv6} \end{Bmatrix} = \begin{Bmatrix} \vec{V_{12}} \\ \vec{V_{23}} \\ \vec{V_{12}} \\ \vec{V_{23}} \end{Bmatrix} \tag{4.1}$$

If the three phase resistance in the series winding are assumed to be identical and equal to R_{sp}, in order to achieve the same phase resistance value in the parallel winding, the resistance value of each parallel path are adjusted as $R_1 = R_2 = R_3 = R_4 = R_5 = R_6 = 2R_{sp}$. Meanwhile in order to keep a same slot fill factor, the number of turns per coils in the parallel winding should be doubled of that in the series winding.

With the opposite coils connected in series (Parallel with OCS) The first winding pattern in the case of the two parallel paths windings is to connect the opposite pole coils in series and the adjacent pole coils in parallel as illustrated in FIG.4.15. Therefore the arrangement of the matrix $[Mcf]$ is identical to that applied in the previous series winding

as displayed in FIG.4.13(a). However, the other winding matrix $[Mpf]$ should be modified as shown in FIG.4.16 to calculate finally the magnetic flux in all six parallel paths.

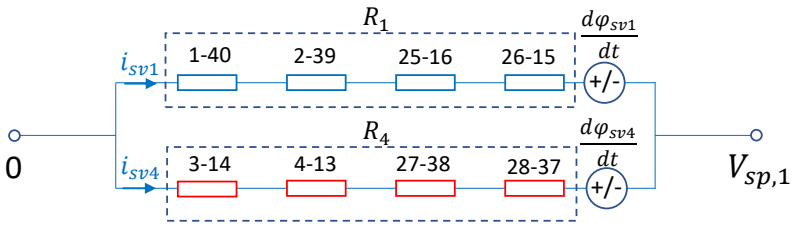

Figure 4.15: Stator parallel winding connections in the first phase.

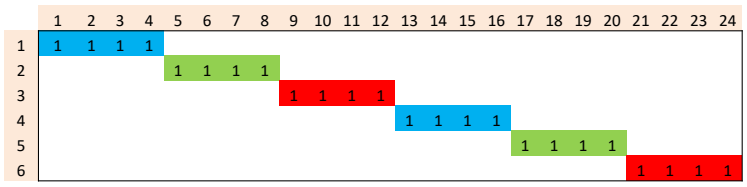

Figure 4.16: Winding matrix $[Mpf]$ distribution about the parallel winding with OCS.

With the adjacent coils connected in series (Parallel with ACS) The second winding pattern of the two parallel path windings is to connect the adjacent pole coils together in each parallel path and then combine the two branches of opposite pole coils in parallel as demonstrated in FIG.4.17. In this case, the winding matrix $[Mcf]$ should be re-arranged in FIG.4.18 to accommodate the two adjacent pole coils in each parallel paths. Meanwhile, the matrix $[Mpf]$ should be kept the same as illustrated in FIG.4.16.

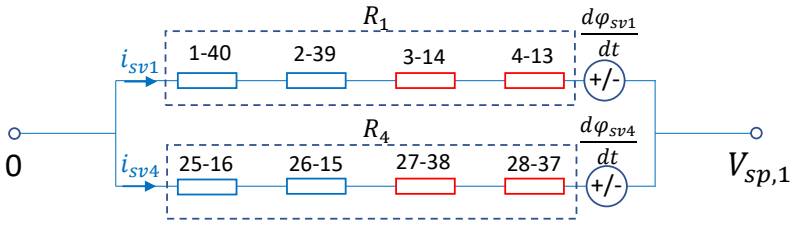

Figure 4.17: Stator parallel winding connections in the first phase

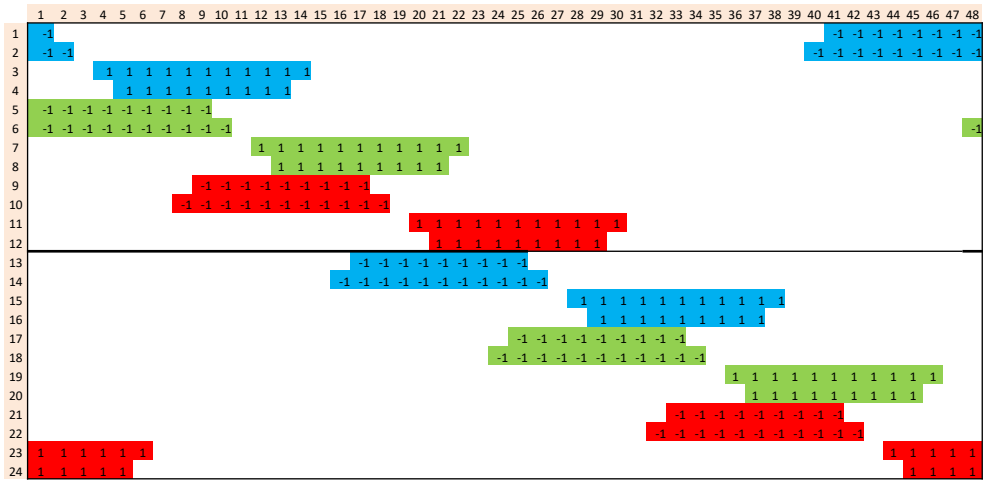

Figure 4.18: Winding matrix $[Mcf]$ distribution about the parallel winding with ACS.

4.3.2.3 Comparison and discussion

The simulations about the three different winding configurations are performed in the case with the static eccentricity of $10\%E_e$ at no load ($T_r = 0Nm$) [1]. Their simulation results about the generated electromagnetic forces (T_{em} and UMP), the instantaneous angular speed (ω_r) and the stator current in the first phase are compared respectively in the followings.

The variations of the electromagnetic torque and the produced instantaneous angular speed in the last 0.1 shaft revolution of the steady state are presented separately in FIG.4.19. Since they are simulated at no load, the generated T_{em} fluctuate finally around zero with a small undulation due to the slot effects. Meanwhile the instantaneous angular speed varies around the synchronous speed $\omega_r = \frac{\omega_s}{P} = \frac{2\times\pi\times50}{2}$ $(rad \cdot s^{-1})$ because

[1] This operating point is chosen here to avoid the extra validation of the model and to simplify the frequency components since there is no motor slip.

there is no slip at the no load state. The simulation results related to different winding configurations are marked in three different colors in all the superimposed comparison figures. It can be seen from the FIG.4.19(a) that there is nearly no difference between the three winding configurations in the waveform of the T_{em}. Although there is a small offset among the variation of ω_r between the parallel winding with ACS and those simulated from the series winding and the parallel winding with ACS, the difference are so small that could be omitted.

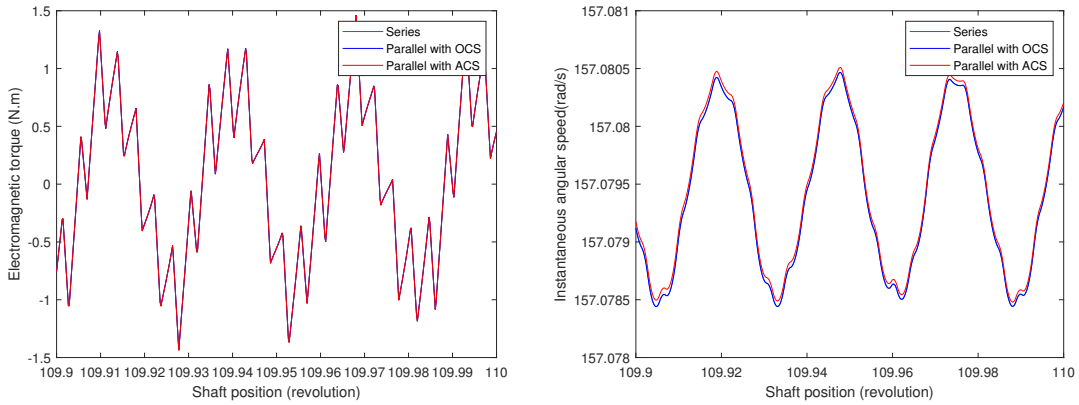

(a) T_{em} (b) ω_r

Figure 4.19: Comparison about the variation of the electromagnetic torque and the instantaneous angular speed with different winding patterns.

The simulation results about the stator currents in the first phase with different winding patterns during the last shaft revolution are compared in FIG.4.20. All the stator currents vary in a similar sinusoidal form and they all fluctuate two times during one shaft revolution because the studied IM "LSES180LUR" has two pole pairs. It is reasonable that the amplitude of the current in the series winding is almost double of that in the parallel windings because the supply voltage and the equivalent phase resistance are kept the same. The waveforms of the currents in two paths are fully coincide in the parallel winding with OCS from FIG.5.26(b). However an evident difference is identified between the variation of the two path currents in the parallel winding with ACS seeing FIG.5.26(c) and this is the reason why the use of parallel windings reduces the net resultant UMP as reported in many literature [61, 62, 180, 181, 182]. This will be explained in details hereafter in the UMP analysis. Their angular spectrum (in the parallel windings it's about the first parallel path current) are compared in FIG.4.21. Similar as discovered in the simulation results from the first IM "LSES132SM" in FIG.2.20(c) and FIG.2.20(f). All the characteristic frequencies related to the input static eccentricity such as: the supply frequency ($f_s = 2\ ev \cdot rev^{-1}$), the combination between the harmonics of the supply frequency and the slot harmonics ($f_{sh} = 40\ ev \cdot rev^{-1}$): $f_{sh} \pm f_s$; $f_{sh} - 3f_s$ and $2f_{sh} \pm f_s$ are identified in all three angular spectrum. Due to the unbalanced currents in the two parallel paths from the case of the parallel winding with ACS, more odd harmonics of the

supply frequency and their combinations with the slot harmonics emerge in its angular spectrum. Generally, it indicates that in the case with the input static eccentricities, only the parallel winding with ACS allows different amplitude currents to flow in the parallel paths as mentioned in [180, 181] which will introduce more harmonics of the supply frequency into the system. And the parallel winding with OCS has the same influence on the generated current value as the series winding does.

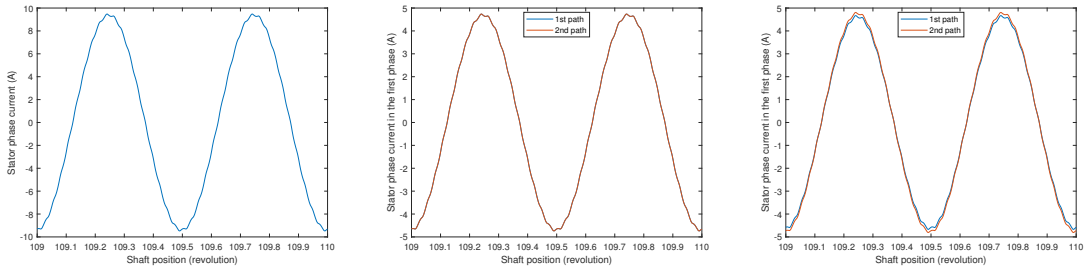

(a) Series (b) Parallel with OCS (c) Parallel with ACS

Figure 4.20: Comparison about the variation of stator first phase current with different winding patterns.

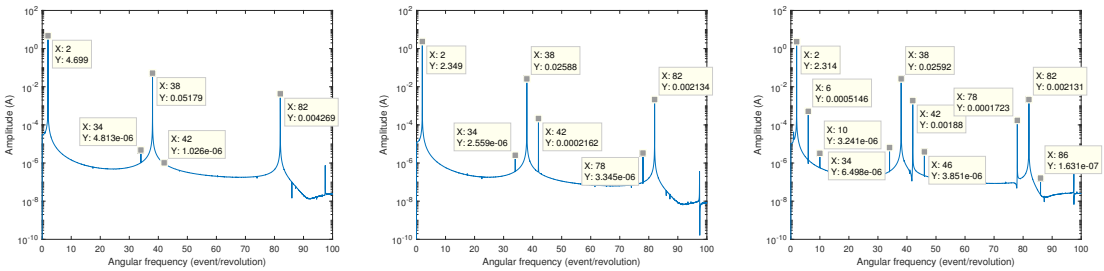

(a) Series (b) Parallel with OCS (c) Parallel with ACS

Figure 4.21: Comparison about the angular spectrum of stator first phase current with different winding patterns.

The comparison about their simulated UMP during the last shaft revolution is illustrated in FIG.4.22. It is clear that the two UMP components simulated in the case with series winding and the parallel winding with OCS are almost identical and each of them fluctuate around two different values with two relatively small undulations. However the waveforms of UMP generated in the case with the parallel winding with ACS appear in two different shapes: they vary around two constant values which are different from those simulated in the two previous winding configuration cases, and with two relatively large undulations. It is regarded that the average value of F_{emx} becomes smaller than before while that of F_{emy} is increased. The magnitudes and the offset angles of the resultant UMP are compared in the polar diagram shown in FIG.4.23. They are plotted in the same

way as described in SEC.2.11.1.1: the arrow represents the average magnitude of the resultant UMP and the orbit at its top end illustrates the variation of UMP during one shaft revolution. It can be noticed that the two arrows related to the series winding and to the parallel winding with OCS are coincident with each other to confirm that those two winding arrangements produce the same UMP. And their variation orbits are too small to be identified due to their small undulations in FIG.4.22(a) and FIG.4.22(b). Comparing with the simulation results marked in red from the parallel winding with ACS, it can be observed that the red arrow is shorter than the blue one which means that the average value of UMP is decreased. But at the same time its variation range becomes larger and its average offset angle becomes bigger than that obtained in the other two winding configurations. Inspired by the findings in [61], it interprets that the effect of the parallel winding with ACS in the stator is similar to that of the squirrel cage in the rotor. Both of them can introduce the UMP offset angle and attenuate the distortion of the air gap field induced by the rotor eccentricity so as to mitigate the resultant UMP. The theoretic explanation about the UMP mitigation by the parallel winding is referred to [61, 180]: In the nonuniform air gap, the inductance is lower in the circuits where the air gap length is larger than the nominal and vice versa. Therefore the currents in the circuits facing the larger air gap are slightly bigger than those facing the smaller air gap since the circuits in the parallel paths are connected to the same voltage. In the parallel winding with OCS, considering that one of the two opposite pole coils is facing the large air gap and the other is facing the small air gap, the unbalanced currents will be offset if they are connected in series. So that the difference in the parallel circuit currents only exist in the parallel winding with ACS as demonstrated in FIG.5.26(c). And this difference of the parallel circuit currents will tend to smooth out the distortion of the air gap magnetic field distribution induced by the rotor eccentricity.

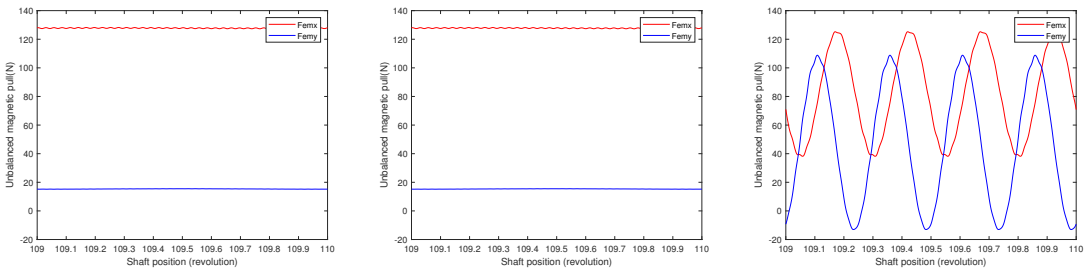

(a) Series (b) Parallel with OCS (c) Parallel with ACS

Figure 4.22: Comparison about the variation of UMP with different winding patterns.

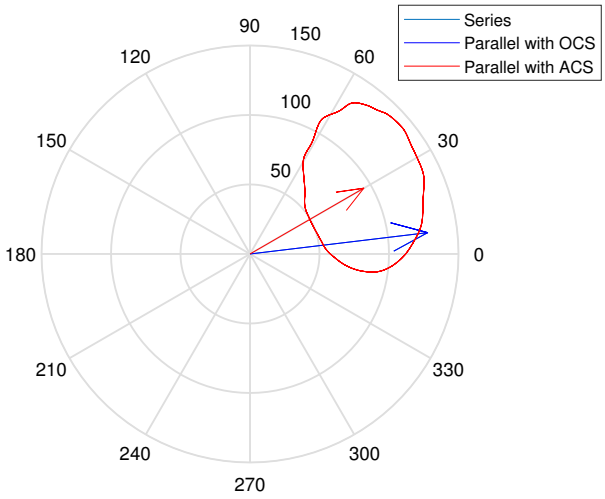

Figure 4.23: Polar diagram of UMP with the static eccentricity of $10\%E_e$ in the last shaft revolution with different winding patterns.

Their angular spectrum are respectively shown in FIG.4.24. All the characteristic frequencies observed in three UMP spectrum: double supply frequency ($2f_s = 4$), slot harmonics ($f_{sh} = 40$) and the combinations between the two ($f_{sh} \pm 2f_s$) are in good agreement with those discussed in the first IM from SEC.2.11.1.1 which can be used to prove the reliability of these characteristic frequency components adopted in the monitoring of the static eccentricity. Similar as discovered in the currents spectrum, more even harmonics of the double supply frequency and their modulations with the slot harmonics arise only in the parallel winding with ACS which is in agreement with the conclusion from [181].

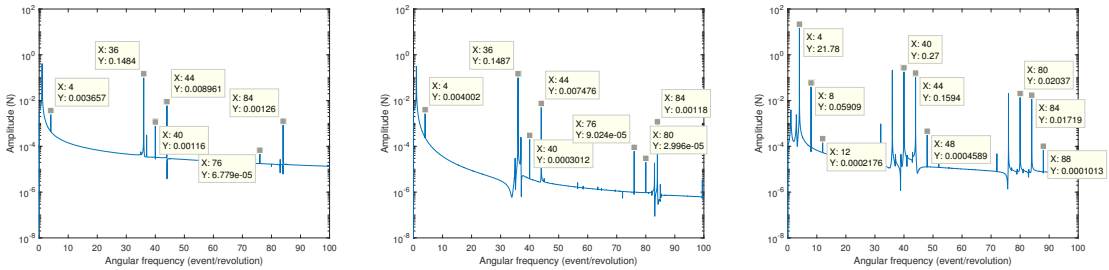

(a) Series (b) Parallel with OCS (c) Parallel with ACS

Figure 4.24: Comparison about the angular spectrum of UMP x-axis force component with different winding patterns.

Overall, the series winding and the parallel winding with OCS have the same influence on the dynamic behavior of the IM while the parallel winding with ACS affects the

system by mitigating the resultant UMP average value with the unbalanced stator currents induced in the two parallel paths of each phase. The current redistribution in this winding configuration also brings higher order of the harmonics in the current and UMP waveform. In addition, the influence of the winding configurations on the rotational movement of the IM (T_{em} and ω_r) is not evident in the case with the static eccentricity of $10\%E_e$.

4.4 Conclusions

With the proposed multiphysics model, the influence of different architectures in the electric motors are investigated from two aspects in this chapter. The equivalent model without the saturation effect about the reference PMSM is adopted to study the influence of different mechanical structures in the first aspect. By comparing the rotor center radial displacements simulated with the same linearly increased rotation speed under the same mass unbalance excitation and the rotor gravity, the influence of three mechanical parameters are analyzed firstly in the case of the classical structure. The increase of the bearing stiffness increases the natural frequency of the rotor system and meanwhile the more rigid stiffness tends to reduce the amplitude of the first resonance excited by the UMP. However the increase of the damping ratio doesn't modify the natural frequency but the amplitude of the first resonance is efficiently reduced in that case. Since the second resonance peak is excited by the mass unbalance, the variation of the mass eccentricity value only changes the amplitude of the second resonance peak. Afterwards, another cantilever structure with two different shaft length arrangements are applied to perform the same simulation in order to compare its simulation result with that from the classic structure. It is finally demonstrated that the mechanical structure with a larger natural frequency is also less vibrated under the excitation of UMP. According to these research results, the severe vibration phenomena such as the rotor-stator contact may be avoided in the operation of electric motors by increasing the natural frequency of the mechanical structure or increasing the global damping of the whole system.

The influence of different winding configurations is studied in the second aspect based on the multiphysics model of the IM. The composition of the 3-phase winding is introduced in the first part. And then the study is mainly realized about different coil arrangements between the lap winding and the concentric winding and about different pole phase coil connections between the series winding and the two types of series-parallel winding. It is identified that the lap winding and the concentric winding have the same influence on the dynamic behavior of the electric motor. Although there is no difference between the simulation results from the series winding and from the parallel winding with the opposite coils in series, the parallel winding with the adjacent coils in series has the different influence on the mechanical structure. The resultant UMP is mitigated in the case of the parallel winding with ACS due to the unbalanced currents induced in the two parallel paths of each stator phase. And this current redistribution also brings higher harmonics in the current and UMP waveform.

As a whole, the proposed multiphysics model about the synchronous and asyn-

chronous motor is ready to study the influence of different architectures on the electrical machines in many different aspects due to its strong electro-magneto-mechanical coupling. Only a few case studies have been presented in this chapter but since they are in good agreement with the findings from other literatures, the proposed model is worth being applied in other investigations about the influence of different architectures in the electric motor.

Chapter 5

General conclusions and future work

Contents

5.1 Conclusions

In the past few decades, the increasing need about the variable speed motors to optimize the performance of the driven system raises the technical challenge to ensure their satisfactory operation over the entire speed range. On the other hand, the requirement for a higher power density electrical machines leads to a design purpose of a higher rotational speed and a lighter mechanical structure. These two design evolutions will be the source of more severe vibration problems. In addition, more and more original architectures appear with the integration of the motor into the driven machine such as the screw compressor with an integrated PMSM as discussed in SEC.1.1. In order to analyses the dynamic behavoir of the global system and in the purpose of an overall optimization of the machine, a multiphysics model about electric motors considering strong couplings between the mechanical structure and the electromagnetic field is a necessary.

In response to this motivation, a multiphysics model about electric motors with a strong electro-magneto-mechanical coupling is established in this thesis. This model is developed in two traditional electrical machines: the squirrel cage IM and the PMSM for analyzing their dynamic behaviors under the influence of different architectures especially the UMP induced by the rotor eccentricity. Different from other multiphysics models of electrical machines, the proposed model takes into account the fully coupling in both the radial and rotational movements. Therefore the relation between the UMP and the rotor center radial displacements is added to reinforce the electromechanical interaction. And the airgap permeance value is calculated as the function of both the rotor center coordinates and the shaft rotation angle considering both the input rotor eccentricities and the mass unbalance excitations. The physical and geometrical nonlinearities are considered in this model in order to better understand and describe the nonlinear phenomena in electric motors which could lead to the instable dynamic behavoir. In addition, the non-stationary operating conditions resulting from the variable loads and the unconventional electrical control are taken into consideration by applying the angular approach to describe the potential failure occurred in the transient state. With the “Angle-Time” relation defined in the angular approach, the real fluctuation of the rotation speed is considered to interpret the transfer path from different angularly-periodic variation field in electric motors. In order to perform the longtime simulations at a reasonable computational effort, the mesh/nodal mixed PNM is adopted to model the magnetic field as 2.5D. The electrical circuits from the stator windings and the rotor cage are represented by a simple network composed of the resistors and the inductors. The mechanical part is discretized into several finite beam elements for simulating the regimes of high speeds and for preparing to describe different mechanical structures. The governing equations about three different physical fields are derived in the direct approach [140] by applying the Newton and Faraday’s laws. The global differential equations can be solved as function of two different state vectors: the phase currents or the phase flux. The simulation results from the two cases with different state vectors are confirmed to be identical and the phase flux is chosen as the final state vector because it is more efficient in the simulation especially for setting up the magnetic saturation effect. An electromagnetic model without the coupling of the mechanical

structure (Model EM) is extracted from the fully coupled model (Model EMM) in order to illustrate the importance of the strong electro-magneto-mechanical couplings. The validation of the proposed model is realized by comparing the simulation results from Model EM and Model FEMM in the quasi-static regime. After this validation, the proposed models about two traditional electric motors are adopted to analyze their dynamic behavior in two operating conditions (stationary and non-stationary) and under two different excitations (with an input static eccentricity and with the mass eccentricity).

In the IM, the physical characteristics and the frequency components related to the rotor eccentricity are firstly identified through the simulation results generated in the stationary operation with an input static eccentricity. In the terms of the physical characteristics, the offset angle of the resultant UMP from the narrowest airgap length is recognized from its polar diagram. This is due to the effect of equalizing currents induced in the rotor cage from the eccentricity which is in accordance with the findings from other literature. The slotting effect could be revealed from the generated rotor center orbit. In terms of the frequency analysis, the double supply frequency and its modulation with the rotor slot harmonics from the angular spectrum of UMP are considered as the characteristic frequencies associated with the input static eccentricity. They also indicate the modulation between the angular and temporal phenomena. Since the same characteristic frequencies also appear in the spectrum of the electromagnetic torque, it is demonstrated that the rotor radial perturbation also influences its rotational movement. These characteristic frequencies could be used for the identification of the static eccentricity in electric motors. Still under stationary operating conditions, the simulation results simulated under the mass unbalance excitation imply that the effect of the mass unbalance excitation can be treated as a rotor synchronous whirling motion while the influence of the gravity is equivalent to an input static eccentricity. The simulations in non-stationary operations are realized by applying a linearly increased load torque. It can be seen that with the increase of the load torque, more harmonics about the double supply frequency are induced in the system with an input static eccentricity while more undulations due to the motor slip appear in the waveform of UMP generated by the mass eccentricity. They may potentially increase the risk of the associated resonance phenomena.

In the case of the PMSM, the magnetic saturation effect is established in the model to take into account the saturation occurred in the rotor magnetic bridges. The simulation results about the decoupled model at the rated operating point but with different input eccentricity values are adopted to study the characteristic phenomena. It is observed that with the increase of the eccentricity value, more imbalance appear in the waveform of the stator parallel path currents in the same phase and more evident undulations emerged in the waveform of UMP. These phenomena introduce more harmonics of the characteristic frequencies related to the static eccentricity in their angular spectrum. Since there is no equalizing currents induced in the rotor part, there is no UMP offset angle in the PMSM. Another equivalent fully coupled model based on the simplified rotor structure is created for the longtime simulations by neglecting the saturation effect. A linearly increased angular speed is defined to perform the simulations in non-stationary operating conditions. Through the analysis of simulation results in three different aspects, two

disturbance peaks are identified in the waveform of UMP and of the rotor center radial displacements where the first is the self-excited rotor vibration induced by the UMP while the second is excited by the modified first natural frequency. Consistent with previous studies, UMP is confirmed to display a negative stiffness effect in the motor system. The amplitude of the self-excited rotor vibration is observed to increase with the decrease of the angular acceleration until the occurrence of the rotor-stator contact. Therefore the proposed model is able to reproduce the similar vibration phenomena discovered in the actual machine. Remarkably similar to the finding of Boy [143], the UMP induced self-excited rotor vibration appear at the critical speed $\omega_c \approx \frac{\tilde{\omega}_0}{P}$.

With the proposed multiphysics model, the influence of different architectures in electric motors are investigated in two aspects. The equivalent model without the saturation effect of the reference PMSM is employed to study the influence of different mechanical structures in the first aspect. It can be concluded that the self-excited rotor vibration could be reduced by increasing the first natural frequency of the structure or by increasing the damping ratio. The increase of the first natural frequency can be realized either by increasing the equivalent bearing stiffness or by modifying the shaft length arrangement. The variation of the mass eccentricity doesn't influence directly the self-excited rotor vibration but it changes the amplitude of the second resonance peak proportionally. These results could be applied to avoid the severe vibration phenomena such as the rotor-stator contact in the running of the electric motors. The second aspect focus on the analysis about the influence of different winding configurations by adopting the model of the IM. It is identified that different coil arrangements between the lap winding and the concentric winding have the same influence on the dynamic behavoir of the electric motor which is in agreement of the industrial knowledges. Compatible with the previous study, the UMP mitigation effect is only identified in the case of the parallel winding with the adjacent coils connected in series because of the unbalanced currents induced in the two parallel paths of each stator phase. And this current redistribution also brings higher harmonics in the current and UMP waveform.

Based on these assessments and knowledges, one can come back to the original issue founded from the industry as described in SEC.1.1. It has also been noted that if the PMSM is replaced by the similar IM, the severe rotor vibration problem disappears. This could be explained as the reduction of the first critical speed in the synchronous machines without damper windings (the rotor cage) and parallel branches is often larger than in cage induction machines because the eccentricity waves can't be damped by the induced unbalanced currents [143]. Although the reference PMSM is equipped with parallel branches in the stator, it still lacks the damper windings when comparing with the similar cage IM.

5.2 Suggestions for future work

Although the proposed multiphysics model of electrical machines are able to simulate the dynamic behavior of two traditional electric motors at all operating conditions in a natural way and it is ready to analyze the influence of different architectures on electri-

cal machines in many different aspects due to its strong electro-magneto-mechanical couplings, there are still some limitations about the developed model and the present research. Therefore, some suggestions are summarized in two aspects from the improvements and the applications of the model for future research activities:

Improvements of the model

Magnetic model

- The permeance network mesh of the magnetic field needs to be refined especially in the airgap region because in the PMSM there is an evident difference between the simulation results about the generated UMP from the proposed model and Model FEMM. And the model sensitivity with respect to the number of permeance network mesh should be evaluated.

- The calculation about setting up the magnetic saturation effect should be accelerated to perform the long-time simulation in non-stationary operations.

- The modal analysis of electrical machines can be introduced by developing the 2.5D model of the magnetic field into 3D. The stator shape under different vibration mode can be expressed by adding a Fourier series of cosine terms to the rotor radius as mentioned in [144].

- The eddy current effect should be added to include the iron loss in the model so that the power loss of electrical machines can be evaluated.

Electrical model

- The power supply controlled by the Pulse Width Modulation (PWM) should be added into the system in order to study the influence of the electromagnetic noise due to the PWM excitation as discussed in [183].

Mechanical model

- Since the validation of the proposed model is realized in the quasi-static regime, the dynamic behavior generated from the strong electro-magneto-mechanical coupling need to be validated through the experimental section (such as the fluctuation of the rotation speed).

- Once the magnetic model is extended into 3D, more airgap eccentricity types such as the curved eccentricity and the inclined eccentricity with the angular deviation and the radial displacement can be considered in this multiphysics model.

- In order to perform the simulation closer to the real situation, other devices in the transmission system should be described with a finer description for example the screw compressor in FIG.1.1 should be represented by the combination of the sinusoidal load torque and radial force instead of a constant load torque.
- The bearing effects can be represented by the nonlinear restoring force as described in [135] or by a developed bearing model from [164]. And the orbits of each node can be compared to study the UMP effect along the shaft as discussed in [161].
- The gyroscopic effect can be added in the system in order to study the rotor forward and backward whirling motion.
- A classic rub impact model can be added to simulate the stator-rotor rub impacts. And the stability of the rotor system can be evaluated through the Floquet theory according to [131].
- The model sensitivity with respect to the number of beam elements should be evaluated.

Applications of the model

- The effect of the parallel windings and of the magnetic saturation on the UMP can be analysed in the non-stationary conditions.
- The effects of different operating points (different load torques for IM and different load angles for PMSM) on the radial and tangential components of UMP can be explored in the non-stationary conditions.
- The relationship between different electric motor defects (such as the bearing defects and stator winding defects) and stator current signals can be studied to provide a theoretical basis for Motor Current Signal Analysis (MCSA).
- By coupling with the acoustic model, the vibrations and noise produced by the electrical machine can be predicted.
- Since the generated UMP could be reduced by adjusting the input stator current, a set of control system could be designed based on this.

Appendix A

Asynchronous motor modeling in the frame of nodal based model

A.1 Permeance network equations

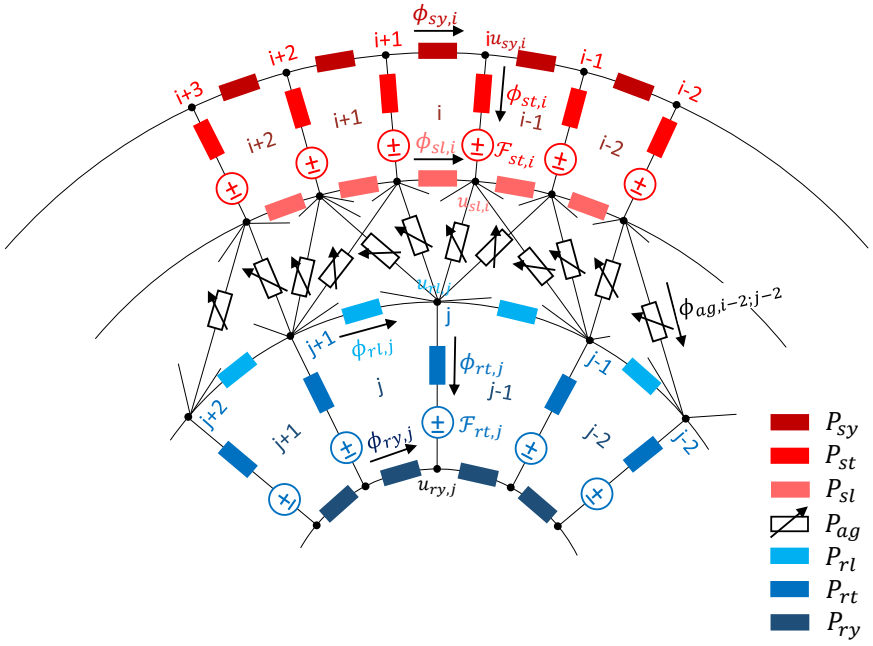

Figure A.1: Nodal based PNM for the squirrel cage induction motor

In the nodal based model shown in FIG.A.1, the magnetic potential of each node are considered as the unknowns which can be separated in 4 groups: the stator yoke $\{u_{sy}\}$; the

stator leakage $\{u_{sl}\}$; the rotor leakage $\{u_{rl}\}$ and the rotor yoke $\{u_{ry}\}$. They are adopted to calculate the magnetic flux passed through each branch with all the permeance elements. In order to apply the Kirchhoff current law (KCL) in each network mesh, the relation between the magnetic potential and the magnetic flux deduced from FIG.2.10 should be re-described as:

$$(u_a - u_b - \mathcal{F}_t) * P = (U_{ab} - \mathcal{F}_t) * P = \phi \tag{A.1}$$

The EQ.A.1 can be developed in all the branches of the permeance network in order to obtain the magnetic flux values passing through each branch. The KCL is then applied at each node considering that the sum of the flux entering each node equals the sum of those leaving this node. It is used to establish finally the permeance network equations of the nodal based model. The circulating directions of the magnetic flux from each part are defined as presented in FIG.A.1. The precise deduction processes in each group are explained in the following.

About the node k in the stator yoke circle:

$$\begin{aligned}
&-\phi_{k-1}^{sy} - \phi_k^{st} + \phi_k^{sy} = 0 \\
\Rightarrow &- p_{k-1}^{sy} \cdot U_{k-1}^{sy} - p_k^{st} \cdot (U_k^{st} - \mathcal{F}_k^{st}) + p_k^{sy} \cdot U_k^{sy} = 0 \\
\Rightarrow &- p_{k-1}^{sy} \cdot (u_k^{sy} - u_{k-1}^{sy}) - p_k^{st} \cdot (u_k^{sy} - u_k^{sl} - \mathcal{F}_k^{st}) + p_k^{sy} \cdot (u_{k+1}^{sy} - u_k^{sy}) = 0 \\
\Rightarrow &\underbrace{p_{k-1}^{sy} \cdot\ u_{k-1}^{sy} - (p_{k-1}^{sy} + p_k^{sy} + p_k^{st}) \cdot u_k^{sy} + p_k^{sy} \cdot u_{k+1}^{sy}}_{[P_{11}]} + \underbrace{p_k^{st} \cdot u_k^{sl}}_{[P_{12}]} + \underbrace{p_k^{st} \cdot \mathcal{F}_k^{st}}_{[P_{15}]} = 0
\end{aligned} \tag{A.2}$$

This can be presented in the form of matrix by developing EQ.A.2 around the stator yoke circle.

$$[P_{11}] \cdot \{u_{sy}\} + [P_{12}] \cdot \{u_{sl}\} + [P_{15}] \cdot \{\mathcal{F}_{st}\} = \{0\}_{n_s * 1} \tag{A.3}$$

where each permeance matrix are defined as:

$$[P_{11}]_{(n_s * n_s)} = \begin{bmatrix}
-(P_{n_s}^{sy} + P_1^{sy} + P_1^{st}) & P_1^{sy} & 0 & \cdots & 0 & P_{n_s}^{sy} \\
P_1^{sy} & -(P_1^{sy} + P_2^{sy} + P_2^{st}) & P_2^{sy} & 0 & \cdots & 0 \\
0 & P_2^{sy} & -(P_2^{sy} + P_3^{sy} + P_3^{st}) & P_3^{sy} & \cdots & 0 \\
: & 0 & \ddots & \ddots & \ddots & 0 \\
0 & \cdots & 0 & P_{n_s-2}^{sy} & -(P_{n_s-2}^{sy} + P_{n_s-1}^{sy} + P_{n_s-1}^{st}) & P_{n_s-1}^{sy} \\
P_{n_s}^{sy} & 0 & \cdots & 0 & P_{n_s-1}^{sy} & -(P_{n_s-1}^{sy} + P_{n_s}^{sy} + P_{n_s}^{st})
\end{bmatrix} \tag{A.4}$$

$$[P_{12}]_{(n_s * n_s)} = [P_{15}]_{(n_s * n_s)} = \begin{bmatrix}
P_1^{st} & 0 & \cdots & 0 \\
0 & P_2^{st} & \cdots & 0 \\
0 & 0 & \ddots & 0 \\
0 & \cdots & 0 & P_{n_s}^{st}
\end{bmatrix} \tag{A.5}$$

Replacing the third term on the left side of EQ.A.3 by the first equation from EQ.2.31, the first group of the permeance network equations is presented as:

$$[P_{11}] \cdot \{u_{sy}\} + [P_{12}] \cdot \{u_{sl}\} + [P_{15}] \cdot [MZs] \cdot \{i_{sp}\} = \{0\}_{n_s * 1} \tag{A.6}$$

About the node k in the stator leakage circle:

$$
\begin{aligned}
&-\phi_{k-1}^{sl}+\phi_{k}^{sl}+\phi_{k}^{st}-\sum_{j=1}^{n_r}\phi_{k,j}^{ag}=0\\
\Rightarrow &-p_{k-1}^{sl}\cdot U_{k-1}^{sl}+p_{k}^{sl}\cdot U_{k}^{sl}+p_{k}^{st}\cdot(U_{k}^{st}-\mathcal{F}_{k}^{st})-\sum_{j=1}^{n_r}p_{k,j}^{ag}\cdot U_{k,j}^{ag}=0\\
\Rightarrow &-p_{k-1}^{sl}\cdot(u_{k}^{sl}-u_{k-1}^{sl})+p_{k}^{sl}\cdot(u_{k+1}^{sl}-u_{k}^{sl})+p_{k}^{st}\cdot(u_{k}^{sy}-u_{k}^{sl}-\mathcal{F}_{k}^{st})-\sum_{j=1}^{n_r}p_{k,j}^{ag}\cdot(u_{k}^{sl}-u_{j}^{rl})=0\\
\Rightarrow &\underbrace{p_{k}^{st}\cdot u_{k}^{sy}}_{[P_{21}]}+\underbrace{p_{k-1}^{sl}\cdot\ u_{k-1}^{sl}-(p_{k-1}^{sl}+p_{k}^{sl}+p_{k}^{st}+\sum_{j=1}^{n_r}p_{k,j}^{ag})\cdot u_{k}^{sl}+p_{k}^{sl}\cdot u_{k+1}^{sl}}_{[P_{22}]}+\underbrace{\sum_{j=1}^{n_r}p_{k,j}^{ag}\cdot u_{j}^{rl}}_{[P_{23}]}-\underbrace{p_{k}^{st}\cdot\mathcal{F}_{k}^{st}}_{[P_{25}]}=0
\end{aligned}
\tag{A.7}
$$

Similarly, this can be presented in the form of matrix by developing EQ.A.7 around the stator leakage circle.

$$
[P_{21}]\cdot\{u_{sy}\}+[P_{22}]\cdot\{u_{sl}\}+[P_{23}]\cdot\{u_{rl}\}-[P_{25}]\cdot\{\mathcal{F}_{st}\}=\{0\}_{n_s*1} \tag{A.8}
$$

with each permeance matrix defined as:

$$
[P_{21}]_{(n_s*n_s)}=[P_{25}]_{(n_s*n_s)}=[P_{12}]_{(n_s*n_s)} \tag{A.9}
$$

$$
[P_{22}]_{(n_s*n_s)}=[P_{22f}]_{(n_s*n_s)}-[P_{22e}]_{(n_s*n_s)} \tag{A.10}
$$

The matrix $[P_{22}]$ is composed of two parts: $[P_{22f}]$ is consisted of the permeances in the iron core and $[P_{22e}]$ includes all the air gap permeances. They are defined separately in EQ.A.11 and EQ.A.12.

$$
[P_{22f}(\{P_{sl}\},\{P_{st}\})]_{(n_s*n_s)}=
\begin{bmatrix}
-(P_{n_s}^{sl}+P_{1}^{sl}+P_{1}^{st}) & P_{1}^{sl} & 0 & \cdots & 0 & P_{n_s}^{sl}\\
P_{1}^{sl} & -(P_{1}^{sl}+P_{2}^{sl}+P_{2}^{st}) & P_{2}^{sl} & 0 & \cdots & 0\\
0 & P_{2}^{sl} & -(P_{2}^{sl}+P_{3}^{sl}+P_{3}^{st}) & P_{3}^{sl} & \cdots & 0\\
: & 0 & \ddots & \ddots & \ddots & 0\\
0 & \cdots & 0 & P_{n_s-2}^{sl} & -(P_{n_s-2}^{sl}+P_{n_s-1}^{sl}+P_{n_s-1}^{st}) & P_{n_s-1}^{sl}\\
P_{n_s}^{sl} & 0 & \cdots & 0 & P_{n_s-1}^{sl} & -(P_{n_s-1}^{sl}+P_{n_s}^{sl}+P_{n_s}^{st})
\end{bmatrix}
\tag{A.11}
$$

$$
[P_{22e}(\{P_{ag}\})]_{(n_s*n_s)}=
\begin{bmatrix}
\sum_{j=1}^{n_r}P_{1,j}^{ag} & 0 & 0 & \cdots & 0 & 0\\
0 & \sum_{j=1}^{n_r}P_{2,j}^{ag} & 0 & \cdots & 0 & 0\\
0 & 0 & \sum_{j=1}^{n_r}P_{3,j}^{ag} & \cdots & 0 & 0\\
: & \cdots & \cdots & \ddots & \cdots & 0\\
0 & 0 & 0 & \cdots & \sum_{j=1}^{n_r}P_{n_s-1,j}^{ag} & 0\\
0 & 0 & 0 & \cdots & 0 & \sum_{j=1}^{n_r}P_{n_s,j}^{ag}
\end{bmatrix}
\tag{A.12}
$$

$$[P_{23}(\{P_{ag}\})]_{(n_s*n_r)} = \begin{bmatrix} P^{ag}_{1,1} & P^{ag}_{1,2} & P^{ag}_{1,3} & \cdots & P^{ag}_{1,n_r} \\ P^{ag}_{2,1} & P^{ag}_{2,2} & P^{ag}_{2,3} & \cdots & P^{ag}_{2,n_r} \\ P^{ag}_{3,1} & P^{ag}_{3,2} & P^{ag}_{3,3} & \cdots & P^{ag}_{3,n_r} \\ \vdots & \vdots & \vdots & \cdots & \vdots \\ P^{ag}_{n_s,1} & P^{ag}_{n_s,2} & P^{ag}_{n_s,3} & \cdots & P^{ag}_{n_s,n_r} \end{bmatrix} \tag{A.13}$$

With the same operation realized between EQ.A.3 and EQ.A.6, EQ.A.8 is finally transformed into the second group of the permeance network equations as defined in EQ.A.14:

$$[P_{21}]\cdot\{u_{sy}\} + [P_{22}]\cdot\{u_{sl}\} + [P_{23}]\cdot\{u_{rl}\} - [P_{25}]\cdot[MZs]\cdot\{i_{sp}\} = \{0\}_{n_s*1} \tag{A.14}$$

About the node k in the rotor leakage circle:

$$\begin{aligned} & -\phi^{rl}_{k-1} + \phi^{rl}_{k} - \phi^{rt}_{k} + \sum_{i=1}^{n_s} \phi^{ag}_{i,k} = 0 \\ \Rightarrow & -p^{rl}_{k-1}\cdot U^{rl}_{k-1} + p^{rl}_{k}\cdot U^{rl}_{k} - p^{rt}_{k}\cdot(U^{rt}_{k} - \mathcal{F}^{rt}_{k}) + \sum_{i=1}^{n_s} p^{ag}_{i,k}\cdot U^{ag}_{i,k} = 0 \\ \Rightarrow & -p^{rl}_{k-1}\cdot(u^{rl}_{k} - u^{rl}_{k-1}) + p^{rl}_{k}\cdot(u^{rl}_{k+1} - u^{rl}_{k}) - p^{rt}_{k}\cdot(u^{rl}_{k} - u^{ry}_{k} - \mathcal{F}^{rt}_{k}) + \sum_{i=1}^{n_s} p^{ag}_{i,k}\cdot(u^{sl}_{i} - u^{rl}_{k}) = 0 \\ \Rightarrow & \underbrace{\sum_{i=1}^{n_s} p^{ag}_{i,k}\cdot u^{sl}_{i}}_{[P_{32}]} + \underbrace{p^{rl}_{k-1}\cdot\ u^{rl}_{k-1} - (p^{rl}_{k-1} + p^{rl}_{k} + p^{rt}_{k} + \sum_{i=1}^{n_s} p^{ag}_{i,k})\cdot u^{rl}_{k} + p^{rl}_{k}\cdot u^{rl}_{k+1}}_{[P_{33}]} + \underbrace{p^{rt}_{k}\cdot u^{ry}_{k}}_{[P_{34}]} + \underbrace{p^{rt}_{k}\cdot\mathcal{F}^{rt}_{k}}_{[P_{36}]} = 0 \end{aligned} \tag{A.15}$$

As discussed before, their relation can be organized in the form of matrix by developing EQ.A.15 in all the rotor leakage circle.

$$[P_{32}]\cdot\{u_{sl}\} + [P_{33}]\cdot\{u_{rl}\} + [P_{34}]\cdot\{u_{ry}\} + [P_{36}]\cdot\{\mathcal{F}_{rt}\} = \{0\}_{n_r*1} \tag{A.16}$$

where each permeance matrix are defined respectively in EQ.A.17, EQ.A.18 and EQ.A.21.

$$[P_{32}]_{(n_r*n_s)} = [P_{23}]^{T}_{(n_s*n_r)} = \begin{bmatrix} P_{1,1} & P_{2,1} & P_{3,1} & \cdots & P_{n_s,1} \\ P_{1,2} & P_{2,2} & P_{3,2} & \cdots & P_{n_s,2} \\ P_{1,3} & P_{2,3} & P_{3,3} & \cdots & P_{n_s,3} \\ \vdots & \vdots & \vdots & \cdots & \vdots \\ P_{1,n_r} & P_{2,n_r} & P_{3,n_r} & \cdots & P_{n_s,n_r} \end{bmatrix} \tag{A.17}$$

Similar as described in EQ.A.10, the permeance matrix $[P_{33}]$ is also composed of two parts: $[P_{33f}]$ and $[P_{33e}]$.

$$[P_{33}]_{(n_r*n_r)} = [P_{33f}(\{P_{rl}\},\{P_{rt}\})] - [P_{33e}] \tag{A.18}$$

with

$$[P_{33f}(\{P_{rl}\},\{P_{rt}\})]_{(n_r*n_r)} =$$
$$\begin{bmatrix} -(P^{rl}_{n_r}+P^{rl}_1+P^{rl}_1) & P^{rl}_1 & 0 & \cdots & 0 & P^{rl}_{n_r} \\ P^{rl}_1 & -(P^{rl}_1+P^{rl}_2+P^{rt}_2) & P^{rl}_2 & 0 & \cdots & 0 \\ 0 & P^{rl}_2 & -(P^{rl}_2+P^{rl}_3+P^{rt}_3) & P^{rl}_3 & \cdots & 0 \\ : & 0 & \ddots & \ddots & \ddots & 0 \\ 0 & \cdots & 0 & P^{rl}_{n_r-2} & -(P^{rl}_{n_r-2}+P^{rl}_{n_r-1}+P^{rt}_{n_r-1}) & P^{rl}_{n_r-1} \\ P^{rl}_{n_r} & 0 & \cdots & 0 & P^{rl}_{n_r-1} & -(P^{rl}_{n_r-1}+P^{rl}_{n_r}+P^{rt}_{n_r}) \end{bmatrix} \tag{A.19}$$

and

$$[P_{33e}]_{(n_r*n_r)} = \begin{bmatrix} \sum_{i=1}^{n_s} P_{i,1} & 0 & 0 & \cdots & 0 & 0 \\ 0 & \sum_{i=1}^{n_s} P_{i,2} & 0 & \cdots & 0 & 0 \\ 0 & 0 & \sum_{i=1}^{n_s} P_{i,3} & \cdots & 0 & 0 \\ : & \cdots & \cdots & \ddots & \cdots & 0 \\ 0 & 0 & 0 & \cdots & \sum_{i=1}^{n_s} P_{i,n_r-1} & 0 \\ 0 & 0 & 0 & \cdots & 0 & \sum_{i=1}^{n_s} P_{i,n_r} \end{bmatrix} \tag{A.20}$$

$$[P_{34}]_{(n_r*n_r)} = [P_{36}]_{(n_r*n_r)} = \begin{bmatrix} P^{rt}_1 & 0 & \cdots & 0 \\ 0 & P^{rt}_2 & \cdots & 0 \\ 0 & 0 & \ddots & 0 \\ 0 & \cdots & 0 & P^{rt}_{n_r} \end{bmatrix} \tag{A.21}$$

Replacing the third term on the left side of EQ.A.16 by the second equation from EQ.2.31, the third group of the permeance network equations is defined as:

$$[P_{32}]\cdot\{u_{sl}\}+[P_{33}]\cdot\{u_{rl}\}+[P_{34}]\cdot\{u_{ry}\}+[P_{36}]\cdot[MZr]\cdot\{\tilde{i_b}\}=\{0\}_{n_r*1} \tag{A.22}$$

About the node k in the rotor yoke circle:

$$\begin{aligned} &-\phi^{ry}_{k-1}+\phi^{rt}_k+\phi^{ry}_k=0 \\ \Rightarrow &-p^{ry}_{k-1}\cdot U^{ry}_{k-1}+p^{rt}_k\cdot(U^{rt}_k-\mathcal{F}^{rt}_k)+p^{ry}_k\cdot U^{ry}_k=0 \\ \Rightarrow &-p^{ry}_{k-1}\cdot(u^{ry}_k-u^{ry}_{k-1})+p^{rt}_k\cdot(u^{rl}_k-u^{ry}_k-\mathcal{F}^{rt}_k)+p^{ry}_k\cdot(u^{ry}_{k+1}-u^{ry}_k)=0 \\ \Rightarrow &\underbrace{p^{rt}_k\cdot u^{rl}_k}_{[P_{43}]}+\underbrace{p^{ry}_{k-1}\cdot\ u^{ry}_{k-1}-(p^{ry}_{k-1}+p^{ry}_k+p^{rt}_k)\cdot u^{ry}_k+p^{ry}_k\cdot u^{ry}_{k+1}}_{[P_{44}]}-\underbrace{p^{rt}_k\cdot\mathcal{F}^{rt}_k}_{[P_{46}]}=0 \end{aligned} \tag{A.23}$$

Their relation is developed in the form of matrix by developing EQ.A.23 in all the rotor yoke circle.

$$[P_{43}]\cdot\{u_{rl}\}+[P_{44}]\cdot\{u_{ry}\}-[P_{46}]\cdot\{\mathcal{F}_{rt}\}=\{0\}_{n_r*1} \tag{A.24}$$

where the three permeance matrix are defined separately in EQ.A.25 and EQ.A.26.

$$[P_{43}]_{(n_r*n_r)}=[P_{46}]_{(n_r*n_r)}=[P_{34}]_{(n_r*n_r)} \tag{A.25}$$

$$[P_{44}]_{(n_r*n_r)}$$
$$\begin{bmatrix} -(P_{n_r}^{ry}+P_1^{ry}+P_1^{rt}) & P_1^{ry} & 0 & \cdots & 0 & P_{n_r}^{ry} \\ P_1^{ry} & -(P_1^{ry}+P_2^{ry}+P_2^{rt}) & P_2^{ry} & 0 & \cdots & 0 \\ 0 & P_2^{ry} & -(P_2^{ry}+P_3^{ry}+P_3^{rt}) & P_3^{ry} & \cdots & 0 \\ : & 0 & \ddots & \ddots & \ddots & 0 \\ 0 & \cdots & 0 & P_{n_r-2}^{ry} & -(P_{n_r-2}^{ry}+P_{n_r-1}^{ry}+P_{n_r-1}^{rt}) & P_{n_r-1}^{ry} \\ P_{n_r}^{ry} & 0 & \cdots & 0 & P_{n_r-1}^{ry} & -(P_{n_r-1}^{ry}+P_{n_r}^{ry}+P_{n_r}^{rt}) \end{bmatrix} \tag{A.26}$$

The rotor MMF vector in EQ.A.24 is replaced by the second equation from EQ.2.31 to construct the fourth group of the permeance network equations as shown in EQ.A.27.

$$[P_{43}]\cdot\{u_{rl}\}+[P_{44}]\cdot\{u_{ry}\}-[P_{46}]\cdot[MZr]\cdot\{\tilde{i_b}\}=\{0\}_{n_r*1} \tag{A.27}$$

Since the last nodal potential in the rotor yoke is chosen to be the reference of the magnetic potentials, it is defined as zero $u_{ry,n_r}=0$. Then only n_r-1 terms in the $\{u_{ry}\}$ are needed to be considered as unknowns. Two modifications have to be realized in the constructed matrix in order to adapt to this change. First, the last column of the matrix $[P_{34}]$ defined in EQ.A.21 needed to be removed in order to correspond with the number of the new vector $\{\tilde{u_{ry}}\}_{(n_r-1)*1}$. Second, there is no need to write the KCL equation about the node n_r in the rotor yoke because it is considered as the zero magnetic potential point. Then the last equation defined in the fourth group EQ.A.27 should be eliminated which means the last row in the matrix $[P_{43}]$ $[P_{46}]$ and $[P_{44}]$ should be removed. Therefore, the third group EQ.A.22 and fourth group EQ.A.27 of permeance equations are re-organized respectively as:

$$[P_{32}]\cdot\{u_{sl}\}+[P_{33}]\cdot\{u_{rl}\}+[\tilde{P_{34}}]\cdot\{\tilde{u_{ry}}\}+[P_{36}]\cdot[MZr]\cdot\{\tilde{i_b}\}=\{0\}_{n_r*1} \tag{A.28}$$

$$[\tilde{P_{43}}]\cdot\{u_{rl}\}+[\tilde{P_{44}}]\cdot\{\tilde{u_{ry}}\}-[\tilde{P_{46}}]\cdot[MZr]\cdot\{\tilde{i_b}\}=\{0\}_{(n_r-1)*1} \tag{A.29}$$

Assembling of the permeance network equations: Four equations deduced from the four groups of the permeance network EQ.A.6, EQ.A.14, EQ.A.28 and EQ.A.29 are combined together to obtain the full set of permeance network equations about the complete motor's cross section in order to describe the relation between all the magnetic node potentials and the stator and rotor phase currents.

$$[PnodU]\cdot\{u_{sr}\}-[HPD]\cdot\{i_p\}=\{0\}_{(2n_s+2n_r-1)*1} \tag{A.30}$$

where each matrix are defined separately as followings:

$$[PnodU]=\begin{bmatrix} [P_{11}]_{(n_s*n_s)} & [P_{12}]_{(n_s*n_s)} & [0]_{(n_s*n_r)} & [0]_{(n_s*(n_r-1))} \\ [P_{21}]_{(n_s*n_s)} & [P_{22}]_{(n_s*n_s)} & [P_{23}]_{(n_s*n_r)} & [0]_{(n_r*(n_r-1))} \\ [0]_{(n_r*n_s)} & [P_{32}]_{(n_r*n_s)} & [P_{33}]_{(n_r*n_r)} & [\tilde{P_{34}}]_{(n_r*(n_r-1))} \\ [0]_{((n_r-1)*n_s)} & [0]_{((n_r-1)*n_s)} & [\tilde{P_{43}}]_{((n_r-1)*n_r)} & [\tilde{P_{44}}]_{((n_r-1)*(n_r-1))} \end{bmatrix} \tag{A.31}$$

$$[HPD] = \begin{bmatrix} -([P_{15}] \cdot [MZs])_{(n_s * n_{ph})} & [0]_{(n_s * (n_r - 1))} \\ ([P_{25}] \cdot [MZs])_{(n_s * n_{ph})} & [0]_{(n_s * (n_r - 1))} \\ [0]_{(n_r * n_{ph})} & -([P_{36}] \cdot [MZr])_{(n_r * (n_r - 1))} \\ [0]_{((n_r - 1) * n_{ph})} & (\tilde{[P_{46}]} \cdot [MZr])_{((n_r - 1) * (n_r - 1))} \end{bmatrix} \tag{A.32}$$

The vector $\{u_{sr}\}$ includes all the magnetic node potentials in the four groups.

$$\{u_{sr}\} = \begin{Bmatrix} \{u_{sy}\}_{n_s * 1} \\ \{u_{sl}\}_{n_s * 1} \\ \{u_{rl}\}_{n_r * 1} \\ \{\tilde{u_{ry}}\}_{(n_r - 1) * 1} \end{Bmatrix} \tag{A.33}$$

And the vector $\{i_p\}$ is the state vector of the electromagnetic part including three stator phases currents $\{i_{sp}\}$ and $(n_r - 1)$ rotor bar currents $\{i_b\}$.

$$\{i_p\} = \begin{Bmatrix} \{i_{sp}\}_{n_{np} * 1} \\ \{\tilde{i_b}\}_{(n_r - 1) * 1} \end{Bmatrix} \tag{A.34}$$

A.2 Flux linkage equations

Considering the relation between the magnetic nodal potential and the magnetic branch flux defined in EQ.A.1 and the stator and rotor tooth branches illustrated in FIG.A.1, it's easy to calculate all the magnetic tooth flux from the basic elements described in the permeance network of the nodal based model. Their relation about the stator and the rotor part is expressed in the matrix format in EQ.A.35.

$$\begin{cases} \{\phi_{st}\} = [P_{12}] \cdot (\{u_{sy}\} - \{u_{sl}\} - \{\mathcal{F}_{st}\}) \\ \{\phi_{rt}\} = [P_{34}] \cdot (\{u_{rl}\} - \{u_{ry}\} - \{\mathcal{F}_{rt}\}) \end{cases} \tag{A.35}$$

where the permeance matrix $[P_{12}]$ and $[P_{34}]$ are defined respectively in EQ.A.5 and EQ.A.21. With the substitution of EQ.2.31, the MMF source are replaced by the state vector of the electromagnetic model, and EQ.A.35 is transformed into:

$$\begin{cases} \{\phi_{st}\} = [P_{12}] \cdot (\{u_{sy}\} - \{u_{sl}\} - [MZs] \cdot \{i_{sp}\}) \\ \{\phi_{rt}\} = [P_{34}] \cdot (\{u_{rl}\} - \{u_{ry}\} - [MZr] \cdot \{\tilde{i_b}\}) \end{cases} \tag{A.36}$$

The relation with the magnetic phase flux is realized by a further substitution of EQ.2.54 and EQ.2.55 into EQ.A.36. Then it is finally transformed into EQ.A.37.

$$\begin{cases} \{\phi_{sp}\} = [ww] \cdot [P_{12}] \cdot (\{u_{sy}\} - \{u_{sl}\} - [MZs] \cdot \{i_{sp}\}) \\ \{\tilde{\phi_{rp}}\} = [\tilde{P_{43}}] \cdot (\{u_{rl}\} - \{u_{ry}\} - [MZr] \cdot \{\tilde{i_b}\}) \end{cases} \tag{A.37}$$

where $[\tilde{P_{43}}]$ is the same as defined in EQ.A.29. EQ.A.37 can be expressed in a more compact matrix format in EQ.A.38.

$$[HPW] \cdot \{u_{sr}\} + [PnodI] \cdot \{i_p\} = \{\phi_p\} \tag{A.38}$$

where $\{u_{sr}\}$ and $\{i_p\}$ have been defined respectively in EQ.A.33 and EQ.A.34. The two coefficient matrix $[HPW]$ and $[PnodI]$ are deduced from EQ.A.37 which are separately organized as:

$$[HPW] = \begin{bmatrix} ([ww]\cdot[P_{12}])_{(n_{ph}*n_s)} & (-[ww]\cdot[P_{12}])_{(n_{ph}*n_s)} & [0]_{(n_{ph}*n_r)} & [0]_{(n_{ph}*(n_r-1))} \\ [0]_{((n_r-1)*n_s)} & [0]_{((n_r-1)*n_s)} & [\tilde{P_{43}}]_{((n_r-1)*n_r)} & -[\tilde{\tilde{P_{43}}}]_{((n_r-1)*(n_r-1))} \end{bmatrix} \tag{A.39}$$

where $[\tilde{\tilde{P_{43}}}]$ is the matrix $[\tilde{P_{43}}]$ after the remove of the last column in order to match with the number of the vector $\{u_{ry}\}$.

$$[PnodI] = \begin{bmatrix} -([ww]\cdot[P_{12}]\cdot[MZs])_{(n_{ph}*n_{ph})} & [0]_{(n_{ph}*(n_r-1))} \\ [0]_{((n_r-1)*n_{ph})} & -([\tilde{P_{43}}]\cdot[MZr])_{((n_r-1)*(n_r-1))} \end{bmatrix} \tag{A.40}$$

A.3 Augmented magnetic equations

Two sets of equations deduced respectively in EQ.A.30 and EQ.A.38 are combined together to construct a larger set of augmented magnetic equations which is described in the following.

$$\begin{bmatrix} [PnodU(\theta, x_r, y_r)] & -[HPD] \\ [HPW] & [PnodI] \end{bmatrix} \cdot \begin{Bmatrix} \{u_{sr}\} \\ \{i_p\} \end{Bmatrix} = \begin{Bmatrix} \{0\}_{(2n_s+2n_r-1)*1} \\ \{\phi_p\}_{(n_{np}+n_r-1)*1} \end{Bmatrix} \tag{A.41}$$

Meanwhile, by eliminating the vector $\{u_{sr}\}$ in EQ.A.41, the direct relation between the phase currents $\{i_p\}$ and the magnetic phase flux $\{\phi_p\}$ is achieved as:

$$([HPW]\cdot[PnodU(\theta, x_r, y_r)]^{-1}\cdot[HPD] + [PnodI])\cdot\{i_p\} = \{\phi_p\} \tag{A.42}$$

Appendix B

Permanent magnet synchronous motor modeling in the frame of nodal based model

B.1 Permeance network equations

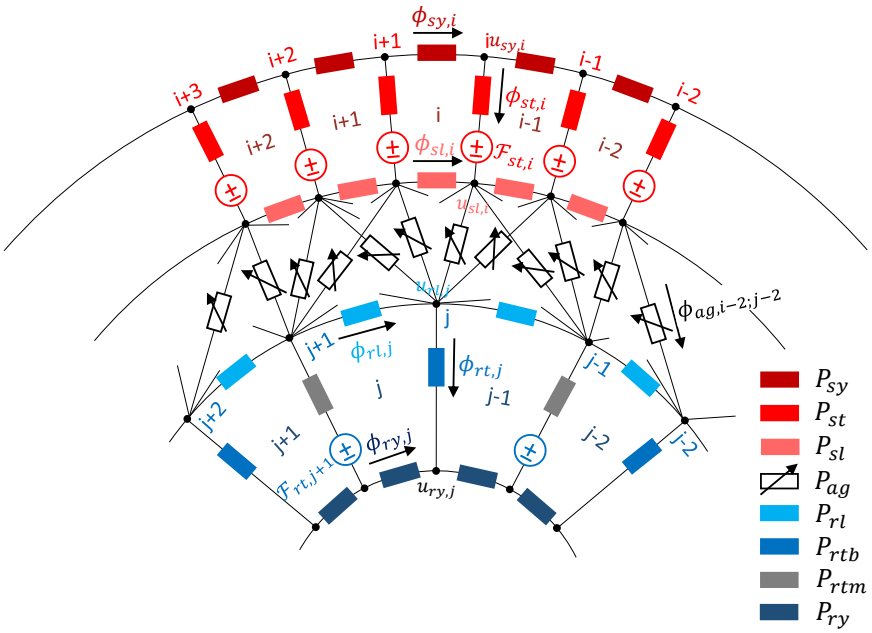

Figure B.1: Nodal based PNM for the embedded permanent magnet synchronous motor

The PNM about the reference PMSM in the nodal based model is illustrated in FIG.B.1. It can be treated in the same way as illustrated in FIG.A.1 if EQ.3.3 and EQ.3.19 are taken into the consideration. Some modifications have to be realized in the equations from each

PNM circle in order to adapt to the changes.

About the node k in the stator yoke circle: Substitution EQ.3.14 into EQ.A.3, one obtains:

$$[P_{11}]\cdot\{u_{sy}\}+[P_{12}]\cdot\{u_{sl}\}+[P_{15}]\cdot[MZs]\cdot\{i_{sv}\}=\{0\}_{n_s*1} \tag{B.1}$$

The linear model equations are obtained by substitution EQ.3.15 into EQ.B.1:

$$[P_{11}]\cdot\{u_{sy}\}+[P_{12}]\cdot\{u_{sl}\}+[P_{15}]\cdot[MZs]\cdot[MIs]\cdot\{\tilde{i_{sv}}\}=-[P_{15}]\cdot[MZs]\cdot\{I_{sp}\} \tag{B.2}$$

The nonlinear model equations are achieved by substitution EQ.3.17 into EQ.B.1:

$$[P_{11}]\cdot\{u_{sy}\}+[P_{12}]\cdot\{u_{sl}\}+[P_{15}]\cdot[MZs]\cdot[M1]\cdot\{\tilde{i_{sv}}\}+[P_{15}]\cdot[MZs]\cdot[M2]\cdot\{\tilde{i_{svs}}\}=\{0\}_{n_s*1} \tag{B.3}$$

About the node k in the stator leakage circle: Similarly, substitution EQ.3.14 into EQ.A.8, one obtains:

$$[P_{21}]\cdot\{u_{sy}\}+[P_{22}]\cdot\{u_{sl}\}+[P_{23}]\cdot\{u_{rl}\}-[P_{25}]\cdot[MZs]\cdot\{i_{sv}\}=\{0\}_{n_s*1} \tag{B.4}$$

The linear model equations are obtained by substitution EQ.3.15 into EQ.B.4:

$$[P_{21}]\cdot\{u_{sy}\}+[P_{22}]\cdot\{u_{sl}\}+[P_{23}]\cdot\{u_{rl}\}-[P_{25}]\cdot[MZs]\cdot[MIs]\cdot\{\tilde{i_{sv}}\}=[P_{25}]\cdot[MZs]\cdot\{I_{sp}\} \tag{B.5}$$

The nonlinear model equations are achieved by substitution EQ.3.17 into EQ.B.4:

$$[P_{21}]\cdot\{u_{sy}\}+[P_{22}]\cdot\{u_{sl}\}+[P_{23}]\cdot\{u_{rl}\}-[P_{25}]\cdot[MZs]\cdot[M1]\cdot\{\tilde{i_{sv}}\}-[P_{25}]\cdot[MZs]\cdot[M2]\cdot\{\tilde{i_{svs}}\}=\{0\}_{n_s*1} \tag{B.6}$$

About the node k in the rotor leakage circle: Substitution EQ.3.19 and EQ.A.21 into EQ.A.16, since the product of $[P_{36}]$ and $\{\mathcal{F}_{rt}\}$ is a constant vector $\{FIm\}$ as defined in EQ.B.7,

$$[P_{36}]\cdot\{\mathcal{F}_{rt}\}=\{FIm\}=\begin{Bmatrix}0\\-\mathcal{F}_m\cdot P_{rtm}\\0\\-\mathcal{F}_m\cdot P_{rtm}\\0\\\mathcal{F}_m\cdot P_{rtm}\\0\\\mathcal{F}_m\cdot P_{rtm}\\0\\-\mathcal{F}_m\cdot P_{rtm}\\0\\-\mathcal{F}_m\cdot P_{rtm}\\0\\\mathcal{F}_m\cdot P_{rtm}\\0\\\mathcal{F}_m\cdot P_{rtm}\end{Bmatrix} \tag{B.7}$$

where $\mathcal{F}_m$ and P_{rtm} are the constant values only relying on the characteristic parameters of the PMs which are not influenced by the magnetic saturation effect. EQ.A.16 is finally transformed into EQ.B.8.

$$[P_{32}] \cdot \{u_{sl}\} + [P_{33}] \cdot \{u_{rl}\} + [P_{34}] \cdot \{u_{ry}\} = -\{FIm\} \tag{B.8}$$

About the node k in the rotor yoke circle: Similarly, substitution EQ.3.19 and EQ.A.25 into EQ.A.24, since $[P_{46}] \cdot \{\mathcal{F}_{rt}\} = \{FIm\}$, EQ.A.24 is finally transformed into EQ.B.9 for the PMSM model.

$$[P_{43}] \cdot \{u_{rl}\} + [P_{44}] \cdot \{u_{ry}\} = \{FIm\} \tag{B.9}$$

Due to the same reason mentioned in EQ.A.28 and EQ.A.29, the last column of the matrix $[P_{34}]$ and the last line of the EQ.B.9 should be removed. Then, EQ.B.8 and EQ.B.9 are respectively modified as:

$$[P_{32}] \cdot \{u_{sl}\} + [P_{33}] \cdot \{u_{rl}\} + [\tilde{P_{34}}] \cdot \{\tilde{u_{ry}}\} = -\{FIm\} \tag{B.10}$$

$$[\tilde{P_{43}}] \cdot \{u_{rl}\} + [\tilde{P_{44}}] \cdot \{\tilde{u_{ry}}\} = \{\tilde{FIm}\} \tag{B.11}$$

Assemblage of the permeance network equations: Four equations deduced from four groups of the PNM are combined together to obtain the full set of permeance network equations about the whole cross section of the PMSM in order to describe the relation between the magnetic node potentials $\{u_{sr}\}$ and the stator path currents $\{\tilde{i_{sv}}\}$.

Without magnetic saturation effect: EQ.B.2, EQ.B.5, EQ.B.10 and EQ.B.11 are adopted to establish the equations in the case without the magnetic saturation effect.

$$[PnodU] \cdot \{u_{sr}\} - [HPT] \cdot \{\tilde{i_{sv}}\} = \{IFI\} \tag{B.12}$$

where $[PnodU]$ and $\{u_{sr}\}$ are available in EQ.A.31 and EQ.A.33 while $[HPT]$ and $\{IFI\}$ are defined respectively as:

$$[HPT] = \begin{bmatrix} -([P_{15}] \cdot [MZs] \cdot [MIs])_{n_s*(n_{ph}*(n_v-1))} \\ ([P_{25}] \cdot [MZs] \cdot [MIs])_{n_s*(n_{ph}*(n_v-1))} \\ [0]_{n_r*(n_{ph}*(n_v-1))} \\ [0]_{(n_r-1)*(n_{ph}*(n_v-1))} \end{bmatrix} \tag{B.13}$$

$$\{IFI\} = \begin{Bmatrix} -([P_{15}] \cdot [MZs] \cdot \{I_{sp}\})_{n_s*1} \\ ([P_{25}] \cdot [MZs] \cdot \{I_{sp}\})_{n_s*1} \\ -\{FIm\}_{n_r*1} \\ \{\tilde{FIm}\}_{(n_r-1)*1} \end{Bmatrix} \tag{B.14}$$

where $n_r = 2 * n_m$ and $n_v = 4$ is the parallel path number.

With magnetic saturation effect: EQ.B.3, EQ.B.6, EQ.B.10 and EQ.B.11 are used to establish the equations taking into account the magnetic saturation effect.

$$[PnodU]\cdot\{u_{sr}\}-[HPTs]\cdot\left\{\begin{matrix}\{\tilde{i_{sv}}\}\\ \{\tilde{i_{svs}}\}\end{matrix}\right\}=\{IFIs\} \tag{B.15}$$

where $\{\tilde{i_{svs}}\}$ is available in EQ.3.18 and $[HPTs]$ and $\{IFIs\}$ are defined respectively as:

$$[HPTs]=\begin{bmatrix}-([P_{15}]\cdot[MZs]\cdot[M1])_{n_s*(n_{ph}*(n_v-1))} & -([P_{15}]\cdot[MZs]\cdot[M2])_{n_s*n_{ph}}\\ ([P_{25}]\cdot[MZs]\cdot[M1])_{n_s*(n_{ph}*(n_v-1))} & ([P_{25}]\cdot[MZs]\cdot[M2])_{n_s*n_{ph}}\\ [0]_{n_r*(n_{ph}*(n_v-1))} & [0]_{n_r*n_{ph}}\\ [0]_{(n_r-1)*(n_{ph}*(n_v-1))} & [0]_{(n_r-1)*n_{ph}}\end{bmatrix} \tag{B.16}$$

$$\{IFIs\}=\left\{\begin{matrix}\{0\}_{n_s*1}\\ \{0\}_{n_s*1}\\ -\{FIm\}_{n_r*1}\\ \{\tilde{FIm}\}_{(n_r-1)*1}\end{matrix}\right\} \tag{B.17}$$

B.2 Flux linkage equations

In the nodal based model, the magnetic tooth flux $\{\phi_{st}\}$ can be expressed by the magnetic nodal potentials at two ends of the corresponding tooth branches and the MMF source in the associated tooth branch as described in EQ.A.35. By substituting EQ.3.14 in it, the first equation in EQ.A.35 is transformed into:

$$\{\phi_{st}\}=[P_{12}]\cdot(\{u_{sy}\}-\{u_{sl}\}-[MZs]\cdot\{i_{sv}\}) \tag{B.18}$$

Substitution EQ.3.28 into EQ.B.18, the latter one is displayed as:

$$\{\phi_{sv}\}=[ww]\cdot[P_{12}]\cdot(\{u_{sy}\}-\{u_{sl}\}-[MZs]\cdot\{i_{sv}\}) \tag{B.19}$$

Without magnetic saturation effect: As mentioned before, the equations in the case without the magnetic saturation effect are developed by substituting EQ.3.15 into EQ.B.19:

$$\{\phi_{sv}\}+[ww]\cdot[P_{12}]\cdot[MZs]\cdot\{I_{sp}\}=[ww]\cdot[P_{12}]\cdot(\{u_{sy}\}-\{u_{sl}\}-[MZs]\cdot[MIS]\cdot\{\tilde{i_{sv}}\}) \tag{B.20}$$

Considering about all the terms in the magnetic nodal potential vector $\{u_{sr}\}$, EQ.B.20 can be rearranged in a compact format:

$$[HPP]\cdot\{u_{sr}\}+[PnodV]\cdot\{\tilde{i_{sv}}\}=\{\phi_{sv}\}+[ww]\cdot[P_{12}]\cdot[MZs]\cdot\{I_{sp}\} \tag{B.21}$$

where the two coefficient matrix $[HPP]$ and $[PnodV]$ are separately organized as:

$$[HPP]=\begin{bmatrix}([ww]\cdot[P_{12}])_{(n_{ph}*n_v)*n_s} & (-[ww]\cdot[P_{12}])_{(n_{ph}*n_v)*n_s} & [0]_{(n_{ph}*n_v)*n_r} & [0]_{(n_{ph}*n_v)*(n_r-1)}\end{bmatrix} \tag{B.22}$$

$$[PnodV]=\begin{bmatrix}-([ww]\cdot[P_{12}]\cdot[MZs]\cdot[MIS])_{(n_{ph}*n_v)*(n_{ph}*(n_v-1))}\end{bmatrix} \tag{B.23}$$

With magnetic saturation effect: And those in the case with magnetic saturation effect are deduced by substituting EQ.3.17 into EQ.B.19:

$$\{\phi_{sv}\} = [ww] \cdot [P_{12}] \cdot (\{u_{sy}\} - \{u_{sl}\} - [MZs] \cdot ([M1] \cdot \{\tilde{i_{sv}}\} + [M2] \cdot \{\tilde{i_{svs}}\})) \tag{B.24}$$

Similarly, taken the complete magnetic nodal potential vector $\{u_{sr}\}$ into account, EQ.B.24 is expressed in a more compact format:

$$[HPPs] \cdot \{u_{sr}\} + [PnodVs] \cdot \{i_{sv}\} = \{\phi_{sv}\} \tag{B.25}$$

where $[HPPs] = [HPP]$, $\{i_{sv}\} = \{\{\tilde{i_{sv}}\}\{\tilde{i_{svs}}\}\}^T$ and the coefficient matrix $[PnodVs]$ is defined as:

$$[PnodVs] = \left[-([ww] \cdot [P_{12}] \cdot [MZs] \cdot [M1])_{(n_{ph}*n_v)*(n_{ph}*(n_v-1))} \quad -([ww] \cdot [P_{12}] \cdot [MZs] \cdot [M2])_{(n_{ph}*n_v)*n_{ph}}\right] \tag{B.26}$$

B.3 Augmented magnetic equations

Two set of augmented magnetic equations are described respectively in the nodal based model, one is applied in the case which don't involve the magnetic saturation effect and another is employed to consider the variation of the permeances in the iron core part as the function of the magnetic field intensity due to the magnetic saturation effect.

Without magnetic saturation effect: Two set of equations deduced respectively in EQ.B.12 and EQ.B.21 are combined here to construct a bigger set of augmented magnetic equations which is described in the following.

$$\begin{bmatrix} [PnodU] & -[HPT] \\ [HPP] & [PnodV] \end{bmatrix} \cdot \begin{Bmatrix} \{u_{sr}\} \\ \{\tilde{i_{sv}}\} \end{Bmatrix} = \begin{Bmatrix} \{IFI\}_{(2n_s+2n_r-1)*1} \\ (\{\phi_{sv}\} + [ww] \cdot [P_{12}] \cdot [MZs] \cdot \{I_{sp}\})_{(n_{np}*n_v)*1} \end{Bmatrix} \tag{B.27}$$

Meanwhile, by eliminating the vector $\{u_{sr}\}$ in EQ.B.27, the direct relation between the path currents $\{\tilde{i_{sv}}\}$ and the magnetic path flux $\{\phi_{sv}\}$ is achieved as:

$$[HPP] \cdot [PnodU]^{-1} \cdot \{IFI\} - [ww] \cdot [P_{12}] \cdot [MZs] \cdot \{I_{sp}\} + ([HPP] \cdot [PnodU]^{-1} \cdot [HPT] + [PnodV]) \cdot \{\tilde{i_{sv}}\} = \{\phi_{sv}\} \tag{B.28}$$

With magnetic saturation effect: Similarly, two set of equations from respectively EQ.B.15 and EQ.B.25 are assembled together to achieve the augmented magnetic equations in the case with the magnetic saturation.

$$\begin{bmatrix} [PnodU] & -[HPTs] \\ [HPPs] & [PnodVs] \end{bmatrix} \cdot \begin{Bmatrix} \{u_{sr}\} \\ \{i_{sv}\} \end{Bmatrix} = \begin{Bmatrix} \{IFIs\}_{(2n_s+2n_r-1)*1} \\ \{\phi_{sv}\}_{(n_{np}*n_v)*1} \end{Bmatrix} \tag{B.29}$$

Identically, by eliminating the vector $\{u_{sr}\}$ in EQ.B.29, the relation between the path currents $\{i_{sv}\}$ and the magnetic path flux $\{\phi_{sv}\}$ is obtained as:

$$[HPPs] \cdot [PnodU]^{-1} \cdot \{IFIs\} + ([HPPs] \cdot [PnodU]^{-1} \cdot [HPTs] + [PnodVs]) \cdot \{i_{sv}\} = \{\phi_{sv}\} \tag{B.30}$$

Appendix C

Motor parameters and Mechanical model characteristics

Parameter	Value
Number of poles	2
Number of phases	3
Number of parallel paths	1
Outer diameter of the stator core [m]	0.2
Inner diameter of the stator core [m]	0.12
Air-gap average length [m]	9.6e-4
Core length [m]	0.165
Number of stator slots	36
Number of rotor slots	30
Skew of rotor slots [°]	1.34
Connection	Y
Rated voltage [V]	400
Rated frequency [Hz]	50
Rated current [A]	13.5
Rated power [kW]	7.5

Table C.1: Motor parameters about the first cage induction motor “LSES132SM”

Parameter	Value
Mass of the rotor [kg]	17.05
Moment of inertia [kg·m^2]	0.01102
Steel Young's modulus [Gpa]	210
Steel density [kg·m^{-3}]	7800
Steel poisson's ratio	0.3
Shaft length [m]	0.325
Shaft diameter [m]	0.043
Modal damping ratio	0.07
Equivalent bearing stiffness [N·m^{-1}]	5e7

Table C.2: Mechanical model characteristics about the first cage induction motor "LSES132SM"

Parameter	Value
Number of poles	4
Number of phases	3
Number of parallel paths	1 or 2
Outer diameter of the stator core [m]	0.27
Inner diameter of the stator core [m]	0.097
Air-gap average length [m]	6e-4
Core length [m]	0.27
Number of stator slots	48
Number of rotor slots	40
Skew of rotor slots [°]	1.22
Connection	Y
Rated voltage [V]	400
Rated frequency [Hz]	50
Rated current [A]	41.4
Rated power [kW]	22

Table C.3: Motor parameters about the second cage induction motor "LSES180LUR"

Parameter	Value
Mass of the rotor [kg]	121.53
Moment of inertia [kg·m^2]	0.1555
Steel Young's modulus [Gpa]	210
Steel density [kg·m^{-3}]	7800
Steel poisson's ratio	0.3
Shaft length [m]	0.556
Shaft diameter [m]	0.066
Modal damping ratio	0.07
Equivalent bearing stiffness [N·m^{-1}]	5e7

Table C.4: Mechanical model characteristics about the second cage induction motor "LSES180LUR"

Parameter	Value
Number of poles	4
Number of phases	3
Number of parallel paths	4
Outer diameter of the stator core [m]	0.2
Inner diameter of the stator core [m]	0.125
Air-gap average length [m]	5.5e-4
Core length [m]	0.06
Number of stator slots	48
Number of permanent magnets	8
Connection	Y
Rated frequency [Hz]	100
Rated current [A]	24.57
Rated power [kW]	15
Residual flux density [T]	1.32

Table C.5: Motor parameters about the permanent magnet synchronous motor

Parameter	Value
Mass of the rotor [kg]	12.89
Moment of inertia [kg·m^2]	0.01291
Steel Young's modulus [Gpa]	210
Steel density [kg·m^{-3}]	7800
Steel poisson's ratio	0.3
Shaft length [m]	0.694
Shaft diameter [m]	0.050
Modal damping ratio	0.07
Equivalent bearing stiffness [N·m^{-1}]	5e7

Table C.6: Mechanical model characteristics about the permanent magnet synchronous motor

Résumé étendu

Introduction générale

Les moteurs électriques sont des dispositifs importants pour convertir l'énergie électrique en travail mécanique. Ils ont été largement utilisés dans de nombreux domaines industriels depuis la création du premier moteur électrique dans les années 1740. L'utilisation de plus en plus répandue de moteurs à vitesse variable qui permettent d'optimiser les performances des systèmes entraînés, soulève de nouveaux défis techniques pour garantir un fonctionnement satisfaisant sur toute la plage de vitesse. D'autre part, la recherche de solutions compactes conduit à l'augmentation des vitesses de rotation ainsi qu'à l'allègement des structures mécaniques, ce qui n'est pas sans conséquences sur le comportement des machines. Par ailleurs, des architectures de plus en plus originales apparaissent avec l'intégration du moteur dans la machine entraînée comme illustré dans la figure FIG.R.1.

Figure R.1: Exemple d'une architecture intégrant le moteur synchrone à aimants permanents et la charge tournante: compresseur à vis avec rotor en porte-à-faux (@ Nidec Leroy Somer).

Le moteur à bride d'origine avec accouplement est remplacé par un simple moteur synchrone à aimants permanents. Ce moteur synchrone est intégré directement sur le même arbre du compresseur à vis sans alignement à l'aide d'un autre palier. Puisque le

rotor est en porte-à-faux monté sur un arbre relativement peu rigide, ce type de structure introduit facilement des problèmes de vibration, de bruit et d'instabilité sur son comportement dynamique. Dans le cas extrême, le contact rotor-stator a été rencontré lors de son fonctionnement sous certaines conditions réelles. Le même problème peut être retrouvé dans d'autres situations similaires: le rotor entre deux paliers mais très allongé et monté sur un arbre relativement peu rigide, le stator sans carter susceptible d'importantes déformations, etc.

Ce phénomène vibratoire pourrait s'expliquer par l'apparition d'un effort radial électromagnétique (UMP) introduit au sein de la machine électrique en raison de l'excentricité de l'entrefer. Dans les structures évoquées précédemment, l'axe du rotor sera inévitablement mal aligné avec celui du stator, sous l'effet de la pesanteur par exemple. Ce désalignement introduit la différence de longueur d'entrefer sur la périphérie du rotor. Dans le cadre du moteur électrique, la majorité de la conversion de l'énergie électromécanique est réalisée sous la forme de composantes de force radiale et tangentielle. Toutes les forces tangentielles sont intégrées sur la périphérie de l'entrefer pour produire le couple électromagnétique tandis que les forces radiales se compensent généralement dans le cas d'un entrefer uniforme. Par l'excentricité de l'entrefer, ces composantes de force radiale magnétique révèlent une force radiale résultante à l'intérieur de la machine électrique appelée UMP. L'effet de cette force est approximativement dans la direction de l'entrefer minimal et va accentuer l'excentricité de l'entrefer. En conséquence, certains problèmes de bruit, des vibrations et des secousses (NVH) apparaissent dans les machines électriques.

Les outils de modélisation avancée ont beaucoup progressé dans les dernières décennies, en particulier grâce à l'analyse par éléments finis, tant en mécanique qu'en électrotechnique. Ils restent cependant cloisonnés dans leur discipline: chacun ne prend en compte la physique de l'autre que très grossièrement, et dans le meilleur des cas en faisant l'hypothèse d'un couplage faible. Dans le but d'une optimisation globale de la machine, une approche multiphysique s'avère indispensable, qui remette en cause un certain nombre d'hypothèses simplificatrices traditionnelles, et permette un couplage fort entre la mécanique et l'électrotechnique. Dans le cadre d'une précédente thèse [4], un modèle original de machine asynchrone a été développé au LaMCoS de l'INSA Lyon. Ce modèle propose un couplage multiphysique entre la partie électro-magnétique, modélisée par des circuits RL et des réseaux de perméances 2D, et la partie mécanique modélisée par des éléments de poutre et des éléments spécifiques pour les supports et les roulements. Une des originalités de ce modèle est d'utiliser une approche dite "angulaire" qui permet de s'affranchir de l'hypothèse de régimes stationnaires en introduisant explicitement le degré de liberté en rotation. Le couplage fort entre la partie électro-magnétique et mécanique se fait essentiellement et uniquement par le couple moteur et la vitesse de rotation (relation angle-temps). Ces premiers travaux, préliminaires à une modélisation réaliste, ont montré la faisabilité d'une telle approche pour les machines asynchrones (architecture conventionnelle et simplifiée) et ont ouvert de nombreuses perspectives.

Les objectifs de cette thèse seront d'explorer ces perspectives dans le cadre d'un partenariat avec une entreprise leader dans le domaine (NIDEC LEROY SOMER) afin

de mieux comprendre et modéliser les phénomènes non linéaires fins qui conduisent à des comportements dynamiques instables exigeant un niveau de modélisation investiguant tous les couplages électro-magnéto-mécaniques, en particulier en effort dans toutes les directions de sollicitation. Par ailleurs, les conditions de fonctionnement non stationnaires, issues de chargements variables et de pilotage électrique non conventionnel, doivent être prises en compte pour décrire les régimes transitoires potentiellement endommageant. Les régimes de vitesse élevée seront également envisagés pour prendre en compte les effets centrifuges présents en dynamique des rotors.

Basé sur le premier modèle d'un moteur asynchrone en effectuant des corrections et des améliorations, un nouveau modèle multiphysique intégrant de forts couplages électro-magnéto-mécaniques dédié à étudier l'influence de UMP sur le comportement dynamique des moteurs électriques est proposé dans cette thèse. Ce modèle entièrement couplé est adopté pour décrire les performances du moteur à induction et du moteur synchrone à aimants permanents avec différentes configurations d'enroulement et dans différentes structures mécaniques. Les phénomènes vibratoires excités par la force UMP, par la force de balourd et par la pesanteur sont analysés respectivement dans deux moteurs électriques traditionnels en conditions non stationnaires. Les non-linéarités physiques et géométriques sont toutes prises en compte dans ce modèle pour interpréter les phénomènes non linéaires de UMP.

Chapitre 1. Modélisation de moteur à induction

Ce chapitre fournit une méthodologie sur l'établissement du modèle multiphysique pour le moteur à induction. Il est constitué généralement de trois parties principales: la modélisation, la validation et l'analyse des résultats simulés. Le moteur asynchrone étudié est un moteur à induction à double cage d'écureuil qui possède 2 pôles, 36 encoches statoriques et 30 barres rotoriques. Le stator est équipé d'un enroulement distribué à une seule couche alimenté par la source de tension triphasée en Y comme le montre la figure FIG.R.2. La double cage de rotor est simplifiée en une seule cage pour conserver la même surface d'encoche rotorique.

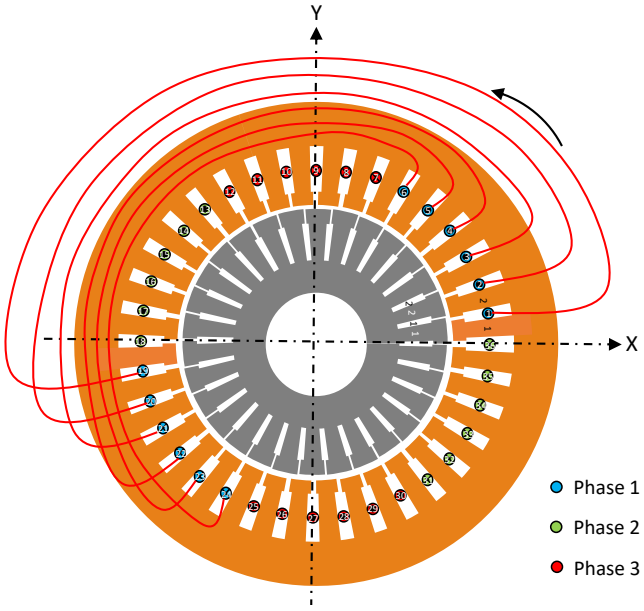

Figure R.2: Vue transversale du moteur à induction.

Modélisation

Les trois champs physiques différents présents dans le moteur électrique à savoir le champ magnétique, les circuits électriques et la structure mécanique sont décrits dans l'ordre par plusieurs équations algébriques ou différentielles. Puisque l'approche du **réseaux de perméances** (PNM) est adoptée pour décrire le champ magnétique qui est la partie centrale du moteur électrique, le maillage du réseaux de perméances et le calcul des valeurs des éléments de base sont d'abord introduits. En appliquant les lois de Kirchhoff, les **équations du réseaux de perméances** sont développées pour décrire la relation entre les inconnues choisies et les sources de force magnétomotrice (MMF) dans toute la section efficace de la machine électrique. Les **équations de liaison de flux** pour calculer le flux magnétique dans chaque phase à partir du flux dans chaque dent sont élaborées. Les deux groupes d'équations sont combinés pour construire les **équations magnétiques augmentées** afin d'obtenir une description complète de l'ensemble du champ magnétique. Comme mentionné précédemment, le modèle magnétique peut être développé avec différents modèles de réseaux de perméances (PNM). Le modèle de nœud étatit adopté dans le modèle précédent de sorte qu'il est réformulé dans cette thèse avec des améliorations. Le modèle mixte maille/nodal cumulant les avantages des deux premiers comme le montre la figure FIG.R.3 est finalement utilisé pour établir le modèle magnétique dans le modèle multiphysique proposé. Un ensemble d'**équations différentielles électriques** sur les circuits électriques dans l'enroulement du stator et dans la cage d'écureuil du rotor est établi pour définir le modèle électrique global. Le **couplage entre les champs électromagnétiques** est ensuite réalisé pour étudier les performances des modèles électromagnétiques avec différents vecteurs d'état établis soit en courant soit

en flux. Il est confirmé que les deux modèles avec des vecteurs d'état différents sont fondamentalement identiques, mais le modèle de flux de phase est à la fois plus efficace dans la simulation et est prêt à mettre en place l'effet de saturation magnétique dans le système. Le **modèle mécanique** du moteur électrique est amélioré ultérieurement en ajoutant l'excitation de balourd. Les forces électromagnétiques sont calculées en appliquant le principe de la méthode de travail virtuel dans le réseaux de perméances défini. Les trois domaines sont finalement assemblés pour réaliser le **couplage multiphysique fort** dans le modèle proposé. Un modèle électromagnétique (Modèle EM) sans la partie mécanique est extrait du modèle couplé (Modèle EMM) pour illustrer l'importance de l'interaction électro-magnéto-mécanique et pour valider le modèle proposé. Il est prouvé que les deux modèles sont équivalents dans le cas sans excentricité ou avec une petite excentricité. Mais pour une excentricité importante ou au point de fonctionnement présentant un couple résistant important, les résultats du Modèle EMM sont plus précis que ceux du Modèle EM. En raison du couplage avec la structure mécanique, le modèle proposé est piloté par le couple de charge externe pour simuler uniquement les points de fonctionnement dans la zone de fonctionnement stable du moteur.

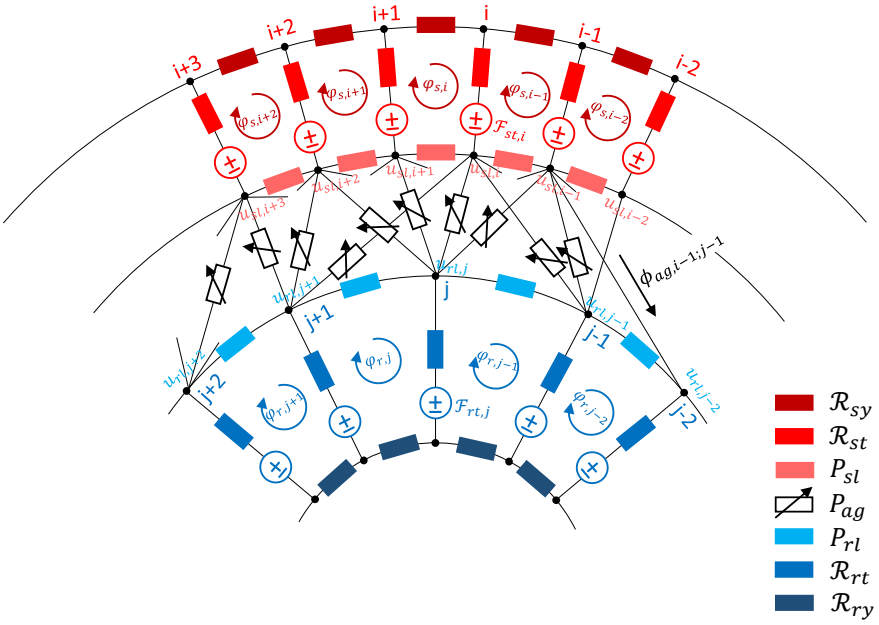

Figure R.3: Réseau de perméances mixte pour le moteur à induction.

Validation

Avant l'analyse des résultats simulés, ce modèle multiphysique est validé en régime quasi-statique en comparaison avec un autre modèle traditionnel basé sur la méthode des éléments finis (FEM) établi dans le logiciel FEMM. Les résultats de simulation entre les

deux modèles sont d'abord comparés au point de fonctionnement nominal pour évaluer les grandeurs caractéristiques et la forme de leur fluctuation en fonction de la rotation de l'arbre. La deuxième comparaison est effectuée entre les résultats simulés du Modèle EM et les données de référence fournis par notre partenaire industriel afin de valider la valeur moyenne en tout point de fonctionnement sur la courbe caractéristique du moteur asynchrone.

Analyse des résultats simulés

Différents résultats simulés du modèle proposé sont analysés d'abord en conditions stationnaires puis en conditions non stationnaires avec une excentricité du rotor, soit générée par la mise en place de l'excentricité statique, soit introduite par le mouvement dynamique du rotor.

Les simulations en fonctionnement stationnaire en imposant une excentricité statique sont réalisées dans deux cas. Dans le premier cas, à partir des résultats simulés avec la même valeur d'excentricité mais en deux points de fonctionnement différents, l'angle entre la direction de l'UMP de la direction d'entrefer minimal est d'abord découvert à partir du diagramme polaire de l'UMP comme le montre la figure FIG.R.4(a). Ceci est dû à l'effet des courants d'égalisation induits dans la cage du rotor par l'excentricité, ce qui est en accord avec d'autres publications. Les effets d'encoche dans le système sont ensuite révélés en traçant l'orbite du centre du rotor voir la figure FIG.R.5. En termes de caractéristiques physiques, il est montré que l'UMP générée au point de fonctionnement avec un glissement plus important a tendance à fluctuer autour de la position de l'excentricité avec des oscillations plus importantes dans la direction verticale comme illustré dans la figure FIG.R.4(b).

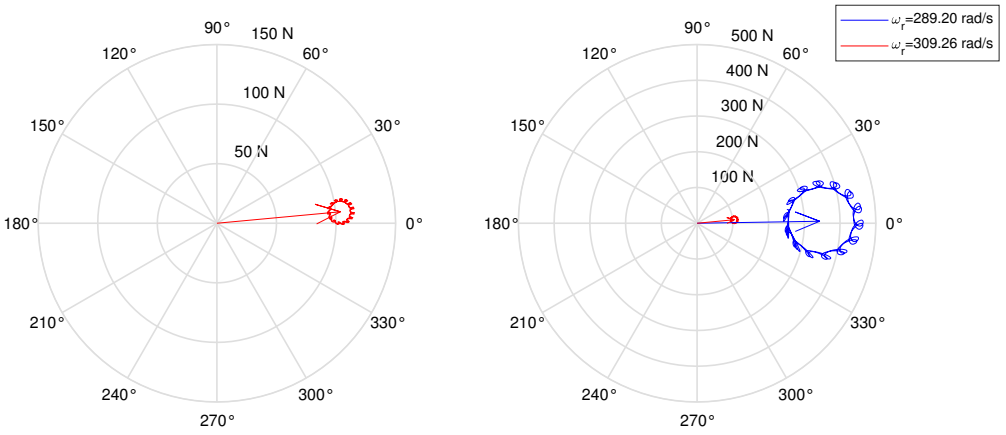

(a) (b)

Figure R.4: Diagramme polaire de l'UMP avec l'excentricité statique de $0.1E_e$ dans le dernier tour de l'arbre. La flêche indique l'effort moyen, la courbe montre la variation d'effort en amplitude et en direction.

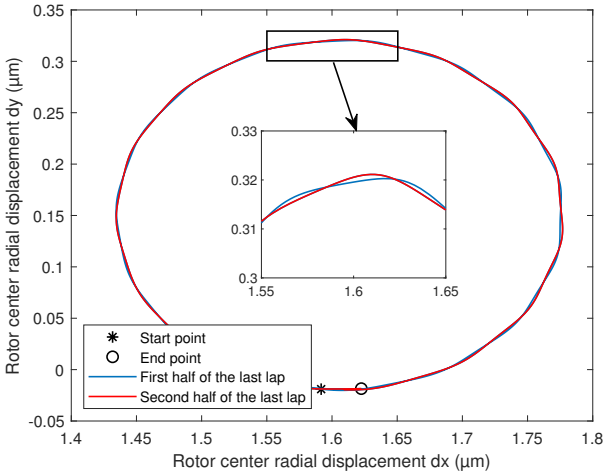

Figure R.5: Orbite du centre du rotor dans la section xoy avec l'excentricité statique de $0.1E_e$.

Ensuite, par leur analyse fréquentielle, plusieurs fréquences caractéristiques associées aux excentricités statiques comme la deuxième harmonique de la fréquence d'alimentation et sa modulation avec les harmoniques de la fréquence du passage de dent rotorique sont identifiées à partir du spectre angulaire de la force UMP voir la figure FIG.R.6. Ceci démontre bien la modulation introduite par le couplage des phénomènes angulaires et temporels. Les mêmes fréquences caractéristiques sont également visibles dans le spectre du couple électromagnétique comme le montre la figure FIG.R.7 pour refléter le fait que la perturbation radiale du rotor influence également son mouvement de rotation.

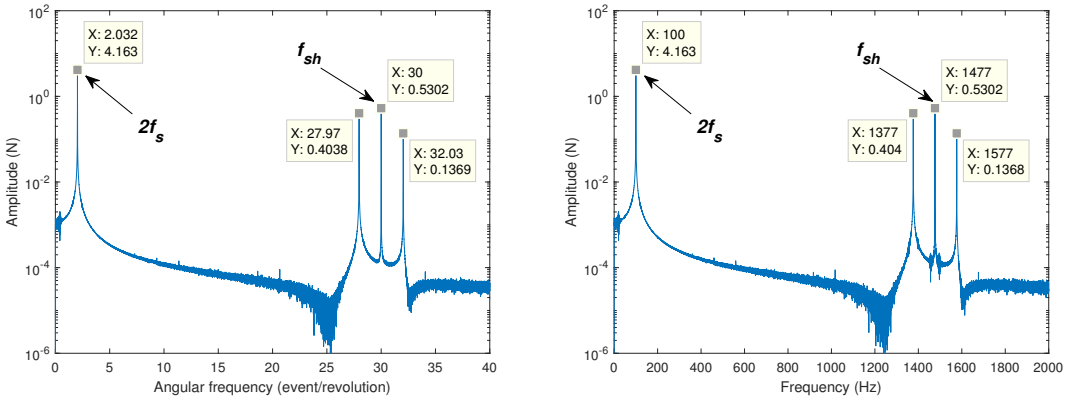

(a) Spectre angulaire (b) Spectre traditionnel

Figure R.6: Spectre de fréquence de l'UMP le long de la direction x avec l'excentricité statique de $0.1E_e$ à $\omega_r = 309.26\ \mathrm{rad}\cdot\mathrm{s}^{-1}$.

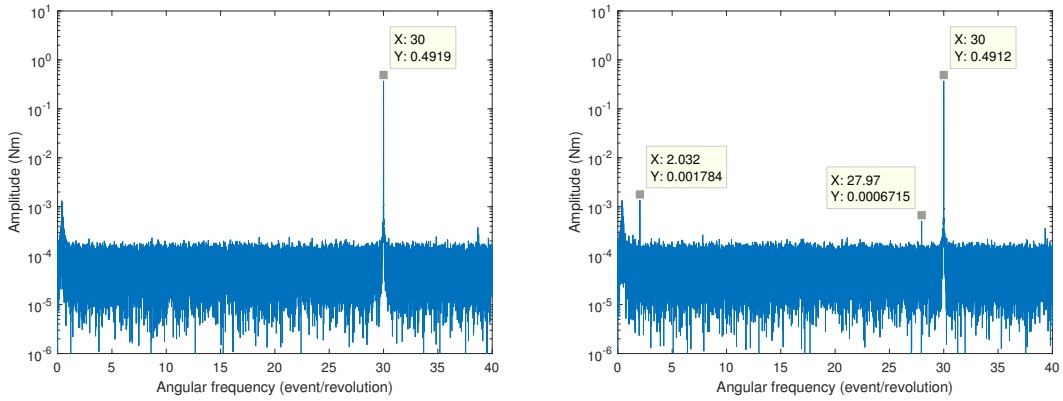

(a) Sans excentricité (b) Avec $0.1E_e$ excentricité

Figure R.7: Spectre angulaire du couple électromagnétique à $\omega_r = 309.26\ \mathrm{rad \cdot s^{-1}}$.

Dans le second cas, en comparant les résultats de simulation au point de fonctionnement nominal mais avec trois valeurs d'excentricité différentes, il est montré que les variations de l'UMP en amplitude et en orientation augmentent linéairement avec la valeur d'excentricité imposée comme le montre la figure FIG.R.8.

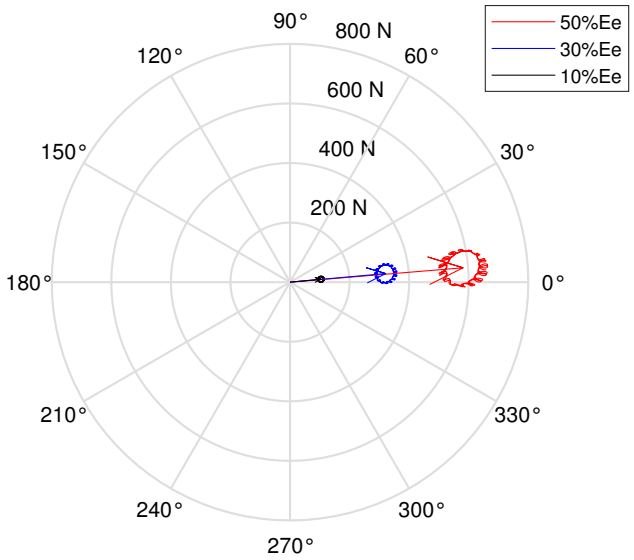

Figure R.8: Diagramme polaire de l'UMP avec différentes valuers d'excentricités au point de fonctionnement nominal

Et en même temps, les ondulations présentes sur le signal de la vitesse de rotation instantanée deviennent de plus en plus évidentes. Plus d'harmoniques de la fréquence d'alimentation apparaissent progressivement dans leur spectre. Ces fréquences caractéristiques identifiées se rapportant à l'excentricité statique apparaissent également dans

le spectre de la vitesse de rotation dans les cas avec excentricité. Toujours en fonctionnement stationnaire, les simulations avec l'excentricité du rotor induite par le mouvement dynamique du rotor sont réalisées sous excitation du balourd et de la pesanteur. Les résultats de simulation concernant l'UMP selon la figure FIG.R.9 et l'orbite du centre du rotor selon la figure FIG.R.10 sont comparés pour les cas avec ou sans effet de la pesanteur. On peut conclure à partir des résultats que l'effet de l'excitation du balourd peut être traité comme un mouvement tourbillonnaire synchrone du rotor tandis que l'influence de la pesanteur est équivalente à une excentricité statique imposée.

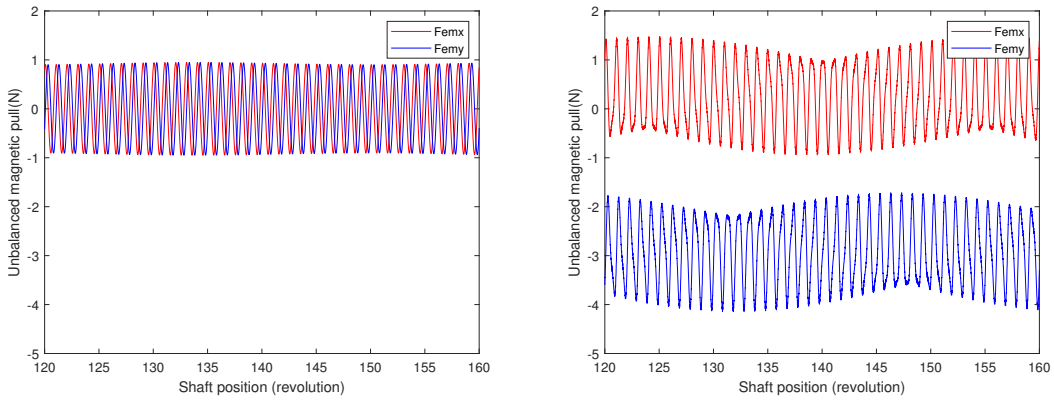

(a) Avec l'excitation du balourd (b) Avec l'excitation du balourd et la pesanteur

Figure R.9: Variation de l'UMP sous le mouvement de rotor dynamique au point de fonctionnement nominal.

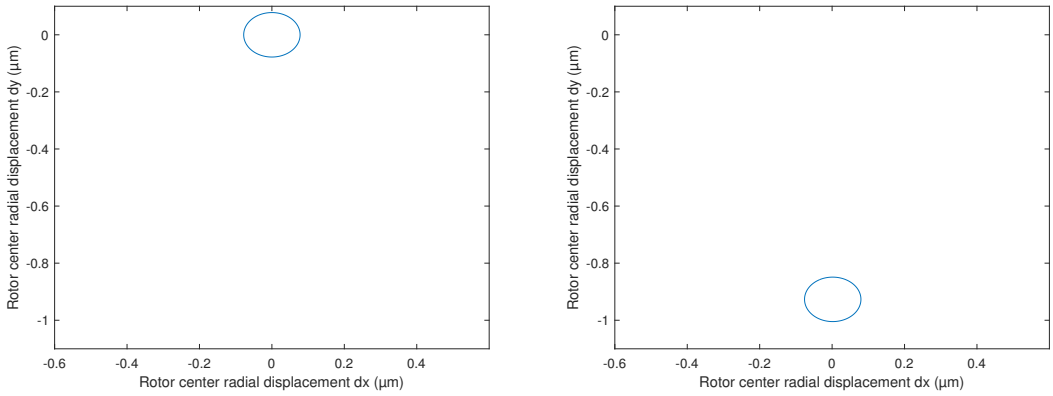

(a) Avec l'excitation du balourd (b) Avec l'excitation du balourd et la pesanteur

Figure R.10: Orbite du centre du rotor sous le mouvement de rotor dynamique au point de fonctionnement nominal.

Les simulations en fonctionnement non stationnaire sont réalisées naturellement en

appliquant un couple résistant qui augmente linéairement. Grâce à l'analyse des résultats simulés avec l'excentricité statique de $0.1E_e$, on s'aperçoit que plus d'harmoniques liées à la fréquence d'alimentation seront induites avec l'augmentation du couple de charge comme illustré sur la figure FIG.R.11, ce qui peut potentiellement augmenter le risque de résonance structurelle. La simulation similaire avec l'excitation du balourd est ensuite étudiée pour découvrir que les ondulations dues au glissement du moteur apparaissent plus évidentes dans l'allure de l'UMP avec l'augmentation du couple de charge.

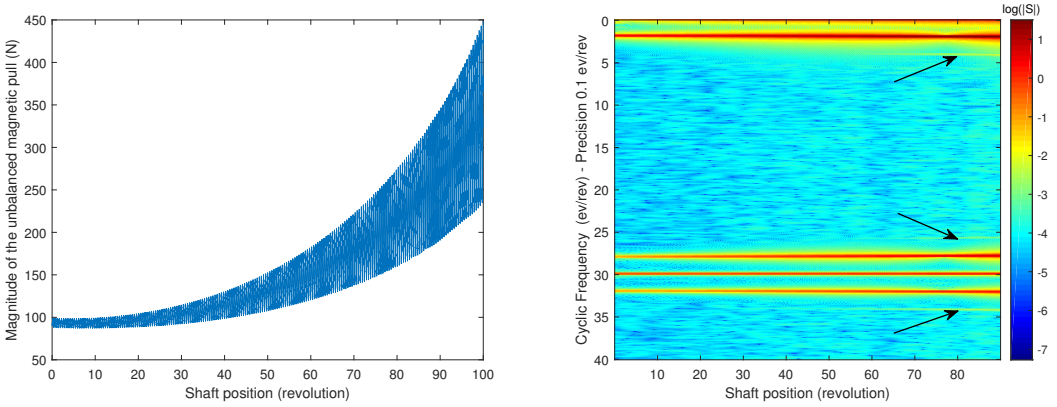

(a) Variation de l'UMP (b) Spectrogramme angulaire de l'UMP

Figure R.11: Composante de force sur l'axe x de l'UMP avec l'excentricité statique de $0.1E_e$ en fonctionnement non-stationnaire.

Dans l'ensemble, le modèle multiphysique proposé de la machine asynchrone basé sur l'approche angulaire est capable de simuler son comportement dynamique dans différents conditions avec différents types d'excentricité du rotor en fonctionnement stationnaire et non stationnaire. Des couplages forts de différents champs physiques à l'intérieur de la machine électrique sont mis en évidence à partir de l'analyse de différents résultats de simulation.

Chapitre 2. Modélisation de moteur synchrone à aimants permanents

Ce chapitre est dédié au développement du modèle multiphysique proposé sur un moteur synchrone à aimants permanents (PMSM). Basé sur le modèle du moteur à induction établi au Chapitre 1, la modélisation des trois sous-systèmes dans le PMSM de référence est réalisé de la même manière dans la partie modélisation. Le moteur synchrone à étudier dans cette thèse est un moteur synchrone à aimants permanents enterrés avec 4 pôles. Son stator posséde 48 encoches équipé d'un bobinage concentrique et son rotor est composé de 8 aimants permanents sous forme de rectangle. La vue transversale du moteur synchrone à aimants permanents est illustrée sur la figure FIG.R.12.

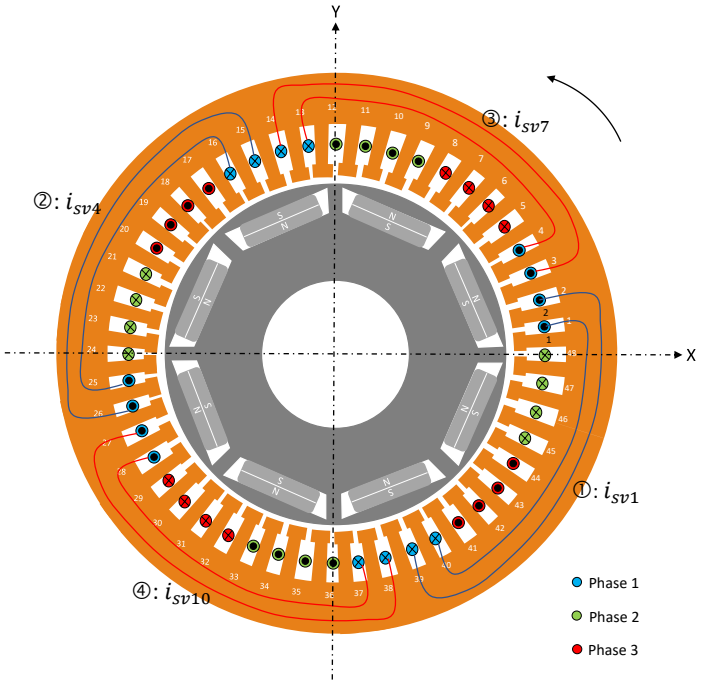

Figure R.12: Vue transversale du moteur synchrone à aimants permanents.

Modélisation

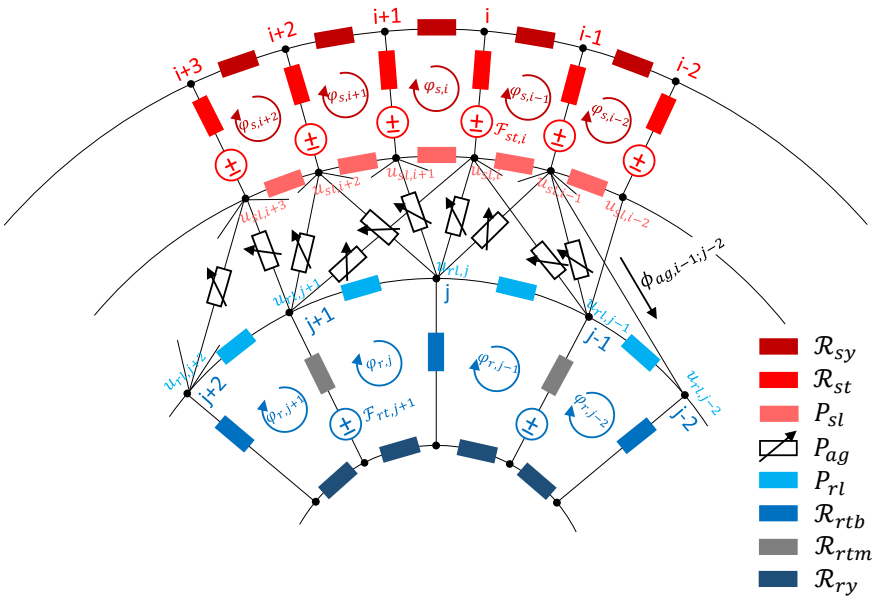

Figure R.13: Réseau de perméances mixte pour le moteur synchrone à aimants permanents enterrés.

En prolongeant le modèle de moteur asynchrone, deux modèles de géométries différentes sur le PMSM de référence sont développés dans ce chapitre pour l'analyse des comportements dynamiques du moteur synchrone respectivement avec et sans effet de saturation magnétique. Afin d'éviter la répétition, seules les parties différentes de celles du modèle de la machine asynchrone sont présentées ici. Les trois différents champs physiques dans le PMSM sont à nouveau décrits selon les différences entre le moteur asynchrone et le moteur synchrone. Le réseaux de perméances mixte pour le moteur synchrone à aimants permanents enterrés est représenté dans la figure FIG.R.13. Dans le modèle magnétique, le réseaux de perméances associé à la partie rotorique est défini en fonction de la géométrie du rotor avec les aimants permanents enterrés de sorte que tous les éléments actifs et passifs du réseaux de perméances sont recalculés, comme les perméances dans la partie rotor et la force magnétomotrice (MMF) apporté par les aimants permanents. Deux ensembles de perméance d'entrefer sont définis pour mieux décrire la distribution du flux magnétique dans l'entrefer du PMSM. Pour le modèle électrique, une nouvelle configuration de bobinage avec deux voies en parallèle est mise en place dans chaque phase statorique et toute la machine est alimentée par la source de courant triphasée. Troisièmement, dans le modèle mécanique, une structure mécanique personnalisée est introduite pour s'adapter à l'hypothèse du modèle électromagnétique 2.5D et préparer la future partie expérimentale. Avec une amplitude de courant de phase statorique donnée, l'angle de phasage de couple est identifié dans le modèle proposé. En faisant varier le courant triphasé du mouvement de synchronisme du rotor, la position angulaire initiale θ_{r0} est choisie comme l'expression alternative de l'angle de couple dans le PMSM pour piloter le point de fonctionnement. Cette stratégie est adoptée à la fois dans le modèle couplé multiphysique et dans le modèle découplé avec la partie mécanique car il n'y a pas de boucle d'asservissement dans le PMSM entre T_{em} et ω_r comme décrit dans la courbe caractéristique du moteur asynchrone. Étant donné qu'aucun système de contrôle n'est pris en compte dans le modèle PMSM actuel, la vitesse de rotation doit être prédéfinie par l'attribution du couple de charge.

Validation

Le modèle proposé est capable d'effectuer des simulations sans et avec effet de saturation magnétique en considérant les perméances dans les parties de fer comme constantes ou variables. Lorsque ces perméances varient en fonction du flux magnétique passant, les équations magnétiques d'origine deviennent non linéaires, ce qui devrait être résolu par la méthode d'itération à chaque pas de résolution des équations différentielles globales. Cela augmentera évidemment le temps de simulation. Afin de surmonter cette difficulté pour la simulation de longue durée requise en situation non stationnaire, un modèle équivalent est créé en supprimant les deux ponts en fer du rotor dans le modèle d'origine. Différents modèles avec des propriétés de réglage différentes basées sur le modèle d'origine et le modèle équivalent sont établis dans les logiciels FEMM et MATLAB. Les abréviations des noms de ces modèles sont disponibles dans le tableau TAB.R.1. En comparant la courbe Couple-Angle entre le Modèle FEMM1 et le Modèle FEMM2, ce

dernier est confirmé comme un bon choix alternatif pour la simulation sans effet de saturation magnétique. Les modèles proposés sont validés sous deux aspects en comparant le Modèle EM avec le Modèle FEMM correspondant en régime quasi-statique. La première validation est effectuée au point de fonctionnement nominal à travers la comparaison entre le Modèle EM1 et le Modèle FEMM1 sur l'allure du couple électromagnétique et de la force UMP dans la direction de l'excentricité. Il est démontré qu'il existe des différences entre leur amplitude de variation ou leur valeur moyenne mais leurs profils de fluctuation sont similaires. La différence pourrait être causée par le maillage grossier du réseaux de perméances dans l'entrefer. Par contre la similitude de leurs allures confirment la fiabilité de l'étude des composantes fréquentielles avec le Modèle EM1. Étant donné que la différence autour de la valeur moyenne de F_{emx} devient plus petite dans le modèle équivalent, cela prouve que l'utilisation du modèle équivalent dans l'analyse de la vibration radiale sous excitation du balourd peut être approchée mais reste fiable. La seconde comparaison est réalisée à tous les points de fonctionnement en comparant leurs courbes Couple-Angle dans respectivement le modèle d'origine et le modèle équivalent. Elles sont toutes identiques dans le profil général et le meilleur accord entre les deux courbes dans le modèle équivalent en fait le bon choix pour effectuer les simulations en fonctionnement non stationnaire.

Géométrie	D'origine		Équivalent
Saturation	Avec	Sans	Sans
Sans couplage mécanique	Modèle FEMM1	Modèle FEMM1_L	Modèle FEMM2
	Modèle EM1	⁄	Modèle EM2
Avec couplage mécanique	Modèle EMM1	⁄	Modèle EMM2

Table R.1: Abréviations des différents noms de modèles sur le PMSM de référence.

Analyse des résultats simulés

Puisqu'il n'y a pas de grande différence entre le Modèle EM et le Modèle EMM comme discuté avant, le Modèle EM1 est utilisé en premier lieu pour étudier les phénomènes caractéristiques des résultats de simulation au point de fonctionnement nominal mais avec en entrée différentes valeurs d'excentricité. Le déséquilibre entre les voies parallèles apparaît dans l'allure du courant statorique dans la même phase avec l'augmentation de la valeur d'excentricité imposée et cela introduit plus d'harmoniques de la fréquence d'alimentation dans le système comme le montre la figure FIG.R.14. L'augmentation de la valeur d'excentricité statique n'a pas beaucoup d'influence sur l'allure du couple électromagnétique mais elle génère une composante fréquentielle au deuxième harmonique de la fréquence d'alimentation et la combinaison de ses harmoniques avec les harmoniques de l'encoche statorique dans le mouvement de rotation. Différent de l'angle de décalage de l'UMP identifié dans le moteur à induction, la valeur moyenne de la force UMP dans la direction orthogonale à la direction de l'excentricitè est nulle dans le PMSM

car il n'y a pas de courants induits dans la partie rotorique selon la figure FIG.R.15. Des ondulations plus évidentes apparaissent dans l'allure de l'UMP avec l'augmentation de la valeur d'excentricité. Similaires à celles identifiées pour le couple électromagnétique, plus d'harmoniques multiples du deuxième harmonique de la fréquence d'alimentation et de leurs modulations avec les harmoniques de l'encoche statorique apparaissent dans leur spectre comme le montre la figure FIG.R.16.

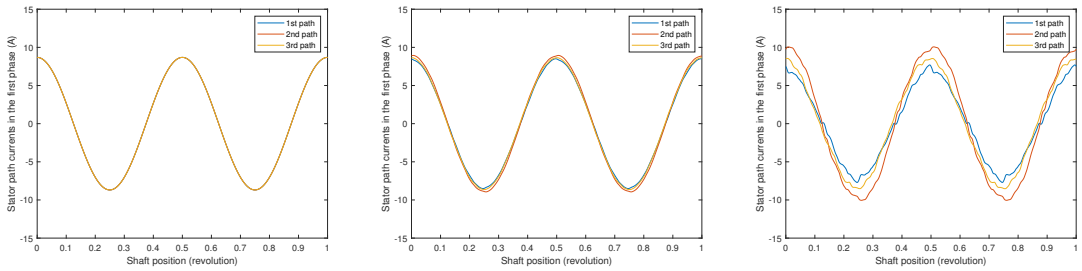

(a) Sans excentricité (b) Avec 10%E_e (c) Avec 50%E_e

Figure R.14: Variation des trois courants de voie dans la première phase en fonction de la position de l'arbre.

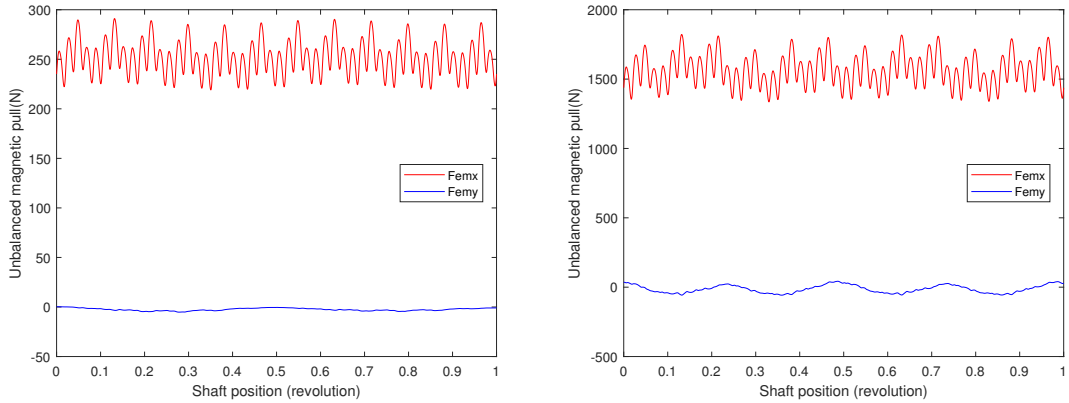

(a) Avec 10%E_e (b) Avec 50%E_e

Figure R.15: Variation de l'UMP en fonction de la position de l'arbre.

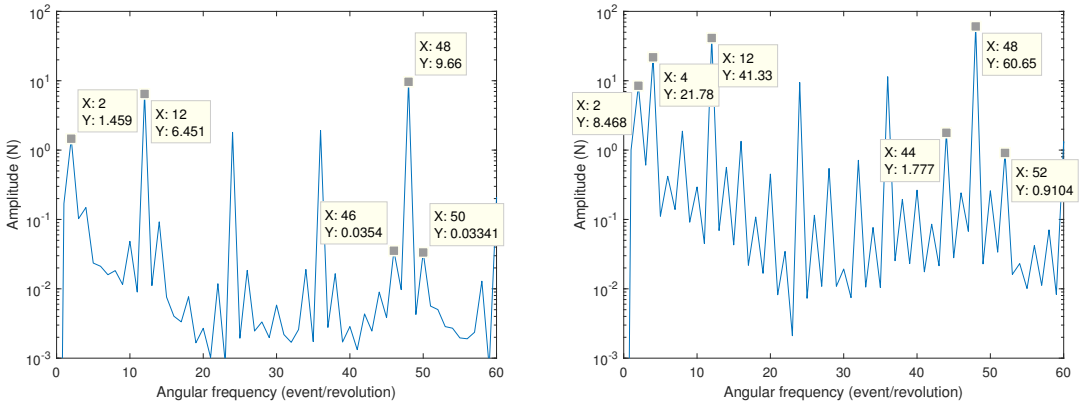

(a) Avec $10\%E_e$ (b) Avec $50\%E_e$

Figure R.16: Spectre angulaire de la force de l'axe x de l'UMP.

Le Modèle EMM2 est ensuite adopté pour étudier l'allure de la vitesse angulaire instantanée en condition stationnaire et puis pour analyser les performances vibratoires sous excitation de balourd et avec la prise en compte de la force de pesanteur du rotor en conditions non stationnaires. Les deux méthodes d'allocation des paramètres de couple résistant afin de maintenir la vitesse de rotation en régime permanent sont validées dans le cas sans excentricité. Certaines fluctuations apparaissent dans la variation de la vitesse instantanée du rotor en raison de l'effet d'encoche car les harmoniques de l'encoche statorique sont identifiées dans son spectre. Les simulations en conditions non stationnaires sont effectuées au point de fonctionnement nominal mais avec une vitesse de rotation qui augmente linéairement. Elles sont analysées respectivement sous trois aspects différents. Le premier concerne l'analyse de tous les résultats de simulation à une certaine accélération angulaire. En traçant les résultats de simulation en fonction de la vitesse de rotation instantanée comme le montre la figure FIG.R.17, deux perturbations sont identifiées dans la variation de l'UMP et des déplacements radiaux du centre rotor. La première apparaît également dans les autres résultats de simulation comme les courants de voie statorique et le couple électromagnétique. L'amplitude de la première perturbation est plus grande que celle de la seconde mais la première se produit à environ 50 Hz tandis que la seconde survient à 107 Hz.

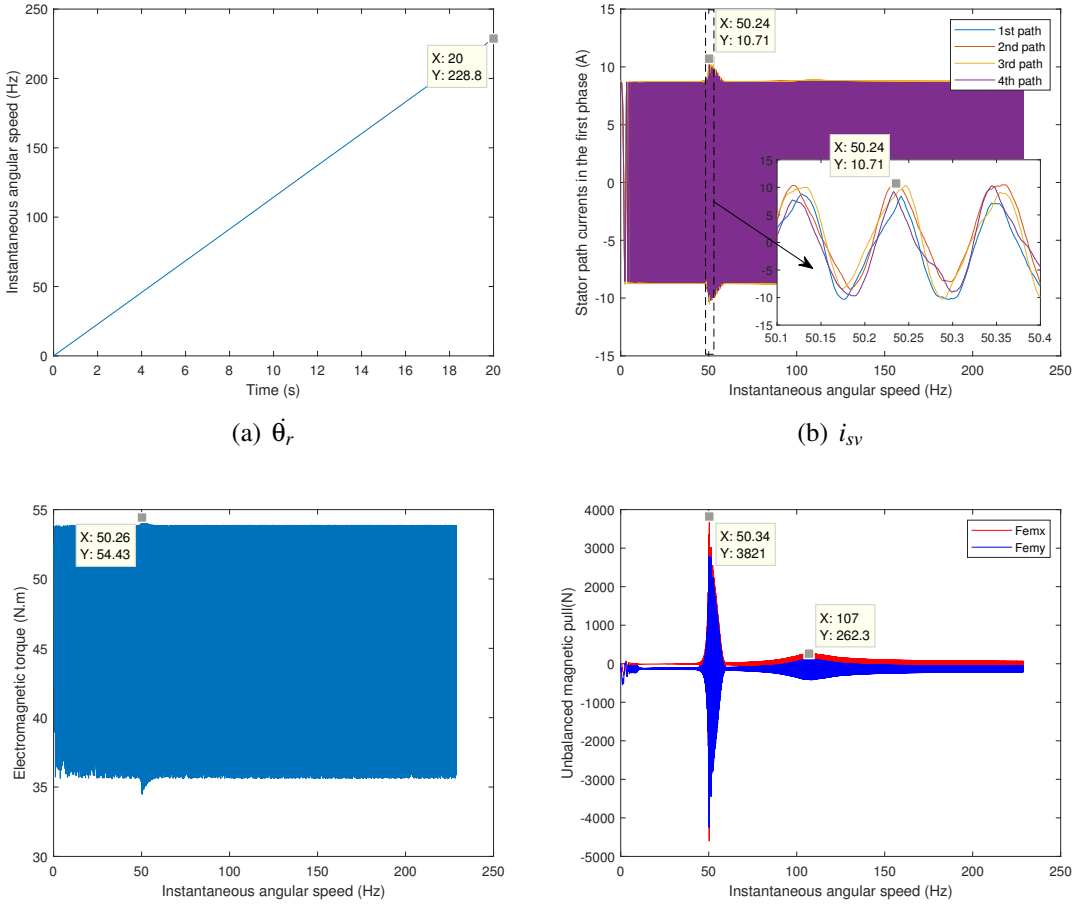

(a) $\dot{\theta}_r$ (b) i_{sv}

(c) T_{em} (d) UMP

Figure R.17: Variation des différents résultats de simulation dans le cas avec $\ddot{\theta}_r = 71.81\ (rad/s^2)$.

Le spectrogramme des déplacements radiaux simulés est similaire au grave problème de vibration qui s'est produit dans le moteur réel comme le montre la figure FIG.R.18, ce qui signifie que le modèle proposé est capable de reproduire les phénomènes de vibration similaires découverts sur la machine réelle. La deuxième analyse concerne l'effet de l'UMP dans le système avec excitation du balourd. En supprimant l'UMP généré dans la simulation d'origine et en comparant les deux déplacements radiaux simulés avec et sans UMP comme le montre la figure FIG.R.19, on observe que l'UMP affiche un effet de rigidité négatif dans le système moteur et qu'il induira une vibration auto-excitée du rotor à la vitesse critique $\omega_c \approx \frac{\tilde{\omega}_0}{P}$. L'influence des différentes accélérations angulaires est analysée en troisième lieu sur la figure FIG.R.20. A travers les simulations avec différentes accélérations angulaires, il est montré que l'amplitude de la première perturbation augmente avec la diminution de l'accélération angulaire jusqu'à l'apparition du contact rotor-stator tandis que la deuxième perturbation apparaît toujours à la même vitesse de rotation et à la même amplitude, ce qui confirme qu'elle est induite par la

fréquence propre modifiée.

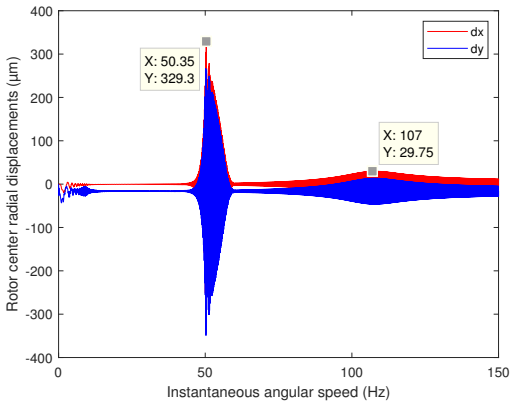

(a) Déplacements du centre du rotor

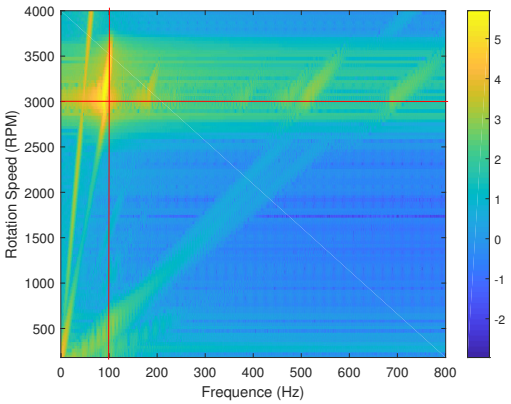

(b) Spectrogramme de dx

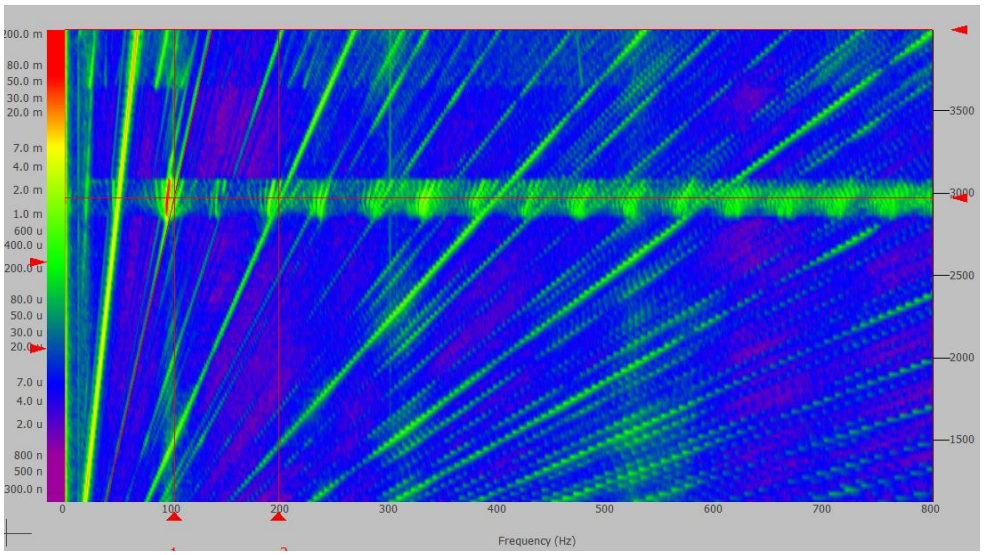

(c) Vibration radiale sur le moteur ARES® de NIDEC Leroy Somer

Figure R.18: Comparaison entre les résultats de la simulation et de la mesure sur la vibration radiale.

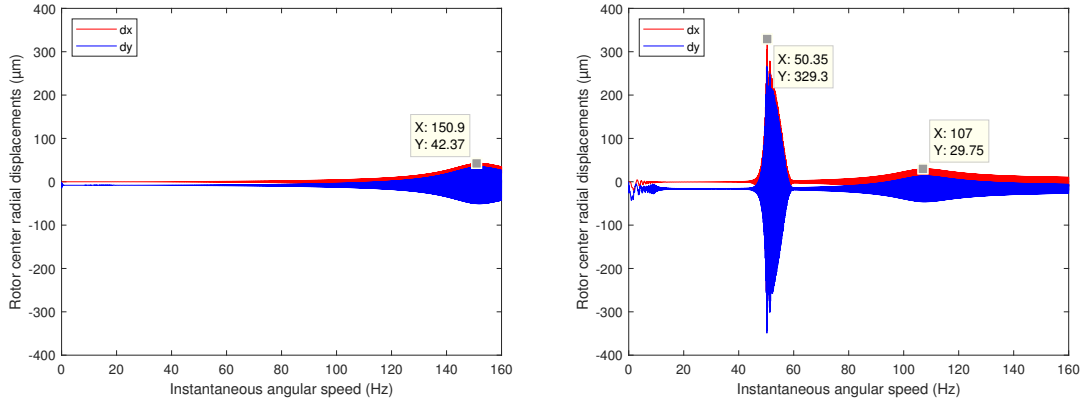

(a) Sans UMP (b) Avec UMP

Figure R.19: Comparaison des déplacements radiaux du centre du rotor entre les cas sans et avec l'UMP.

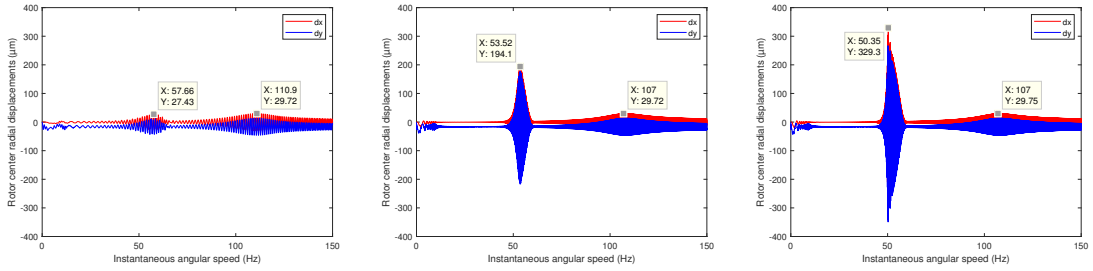

(a) $\ddot{\theta}_r = 753.98\ (rad/s^2)$ (b) $\ddot{\theta}_r = 100.53\ (rad/s^2)$ (c) $\ddot{\theta}_r = 71.81\ (rad/s^2)$

Figure R.20: Déplacements radiaux du centre du rotor à différentes accélérations angulaires.

En général, le modèle multiphysique étendu basé sur l'approche angulaire pour le moteur synchrone à aimants permanents est capable de simuler ces comportements dynamiques dans les deux cas avec et sans effet de saturation magnétique pour respectivement l'analyse des composantes fréquentielles et pour l'étude des performances vibratoires.

Chapitre 3. Influence des différents architectures

L'un des principaux objectifs de cette recherche est l'étude de l'influence de différentes architectures sur le comportement dynamique des machines électriques, il est réalisé dans ce chapitre en adoptant le modèle proposé. Comme le modèle multiphysique comporte de forts couplages électro-magnéto-mécaniques, nous proposons d'étudier l'effet

de l'architecture: sur les différentes structures mécaniques et avec différentes configurations de bobinage. Pour éviter la répétition, le premier cas est discuté dans le cadre du modèle de moteur synchrone à aimants permanents tandis que la seconde est réalisée dans le modèle du moteur à induction.

Différentes structures mécaniques

Le modèle équivalent sans effet de saturation du PMSM est adopté pour étudier l'influence de différentes structures mécaniques dans un premier temps. En comparant les déplacements radiaux du centre du rotor simulés avec la même vitesse de rotation qui augmente linéairement sous la même excitation de balourd et le poids du rotor, l'influence de trois paramètres mécaniques est analysée dans le cas de la structure classique. L'augmentation de la rigidité du roulement (k) augmente la fréquence propre du système rotorique et en même temps tend à réduire l'amplitude de la première perturbation excitée par l'UMP comme le montre la figure FIG.R.21.

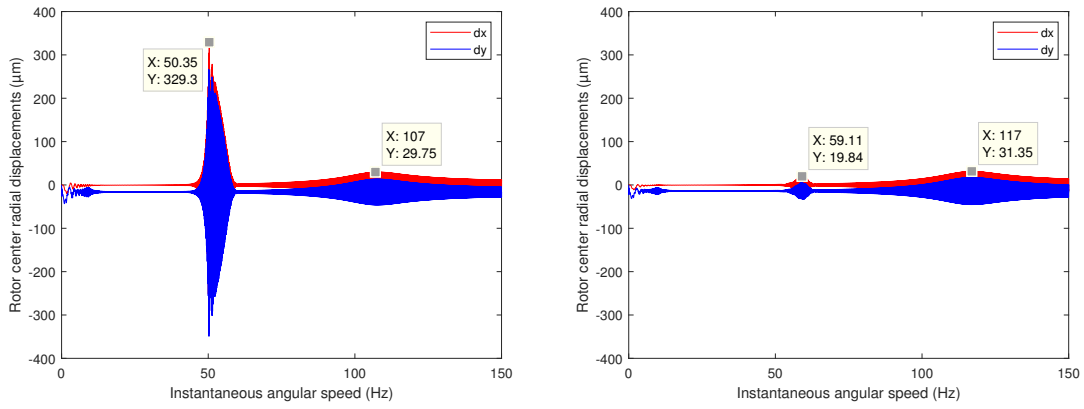

(a) $k = 5e7\ N \cdot m^{-1}$ (b) $k = 1e8\ N \cdot m^{-1}$

Figure R.21: Déplacements radiaux du centre du rotor avec différentes rigidités de roulement.

Cependant l'augmentation du taux d'amortissement (d) ne modifie pas la fréquence propre mais l'amplitude du premier pic est efficacement réduite dans ce cas selon la figure FIG.R.22.

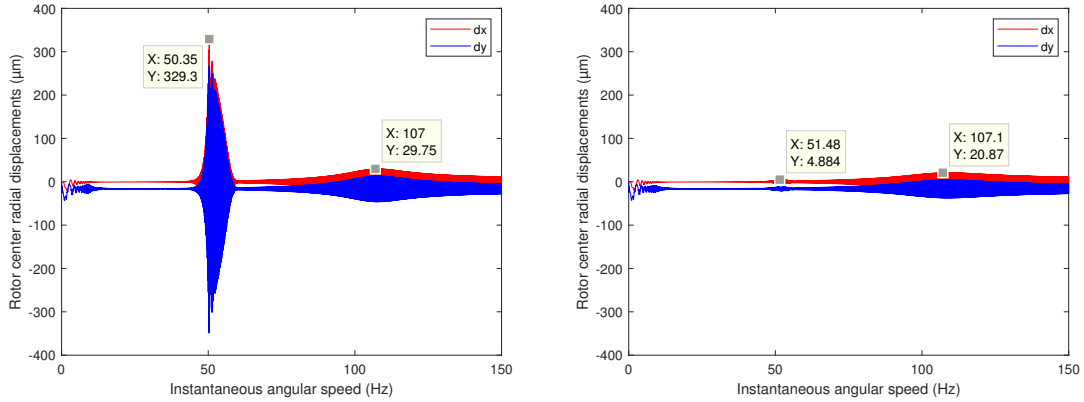

(a) $d = 0.07$ (b) $d = 0.1$

Figure R.22: Déplacements radiaux du centre du rotor avec différents amortissements structurels.

Étant donné que le deuxième pic de résonance est excité par le balourd, la variation de la valeur du balourd spécifique résiduel (δ_m) ne modifie que l'amplitude du deuxième pic comme illustré dans la figure FIG.R.23. Ensuite, une autre structure en porte-à-faux avec deux dispositions de longueur d'arbre différentes comme le montre la figure FIG.R.24 est appliquée pour effectuer la même simulation afin de comparer la structure classique. Il est enfin démontré que la structure mécanique avec une fréquence propre plus grande présente des vibrations de moindre amplitude sous l'excitation de l'UMP. Selon ces résultats de recherche, les phénomènes vibratoires tels que le contact rotor-stator peuvent être évités pendant le fonctionnement du moteur électrique en augmentant la fréquence propre de la structure mécanique ou en augmentant l'amortissement global de l'ensemble du système.

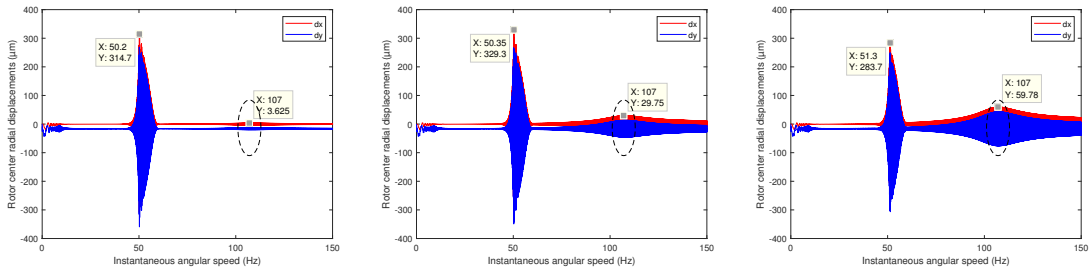

(a) $\delta_m = 1e^{-6}\ m$ (b) $\delta_m = 8e^{-6}\ m$ (c) $\delta_m = 16e^{-6}\ m$

Figure R.23: Déplacements radiaux du centre du rotor avec différentes valeurs du balourd.

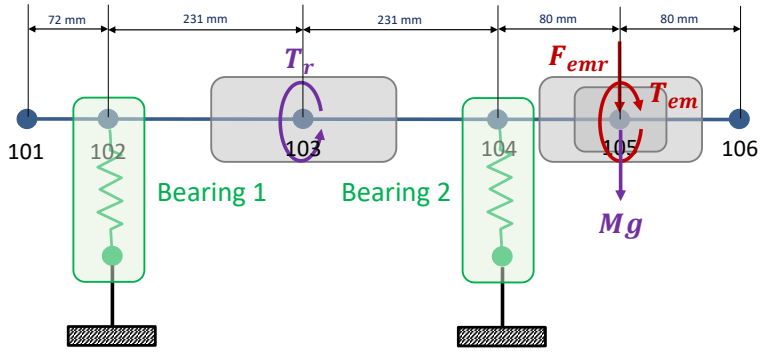

(a) Structure en porte-à-faux V1

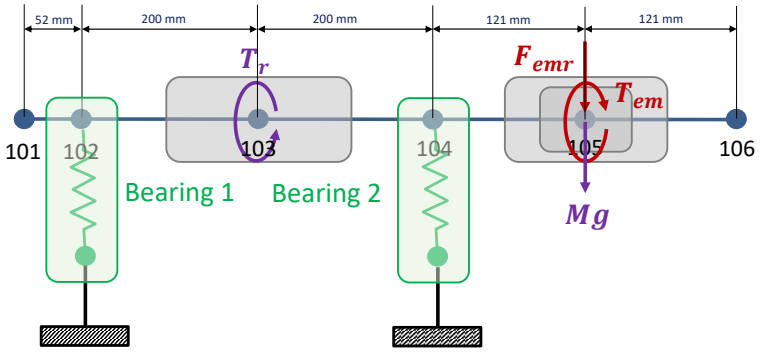

(b) Structure en porte-à-faux V2

Figure R.24: Structure en porte-à-faux avec deux dispositions de longueur d'arbre différentes.

Différentes configurations de bobinage

L'influence de différentes configurations de bobinage est étudiée dans un deuxième temps basé sur le modèle multiphysique du moteur à induction. La composition de bobinage triphasé est introduite dans la première partie. Puis l'étude est principalement réalisée sur les différents arrangements de bobines (entre le bobinage imbriqué diamétral à pôles conséquents "IPC" et le bobinage concentrique à pôles non conséquents "CPNC") ainsi que sur les différentes connexions des pôles (en série et en série-parallèle). Il est montré que le bobinage IPC et le bobinage CPNC ont la même influence sur le comportement dynamique du moteur électrique. Bien qu'il n'y ait pas de différence entre les résultats de simulation du bobinage en série et du bobinage en série-parallèle (avec les bobines opposé en séries "OCS" comme le montre la figure FIG.R.25 (a)), celle avec les bobines adjacentes en série "ACS" comme le montre la figure FIG.R.25 (b) a une influence différente.

L'UMP est atténuée dans le cas avec le bobinage en série-parallèle avec "ACS" selon la figure FIG.R.27 en raison des courants déséquilibrés induits dans les deux voies parallèles de chaque phase du stator comme illustré sur la figure FIG.R.26. Et cette redistribution de courant apporte également des harmoniques plus élevées dans le signal de courant et sur l'allure de l'UMP.

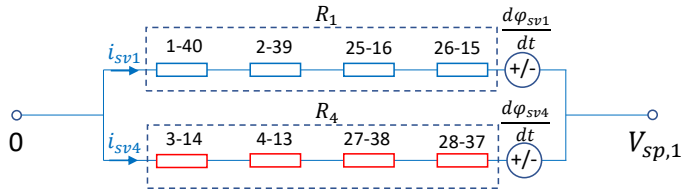

(a) Avec les bobines opposé en série "OCS"

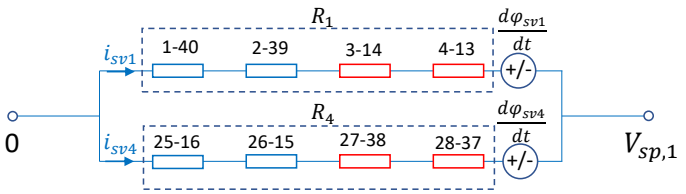

(b) Avec les bobines adjacentes en série "ACS"

Figure R.25: Connexions des bobinages statoriques en série-parallèle.

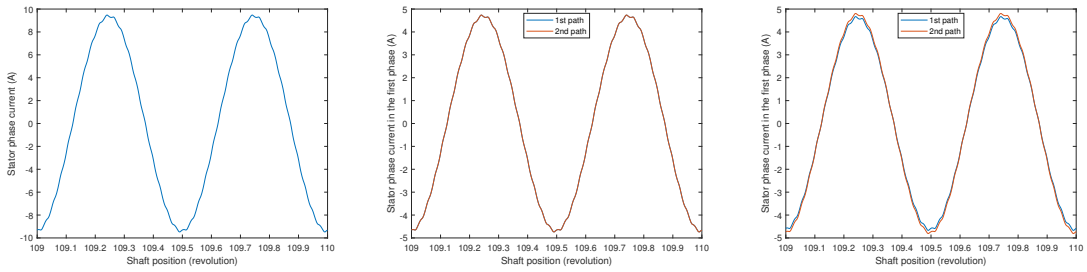

(a) Série (b) Série-parallèle avec OCS (c) Série-parallèle avec ACS

Figure R.26: Comparaison de la variation du courant de la première phase du stator avec différents configurations de bobinages.

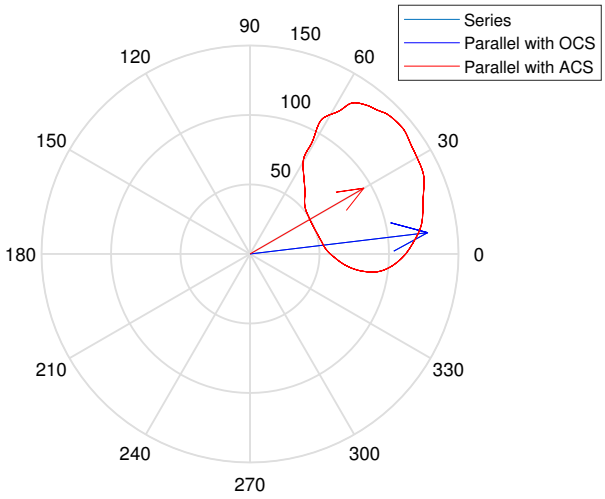

Figure R.27: Diagramme polaire de l'UMP avec l'excentricité statique de 10%E_e dans le dernier tour de l'arbre avec différents configurations de bobinages.

Conclusions générales et perspectives

Le dernier chapitre résume les travaux effectués et présentés dans les chapitres précédents. Des suggestions pour de futures études sont également proposées en fin de chapitre.

Conclusions générales

Un modèle multiphysique sur les moteurs électriques à fort couplage électro-magnéto-mécanique est établi dans cette thèse. Ce modèle est développé dans deux machines électriques traditionnelles : le moteur à induction à cage d'écureuil et le moteur synchrone à aimants permanents pour analyser leurs comportements dynamiques sous l'influence de différents phénomènes notamment l'excitation de la force de traction (UMP) induite par l'excentricité du rotor. Différent des autres modèles multiphysiques de machines électriques, le modèle proposé prend en compte le couplage complet à la fois des mouvements radiaux et de rotation. Par conséquent, la relation entre l'UMP et les déplacements radiaux du centre du rotor est ajoutée pour renforcer l'interaction électromécanique. La valeur de perméance de l'entrefer est calculée en fonction des coordonnées du centre du rotor et de l'angle de rotation de l'arbre en tenant compte à la fois des excentricités du rotor imposées et des excitations de balourd. Les non-linéarités physiques et géométriques sont considérées dans ce modèle afin de mieux comprendre et décrire les phénomènes non linéaires dans les moteurs électriques qui pourraient conduire au comportement dynamique instable. De plus, les conditions de fonctionnement non stationnaires résultant des charges variables et de la commande électrique non conventionnelle sont prises en considération en appliquant l'approche angulaire pour décrire les endommagements potentiels survenus en régime transitoire. Avec la relation "Angle-Temps" définie dans

l'approche angulaire, la fluctuation réelle de la vitesse de rotation est considérée pour interpréter la voie de transfert à partir de différents champs de variation angulairement périodiques dans les moteurs électriques. Afin d'effectuer les simulations de longue durée avec un effort de calcul raisonnable, le modèle de réseaux de perméances (PNM) mixte est adopté pour modéliser le champ magnétique en 2.5D. Les circuits électriques du bobinage du stator et de la cage du rotor sont représentés par un réseau simple composé de résistances et d'inducteurs. La partie mécanique est discrétisée en plusieurs éléments finis de poutre pour simuler les régimes de vitesses élevées et pour se préparer à décrire différentes structures mécaniques. Les équations régissant trois champs physiques différents sont dérivées de l'approche directe [140] en appliquant les lois de Newton et de Faraday. Les équations différentielles peuvent être résolues en fonction de deux vecteurs d'état différents : les courants de phase ou les flux de phase. Les résultats de simulation des deux cas avec des vecteurs d'état différents sont confirmés identiques et le flux de phase est choisi comme le vecteur d'état final car il est plus efficace dans la simulation en particulier pour la mise en place de l'effet de saturation magnétique. Un modèle électromagnétique sans couplage de la structure mécanique (Modèle EM) est extrait du modèle entièrement couplé (Modèle EMM) afin d'illustrer l'importance des forts couplages électro-magnéto-mécaniques. La validation du modèle proposé est réalisée en comparant les résultats de simulation du Modèle EM et d'un modèle éléments finis FEMM en régime quasi-statique. Après cette validation, les modèles proposés autour de deux moteurs électriques traditionnels sont adoptés pour analyser leur comportement dynamique dans deux conditions de fonctionnement (stationnaire et non stationnaire) et sous deux excitations différentes (avec une excentricité statique imposée ou avec l'excitation du balourd).

Pour le moteur à induction, les caractéristiques physiques et les composantes fréquentielles liées à l'excentricité du rotor sont d'abord identifiées grâce aux résultats de simulation générés dans les conditions stationnaires avec une excentricité statique imposée. En termes de caractéristiques physiques, l'angle entre la direction de l'UMP et la direction d'entrefer minimal est caratérisé à partir de son diagramme polaire. Ceci est dû à l'effet d'égalisation des courants induits dans la cage du rotor due à l'excentricité, ce qui est conforme aux conclusions d'autres publications. L'effet d'encoche peut être révélé à partir de l'orbite du centre du rotor. Au niveau de l'analyse fréquentielle, la deuxième harmonique de la fréquence d'alimentation et sa modulation avec les harmoniques du passage de dent rotorique dans le spectre angulaire de l'UMP sont identifiées comme les fréquences caractéristiques associées à l'excentricité statique imposée. Ils indiquent également la modulation entre les phénomènes angulaires et temporels. Puisque les mêmes fréquences caractéristiques apparaissent également dans le spectre du couple électromagnétique, il est démontré que la perturbation radiale du rotor influence également son mouvement de rotation. Ces fréquences caractéristiques pourraient être utilisées pour l'identification de l'excentricité statique dans les moteurs électriques. Toujours dans les conditions stationnaires, les résultats simulés sous excitation de balourd et prenant en compte la pesanteur impliquent que l'effet de l'excitation du balourd peut être traité comme un mouvement tourbillonnaire synchrone du rotor tandis que l'influence de

la pesanteur est équivalente à une excentricité statique imposée. Les simulations dans les conditions non stationnaires sont réalisées en appliquant un couple de charge linéairement augmenté. On peut voir qu'avec l'augmentation du couple de charge, plus d'harmoniques multiples de la deuxième harmonique de la fréquence d'alimentation sont induites dans le système avec une excentricité statique imposée tandis que plus d'ondulations dues au glissement du moteur apparaissent dans l'allure de l'UMP générée par l'excitation de balourd. Ils peuvent potentiellement augmenter le risque de phénomènes de résonance associés.

Pour le moteur synchrone à aimants permanents, l'effet de saturation magnétique est établi dans le modèle pour prendre en compte ce phénomène dans les ponts magnétiques du rotor. Les résultats de simulation sur le modèle découplé au point de fonctionnement nominal mais avec différentes valeurs d'excentricité statique imposées sont présentés pour étudier les phénomènes caractéristiques. On observe qu'avec l'augmentation de la valeur d'excentricité, plus le déséquilibre apparaît dans l'allure des courants de voie parallèle du stator dans la même phase et plus les ondulations évidentes apparaissent dans l'allure de l'UMP. Ces phénomènes introduisent également plus d'harmoniques des fréquences caractéristiques liées à l'excentricité statique dans leur spectre angulaire. Comme il n'y a pas de courants induits dans la partie rotor, il n'y a pas d'angle de décalage de l'UMP dans le PMSM. Un autre modèle équivalent entièrement couplé basé sur la structure simplifiée du rotor est créé pour les simulations sur des durées longues en approximant l'effet de saturation. Une vitesse angulaire qui augmente linéairement est définie pour effectuer les simulations dans les conditions de fonctionnement non stationnaires. Grâce à l'analyse des résultats de simulation sous trois aspects différents, deux pics de perturbation sont identifiés dans l'allure de l'UMP et des déplacements radiaux du centre du rotor où le premier est la vibration auto-excitée du rotor induite par l'UMP tandis que le second est excité autour de la première fréquence naturelle modifiée. Conformément aux études précédentes, il est confirmé que l'UMP présente un effet de rigidité négatif dans le système de moteur. On observe que l'amplitude de la vibration auto-excitée du rotor augmente avec la diminution de l'accélération angulaire jusqu'à l'apparition du contact rotor-stator. Par conséquent, le modèle proposé est capable de reproduire les phénomènes de vibration similaires à ceux rencontrés dans la machine réelle. Remarquablement similaire aux travaux de Boy [143], la vibration auto-excitée du rotor induite par l'UMP apparaît à la vitesse critique $\omega_c \approx \frac{\tilde{\omega}_0}{P}$.

Avec le modèle multiphysique proposé, l'influence de différentes architectures dans les moteurs électriques est étudiée sous deux aspects. Le modèle équivalent sans effet de saturation du PMSM est utilisé pour étudier l'influence de différentes structures mécaniques dans un premier temps. On peut conclure que la vibration auto-excitée du rotor pourrait être réduite en augmentant la première fréquence propre de la structure ou en augmentant le taux d'amortissement. L'augmentation de la première fréquence propre peut être réalisée soit en augmentant la rigidité équivalente du roulement, soit en modifiant la disposition de la longueur de l'arbre. La variation de l'excentricité de la masse n'influence pas directement la vibration auto-excitée du rotor mais elle modifie proportionnellement l'amplitude du deuxième pic de résonance. Ces résultats pourraient être

utilisés pour éviter les phénomènes vibratoires sévères tels que le contact rotor-stator dans le fonctionnement des moteurs électriques. Le deuxième aspect se concentre sur l'analyse de l'influence des différentes configurations de bobinage en adoptant le modèle du moteur à induction. Il est montré que les bobinages IPC et CPNC ont la même influence sur le comportement dynamique du moteur électrique qui est en accord avec les connaissances industrielles. Compatible avec l'étude précédente, l'effet d'atténuation de l'UMP n'est identifié que dans le cas du bobinage en série-parallèle (les bobines adjacentes en série) en raison des courants déséquilibrés induits dans les deux voies parallèles de chaque phase du stator. Et cette redistribution de courant apporte également des harmoniques plus élevées dans le courant et l'allure de l'UMP.

Perspectives

Afin d'améliorer le modèle multiphysique proposé et d'explorer plus d'applications de ce modèle, des suggestions sont résumées en deux grandes parties pour les activités de recherche futures:

Les améliorations du modèle peuvent être discutées en trois aspects correspondant aux trois champs physiques différents dans le moteur électrique. Pour **le modèle magnétique**, d'abord le maillage du réseau de perméance doit être affiné, en particulier dans la région de l'entrefer. En effet dans le PMSM, il existe une différence évidente entre les résultats de la simulation concernant l'UMP généré à partir du modèle proposé et du Modèle FEMM. La sensibilité du modèle par rapport au nombre de mailles du réseau de perméance doit être évaluée. Ensuite, le calcul sur la mise en place de l'effet de saturation magnétique doit être accéléré pour effectuer la simulation sur des durées longues dans des conditions non stationnaires. Et puis, un modèle modal des machines électriques peut être introduite en développant le modèle magnétique du 2.5D au 3D. Enfin, l'effet des courants de Foucault doit être ajouté pour inclure la perte de fer dans le modèle afin que la perte de puissance des machines électriques puisse être évaluée. Dans **le modèle électrique**, l'alimentation contrôlée par la modulation de largeur d'impulsion (PWM) doit être ajoutée au système afin d'étudier l'influence du bruit électromagnétique dû à l'excitation PWM. Pour **le modèle mécanique**, puisque la validation du modèle proposé est réalisée en régime quasi-statique, le comportement dynamique généré par le couplage fort électro-magnéto-mécanique doit être validé par une étude expérimentale (comme la fluctuation de la vitesse de rotation). La sensibilité du modèle par rapport au nombre d'éléments de poutre doit également être évaluée. Une fois le modèle magnétique étendu en 3D, plusieurs types d'excentricité d'entrefer telles que l'excentricité incurvée et l'excentricité inclinée avec la déviation angulaire et le déplacement radial peuvent être considérés dans ce modèle multiphysique. Afin d'effectuer la simulation au plus près des conditions réelles, les autres dispositifs du système de transmission doivent être décrits avec une description plus fine. Par exemple le compresseur à vis dans la figure FIG.R.1 doit être représenté par la combinaison du couple de charge sinusoïdal et de la force radiale au lieu d'un couple de charge constant. D'autre part, les effets d'appui peuvent être représentés par la force de rappel non linéaire telle que décrite dans [135] ou par un modèle de roulement développé

dans [164]. Les orbites de chaque nœud peuvent être comparées pour étudier l'effet de l'UMP le long de l'arbre. D'ailleurs, en ce qui concerne la dynamique du rotor, l'effet gyroscopique peut être ajouté dans le modèle afin d'étudier le mouvement de rotation en précession directe ou inverse du rotor et un modèle d'impact peut être ajouté pour simuler les effets de contact stator-rotor. La stabilité du système rotorique pouvait également être évaluée par la théorie de Floquet.

Pour les applications du modèle, on peut maintenant envisager d'étudier les effets des bobinages parallèles et de la saturation magnétique sur l'UMP dans les conditions non stationnaires. L'étude de différents points de fonctionnement (différents couples de charge pour le moteur à induction et différents angles de charge pour le moteur à aimants permanents) sur les composantes radiales et tangentielles de l'UMP peuvent être explorés dans les conditions non stationnaires. Il est intéressant d'étudier la relation entre les différents défauts du moteur électrique (tels que les défauts de roulement et les défauts de bobinage du stator) et les signaux de courant statorique pour fournir une preuve théorique pour la méthode de l'analyse des signaux de courant du moteur (MCSA). Enfin, en couplant avec un modèle acoustique, les vibrations et le bruit produits par la machine électrique peuvent être prédits. Étant donné que l'UMP généré pourrait être réduit en ajustant le courant statorique d'entrée, un ensemble de systèmes de contrôle pourrait être conçu sur cette base de modélisation réaliste.

Bibliography

[1] A. Fourati, A. Bourdon, N. Feki, D. Rémond, F. Chaari, M. Haddar, Angular-based modeling of induction motors for monitoring, Journal of Sound and Vibration 395 (2017) 371–392.
URL https://doi.org/10.1016%2Fj.jsv.2016.12.031

[2] V. Ostović, Dynamics of Saturated Electric Machines, Springer New York, New York, NY, 1989.
URL http://public.eblib.com/choice/publicfullrecord.aspx?p=3079121

[3] X. Xu, Q. Han, F. Chu, Review of electromagnetic vibration in electrical machines, Energies 11 (7) (2018) 1779. doi:10.3390/en11071779.
URL http://www.mdpi.com/1996-1073/11/7/1779

[4] A. Fourati, Modélisation électro-magnéto-mécanique d'une machine asynchrone sous approach angulaire application au diagnostic des défauts de roulements en regime non-stationnaire, Ph.D. thesis.

[5] R. Belmans, A. Vandenput, W. Geysen, Calculation of the flux-density and the unbalanced pull in 2 pole induction machines, Electrical Engineering 70 (3) (1987) 151–161.

[6] A. Di Gerlando, G. M. Foglia, R. Perini, Analytical modelling of unbalanced magnetic pull in isotropic electrical machines, in: 2008 18th International Conference on Electrical Machines, IEEE, 2008, pp. 1–6.

[7] D. G. Dorrell, W. T. Thomson, S. Roach, Analysis of airgap flux, current, and vibration signals as a function of the combination of static and dynamic airgap eccentricity in 3-phase induction motors, IEEE Transactions on Industry applications 33 (1) (1997) 24–34.

[8] X. Chen, Z. Deng, J. Hu, T. Deng, An analytical model of unbalanced magnetic pull for pmsm used in electric vehicle: numerical and experimental validation, International Journal of Applied Electromagnetics and Mechanics 54 (4) (2017) 583–596.

[9] A. Borisavljevic, H. Polinder, J. Ferreira, Calculation of unbalanced magnetic force in slotless pm machines, in: conference; Electrimacs 2011, Cergy-Pontoise, France: University of Cergy-Pontoise–Paris; 2011-06-06; 2011-06-08, E Monmasson, 2011, pp. 1–6.

[10] Z. Zhu, D. Howe, Effect of rotor eccentricity and magnetic circuit saturation on acoustic noise and vibration of single-phase induction motors, Electric machines and power systems 25 (5) (1997) 443–457.

[11] B. Lapôtre, N. Takorabet, F. Meibody-Tabarb, Permanent magnet bearingless motors: Modelling, design and drive, in: 2017 IEEE Workshop on Electrical Machines Design, Control and Diagnosis (WEMDCD), IEEE, 2017, pp. 119–126.

[12] Z. Zhu, D. Howe, E. Bolte, B. Ackermann, Instantaneous magnetic field distribution in brushless permanent magnet dc motors. i. open-circuit field, IEEE transactions on magnetics 29 (1) (1993) 124–135.

[13] Z. Zhu, D. Howe, Instantaneous magnetic field distribution in brushless permanent magnet dc motors. ii. armature-reaction field, IEEE transactions on magnetics 29 (1) (1993) 136–142.

[14] U. Kim, D. K. Lieu, Magnetic field calculation in permanent magnet motors with rotor eccentricity: without slotting effect, IEEE Transactions on Magnetics 34 (4) (1998) 2243–2252.

[15] U. Kim, D. K. Lieu, Magnetic field calculation in permanent magnet motors with rotor eccentricity: With slotting effect considered, IEEE Transactions on Magnetics 34 (4) (1998) 2253–2266.

[16] U. Kim, D. K. Lieu, Effects of magnetically induced vibration force in brushless permanent-magnet motors, IEEE Transactions on Magnetics 41 (6) (2005) 2164–2172.

[17] D. Kim, M. D. Noh, Y.-w. Park, Unbalanced magnetic forces due to rotor eccentricity in a toroidally wound bldc motor, IEEE Transactions on Magnetics 52 (7) (2016) 1–4.

[18] P. Kumar, P. Bauer, Improved analytical model of a permanent-magnet brushless dc motor, IEEE Transactions on Magnetics 44 (10) (2008) 2299–2309.

[19] K. Boughrara, R. Ibtiouen, Analytical modeling of double cage rotor induction motors in healthy and broken bars conditions, in: 2014 International Conference on Electrical Sciences and Technologies in Maghreb (CISTEM), IEEE, 2014, pp. 1–8.

[20] Y. Li, Q. Lu, Z.-Q. Zhu, Unbalanced magnetic force prediction in permanent magnet machines with rotor eccentricity by improved superposition method, IET Electric Power Applications 11 (6) (2017) 1095–1104.

[21] D. Dorrell, A. Smith, Calculation of ump in induction motors with series or parallel winding connections, IEEE Transactions on Energy Conversion 9 (2) (1994) 304–310.

[22] J. Li, Z. Liu, L. Nay, Effect of radial magnetic forces in permanent magnet motors with rotor eccentricity, IEEE Transactions on Magnetics 43 (6) (2007) 2525–2527.

[23] S. T. Boroujeni, P. Jalali, N. Bianchi, Analytical modeling of slotless eccentric surface-mounted pm machines using a conformal transformation, IEEE Trans. Energy Convers. 32 (2017) 659–662.

[24] J.-P. Wang, D. K. Lieu, Magnetic lumped parameter modeling of rotor eccentricity in brushless permanent-magnet motors, IEEE transactions on magnetics 35 (5) (1999) 4226–4231.

[25] Z. Zhu, D. Howe, Instantaneous magnetic field distribution in brushless permanent magnet dc motors. iii. effect of stator slotting, IEEE transactions on magnetics 29 (1) (1993) 143–151.

[26] Z. Zhu, D. Howe, Instantaneous magnetic field distribution in permanent magnet brushless dc motors. iv. magnetic field on load, IEEE Transactions on Magnetics 29 (1) (1993) 152–158.

[27] S. J.-c. Tian Mu-qin, Li Shuang-shuang, L. Ling-yan, Effects of the mixed fault of broken bars and static eccentricity on current of induction motor, Electric Machines and Control 21 (6) (2017) 2–9.

[28] A. Ghoggal, S. Zouzou, M. Sahraoui, H. Derghal, A. Hadri-Hamida, A winding function-based model of air-gap eccentricity in saturated induction motors, in: 2012 XXth International Conference on Electrical Machines, IEEE, 2012, pp. 2739–2745.

[29] A. R. Munoz, T. A. Lipo, Complex vector model of the squirrel-cage induction machine including instantaneous rotor bar currents, IEEE Transactions on industry applications 35 (6) (1999) 1332–1340.

[30] A. K. Ibrahim, M. I. Marei, H. El-Goharey, S. A. Shehata, Modeling of induction motor based on winding function theory to study motor under stator/rotor internal faults, in: 14th Int. Middle East Power Systems Conference,(MEPCON'10), Cairo, Egypt, 2010.

[31] M. Sahraoui, A. Ghoggal, S.-E. Zouzou, M. Benbouzid, Dynamic eccentricity in squirrel cage induction motors–simulation and analytical study of its spectral signatures on stator currents, Simulation Modelling Practice and Theory 16 (9) (2008) 1503–1513.

[32] W. Chu, Z. Zhu, Average torque separation in permanent magnet synchronous machines using frozen permeability, IEEE Transactions on Magnetics 49 (3) (2012) 1202–1210.

[33] S. Nandi, R. M. Bharadwaj, H. A. Toliyat, Mixed eccentricity in three phase induction machines: analysis, simulation and experiments, in: Conference Record of the 2002 IEEE Industry Applications Conference. 37th IAS Annual Meeting (Cat. No. 02CH37344), Vol. 3, IEEE, 2002, pp. 1525–1532.

[34] S. Nandi, R. M. Bharadwaj, H. A. Toliyat, Performance analysis of a three-phase induction motor under mixed eccentricity condition, IEEE Transactions on Energy Conversion 17 (3) (2002) 392–399.

[35] H. R. Akbari, S. Sadeghi, Calculation of inductances of induction machines under axial nonuniformity conditions, in: 2007 IEEE International Symposium on Industrial Electronics, IEEE, 2007, pp. 1113–1118.

[36] X. Tu, L.-A. Dessaint, N. Fallati, B. De Kelper, Modeling and real-time simulation of internal faults in synchronous generators with parallel-connected windings, IEEE Transactions on Industrial Electronics 54 (3) (2007) 1400–1409.

[37] M. Babaei, J. Faiz, B. M. Ebrahimi, S. Amini, J. Nazarzadeh, A detailed analytical model of a salient-pole synchronous generator under dynamic eccentricity fault, IEEE Transactions on Magnetics 47 (4) (2011) 764–771.

[38] F. Wang, L. Xu, Calculation and measurement of radial and axial forces for a bearingless pmdc motor, in: Conference Record of the 2000 IEEE Industry Applications Conference. Thirty-Fifth IAS Annual Meeting and World Conference on Industrial Applications of Electrical Energy (Cat. No. 00CH37129), Vol. 1, IEEE, 2000, pp. 249–252.

[39] S. Jagasics, I. Vajda, Comparison of different pmsm rotor configurations, in: 2014 IEEE International Electric Vehicle Conference (IEVC), IEEE, 2014, pp. 1–5.

[40] Y. Zhilichev, Analysis of permanent magnet machines using crossing macroelements, IEEE transactions on magnetics 36 (5) (2000) 3122–3124.

[41] H.-f. ZHU, C.-s. ZHU, Electromagnetic racial force analysis of asynchronous motors under static eccentricity (cn), Journal of Mechanical and Electrical Engineering 30 (8) (2013) 981–986.

[42] M. DeBortoli, S. Salon, D. Burow, C. Slavik, Effects of rotor eccentricity and parallel windings on induction machine behavior: A study using finite element analysis, IEEE Transactions on Magnetics 29 (2) (1993) 1676–1682.

[43] P. V. J. Rodríguez, A. Belahcen, A. Arkkio, A. Laiho, J. A. Antonino-Daviu, Air-gap force distribution and vibration pattern of induction motors under dynamic eccentricity, Electrical engineering 90 (3) (2008) 209–218.

[44] B. M. Ebrahimi, J. Faiz, M. Javan-Roshtkhari, A. Z. Nejhad, Static eccentricity fault diagnosis in permanent magnet synchronous motor using time stepping finite element method, IEEE Transactions on Magnetics 44 (11) (2008) 4297–4300.

[45] B. M. Ebrahimi, J. Faiz, M. J. Roshtkhari, Static-, dynamic-, and mixed-eccentricity fault diagnoses in permanent-magnet synchronous motors, IEEE Transactions on Industrial Electronics 56 (11) (2009) 4727–4739.

[46] B. Ebrahimi, J. Faiz, Magnetic field and vibration monitoring in permanent magnet synchronous motors under eccentricity fault, IET electric power applications 6 (1) (2012) 35–45.

[47] M. Sedky, Diagnosis of static, dynamic and mixed eccentricity in line start permanent magnet synchronous motor by using fem, International journal of electrical, robotics, electronics and communications engineering 8 (1) (2014) 29–34.

[48] B. Silwal, P. Rasilo, A. Belahcen, A. Arkkio, Influence of the rotor eccentricity on the torque of a cage induction machine, Archives of Electrical Engineering 66 (2) (2017).

[49] I. P. Brown, D. M. Ionel, D. G. Dorrell, Unbalanced operation of current regulated sine-wave interior permanent magnet machines, in: 2010 IEEE Energy Conversion Congress and Exposition, IEEE, 2010, pp. 4123–4130.

[50] J.-K. Kang, H.-S. Lim, K.-C. Kim, A study on distributed and concentric winding of permanent magnet brushless ac motor, International Journal of Pure and Applied Mathematics 118 (19) (2018) 1805–1815.

[51] Y. Zhou, X. Bao, M. Ma, C. Wang, Calculation and analysis of unbalanced magnetic pulls of different stator winding setups in static eccentric induction motor, Chinese Physics B 27 (8) (2018) 088401.

[52] Y. Zhou, X. Bao, C. Di, L. Wang, Analysis of dynamic unbalanced magnetic pull in induction motor with dynamic eccentricity during starting period, IEEE Transactions on Magnetics 52 (7) (2016) 1–4.

[53] A. Aggarwal, E. G. Strangas, J. Agapiou, Analysis of unbalanced magnetic pull in pmsm due to static eccentricity, in: 2019 IEEE Energy Conversion Congress and Exposition (ECCE), IEEE, 2019, pp. 4507–4514.

[54] A. Arkkio, M. Antila, K. Pokki, A. Simon, E. Lantto, Electromagnetic force on a whirling cage rotor, IEE Proceedings-Electric Power Applications 147 (5) (2000) 353–360.

[55] A. Tenhunen, T. Holopainen, A. Arkkio, Effects of equalizing currents on electromagnetic forces of whirling cage rotor, in: IEEE International Electric Machines and Drives Conference, 2003. IEMDC'03., Vol. 1, IEEE, 2003, pp. 257–263.

[56] A. Tenhunen, T. P. Holopainen, A. Arkkio, Effects of saturation on the forces in induction motors with whirling cage rotor, IEEE Transactions on Magnetics 40 (2) (2004) 766–769.

[57] A. Tenhunen, T. Holopainen, A. Arkkio, Impulse method to calculate the frequency response of the electromagnetic forces on whirling cage rotors, IEE Proceedings-Electric Power Applications 150 (6) (2003) 752–756.

[58] A. Tenhunen, T. Benedetti, T. Holopainen, A. Arkkio, Electromagnetic forces in cage induction motors with rotor eccentricity, in: IEEE International Electric Machines and Drives Conference, 2003. IEMDC'03., Vol. 3, IEEE, 2003, pp. 1616–1622.

[59] T. Holopainen, A. Tenhunen, E. Lantto, A. Arkkio, Unbalanced magnetic pull induced by arbitrary eccentric motion of cage rotor in transient operation. part 1: Analytical model, Electrical Engineering 88 (1) (2005) 13–24.

[60] T. Holopainen, A. Tenhunen, E. Lantto, A. Arkkio, Unbalanced magnetic pull induced by arbitrary eccentric motion of cage rotor in transient operation. part 2: Verification and numerical parameter estimation, Electrical Engineering 88 (1) (2005) 25–34.

[61] A. Burakov, A. Arkkio, Comparison of the unbalanced magnetic pull mitigation by the parallel paths in the stator and rotor windings, IEEE Transactions on Magnetics 43 (12) (2007) 4083–4088.

[62] A. Burakov, A. Arkkio, Low-order parametric force model for eccentric-rotor electrical machine equipped with parallel stator windings and rotor cage, IET Electric Power Applications 1 (4) (2007) 532–542.

[63] E. Lwithwaite, Magnetic equivalent circuits for electrical machines, in: Proceedings of the Institution of Electrical Engineers, Vol. 114, IET, 1967, pp. 1805–1809.

[64] C. Carpenter, Magnetic equivalent circuits, in: Proceedings of the Institution of Electrical Engineers, Vol. 115, IET, 1968, pp. 1503–1511.

[65] G. Slemon, An equivalent circuit approach to analysis of synchronous machines with saliency and saturation, IEEE Transactions on Energy Conversion 5 (3) (1990) 538–545.

[66] Y. Xiao, G. Slemon, M. Iravani, Implementation of an equivalent circuit approach to the analysis of synchronous machines, IEEE transactions on energy conversion 9 (4) (1994) 717–723.

[67] P. Sewell, K. Bradley, J. Clare, P. Wheeler, A. Ferrah, R. Magill, Efficient dynamic models for induction machines, International Journal of Numerical Modelling: Electronic networks, devices and fields 12 (6) (1999) 449–464.

[68] K. Nakamura, K. Kimura, O. Ichinokura, Electromagnetic and motion-coupled analysis for switched reluctance motor based on reluctance network analysis, Journal of Magnetism and Magnetic Materials 290 (2005) 1309–1312.

[69] S. Alli, N. Bracikowski, L. Moreau, M. Zaïm, Reluctance network modeling of a low speed doubly salient permanent magnet machine, in: IECON 2017-43rd Annual Conference of the IEEE Industrial Electronics Society, IEEE, 2017, pp. 2138–2143.

[70] A. Dziechciarz, C. Martis, Magnetic equivalent circuit of synchronous reluctance machine, in: 2016 ELEKTRO, IEEE, 2016, pp. 500–503.

[71] J. Farooq, S. Srairi, A. Djerdir, A. Miraoui, Use of permeance network method in the demagnetization phenomenon modeling in a permanent magnet motor, IEEE Transactions on Magnetics 42 (4) (2006) 1295–1298.

[72] A. Hanic, D. Zarko, Z. Hanic, A novel method for no-load magnetic field analysis of saturated surface permanent-magnet machines using conformal mapping and magnetic equivalent circuits, IEEE Transactions on Energy Conversion 31 (2) (2015) 740–749.

[73] H. Ghoizad, M. Mirsalim, M. Mirzayee, W. Cheng, Coupled magnetic equivalent circuits and the analytical solution in the air-gap of squirrel cage induction machines, International Journal of Applied Electromagnetics and Mechanics 25 (1-4) (2007) 749–754.

[74] W. Xie, G. Dajaku, D. Gerling, Analytical method for predicting the air-gap flux density of dual-rotor permanent-magnet (drpm) machine, in: 2012 XXth International Conference on Electrical Machines, IEEE, 2012, pp. 2766–2771.

[75] Z. Zaimin, J. Shang, Z. Guangyao, Magnetic equivalent circuit model of interior permanent-magnet synchronous machine considering magnetic saturation, in: EVS28 International Electric Vehicle Symposium and Exhibition, KINTEX, 2015, pp. 1–10.

[76] A. Tessarolo, M. Degano, N. Bianchi, On the analytical estimation of the airgap field in synchronous reluctance machine, in: 2014 International Conference on Electrical Machines (ICEM), IEEE, 2014, pp. 239–244.

[77] A. Hemeida, P. Sergeant, Analytical modeling of surface pmsm using a combined solution of maxwell–s equations and magnetic equivalent circuit, IEEE Transactions on Magnetics 50 (12) (2014) 1–13.

[78] V. Ostovic, A method for evaluation of transient and steady state performance in saturated squirrel cage induction machines, IEEE transactions on energy conversion (3) (1986) 190–197.

[79] V. Ostovic, Computation of saturated permanent-magnet ac motor performance by means of magnetic circuits, IEEE transactions on industry applications (5) (1987) 836–841.

[80] V. Ostovic, A novel method for evaluation of transient states in saturated electric machines, IEEE Transactions on Industry Applications 25 (1) (1989) 96–100.

[81] C. Delforge, B. Lemaire-Semail, Induction machine modeling using finite element and permeance network methods, IEEE transactions on magnetics 31 (3) (1995) 2092–2095.

[82] C. Delforge-Delmotte, B. Lemaire-Semail, Modélisation d'une machine asynchrone par réseaux de perméances en vue de sa commande, Journal de Physique III 6 (12) (1996) 1785–1809.

[83] W. Kemmetmüller, D. Faustner, A. Kugi, Modeling of a permanent magnet synchronous machine with internal magnets using magnetic equivalent circuits, IEEE transactions on magnetics 50 (6) (2014) 1–14.

[84] S. D. Sudhoff, B. T. Kuhn, K. A. Corzine, B. T. Branecky, Magnetic equivalent circuit modeling of induction motors, IEEE Transactions on Energy Conversion 22 (2) (2007) 259–270.

[85] B. Asghari, V. Dinavahi, Permeance network based real-time induction machine model, in: Proceedings of the International Conference on Power Systems Transients, 2009.

[86] B. Asghari, V. Dinavahi, Novel transmission line modeling method for nonlinear permeance network based simulation of induction machines, IEEE transactions on magnetics 47 (8) (2011) 2100–2108.

[87] B. Asghari, V. Dinavahi, Experimental validation of a geometrical nonlinear permeance network based real-time induction machine model, in: 2012 IEEE Power and Energy Society General Meeting, IEEE, 2012, pp. 1–15.

[88] P. B. Johns, M. O'Brien, Use of the transmission-line modelling (tlm) method to solve non-linear lumped networks, Radio and Electronic Engineer 50 (1) (1980) 59–70.

[89] F. E. Fleming, C. S. Edrington, Real-time emulation of switched reluctance machines via magnetic equivalent circuits, IEEE Transactions on Industrial Electronics 63 (6) (2016) 3366–3376.

[90] H. Roisse, M. Hecquet, P. Brochet, Simulations of synchronous machines using a electric-magnetic coupled network model, IEEE Transactions on magnetics 34 (5) (1998) 3656–3659.

[91] M. Hecquet, P. Brochet, Time variation of forces in a synchronous machine using electric coupled network model, IEEE transactions on magnetics 34 (5) (1998) 3214–3217.

[92] A. Mahyob, P. Reghem, G. Barakat, Permeance network modeling of the stator winding faults in electrical machines, IEEE transactions on magnetics 45 (3) (2009) 1820–1823.

[93] Y. Amara, G. Barakat, Modeling and diagnostic of stator faults in induction machines using permeance network method, in: PIERS Proceedings, 2011.

[94] N. Leboeuf, T. Boileau, B. Nahid-Mobarakeh, N. Takorabet, F. Meibody-Tabar, G. Clerc, Inductance calculations in permanent-magnet motors under fault conditions, IEEE transactions on magnetics 48 (10) (2012) 2605–2616.

[95] N. Leboeuf, T. Boileau, B. Nahid-Mobarakeh, N. Takorabet, F. Meibody-Tabar, G. Clerc, Effects of imperfect manufacturing process on electromagnetic performance and online interturn fault detection in pmsms, IEEE transactions on Industrial electronics 62 (6) (2015) 3388–3398.

[96] A. Mahyob, M. O. Elmoctar, P. Reghem, G. Barakat, Induction machine modelling using permeance network method for dynamic simulation of air-gap eccentricity, in: 2007 European Conference on Power Electronics and Applications, IEEE, 2007, pp. 1–9.

[97] N. Féki, G. Clerc, P. Velex, Gear and motor fault modeling and detection based on motor current analysis, Electric power systems research 95 (2013) 28–37.

[98] Q. Han, Z. Ding, X. Xu, T. Wang, F. Chu, Stator current model for detecting rolling bearing faults in induction motors using magnetic equivalent circuits, Mechanical Systems and Signal Processing 131 (2019) 554–575.

[99] C. Rasmussen, E. Ritchie, A magnetic equivalent circuit approach for predicting pm motor performance, in: IAS'97. Conference Record of the 1997 IEEE Industry Applications Conference Thirty-Second IAS Annual Meeting, Vol. 1, IEEE, 1997, pp. 10–17.

[100] S. Randi, R. Benlamine, F. Dubas, C. Espanet, Semi-analytical method based on magnetic equivalent circuit for synchronous permanent-magnet machines in ev and hev applications, Mediterranean Journal of Modeling and Simulation 1 (1) (2014).

[101] D. Gómez, A. Rodríguez, I. Villar, A. López-de Heredia, I. Etxeberria-Otadui, Z. Zhu, Improved permeance network model for embedded magnet synchronous machines, in: 2014 International Conference on Electrical Machines (ICEM), IEEE, 2014, pp. 1231–1237.

[102] D. Gómez, A. Rodríguez, I. Villar, A. López-de Heredia, I. Etxeberria-Otadui, Z. Zhu, Experimental validation of an enhanced permeance network model for embedded magnet synchronous machines, Electric Power Systems Research 140 (2016) 836–845.

[103] S. Asfirane, S. Hlioui, Y. Amara, O. De La Barriere, G. Barakat, M. Gabsi, Global quantities computation using mesh-based generated reluctance networks, IEEE Transactions on Magnetics 54 (11) (2018) 1–4.

[104] S. Asfirane, S. Hlioui, S. Mezani, Y. Amara, O. De La Barriere, G. Barakat, M. Gabsi, Scalar magnetic potential interpolation for non-conformal meshing in mesh-based generated reluctance networks, IEEE Transactions on Magnetics 55 (7) (2019) 1–8.

[105] M. Cheng, K. Chau, C. Chan, E. Zhou, X. Huang, Nonlinear varying-network magnetic circuit analysis for doubly salient permanent-magnet motors, IEEE Transactions on Magnetics 36 (1) (2000) 339–348.

[106] M.-F. Hsieh, Y.-C. Hsu, A generalized magnetic circuit modeling approach for design of surface permanent-magnet machines, IEEE Transactions on Industrial Electronics 59 (2) (2011) 779–792.

[107] B. Sheikh-Ghalavand, S. Vaez-Zadeh, A. H. Isfahani, An improved magnetic equivalent circuit model for iron-core linear permanent-magnet synchronous motors, IEEE Transactions on Magnetics 46 (1) (2009) 112–120.

[108] M. Zhu, Y. Fang, X. Huang, X. Yin, Dynamic reluctance mesh modeling and losses evaluation of permanent magnet traction motor, in: 2016 IEEE Conference on Electromagnetic Field Computation (CEFC), IEEE, 2016, pp. 1–1.

[109] J. M. Kokernak, D. A. Torrey, Magnetic circuit model for the mutually coupled switched-reluctance machine, IEEE Transactions on magnetics 36 (2) (2000) 500–507.

[110] S.-H. Han, T. M. Jahns, W. L. Soong, A magnetic circuit model for an ipm synchronous machine incorporating moving airgap and cross-coupled saturation effects, in: 2007 IEEE International Electric Machines & Drives Conference, Vol. 1, IEEE, 2007, pp. 21–26.

[111] J. K. Tangudu, T. M. Jahns, E.-R. Ayman, Z. Zhu, Lumped parameter magnetic circuit model for fractional-slot concentrated-winding interior permanent magnet machines, in: 2009 IEEE Energy Conversion Congress and Exposition, IEEE, 2009, pp. 2423–2430.

[112] A. R. Tariq, C. E. Nino-Baron, E. G. Strangas, Iron and magnet losses and torque calculation of interior permanent magnet synchronous machines using magnetic equivalent circuit, IEEE transactions on magnetics 46 (12) (2010) 4073–4080.

[113] H. W. Derbas, J. M. Williams, A. C. Koenig, S. D. Pekarek, A comparison of nodal- and mesh-based magnetic equivalent circuit models, IEEE Transactions on Energy Conversion 24 (2) (2009) 388–396.

[114] J. Law, T. Busch, T. Lipo, Magnetic circuit modelling of the field regulated reluctance machine. part i: Model development, IEEE transactions on energy conversion 11 (1) (1996) 49–55.

[115] T. J. Busch, J. Law, T. Lipo, Magnetic circuit modeling of the field regulated reluctance machine. part ii: Saturation modeling and results, IEEE transactions on energy conversion 11 (1) (1996) 56–61.

[116] F. Pedrayes, C. Rojas, M. Cabanas, M. Melero, G. Orcajo, J. Cano, Application of a dynamic model based on a network of magnetically coupled reluctances to rotor fault diagnosis in induction motors, in: 2007 IEEE International Symposium on Diagnostics for Electric Machines, Power Electronics and Drives, IEEE, 2007, pp. 241–246.

[117] M. L. Bash, J. M. Williams, S. D. Pekarek, Incorporating motion in mesh-based magnetic equivalent circuits, IEEE Transactions on Energy Conversion 25 (2) (2010) 329–338.

[118] M. L. Bash, S. D. Pekarek, Modeling of salient-pole wound-rotor synchronous machines for population-based design, IEEE Transactions on Energy Conversion 26 (2) (2011) 381–392.

[119] R. Wang, M. Bash, S. Pekarek, A. Larson, R. van Maaren, A voltage input-based magnetic equivalent circuit model for wound rotor synchronous machines, in: 2013 International Electric Machines & Drives Conference, IEEE, 2013, pp. 586–593.

[120] R. Wang, S. Pekarek, M. L. Bash, A. Larson, R. Van Maaren, Incorporating dynamics in a mesh-based magnetic equivalent circuit model of synchronous machines, IEEE Transactions on Energy Conversion 30 (3) (2015) 821–832.

[121] S. Serri, A. Tani, G. Serra, A method for non-linear analysis and calculation of torque and radial forces in permanent magnet multiphase bearingless motors, in: International Symposium on Power Electronics Power Electronics, Electrical Drives, Automation and Motion, IEEE, 2012, pp. 75–82.

[122] D. C. Horvath, S. D. Pekarek, S. D. Sudhoff, A scaled mesh/nodal formulation of magnetic equivalent circuits with motion, IEEE Transactions on Energy Conversion 34 (1) (2018) 58–69.

[123] A. Smith, D. Dorrell, Calculation and measurement of unbalanced magnetic pull in cage induction motors with eccentric rotors. part 1: Analytical model, IEE Proceedings-Electric Power Applications 143 (3) (1996) 193–201.

[124] D. GUO, F.-l. CHU, D. Chen, The unbalanced magnetic pull and its effects on vibration in a three-phase generator with eccentric rotor, Journal of sound and Vibration 254 (2) (2002) 297–312.

[125] X. Xu, Q. Han, F. Chu, Nonlinear vibration of a generator rotor with unbalanced magnetic pull considering both dynamic and static eccentricities, Archive of Applied Mechanics 86 (8) (2016) 1521–1536.

[126] J. Stephenson, J. Corda, Computation of torque and current in doubly salient reluctance motors from nonlinear magnetisation data, in: Proceedings of the Institution of Electrical Engineers, Vol. 126, IET, 1979, pp. 393–396.

[127] H. Duru, A method for the modeling and analysis of permanent magnet synchronous machines (2007).

[128] R. Belmans, A. Vandenput, W. Geysen, Influence of unbalanced magnetic pull on the radial stability of flexible-shaft induction machines, in: IEE Proceedings B (Electric Power Applications), Vol. 134, IET, 1987, pp. 101–109.

[129] B. Wu, W. Sun, Z. Li, Z. Li, Circular whirling and stability due to unbalanced magnetic pull and eccentric force, Journal of Sound and vibration 330 (21) (2011) 4949–4954.

[130] X. Xu, Q. Han, F. Chu, A four degrees-of-freedom model for a misaligned electrical rotor, Journal of Sound and Vibration 358 (2015) 356–374.

[131] X. Xu, Q. Han, F. Chu, A general electromagnetic excitation model for electrical machines considering the magnetic saturation and rub impact, Journal of Sound and Vibration 416 (2018) 154–171.

[132] X. Chen, S. Yuan, Z. Peng, Nonlinear vibration for pmsm used in hev considering mechanical and magnetic coupling effects, Nonlinear Dynamics 80 (1) (2015) 541–552.

[133] C. Xiang, F. Liu, H. Liu, L. Han, X. Zhang, Nonlinear dynamic behaviors of permanent magnet synchronous motors in electric vehicles caused by unbalanced magnetic pull, Journal of Sound and Vibration 371 (2016) 277–294.

[134] F. Liu, C. Xiang, H. Liu, L. Han, Y. Wu, X. Wang, P. Gao, Asymmetric effect of static radial eccentricity on the vibration characteristics of the rotor system of permanent magnet synchronous motors in electric vehicles, Nonlinear Dynamics 96 (4) (2019) 2581–2600.

[135] H. Liu, Y. Wu, X. Wang, P. Yan, X. Zhang, Nonlinear normal modes and primary resonance for permanent magnet synchronous motors with a nonlinear restoring force and an unbalanced magnetic pull, Nonlinear Dynamics 97 (2) (2019) 1197–1213.

[136] T. Holopainen, A. Tenhunen, A. Arkkio, Electromagnetic circulatory forces and rotordynamic instability in electric machines, in: Proceedings of the 6th International Conference on Rotor Dynamics. Sydney, Australia, 2002, pp. 30–9.

[137] T. P. Holopainen, A. Tenhunen, A. Arkkio, Electromechanical interaction in rotordynamics of cage induction motors, Journal of sound and vibration 284 (3-5) (2005) 733–755.

[138] T. P. Holopainen, A. Tenhunen, A. Arkkio, Electromechanical interaction in rotor vibrations of electric machines, in: Proceedings of the 5th World Congress on Computational Mechanics, Vol. 10, Vienna University of Technology, 2002.

[139] X. Han, A. Palazzolo, Unstable force analysis for induction motor eccentricity, Journal of Sound and Vibration 370 (2016) 230–258.

[140] F. Boy, H. Hetzler, A co-energy based approach to model the rotordynamics of electrical machines, in: International Conference on Rotor Dynamics, Springer, 2018, pp. 190–204.

[141] F. Boy, H. Hetzler, An asymptotic approximation of the magnetic field and forces in electrical machines with rotor eccentricity, Electrical Engineering 100 (2) (2018) 389–399.

[142] F. Boy, H. Hetzler, The effect of field damping on rotordynamics of non-salient pole generators, Technische Mechanik-European Journal of Engineering Mechanics 37 (2-5) (2017) 384–393.

[143] F. Boy, Modelling the Rotordynamics of Saturated Electrical Machines Due to Unbalanced Magnetic Pull, Kassel University Press, 2020.

[144] N. L. Lundström, J.-O. Aidanpää, Dynamic consequences of electromagnetic pull due to deviations in generator shape, Journal of Sound and Vibration 301 (1-2) (2007) 207–225.

[145] N. L. Lundström, A. Grafström, J.-O. Aidanpää, Small shape deviations causes complex dynamics in large electric generators, The European Physical Journal Applied Physics 66 (2) (2014) 20903.

[146] H. Im, H. H. Yoo, J. Chung, Dynamic analysis of a bldc motor with mechanical and electromagnetic interaction due to air gap variation, Journal of Sound and Vibration 330 (8) (2011) 1680–1691.

[147] D. Mazur, M. Trojnar, Modelling of electrical and mechanical phenomena in induction motors with air-gap eccentricity, in: Proc. International Conference on Renewable Energy and Power Quality ICREPQ, 2003, p. 2003.

[148] M. Donát, Computational modelling of the unbalanced magnetic pull by finite element method, Procedia Engineering 48 (2012) 83–89.

[149] M. Donat, Computational modeling of the dynamic behavior of the induction motor rotor, in: I Annals of DAAAM for 2012 & Proceedings of the 23rd International DAAAM Symposium, Vol. 23, 2012, pp. 0191–0194.

[150] M. Donát, D. Dušek, Eccentrically mounted rotor pack and its influence on the vibration and noise of an asynchronous generator, Journal of Sound and Vibration 344 (2015) 503–516.

[151] J. Martinez, A. Belahcen, J. Detoni, A 2d magnetic and 3d mechanical coupled finite element model for the study of the dynamic vibrations in the stator of induction motors, Mechanical Systems and Signal Processing 66 (2016) 640–656.

[152] V. Climente-Alarcon, R. Sundaria, J. Panchal, A. Arkkio, Simulation of an induction motor's rotor after connection, IEEE Transactions on Magnetics 53 (6) (2017) 1–4.

[153] A. Laiho, T. P. Holopainen, P. Klinge, A. Arkkio, Distributed model for electromechanical interaction in rotordynamics of cage rotor electrical machines, Journal of sound and vibration 302 (4-5) (2007) 683–698.

[154] X. Chen, H. Wei, T. Deng, Z. He, S. Zhao, Investigation of electromechanical coupling torsional vibration and stability in a high-speed permanent magnet synchronous motor driven system, Applied Mathematical Modelling 64 (2018) 235–248.

[155] P. Pennacchi, L. Frosini, Dynamical behaviour of a three-phase generator due to unbalanced magnetic pull, IEE Proceedings-Electric Power Applications 152 (6) (2005) 1389–1400.

[156] P. Pennacchi, L. Frosini, Computational model for calculating the dynamical behaviour of generators caused by unbalanced magnetic pull and experimental validation, in: International Design Engineering Technical Conferences and Computers and Information in Engineering Conference, Vol. 48027, 2007, pp. 1313–1326.

[157] L. Frosini, P. Pennacchi, C. M. Stoisser, Analysis of unbalanced magnetic pull calculation in generators with two pole pairs, in: International Design Engineering Technical Conferences and Computers and Information in Engineering Conference, Vol. 48982, 2009, pp. 1195–1203.

[158] R. K. Gustavsson, J.-O. Aidanpää, The influence of nonlinear magnetic pull on hydropower generator rotors, Journal of Sound and Vibration 297 (3-5) (2006) 551–562.

[159] M. Mair, B. Weilharter, K. Ellermann, Rotor vibrations in electrical machines due to electromagnetic forces, in: Proceedings of the 9th IFToMM International Conference on Rotor Dynamics, Springer, 2015, pp. 601–611.

[160] X. Li, A. Bourdon, D. Rémond, S. Kœchlin, D. Prieto, Angular-based modeling of unbalanced magnetic pull for analyzing the dynamical behavior of a 3-phase induction motor, Journal of Sound and Vibration 494 (2021) 115884.

[161] A. Zhang, Y. Bai, B. Yang, H. Li, Analysis of nonlinear vibration in permanent magnet synchronous motors under unbalanced magnetic pull, Applied Sciences 8 (1) (2018) 113.

[162] H. Kim, A. Posa, J. Nerg, J. Heikkinen, J. T. Sopanen, Analysis of electromagnetic excitations in an integrated centrifugal pump and permanent magnet synchronous motor, IEEE Transactions on Energy Conversion 34 (4) (2019) 1759–1768.

[163] H. Kim, A. Posa, J. Nerg, J. Heikkinen, J. Sopanen, Vibration effect by unbalanced magnetic pull in a centrifugal pump with integrated permanent magnet synchronous motor, in: International Conference on Rotor Dynamics, Springer, 2018, pp. 221–233.

[164] J. L. Gomez, A. Bourdon, H. André, D. Rémond, Modelling deep groove ball bearing localized defects inducing instantaneous angular speed variations, Tribology International 98 (2016) 270–281. doi:10.1016/j.triboint.2016.02.032. URL https://linkinghub.elsevier.com/retrieve/pii/S0301679X16001171

[165] D. Rémond, J. Antoni, R. B. Randall, Instantaneous angular speed (ias) processing and related angular applications, Mechanical Systems and Signal Processing 1 (45) (2014) 24–27.

[166] I. Boldea, S. A. Nasar, The induction machine handbook, Electric power engineering series, CRC Press, Boca Raton, 2002.

[167] AFNOR, Mechanical vibration, balance quality requirements for rotors in a constant (rigid) state. iso 1940-1:2003(f).pdf.

[168] D. Guo, F. Chu, D. Chen, The unbalanced magnetic pull and its effects on vibration in a three-phase generator with eccentric rotor, Journal of Sound and Vibration 254 (2) (2002) 297–312. doi:10.1006/jsvi.2001.4088.
URL http://linkinghub.elsevier.com/retrieve/pii/S0022460X0194088X

[169] D. C. Meeker, Finite element method magnetics (version 4.2) (28 Feb 2018).
URL https://www.femm.info

[170] J. F. Gieras, Permanent magnet motor technology: design and applications, 3rd Edition, CRC Press, Boca Raton, 2010, oCLC: ocn426147339.

[171] PHANIBABU, Torque angle versus load or power angle (16 June 2019).
URL https://electengmaterials.com/torque-angle-versus-load-or-power-angle/

[172] E. C. Lovelace, M. J. Thomas, H. L. Jeffrey, A saturating lumped parameter model for an interior pm synchronous machine.pdf, IEEE Transactions on Industry Applications 38 (3) (2002) 645–650.

[173] C. Neagoe, F. Ossart, Analysis of convergence in nonlinear magnetostatic finite elements problems, IEEE Trans. Magn. 30 (5) (1994) 2865–2868. doi:10.1109/20.312534.
URL http://ieeexplore.ieee.org/document/312534/

[174] A. Marrocco, Analyse numerique de problemes d'electrotechnique, Ann. Sc. Math. Québec 1 (2) (1997) 271–296.

[175] D. C. Horvath, S. D. Pekarek, S. D. Sudhoff, A scaled mesh/nodal formulation of magnetic equivalent circuits with motion, IEEE Trans. Energy Convers. 34 (1) (2019) 58–69. doi:10.1109/TEC.2018.2855100.
URL https://ieeexplore.ieee.org/document/8409995/

[176] H. W. Derbas, J. M. Williams, A. C. Koenig, S. D. Pekarek, A comparison of nodal- and mesh-based magnetic equivalent circuit models, IEEE Trans. Energy Convers. 24 (2) (2009) 388–396. doi:10.1109/TEC.2008.2002037.
URL http://ieeexplore.ieee.org/document/4957571/

[177] M. L. Bash, S. D. Pekarek, Incorporating motion in mesh-based magnetic equivalent circuits, IEEE TRANSACTIONS ON ENERGY CONVERSION 25 (2) (2010) 10.

[178] S. D. Sudhoff, B. T. Kuhn, K. A. Corzine, B. T. Branecky, Magnetic equivalent circuit modeling of induction motors, IEEE Trans. On Energy Conversion 22 (2) (2007) 259–270. doi:10.1109/TEC.2006.875471.
URL http://ieeexplore.ieee.org/document/4207473/

[179] H. Kim, A. Posa, J. Nerg, J. Heikkinen, J. T. Sopanen, Analysis of electromagnetic excitations in an integrated centrifugal pump and permanent magnet synchronous motor, IEEE Trans. Energy Convers. 34 (4) (2019) 1759–1768. doi:10.1109/TEC.2019.2935785.
URL https://ieeexplore.ieee.org/document/8805163/

[180] M. J. DeBortoli, M. Corp, S. J. Salon, C. J. Slavik, Effects of rotor eccentricity and parallel windings on induction machine behavior: A study using finite element analysis 7.

[181] A. Sathyan, H. Dadkhah, B. Bilgin, A. Emadi, J. W. Jiang, Analysis of unbalanced magnetic pull in eccentric interior permanent magnet machines with series and parallel windings, IET Electric Power Applications 10 (6) (2016) 526–538. doi:10.1049/iet-epa.2015.0186.
URL https://digital-library.theiet.org/content/journals/10.1049/iet-epa.2015.0186

[182] C. Smith, Calculation o f u.m.p. i n induction motors with series or parallel winding connections 7.

[183] M. Topenot, M. Ouisse, G. Chevallier, D. Vaillant, Structural dynamics of electric machines subjected to pwm excitations, in: SURveillance VIbrations SHocks NOise, 2019.

FOLIO ADMINISTRATIF

THESE DE L'UNIVERSITE DE LYON OPEREE AU SEIN DE L'INSA LYON

NOM : LI

DATE de SOUTENANCE : 01/09/2021

Prénoms : Xiaowen

TITRE : Angular approach based multiphysics modeling of electric motors for analyzing dynamic behaviors under the influence of different architectures

NATURE : Doctorat

Numéro d'ordre : 2021LYSEI048

Ecole doctorale : MEGA

Spécialité : Mécanique - Génie Mécanique - Génie Civil

RESUME :

The requirement for a more compact solution in electrical machines leads to a design trend of increasing rotational speeds and lightening mechanical structures. These changes can lead to non-linear vibrations and even to the rotor-stator contact in the worst case. These vibrational phenomena are mainly generated by the unbalanced magnetic pull (UMP) inside the machine due to the air gap eccentricity. In order to study the influence of different architectures on these complex vibrational phenomena, a multiphysics electrical machine model with strong electro-magnetic-mechanical couplings is developed in this thesis. The different interaction paths between the UMP force and the radial displacements of the rotor have been introduced to fully strengthen this coupling considered on both radial and rotational movements. The proposed model is established on the basis of the angular approach so that an originality of this work lies in the fine understanding of the instantaneous angular velocity (or angle-time relationship) of the motor shaft. This originality also provides the formalism and the framework to solve the problems in the non-stationary operating conditions. The mixed mesh/nodal permeance network is also adopted to model the deformed magnetic field under the effect of the rotor eccentricity and the mass eccentricity. This multiphysics model is validated by comparing with a more classical finite element model in the quasi-static regime. Two traditional electric motor architectures (the squirrel cage induction motor and the permanent magnet synchronous motor) are chosen as examples of the application of the proposed model. The physical characteristics of the UMP force and its frequency components associated with the input static eccentricity are studied in the case of the induction motor. Then, the self-excited vibration of the rotor is analyzed through the UMP waveform and the radial displacements of the rotor center in the case of a permanent magnet synchronous motor architecture. The resonance peak generated at the modified natural frequency by the mass unbalance excitation is also identified from the two results. The two models are finally used respectively to study the influence of different mechanical structures and the effect of different winding configurations.

MOTS-CLÉS: Multiphysics model, Electric motors, Angular approach, Rotor eccentricity, Mass eccentricity, Unbalanced magnetic pull, Non-stationary operating conditions

Laboratoire (s) de recherche : Laboratoire de Mécanique des Contacts et des Structures
UMR CNRS 5259 - INSA de Lyon
18-20 rue des Sciences
69621 Villeurbanne Cedex FRANCE

Directeur de thèse : M. Didier REMOND

Président de jury :

Composition du jury : H. HETZLER, B. LEMAIRE SEMAIL, G. CHEVALLIER, M. MCCLELLAND, G. CLERC, A. BOURDON, D. REMOND, S. KOECHLIN